TECHNISCHE UNIVERSITÄT MÜNCHEN
Department Chemie
Lehrstuhl II
für Organische Chemie

Structure and Dynamics using NMR Spectroscopy

Jochen Jan Klages

Vollständiger Abdruck der von der Fakultät für Chemie der Technischen Universität München zur Erlangung des akademischen Grades eines

Doktors der Naturwissenschaften

genehmigten Dissertation.

Vorsitzender:	Univ.-Prof. Dr. St. J. Glaser
Prüfer der Dissertation:	1. Univ.-Prof. Dr. H. Kessler
	2. Univ.-Prof. Dr. W. Domcke
	3. Priv.-Doz. Dr. B. W. Luy

Die Dissertation wurde am 17.06.2008 bei der Technischen Universität München eingereicht und durch die Fakultät für Chemie am 29.09.2008 angenommen.

To my parents.

Die Grenzen meiner
Sprache bedeuten die
Grenzen meiner Welt.

(Ludwig Wittgenstein)

Acknowledgement

The work presented in this thesis was prepared from October 2003 until Feburary 2008 in the group of Prof. Dr. Horst Kessler at the Department of Chemistry of the Technical University of Munich, Germany.

I would like to thank my supervisor Prof. Dr. Kessler for giving me the opportunity to join his group, for the excellent research facilities, for unrestricted support, and for giving me lots of personal freedom.

Of course there are a lot of other people I would like to thank:

- The staff members of the NCE: Dr. Murray Coles, Dr. Sandra Groscurth, Dr. Vincent Truffault, Dr. Michael John, Dr. Markus Heller, Dr. Melina Haupt, and Dr. Ilka Varnay for the great atmosphere and ambitious science.
- Dr. Gustav Gemmecker, Dr. Murray Coles, Dr. Burkhard Luy, and Dr. Sandra Groscurth for critical reading of my thesis and providing constructive suggestions, especially where to place a comma.
- Dr. Burkhard Luy for not only the nice collaborations but also for teaching me lot on NMR and other interresting things.
- My students Cajethan Neubauer, Denis Jurkin, Wilhelm Palm, Claudia Wurzenberger, and Michael Braun.
- The system administrators Dr. Rainer Haessner and Alexander Frenzel for their support.
- Dr. Rainer Haessner for his support in NMR spectrometer hardware concerns and fighting all the other world threatening issues.
- Dr. Alexander Kotzsch and Prof. Dr. Thomas Müller for the nice and interresting cooperation at the BMPR-IA project.

- The secretaries Beate Diaw, Marianne Machule, and Evelyn Bruckmaier for their professional work.
- My hockey team from 'HC Wacker München' for reminding me that there is a life beside chemistry.
- Franz Hagn for some nice trips to the ENC.
- My flat mates Alexandra Gonaus, Ricarda Brandes, and Marc Scheloske for sharing the 'WG' with me and supporting me with lots of M&M's during writing.
- Dr. Gerd Hauser for picking me up each lunch break though I was always late, for interessing discussions on the 'Wahlrecht', the newest popcorn movies, and for always 'cleaning up' the trays at the Mensa.
- Dr. Björn Heitmann for giving me the opportunity to spend my life in Switzerland, voting me the 'MDM', and being a very good 'lala'.
- Dr. Hans Rainer Porth for introducing me to chemistry and supporting me during my first years as scientist.
- The 'Kicker' crew for helping me to digest the sometimes stodgy Mensa food.
- All other group members for a wonderful time inside and outside the lab.
- Martina Dressel for endless patience throughout the admittedly quite long time of the preparation of this thesis, her love which relieved this process and for so many other things that would take ages to note down and would prolong the process of writing even further and are therefore left to a quiet moment.

I am deeply grateful to my family, especially to my parents, for their endless support over the years. All this would not have been possible without them.

Thank you.

Parts of this thesis have been published:

J. Klages, C. Neubauer, M. Coles, H. Kessler, B. Luy, 'Structure Refinement of Cyclosporin A in Chloroform by Using RDCs Measured in a Stretched PDMS-gel', *ChemBioChem* **6**, *2005*, 1672–1678.

J. Klages, S. Glaser, H. Kessler, B. Luy, 'J-ONLY-TOCSY: Efficient Suppression of RDC-Induced Transfer in Homonuclear TOCSY Experiments Using JESTER-1-Derived Multiple Pulse Sequences', *J. Magn. Reson.* **189**, *2007*, 217–227.

J. Klages, A. Kotzsch, M. Coles, J. Nickel, T. Müller, H. Kessler, 'The Solution Structure of BMPR-IA Reveals a Local Disorder-to-Order Transition upon BMP-2 Binding', *Biochemistry* **47**, *2008*, 11930–11939.

Published review articles:

J. Klages, M. Coles, H. Kessler, 'NMR-based screening: a powerful tool in fragment-based drug discovery', *Mol. BioSyst.* **2**, *2006*, 318–332.

J. Klages and H. Kessler, 'NMR in Drug Discovery', in Comprehensive Medicinal Chemistry II, Eds. D. J. Triggle and J. B. Taylor, Elsevier: Oxford 2006.

Contents

List of Figures

List of Tables

Abbreviations and Symbols

	Abbrevations
1D	One-dimensional
2D	Two-dimensional
3D	Three-dimensional
AA	Amino acid
BMPR-IA	Bone morphogenetic protein receptor IA
BMPR-IA$_{ec}$	BMPR-IA extracellular domain
BMPR-IA$_{ec/sf}$	BMPR-IA$_{ec}$ truncated form
COSY	Correlation spectroscopy
CSA	Chemical shift anisotropy
CsA	Cyclosporin A
CSI	Chemical shift index
cw	Continuous wave
DD	Dipole-dipole interaction
DNA	Deoxyribonucleic acid
E.COSY	Exclusive correlation spectroscopy
EXSY	Exchange spectroscopy
HIHAHA	Heteronuclear isotropic Hartmann-Hahn
HOHAHA	Homonuclear Hartmann-Hahn
HMQC	Heteronuclear multi quantum correlation
HSQC	Heteronuclear single quantum correlation
INEPT	Insensitive nuclei enhanced by polarization transfer
MD	Molecular dynamics
MF	Model-free
NMR	Nuclear magnetic resonance
hetNOE	Heteronuclear Overhauser enhancement
NOE	Nuclear Overhauser enhancement
NOESY	Nuclear Overhauser enhancement spectroscopy

RCSA	Residual chemical shift anisotropy
RDC	Residual dipolar coupling
rf	Radio frequency
RNA	Ribonucleic acid
ROE	Rotating frame nuclear Overhauser enhancement
ROESY	Rotating frame nuclear Overhauser enhancement spectroscopy
RQC	Residual quadrupolar coupling
TOCSY	Total correlation spectroscopy
TROSY	Transverse relaxation optimized spectroscopy

Chemicals

AIBN	Azobisiso-butyronitrile
APS	Ammonium persulfate
DBPA	2,3-Dibromopro-pionic acid
DMSO	Dimethylsulfoxide
IPTG	Isopropyl-β-D-thio-galactopyranoside
PDMS	Polydimethyl-siloxane
PS	Polystyrene
TFE	Trifluoroethanol
THF	Tetrahydrofuran
TMEDA	Tetramethyl-ethylenediamine
TMS	Tetramethylsilane
TRIS	Tris-(hydroxy-methyl)-amino-methane
TSP	Trimethylsilyl propionate

Symbols

B_0	Static magnetic field strength
C	CSA coupling constant
$C(t)$	Rotational correlation function
$C_\mathrm{i}(t)$	Correlation function of the internal motion
$C_\mathrm{o}(t)$	Correlation function of the overall motion
$\chi^{1,2}$	Sidechain dihedral angles
D	Dipolar coupling constant
$\mathbf{D}$	Dipolar coupling tensor
$D_\parallel$	Parallel component of the rotational diffusion tensor
$D_\perp$	Perpendicular component of the rotational diffusion tensor

δ	Chemical shift difference
Δ_s	Resonance splitting
γ	Gyromagnetic ratio
$\Gamma_{\delta}^{w,w'}$	Partial relaxation rate
$\mathcal{H}$	Hamiltonian
$\hbar$	Planck constant divided by 2π
$J(\omega)$	Orientational spectral density function
J	Scalar coupling constant
$\mathbf{J}$	Scalar coupling tensor
k_{B}	Boltzmann constant
ν	Frequency
ν^R	Rabi frequency
ω	Larmor frequency
Ω	Larmor frequency difference
Φ, Ψ	Backbone dihedral angles
R_{ex}	Exchange contribution to the relaxation rate constant
R_1	Longitudinal or spin-lattice relaxation rate constant
$R_{1\rho}$	Transverse relaxation rate constant in the rotating frame
R_2	Transverse or spin-spin relaxation rate constant
r	Interatomic distance
σ	Spin density matrix
σ_{xx}, σ_{yy}, σ_{zz}	Principal components of the CSA tensor
S^2	Generalized squared order parameter of the internal motion
S_f^2	Generalized squared order parameter of the fast internal motion
S_s^2	Generalized squared order parameter of the slow internal motion
T	Temperature
T_{α}^{ij}	Transfer amplitude
T_1	Longitudinal or spin-lattice relaxation time constant
$T_{1\rho}$	Transverse relaxation time constant in the rotating frame
T_2	Transverse or spin-spin relaxation time constant

τ_{cycl}	Cycle time
τ_c	Rotational correlation time
τ_f	Correlation time of the fast internal motion
τ_i	Correlation time of the internal motion
τ_s	Correlation time of the slow internal motion
U	Propagator

Units

Å	Ångstrøm
°C	Degree Celsius
g	Gram
kGy	Kilogray
Hz	Hertz
kHz	Kilohertz
MHz	Megahertz
K	Kelvin
L	Liter
μL	Microliter
mL	Milliliter
m	Meter
mm	Millimeter
pm	Picometer
mM	Millimolar
min	Minutes
ppb	Parts per billion (10^{-9})
ppm	Parts per million (10^{-6})
μs	Microsecond
ms	Millisecond
ns	Nanosecond
ps	Picosecond
s	Second
T	Tesla

Chapter 1

Introduction

'*Who solely wants to determine structures with NMR spectroscopy has not understood anything*'. This statement was given by *Richard R. Ernst*[1] on the NMR symposium 'Future perspectives in biomolecular NMR spectroscopy' in Munich 2008. Though rather provocative, it still meets a key point in nowadays understanding of molecular structure, especially in the understanding of structures of large biomacromolecules. Of course, NMR spectroscopy is a handy tool to determine structures of proteins, nucleic acids or other molecules and materials, but X-ray crystallography is probably the faster and more reliable technique in many cases. Just in some situations NMR spectroscopy is the better or only choice to obtain structural information at atomic resolution, for example in case of molecules with large unstructured parts, molecules showing chemical exchange, or inherently unfolded molecules – basically, everything that does not crystallize.

Today, structures are published with steadily increasing resolution, which leads to the illusion that these structures are 'rock solid'. But the picture of a rigid molecule is anything but correct. Even for the most structured parts fast librational components are observed, as was shown by high level MD simulations. It has to be kept in mind, that structural coordinates, as found in the RCSB protein data bank (PDB) for example, only represent the *time averaged structure* of a molecule.

1 Nobel prize laureate in 1991 for his achievements in NMR spectroscopy.

Though structures are very important for the understanding of molecular properties and functions it has been more and more recognized that also the dynamics of a biomacromolecule plays an important role for its function.For example enzymatic catalysis, ligand binding, and allosteric regulation are processes where the function is causally related to the dynamics. The above quotation refers to this fact and highlights the unique position of NMR spectroscopy in this context. Unlike other techniques NMR spectroscopy offers the opportunity to sample molecular motions on an atomic level. Here, a wide range of timescales is accessible ranging from very fast motions on the ps-ns timescale to comparably slow motions that can be monitored by 'real-time' spectroscopy. Therefore, the structure and the dynamics of a molecule may be regarded as the two sides of a coin which are inseparable connected to each other.

In contrast to X-ray crystallography, where basically only one parameter is observable, i.e., the electron density, several parameters can be monitored in NMR spectroscopy, e.g., chemical shifts, couplings, or relaxational parameters. In principal, all of these parameters are sensitive to the dynamics of the molecule, but each samples motions on a different timescale. This is a further advantage of NMR spectroscopy over other methods, as the individual modes of the complex dynamical behavior can be observed separately. X-ray crystallography only offers the electron density as experimental observable, which translates into resolution and is encoded in the individual 'B-factors'. But these B-factors, if at all, may only give a qualitative picture of the dynamical properties. As a rule of thumb, it can be stated that an undefined electron density roughly correlates with increased motions on the ps-ns timescale, but that motions on the μs-ms timescale, i.e., conformational exchange, tend to crystalize in only one conformation.

NMR parameters like scalar couplings, isotropic chemical shifts, nuclear Overhauser enhancements, or simply the linewidth, are often referred to as 'classical' NMR parameters. Since the discovery of weakly aligning media in 1995 for the use in high resolution NMR spectroscopy 'new' parameters were made accessible, which offer a wealth of information. These parameters rely on the fact that anisotropic parameters, which depend on the orientation of the molecule relative to the external magnetic field, do not completely average to zero in the alignment medium. The most prominent anisotropic parameters are perhaps residual dipolar couplings (RDCs), but also residual chemical shift anisotropy (RCSA) and residual quadrupolar couplings (RQCs) become observable. The amenity of these parameters is their comparable easy measurability and straightforward relation to struc-

ture and dynamics. Hence, their benefits are increasingly used for these tasks and even facilitated the analysis of inherently unfolded molecules.

In this thesis, Chapter 3 deals with the measurement of RDCs or more precisely, ^{1}H-^{1}H RDCs which have been largely unaccessible for long times. These couplings are especially interesting for small molecules were no isotopic labeling schemes are available and measurements are usually restricted to $^{1}D_{CH}$-couplings. The newly developed technique is based on total correlation spectroscopy (TOCSY) which enables a scaling of the dipolar couplings by the use of different mixing sequences and consequently allows for the extraction of the desired information.

In Chapter 4 the structure and the dynamics of the extracellular domain of bone morphogenetic protein receptor IA is investigated. This receptor binds the transforming growth factors-β which are responsible for several steps in the embryonic development and regeneration processes in the adult organism. The investigation of the receptor enables a detailed view on the binding mechanism. Here, the studies are mainly based on 'classical' NMR parameters.

Chapter 5 is concerned with the inclusion of RDCs as new orientational parameter into structure calculations of cyclic peptides. As pointed out above, only the time averaged structure can be investigated, however, this deviates significantly from the structure obtained only with 'classical' NMR parameters. Here, the impact and wealth of anisotropic parameters in the analysis of small molecules could be shown.

Chapter 2

Theoretical Aspects

In this chapter the theoretical foundations of the experiments presented in this thesis are described. Equations of central importance are derived and discussed. In Section 2.1 the theory of Hartmann-Hahn experiments is discussed briefly, which forms the basis for the experiments presented in Chapter 3. Section 2.2 reviews the theoretical aspects of RDCs which are used especially in Chapter 3 and Chapter 5. Moreover, a rough overview on relaxation theory is given in Section 2.3, emphasizing the aspects of ^{15}N-relaxation in proteins, as these are used in Chapter 4 for analysis.

2.1 Hartmann-Hahn Transfer

One of the central building blocks in modern, multidimensional NMR spectroscopy is formed by the transfer steps for coherences and polarization. There are two fundamentally different phenomena which may underly these steps, either they are *incoherent* or *coherent*. Incoherent transfer is associated with relaxation phenomena and is therefore discussed in Section 2.3. This section deals with coherent transfer of magnetization and in particular with homonuclear *Hartmann-Hahn* (HOHAHA) or *TOCSY*[1] experiments in liquids.

Energy transfer in physically coupled systems is closely related to a match of energy levels. For example, a pair of coupled pendula may only exchange their energy fully if the two pendula have the same oscillatory fre-

quency in the absence of a coupling. Likewise, the interchange of charges in a resonant circuit is most efficient if the circuit is accurately tuned, i.e., the capacity of the capacitor matches the coils inductance. The same principles also apply to nuclear spins which may exchange energy if their resonance frequencies are matched.[1] Typically, nuclear spins do not exhibit the same resonance frequency, so energy-matched conditions have to be created artificially by rf-irradiation schemes (see Sec. 2.1.2). In the following discussion the equations underlying homonuclear Hartmann-Hahn transfer are derived and discussed.

Consider a homonuclear spin system with two spin-$\frac{1}{2}$ nuclei, termed I_1 and I_2. If these spins are placed in an external magnetic field with its main axis pointing along the z-axis, the spins will have the two resonance frequencies ν_1 and ν_2 in the rotating frame of reference. The strength of the coupling will be given by the scalar coupling constant J_{12}. This will result in the Hamiltonian $\mathcal{H}_0$ for the spin system

$$\mathcal{H}_0 = \mathcal{H}_Z + \mathcal{H}_J. \tag{2.1}$$

Here $\mathcal{H}_Z$ is the *Zeeman* term

$$\mathcal{H}_Z = 2\pi\nu_1 I_{1z} + 2\pi\nu_2 I_{2z} \tag{2.2}$$

and $\mathcal{H}_J$ the isotropic, scalar coupling Hamiltonian

$$\mathcal{H}_J = 2\pi J_{12}\mathbf{I}_1\mathbf{I}_2 = 2\pi J_{12}\left(I_{1x}I_{2x} + I_{1y}I_{2y} + I_{1z}I_{2z}\right). \tag{2.3}$$

Suppose the spin system is prepared with the first spin polarized along the z-axis and the second spin saturated, the initial density matrix is then given by:

$$\sigma_0 = I_{1z}. \tag{2.4}$$

The evolution of the spin system under the Hamiltonian given in Eq. 2.1 can easily be calculated numerically and is plotted in Fig. 2.1. However, for a better understanding of the processes a separation of the original Hamiltonian $\mathcal{H}_0$ into $\mathcal{H}_0'$ and $\mathcal{H}_0''$ is reasonable

$$\mathcal{H}_0' = 2\pi\left(\nu_1 - \nu_2\right)\frac{I_{1z} - I_{2z}}{2} + 2\pi J_{12}\left(I_{1x}I_{2x} + I_{1y}I_{2y}\right) \tag{2.5}$$

1 Interestingly, the pendula analogy is not only a pictorial equivalent. Identical differential equations describe the energy transfer within a network of nuclear spins and a group of pendula. This equivalence holds true if not more than three oscillators are considered.[2]

$$\mathcal{H}_0'' = 2\pi\,(\nu_1 + \nu_2)\,\frac{I_{1z} + I_{2z}}{2} + 2\pi J_{12}\,(I_{1z} I_{2z})\,. \tag{2.6}$$

As the Hamiltonian $\mathcal{H}_0''$ commutes with the density matrix σ_0 it does not influence the evolution of the spin system. Consequently, only the effect of $\mathcal{H}_0'$ has to be taken into account. If the difference of the two resonance frequencies $\nu_1 - \nu_2$ is combined to $\Delta\nu_{12}$, three characteristic cases can be distinguished:

weak coupling limit	$\lvert\Delta_{12}\rvert \gg \lvert J_{12}\rvert$
strong coupling limit	$\lvert\Delta_{12}\rvert \approx \lvert J_{12}\rvert$
Hartmann-Hahn limit	$\lvert\Delta_{12}\rvert \ll \lvert J_{12}\rvert$

In the weak coupling limit the density matrix does not evolve and the magnetization on the first spin is conserved: $\sigma_t = \sigma_0 = I_{1z}$. However, in the strong coupling limit the initial density matrix evolves into the operators I_{1z}, I_{2z}, $ZQ_y = I_{1y}I_{2x} - I_{1x}I_{2y}$, and $ZQ_x = I_{1x}I_{2x} + I_{1y}I_{2y}$. The expectation values of these operators oscillate periodically and magnetization is transferred to the second spin (I_{2z}). The third case is of special interest. In the infinitely strong coupling limit (Hartmann-Hahn limit) only the terms I_{2z} and ZQ_y are generated. In contrast to the strong coupling limit, magnetization starting from I_{1z}, is transferred *fully* to the second spin ($\langle I_{2z}\rangle = 1$). This process requires a period of $1/(2J_{12})$ which translates into a time interval of 50 ms when a coupling constant of $J_{12} = 10$ Hz is assumed. This transfer is therefore *twice* as fast as a comparable COSY or INEPT transfer step and makes TOCSY experiments one of the most valuable building blocks in NMR spectroscopy.[2]

2.1.1 Hartmann-Hahn Transfer in the Product Operator Formalism

To find an analytical expression for the transfer function in homonuclear Hartmann-Hahn experiments, two different formalisms may be applied - the description in the zero-quantum frame or the description in the product operator formalism. Here only the latter is presented in detail, while the other may be found in corresponding texts.[3]

2 This applies only to homonuclear spin systems. Corresponding heteronuclear experiments rely on a different coupling Hamiltonian $\mathcal{H}_J$ which is comparable to the coupling Hamiltonian present in the weak coupling limit and therefore has transfer times equal to COSY and INEPT transfer steps.

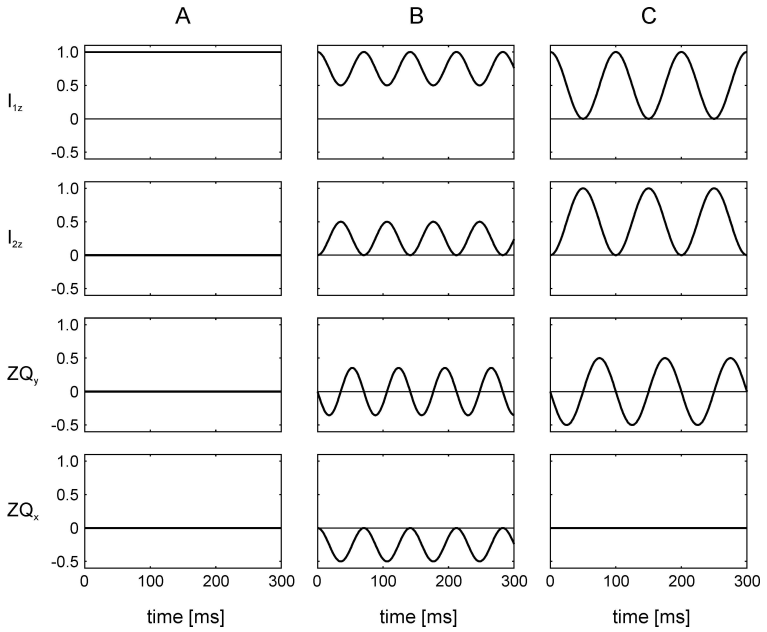

FIGURE 2.1: The evolution of the density matrix $\sigma_0 = I_{1z}$ in a two spin-$\frac{1}{2}$ system under the influence of the Hamiltonian $\mathcal{H}'_0$ (cf. Eq. 2.5). For all three coupling regimes the expectation values $\langle I_{1z}\rangle$, $\langle I_{2z}\rangle$, $\langle ZQ_y\rangle$, and $\langle ZQ_x\rangle$ are plotted, assuming a coupling constant $J_{12} = 10$ Hz. For the weak coupling limit (A) the resonance frequencies are $\nu_1 = 1000$ Hz and $\nu_2 = 2000$ Hz, in the strong coupling limit (B) $\nu_1 = 1000$ Hz and $\nu_2 = 1010$ Hz, and in the Hartmann-Hahn-limit (C) $\nu_1 = 1000$ Hz and $\nu_2 = 1000$ Hz

The product operator formalism offers the oppertunity to calculate the evolution of a spin system analytically, if the Hamiltonian can be expanded into a linear combination of commuting operators. While this prerequisite is always fulfilled in the weak coupling regime, complications might occur in the strong coupling limit. Fortunately, all relevant terms commute for TOCSY experiments, if chemical shift evolution is neglected. This assumption is valid due to the fact that $|\Delta_{12}| \ll |J_{12}|$ and therefore a rotating frame of reference may always be found where to a good approximation all chemical shift terms vanish. Hence, only the coupling term $\mathcal{H}_J$ of the Hamiltonian of Eq. 2.1 must be taken into account.

$$\mathcal{H}_J = 2\pi J_{12}\mathbf{I}_1\mathbf{I}_2 = 2\pi J_{12}\left(I_{1x}I_{2x} + I_{1y}I_{2y} + I_{1z}I_{2z}\right). \tag{2.7}$$

If $\sigma_0 = I_{1z}$ is chosen as initial density matrix, the influence of the product operators $2I_{1x}I_{2x}$, $2I_{1y}I_{2y}$, and $2I_{1z}I_{2z}$ can be calculated consecutively:

$$\sigma_0 \xrightarrow{\pi J_{12}t(2I_{1x}I_{2x})} \xrightarrow{\pi J_{12}t\left(2I_{1y}I_{2y}\right)} \xrightarrow{\pi J_{12}t(2I_{1z}I_{2z})} \sigma_t. \tag{2.8}$$

Here the notation $A \xrightarrow{\varphi B} C$ indicates the transformation $\exp(-i\varphi B)A\exp(i\varphi B)$ and results in

$$C = \begin{cases} A & \text{if } [A,B] = 0 \\ A\cos(\varphi) + i[A,B]\sin(\varphi) & \text{if } [A,B] \neq 0 \end{cases} \tag{2.9}$$

Consequently, the operator $2I_{1z}I_{2z}$ does not have an influence on the spin system, as it commutes with the initial density matrix. In contrast, the other two components of the isotropic coupling Hamiltonian (Eq. 2.7) do not commute with I_{1z}. Taking the commutator rules

$$\begin{aligned} [I_{1z}, 2I_{1x}I_{2x}] &= i(2I_{1y}I_{2x}) \\ [I_{1z}, 2I_{1y}I_{2y}] &= -i(2I_{1x}I_{2y}) \end{aligned} \tag{2.10}$$

and the identity $\varphi = \pi J_{12}t$, the transformation caused by $2I_{1x}I_{2x}$ and $2I_{1y}I_{2y}$ can be calculated:

$$\begin{aligned} I_{1z} &\xrightarrow{\pi J_{12}t(2I_{1x}I_{2x})} I_{1z}\cos(\pi J_{12}t) - 2I_{1y}I_{2x}\sin(\pi J_{12}t) \\ &\xrightarrow{\pi J_{12}t\left(2I_{1y}I_{2y}\right)} I_{1z}\cos(\pi J_{12}t)\cos(\pi J_{12}t) + 2I_{1x}I_{2y}\sin(\pi J_{12}t) \\ &\quad - 2I_{1y}I_{2x}\sin(\pi J_{12}t)\cos(\pi J_{12}t) + I_{2z}\sin(\pi J_{12}t)\sin(\pi J_{12}t). \end{aligned} \tag{2.11}$$

Therefore, the periodic build-up of the operator I_{2z} follows a $\sin^2$-function. As a result, the expectation value is always positive in the two-spin case.[3] In concert with the formation of I_{2z} the zero-quantum term ZQ_y is produced, whose evolution equals a sine-function ($\frac{1}{2}\sin(2\pi Jt)$). The influence of this term will be discussed in Sec. 2.1.8 in more detail. Of central importance is the observation that the transfer amplitude is proportional to $\sin^2$ (see Sec. 3.3.3). This observation holds true even for larger spin systems when only short transfer times are considered.

The derivation presented here can be easily expanded to the general coupling term $\mathcal{H}_{coup}$:

$$\begin{aligned}\mathcal{H}_{coup} &= a_{xx}(2I_{1x}I_{2x}) + a_{yy}(2I_{1y}I_{2y}) + a_{zz}(2I_{1z}I_{2z}) \\ &= a_{ZQ}(ZQ_x) + a_{DQ}(DQ_x) + a_{zz}(2I_{1z}I_{2z}),\end{aligned} \tag{2.12}$$

where the coefficients of the zero- and double-quantum term (ZQ_x and DQ_x) are given by $a_{ZQ} = (a_{xx} + a_{yy})$ and $a_{DQ} = (a_{xx} - a_{yy})$. The transfer function $T_{12}^z(t)$ then results in:

$$T_{12}^z(t) = \sin(a_{xx}t)\sin(a_{yy}t) = \frac{1}{2}(\cos(a_{DQ}t) - \cos(a_{ZQ}t)). \tag{2.13}$$

The last equation contains some important implications for homonuclear Hartmann-Hahn transfer. In the case of $a_{xx} = 0$ and/or $a_{yy} = 0$ the transfer amplitude $T_{12}^z(t)$ is equal to zero for all times $t \geq 0$. Consequently, the Hamiltonian determining the transfer must consist of the bilinear x-term as well as the bilinear y-term. Moreover complete transfer ($|T_{12}^z(t)| = 1$) is only possible when the condition $a_{xx} = \pm a_{yy}$ is met.

The analysis showed, that by creating the coupling Hamiltonian $\mathcal{H}_{coup} = a_{xx}(2I_{1x}I_{2x}) + a_{yy}(2I_{1y}I_{2y}) + a_{zz}(2I_{1z}I_{2z})$ homonuclear Hartmann-Hahn transfer is enabled. However, it is not important *how* this Hamiltonian is created; $\mathcal{H}_{coup}$ may represent a *real* Hamiltonian or only an *effective* Hamiltonian. The latter may be created by multiple pulse sequences as described in the next section.

2.1.2 Multiple Pulse Sequences

In the previous sections the transfer of magnetization in a two spin system under the influence of an isotropic coupling Hamiltonian was discussed in

3 Spin systems with more than five spins may also exhibit negative transfer amplitudes under certain circumstances.[4]

detail. However, so far the experimental realization of such an element was left untouched. To create a given (effective) coupling Hamiltonian in practice, multiple pulse sequences are of essential importance. They are composed of many defined pulses (Fig. 2.2), thus creating specific mixing conditions for a given spin system.

In general, multiple pulse sequences are constructed from smaller building blocks, the *basis sequences*, which are themselves composed of a defined number of pulses. The N pulses of the basis sequence may have different durations τ_k, amplitudes ν_k^R, phases φ_k, and offsets ν_k^{rf}. Therefore an overall number of $4N$ is needed to describe a basis sequence completely, although this number might be reduced due to certain symmetries within the sequence. All n basis sequences forming the full mixing sequence have a duration of τ_b and are identical to one another. Usually, the pulses of the basis sequence can be grouped to so-called *basic composite pulses*. These composite pulses are equal to each other apart from their relative phase. This phase is determined by the iterating scheme. The most common schemes are listed in Tab. 2.1.

Another very important parameter for multiple pulse sequences is the *average rf-power*, as it is responsible for sample heating. It is defined via the *Rabi frequency*

$$\nu_k^R = -\frac{1}{2\pi}\gamma B_k \tag{2.14}$$

and is given by

$$\overline{(\nu^R)^2} = \frac{1}{\tau}\int_0^\tau (\nu^R)^2 \mathrm{d}t = \frac{1}{\tau_b}\sum_{k=1}^{N}(\nu_k^R)^2\tau_k. \tag{2.15}$$

2.1.3 Liouville- von Neumann Equation

The evolution of any spin system under the influence of a certain Hamiltonian can be calculated by solving the *Liouville- von Neumann* equation

$$\frac{\mathrm{d}}{\mathrm{d}t}\sigma_t = -i[\mathcal{H}_0 + \mathcal{H}_{rf}, \sigma_t] - \widehat{\Gamma}(\sigma_t - \sigma_0). \tag{2.16}$$

Here $\mathcal{H}_0$ is the time-independent free-evolution Hamiltonian, $\mathcal{H}_{rf}(t)$ the time-dependent Hamiltonian associated with rf-pulses, and $\widehat{\Gamma}$ the relaxation superoperator. The relaxation superoperator comprises the effects of auto- and cross-relaxation (incoherent processes), while the other two

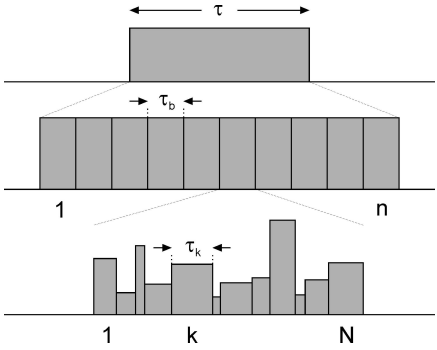

FIGURE 2.2: General construction scheme for multiple pulse sequences. The mixing period of duration τ consists of n equal building blocks, the basis sequence of length τ_b. The basis sequence itself is constructed from N rf-pulses, each with duration τ_k, phase φ_k, amplitude ν_k^R, and offset ν_k^{rf}.

TABLE 2.1: The most common supercycles. Given are the relative phases for the basis sequence, where R and $\overline{R}$ indicate phases differing by 180° and X and Y indicate phases differing by 90°.

supercycle	expansion scheme
MLEV-4 (type A)	$RR\overline{RR}$
MLEV-4 (type B)	$R\overline{RR}R$
MLEV-8	$RR\overline{RR}\,\overline{R}RR\overline{R}$
MLEV-16	$RR\overline{RR}\,\overline{R}RR\overline{R}\,R\overline{RR}R\,\overline{RR}RR$
MLEV-32	$RR\overline{RR}\,\overline{R}RR\overline{R}\,R\overline{RR}R\,\overline{RR}RR$
	$RRR\overline{R}\,\overline{RR}RR\,\overline{RR}R\overline{R}\,RR\overline{RR}$
XY-8	$XYXY\;YXYX$
XY-16	$XYXY\;YXYX\;\overline{XYXY}\;\overline{YXYX}$
M4P5[a]	0° 0° 150° 60° 0°
M4P9[a]	0° 15° 180° 165° 165° 180° 15° 0°

[a] The given expansion scheme is additionally expanded with a MLEV-4 supercycle.

operators describe all coherent processes. Mostly, relaxation effects can be treated in a semiquantitative fashion and the evolution of the spin system can be calculated assuming just coherent transfer pathways (Sec. 2.3). The advantage of this approach is its simplicity and the general applicability. Unfortunately, although efforts are made to reduce the complexity of the problem,[5] this approach fails when large spin systems are considered, as the computational expenses scale exponentially with the number of spins. Moreover this approach provides only little insight to the mechanisms active during a multiple pulse sequence. Therefore the evolution of the spin system can be conveniently analyzed with average Hamiltonian theory if relaxation effects can be neglected. This approooach describes the *overall* effect of a multiple pulse sequence by an *effective* Hamiltonian $\mathcal{H}_{\mathit{eff}}$ which is composed of *effective* magnetic fields and *effective* coupling terms.

2.1.4 Effective Hamiltonian

The effective Hamiltonian of a multiple pulse sequence can always be calculated when the sequence is dissected into N short square pulses. Usually, the pulses used for such sequences already have a square shape and readily fulfill this prerequisite. Hence, the time-dependent Hamiltonian active during the course of a multiple pulse sequence is divided into N time-independent Hamiltonians. The Hamiltonian acting during the k-th square pulse is constant and can be written as the sum of the free evolution Hamiltonian $\mathcal{H}_0$ and the Hamiltonian for the rf-pulse $\mathcal{H}_{k,rf}$

$$\mathcal{H}_k = \mathcal{H}_0 + \mathcal{H}_{k,rf}. \tag{2.17}$$

The free evolution Hamiltonian $\mathcal{H}_0$ is composed of the Zeeman term

$$\mathcal{H}_Z = 2\pi \sum_i \nu_i I_{iz} \tag{2.18}$$

and the isotropic coupling term

$$\mathcal{H}_J = 2\pi \sum_{i<j} J_{ij}(I_{ix}I_{jx} + I_{iy}I_{jy} + I_{iz}I_{jz}). \tag{2.19}$$

The rf-term is defined via its Rabi frequency ν_k^R and its phase φ_k

$$\mathcal{H}_{k,rf} = 2\pi\nu_k^R \sum_i (I_{ix}\cos\varphi_k + I_{iy}\sin\varphi_k). \tag{2.20}$$

Consequently, the propagator acting during the k-th square pulse on the density matrix can be expressed as

$$U_k = \exp(-i\mathcal{H}_k\tau_k), \tag{2.21}$$

where τ_k is the duration of the k-th square pulse. The overall effect of the N square pulses of the basis sequence with duration τ_b can be calculated by the time-ordered product of all N propagators

$$U(\tau_b) = U_N \cdots U_k \cdots U_1 = T\exp\left(-i\int_0^{\tau_b}(\mathcal{H}_{rf}(t) + \mathcal{H}_0)\mathrm{d}t\right), \tag{2.22}$$

with the Dyson time-ordering operator T. Therefore, the total propagator of the basis sequence acting on the spin density matrix is given by

$$U(\tau_b) = \exp\left(-i\mathcal{H}_{\mathit{eff}}\tau_b\right). \tag{2.23}$$

Here $\mathcal{H}_{\mathit{eff}}$ is the fictitious effective Hamiltonian which would have the same overall effect on the spin system as the consecutive application of all Hamiltonians of the multiple pulse sequence. Because all basis sequences within a multiple pulse sequence are identical and only integer multiples of it are applied to the spin system, the total propagator can be easily expressed as

$$U(n\tau_b) = U(\tau_b)^n = \exp\left(-i\mathcal{H}_{\mathit{eff}}n\tau_b\right). \tag{2.24}$$

To find a valid effective Hamiltonian for a given total propagator the logarithm has to be taken

$$\mathcal{H}_{\mathit{eff}} = \frac{i}{\tau_b}\ln\left(U(\tau_b)\right). \tag{2.25}$$

This operation is not unambiguous because the logarithm is just defined up to an integer multiple of $i2\pi$ and therefore an infinite number of solutions exist. While all these Hamiltonians yield the same density matrix for an integer multiple of τ_b, they will give very different results for times deviating from this condition. As a consequence the evolution of a spin system can only be predicted for time points where the entire basis sequence is completed. The criteria for the right choice of an effective Hamiltonian are simplicity and continuity. If effective Hamiltonians are calculated numerically, the computer will usually choose the solution with the smallest absolute value ($-i\pi < \ln(U_{ii} < i\pi)$) for each diagonal element. This solution is very often also the most simple effective Hamiltonian. However,

although this approach is very flexible and an effective Hamiltonian can always be calculated numerically, it offers just little insight into the way how a multiple pulse sequence creates a certain effective Hamiltonian. In the next section a more intuitive approach is presented.

2.1.5 Average Hamiltonian Theory

For a deeper insight to the processes or mechanisms of a multiple pulse sequence it would be desirable to go directly from the time-dependent Hamiltonian $\mathcal{H}(t)$ to the effective Hamiltonian $\mathcal{H}_{\mathit{eff}}$, rather than taking the detour via the total propagator $U(\tau_b)$. For this purpose the *Magnus expansion* has proven to be beneficial. With its help the effective Hamiltonian can be divided into contributions of different orders

$$\mathcal{H}_{\mathit{eff}} = \mathcal{H}^0_{\mathit{eff}} + \mathcal{H}^1_{\mathit{eff}} + \mathcal{H}^2_{\mathit{eff}} + \cdots , \tag{2.26}$$

with

$$\mathcal{H}^0_{\mathit{eff}} = \overline{\mathcal{H}} = \frac{1}{\tau_b}\int_0^{\tau_b} \mathcal{H}(t)\mathrm{d}t, \tag{2.27}$$

$$\mathcal{H}^1_{\mathit{eff}} = -\frac{i}{2\tau_b}\int_0^{\tau_b}\int_0^{t'} [\mathcal{H}(t'),\mathcal{H}(t)]\mathrm{d}t'\mathrm{d}t, \tag{2.28}$$

and

$$\begin{aligned}\mathcal{H}^2_{\mathit{eff}} = -\frac{i}{6\tau_b}\int_0^{\tau_b}\int_0^{t'}\int_0^{t''} \{&[\mathcal{H}(t''),[\mathcal{H}(t'),\mathcal{H}(t)]] \\ &+ [[\mathcal{H}(t''),\mathcal{H}(t')],\mathcal{H}(t)]\}\mathrm{d}t''\mathrm{d}t'\mathrm{d}t.\end{aligned} \tag{2.29}$$

It is readily visible that the zero-order term is given by the time-average of $\mathcal{H}(t)$ over the duration τ_b of the entire basis sequence. The average Hamiltonian $\overline{\mathcal{H}}$ therefore forms the link between the effective Hamiltonian and the time-dependent Hamiltonian. Of course, the average Hamiltonian is only an approximation of the effective Hamiltonian and is only valid if all terms $\mathcal{H}^n$ of the Magnus expansion with $n \geq 1$ can be neglected. This is always the case if the Hamiltonian $\mathcal{H}(t')$ commutes with $\mathcal{H}(t)$ for all times $0 \leq t,\, t' \leq \tau_b$. But even if this condition is not fulfilled the average Hamiltonian is a good approximation of the effective Hamiltonian, if the duration of the basis sequence τ_b is short:

$$\tau_b \ll \frac{2\pi}{\|\mathcal{H}\|}. \tag{2.30}$$

Here, $\|\mathcal{H}\|$ represents the characteristic strength of the time-dependent Hamiltonian $\mathcal{H}(t)$. Suppose the time-dependent Hamiltonian is dominated by rf-fields with amplitudes of 10 kHz, then the Magnus-expansion converges rapidly only if

$$\tau_b \ll \frac{1}{10 \text{ kHz}} = 100 \ \mu\text{s}. \tag{2.31}$$

Typically, Hartmann-Hahn experiments consist of mixing sequences which have a duration of several milliseconds and do not fulfill the above condition. Therefore the average Hamiltonian is not a useful approximation of the effective Hamiltonian, which suggests that average Hamiltonian theory is not beneficial at a first glance. However, average Hamiltonian theory has proven to be of broad practical relevance as its validity can be expanded. This can be achieved with the transformation into the toggling frame, which is presented in the next section.

2.1.6 The Toggling Frame

The concept of the toggling frame is fundamentally independent from average Hamiltonian theory, but only in combination these two techniques gain their full efficiency. A broad application of average Hamiltonian theory is only possible if the unwanted large rf-terms are removed from the time-dependent Hamiltonian, as these usually determine the characteristic strength $\|\mathcal{H}\|$. For this purpose one makes use of the fact that the propagator $U_{rf}(t)$ corresponding to the Hamiltonian of the rf-term is composed of a series of simple rotations. If these rotations are used to define the reorientation of the toggling frame, the resulting time-dependent Hamiltonian does not contain these rf-terms anymore. As a consequence, Hamiltonians contributing to the free-evolution Hamiltonian which are time-independent in the rotating frame become time-dependent in the toggling frame. The time-dependence of the free-evolution Hamiltonian can be expressed as

$$\mathcal{H}_0^{tog}(t) = U_{rf}^{\dagger}(t)\mathcal{H}_0 U_{rf}(t) = \mathcal{H}_Z^{tog}(t) + \mathcal{H}_J^{tog}(t) \tag{2.32}$$

with

$$U_{rf}(t) = T \exp\left(-i \int_0^t (\mathcal{H}_{rf}(t')\mathrm{d}t'\right). \tag{2.33}$$

The evolution of the spin system is therefore guided by the propagator

$$U_0^{tog}(t) = T \exp\left(-i \int_0^t (\mathcal{H}_0^{tog}(t')\mathrm{d}t'\right). \tag{2.34}$$

Equivalently to the rotating frame an effective Hamiltonian $\mathcal{H}_{eff}^{tog}$ can be defined for the toggling frame. For the effective Hamiltonian in the toggling frame the same rules hold true as for the effective Hamiltonian in the rotating frame. It can also be approximated by an average Hamiltonian $\overline{\mathcal{H}_{eff}^{tog}}$ which is only a good approximation if the basis sequence is short compared to the characteristic strength. Because the strong rf-terms have been removed from the time-dependent Hamiltonian, the approximation is now valid for much longer basis sequences:

$$\tau_b \ll \frac{2\pi}{\|\mathcal{H}_0^{tog}\|}. \tag{2.35}$$

If the rotating frame and the toggling frame coincide at the beginning and at the end of a basis sequence, i.e., that the basis sequence is cyclic with $U_{rf}(\tau_b) = 1$, then the effective Hamiltonian in the toggling frame is also an effective Hamiltonian in the rotating frame and (*vide supra*) the effective Hamiltonian in the toggling frame can be approximated by an average Hamiltonian; it follows that

$$\mathcal{H}_{eff} = \mathcal{H}_{eff}^{tog} \approx \overline{\mathcal{H}_{eff}^{tog}}. \tag{2.36}$$

2.1.7 Invariant Trajectory

In the analysis of multiple pulse sequences one often faces the problem that magnetization transfer occurs not only due to coherent processes but also due to relaxation effects. For a quantification of these processes and the calculation of auto- and cross-relaxation rates the *invariant trajectory* approach[6] has proven to be a valuable tool. It offers the possibility to improve cross-relaxation properties in Hartmann-Hahn experiments (as it is done in *clean* TOCSY experiments[7–9]) or the offset dependence in ROESY experiments.

The time evolution of a normalized magnetization vector n^i under the influence of a multiple pulse sequence is called invariant trajectory if this vector returns to its initial position after τ_b

$$\mathrm{n}^i(\tau_b) = \mathrm{n}^i(0). \tag{2.37}$$

If the pulse sequences creates non-vanishing effective fields B_i^{eff} this condition can only be fulfilled if $\mathrm{n}^i(0)$ is oriented parallel or antiparallel to the

effective field. The reorientation of the magnetization vector with components $n_x^i(t)$, $n_y^i(t)$, and $n_z^i(t)$ can be described as follows

$$n_\alpha^i(t) = \sum_\beta a_{\alpha\beta}^i(t) n_\beta^i(0). \tag{2.38}$$

Here, the coefficients $a_{\alpha\beta}^i(t)$ are the elements of a real, three-dimensional rotation matrix with $\alpha = x$, y, or z.[10]

Pulse sequences can be separated into different classes according to the effective field they exhibit. This classification is useful for a later discussion of cross-relaxation. Suppose the spin system consists of at least two spins, I_1 and I_2:

1. If the relation $B_{I_1}^{eff} = B_{I_2}^{eff} = 0$ is valid for all spins of the spin system, no net rotations occur and the sequence is called *isotropic*. All trajectories are said to be energy-matched.

2. If $B_{I_1}^{eff} = B_{I_2}^{eff} \neq 0$ for all considered spins, an identical net rotation for all operators parallel and perpendicular to the invariant trajectory occurs. Sequences of this type are classified as *energy-matched*. All homonuclear Hartmann-Hahn sequences belong to this class.

3. In the case of $B_{I_1}^{eff} \neq B_{I_2}^{eff}$ each spin shows its own invariant trajectory and all orthogonal components are dephased during the time course of the experiment. These sequences are classified as *energy-mismatched*.

In the first two classes cross-relaxation not only occurs between components parallel to the invariant trajectory, but also between components perpendicular to this trajectory, while for sequences of the third type only components parallel to the invariant trajectory have to be taken into account. However, in practice it is often sufficient to consider cross-relaxation only between components parallel to the invariant trajectories, as B_1-field inhomogeneities rapidly dephase all orthogonal components.

The effective cross-relaxation σ_{eff}^{ij} rate between a spin pair i and j during the course of a multiple pulse sequence is given by

$$\sigma_{eff}^{ij} = w_t^{ij} \sigma_{ROE}^{ij} + w_l^{ij} \sigma_{NOE}^{ij}, \tag{2.39}$$

where σ_{ROE}^{ij} and σ_{NOE}^{ij} represent the transverse and the longitudinal cross-relaxation rate, respectively. The weights w_t^{ij} and w_l^{ij} depend on the offset of spins i and j and on the multiple pulse sequence. If the basis sequence

belongs to the first or second type and is repeated n times, it is sufficient to determine the weights w_t^{ij} and w_l^{ij} only for the duration τ_b:

$$w_t^{ij} = \frac{1}{\tau_b} \int_0^{\tau_b} \left(n_x^i(t) n_x^j(t) + n_y^i(t) n_y^j(t) \right) \tag{2.40}$$

and

$$w_l^{ij} = \frac{1}{\tau_b} \int_0^{\tau_b} n_z^i(t) n_z^j(t). \tag{2.41}$$

These last equations are of fundamental importance. They allow the calculation of offset profiles of the effective cross-relaxation rate and therefore give a quantitative measure for the error which is introduced into the transfer amplitudes of Hartmann-Hahn experiments.

2.1.8 Zero-Quantum Suppression

Zero-quantum artifacts are disturbing phenomena in many types of homonuclear experiments such as TOCSY, COSY, ROESY, and NOESY spectra. They give rise to anti-phase contributions and dispersive components in the spectrum, thereby introducing misleading correlations and distorted lineshapes. Theoretically, these contributions do not consequently lead to an erroneous volume integral as anti-phase components usually add to zero. However, in homonuclear Hartmann-Hahn sequences zero-quantum artifacts present before the actual TOCSY-mixing will alter also the intensity of the transfer amplitude deteriorating a quantitative analysis. This is due to the fact that TOCSY experiments essentially rely on zero-quantum transfer, as can be seen from Eq. 2.11 and Fig. 2.1. Therefore, it is essential to remove these contributions *before* and *after* the mixing period.

There are different strategies to suppress zero-quantum coherences[11–14] but the most elaborate technique was presented by Thrippleton *et al.*[15] and is discussed further here. A pulsed field gradient is applied simultaneously with a frequency swept inversion pulse which leads to high suppression rates. In principle, it is an extension of the procedure published by Baur and Kessler.[16]

Consider two coupled spins with chemical shift difference Ω_{ZQ}. Suppose these spins are prepared in a spin state which can be described by the spin density matrix σ_0, which is a sum of populations, zero-, single-, and double-quantum coherences:

$$\sigma_0 = \sigma^p + \sigma^0 + \sigma^{\pm 1} + \sigma^{\pm 2}. \tag{2.42}$$

A pulsed field gradient applied to this spin system will destroy all higher quantum contributions and only the first two terms will survive. Assume that the gradient is operating along the z-axis of the sample tube and is strong, i.e., that the linewidth in the presence of the gradient is much larger than the chemical shift difference Ω_{ZQ}. Moreover, the height of the sample volume is equal to the unit interval. Using a frequency swept inversion pulse of duration τ_p that inverts the entire broadened line but essentially no larger range, causes the spatial variable z to be transformed into a time variable t. This holds true only if the sweep rate is fast enough to invert spins differing in frequency by Ω_{ZQ} nearly simultaneously. When the experiment is set up correctly, at position $z = 0$ the time variable $t \approx 0$ and at position $z = 1$ $t \approx \tau_p$.

During the time course of the filter element, in each layer of the sample zero-quantum coherence evolves, is then inverted, and finally evolves again for the remainder of the time period. This leads to the following equation, when ZQ_y-magnetization is present initially:

$$ZQ_y \xrightarrow{t-180^\circ-(\tau_p-t)} -ZQ_y \cos(\Omega_{ZQ}(2t-\tau_p)) + ZQ_x \sin(\Omega_{ZQ}(2t-\tau_p)). \tag{2.43}$$

When a linear inversion rate is assumed then $t = z\tau_p$ and Eq. 2.43 can be rewritten in the form

$$ZQ_y = -ZQ_y \cos(\Omega_{ZQ}(z-1)) + ZQ_x \sin(\Omega_{ZQ}(2z-1)). \tag{2.44}$$

The integration over z then gives the normalized attenuation factors for a z-gradient of duration τ_b

$$\begin{aligned} A_z(ZQ_y \rightarrow ZQ_y) &= \frac{-\int_0^1 \cos(\Omega_{ZQ}\tau_p(2z-1))\mathrm{d}z}{-\int_0^1 \mathrm{d}z} \\ &= \frac{\sin(\Omega_{ZQ}\tau_p)}{\Omega_{ZQ}\tau_p} \end{aligned} \tag{2.45}$$

and

$$A_z(ZQ_y \rightarrow ZQ_x) = \frac{-\int_0^1 \sin(\Omega_{ZQ}\tau_p(2z-1))\mathrm{d}z}{-\int_0^1 \mathrm{d}z} = 0. \tag{2.46}$$

Analogous relations result when ZQ_x-coherence is assumed as initial spin state. Consequently, the overall attenuation factor is determined by the sinc-function of Eq. 2.45. The dependence of such a filter element on the

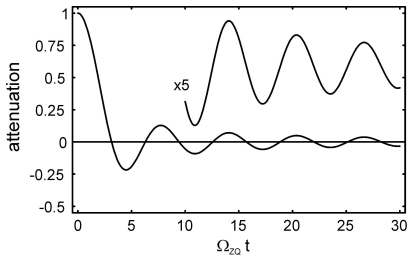

Figure 2.3: Attenuation of zero-quantum artifacts by a filter element according to Eq. 2.45. The zero-quantum frequency Ω_{ZQ} is given in Hz.

duration of the inversion pulse τ_p and the zero-quantum frequency Ω_{ZQ} is depicted in Fig. 2.3. Further investigations and experimental results are shown in Sec. 3.3.1.

2.2 Residual Dipolar Couplings

2.2.1 General Considerations

Like all magnetic dipoles also nuclear spins sense an attractive or repulsive force if brought together. This interaction is called *dipolar interaction* and depends on the distance between the two nuclei and their orientation with respect to each other. The dipolar interaction is fairly strong and usually dominates all other interactions (Fig. 2.4), hence, the spectral outcome in solid samples, where it leads to broad lines and distorted lineshapes if no precautions are taken, is rendered unanalyzable. In contrast, liquid samples seem to lack this interaction as they exhibit narrow and absorptive lineshapes. However, this statement is by no means true, molecules in the liquid phase exhibit dipolar interactions as well, but these are averaged to zero due to the fast Brownian motion.[4] Furthermore, all other anisotropic interactions, like chemical shift anisotropy and quadrupolar couplings, are averaged to zero, too. Elimination of these anisotropic parameters is on the one hand favourable but on the other hand valuable structural infor-

4 This effect is nowadays also used in solid state NMR where *magic angle sample spinning* leads to a reduction of dipolar contributions. To fully average out the dipolar interaction the reorientation of the internuclear vector has to be faster than the maximum dipolar coupling.

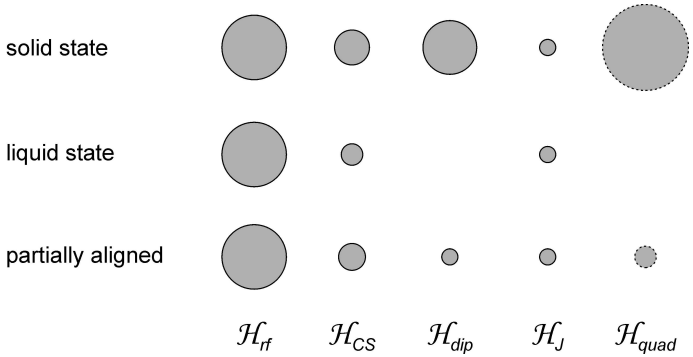

FIGURE 2.4: The relative size of the different NMR parameters. In the solid state all interactions (dipolar couplings, scalar couplings, quadrupolar couplings, and chemical shifts) are observable. In the liquid state especially dipolar couplings and quadrupolar couplings are scaled to zero, while all other parameters remain. When molecules are weakly aligned, dipolar and quadrupolar interactions are reintroduced.

mation is lost. Therefore it is desirable to *partially* align the molecules to regain this information while retaining the merits of the liquid state. This is achieved by an alignment medium (see Sec. 2.2.2) which leads to the observation of *residual dipolar couplings*.

To predict the result of a measurement of a weakly aligned molecule, knowledge about the *alignment tensor* is crucial. The alignment tensor is fixed to the molecular frame of reference and gives information about the size and the sign of the expected dipolar coupling between an arbitrary pair of spins within the molecule. Moreover, it provides information about the degree of alignment, i.e., it is a statistical measure of how strongly a certain orientation of the molecule within the alignment medium is favoured (disfavoured) to another orientation. In the following the alignment tensor is derived and commonly used expressions are given.

In the lab frame with the magnetic field pointing along the z-axis the (truncated[5]) dipolar Hamiltonian has the form

$$\mathcal{H}_D = 2\pi D \mathbf{I}_1 \overline{\mathbf{D}} \mathbf{I}_2 = 2\pi D \{ I_{1z} I_{2z} - \frac{1}{2} I_{1x} I_{2x} - \frac{1}{2} I_{1y} I_{2y} \}. \tag{2.47}$$

5 Non-secular interactions are neglected.[17]

Here D is the dipolar coupling constant and $\overline{\mathbf{D}}$ is the dipolar coupling tensor (see Chapter 3). The dipolar coupling constant can be expressed as

$$D = \frac{\kappa}{r^3}(\cos^2(\theta) - \frac{1}{3}), \tag{2.48}$$

where r is the distance between the two nuclei and θ the angle between the internuclear vector and the magnetic field. The term

$$\kappa = -\frac{3}{8\pi^2}\gamma_1\gamma_2\mu_0\hbar \tag{2.49}$$

only depends on physical constants: the gyromagnetic ratios γ_1 and γ_2 of spins I_1 and I_2, respectively, the Planck constant $\hbar$, and the permeability of the vacuum μ_0.

Consider two spins I_1 and I_2. Due to Brownian motion the orientation between the internuclear vector and the magnetic field changes constantly. Moreover the distance between the two nuclei might change as well. Here, a rigid molecule is assumed for simplicity and therefore only the term $\cos^2(\theta)$ has to be averaged.[6] Hence, the equation for the dipolar coupling constant can be rewritten as

$$\overline{D} = \frac{\kappa}{r^3}(\overline{\cos^2(\theta)} - \frac{1}{3}). \tag{2.50}$$

In isotropic solution the average over all orientations of the internuclear vector is equal to $\frac{1}{3}$ and consequently dipolar couplings average to zero. In a solid sample the angle θ is fixed and adopts values between 0 and 1. For $\cos^2(\theta) = 1$ the dipolar coupling reaches its maximum value D_{max}, e.g., 21.7 kHz for a ^{1}H-^{15}N spin pair in a protein when a distance of $r = 1.04$ Å is assumed.[7] If the molecule is in solution but weakly aligned the averaging process is not complete. Then it is convenient to move from the lab frame (x, y, z) to a frame of reference which is fixed to the molecule. Here the averaging process can conveniently be expressed with the probability tensor $\mathbf{P}$ which is a second order approximation of the orientational probability distribution of the direction of the external magnetic field in the molecular fixed frame of reference. The principal values $P_{\hat{x}}$, $P_{\hat{y}}$, $P_{\hat{z}}$ of the probability

6 It is important to note that the average is a time-average and not an ensemble-average. An ensemble average would lead to spectra as they are observed for powders and amorphous solids.

7 This is also the reason why solid state NMR does not rely on the measurement of the ^{1}H-nucleus. A pair of protons in a CH_2 moiety will have a maximum dipolar coupling of 44.8 kHz and therefore the sample has to be spun with an even higher frequency to average the dipolar couplings.

tensor correspond to the probabilities to find the magnetic field along the principal axes $\hat{x}$, $\hat{y}$, and $\hat{z}$ of the probability tensor. As the probability tensor is normalized ($P_{\hat{x}} + P_{\hat{y}} + P_{\hat{z}} = 1$) the term $\overline{\cos^2(\theta)}$ has the form

$$\overline{\cos^2(\theta)} = P_{\hat{x}} r_{\hat{x}}^2 + P_{\hat{y}} r_{\hat{y}}^2 + P_{\hat{z}} r_{\hat{z}}^2, \tag{2.51}$$

with $r_{\hat{x}}$, $r_{\hat{y}}$, and $r_{\hat{z}}$ being the Cartesian components of any given internuclear unit vector $\vec{r}$. In a pictorial way the probability tensor can be imagined as an ellipsoid whose orientation is fixed to the molecular frame of reference. For example, when the molecule tumbles isotropically in solution there are equal probabilities to find the magnetic field vector along all the three principal axes of the probability tensor and as a consequence the ellipsoid reduces to a sphere.

Usually, not the probability tensor **P** is used in literature but the alignment tensor **A**. The alignment tensor, in mathematical terms, is the traceless part of the probability tensor

$$\mathbf{A} = \mathbf{P} - \frac{1}{3}\mathbf{1}, \tag{2.52}$$

with $A_{\hat{x}} + A_{\hat{y}} + A_{\hat{z}} = 0$. It describes how strongly the molecule deviates from isotropic tumbling, i.e., if it is less likely or more likely to find the molecule within a certain orientation compared to an isotropic distribution (cf. Fig. 2.5). The alignment tensor has the same principal axes system as the probability tensor, thus Eq. 2.51 can be rewritten as

$$\left(\overline{\cos^2(\theta)} - \frac{1}{3}\right) = A_{\hat{x}} r_{\hat{x}}^2 + A_{\hat{y}} r_{\hat{y}}^2 + A_{\hat{z}} r_{\hat{z}}^2. \tag{2.53}$$

It is important to note that by convention the principal values of the alignment tensor **A** and the probability tensor **P** are ordered with increasing *magnitude*, which might lead to a reordering of the axis label. For example, if the principal components of the probability tensor are $P_{\hat{x}} = 0.2$, $P_{\hat{y}} = 0.3$, and $P_{\hat{z}} = 0.5$, the following principal components will result for the alignment tensor $A_{\hat{x}} = -0.0\bar{3}$, $A_{\hat{y}} = -0.1\bar{3}$, and $A_{\hat{z}} = 0.1\bar{6}$.

The definition of the alignment tensor is based on work pioneered by SAUPE *et al.*[18–20] who defined the so-called *Saupe matrix* **S**. The alignment tensor and the Saupe matrix are simply related to each other by a scaling factor of $\frac{3}{2}$

$$\mathrm{S} = \frac{3}{2}\mathrm{A}. \tag{2.54}$$

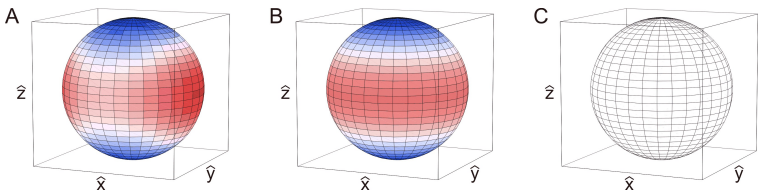

Figure 2.5: Schematic representation of the alignment tensor. Shown are the three different cases of a fully anisotropic (A), an axially symmetric (B), and an isotropic (C) alignment tensor. The colour coding indicates if it is more (blue), less (red), or equally likely to find the molecule within a certain orientation campared to an isotropic distribution.

In many publications the unit vector $\vec{r}$ is not expressed in Cartesian, but in polar coordinates. Therefore the components $r_{\hat{x}}$, $r_{\hat{y}}$, and $r_{\hat{z}}$ have to be rewritten in terms of the angles ϑ and φ

$$\left(\overline{\cos^2(\theta)} - \frac{1}{3}\right) = \frac{A_{\hat{z}}}{2}(3\cos^2\vartheta - 1) + \frac{A_{\hat{x}} - A_{\hat{y}}}{2}\sin^2\vartheta\cos 2\varphi. \tag{2.55}$$

Furthermore, this leads to the definition of the *axial component* A_a and the *rhombic component* A_r

$$A_a = \frac{3}{2}A_{\hat{z}} = S_{\hat{z}}, \quad A_r = A_{\hat{x}} - A_{\hat{y}} = \frac{3}{2}(S_{\hat{x}} - S_{\hat{y}}). \tag{2.56}$$

To complete this confusing multitude of definitions and different expression of basically the *same* tensor, the *rhombicity* R and the *asymmetry parameter* η have been introduced

$$R = \frac{A_r}{A_a} = \frac{2}{3}\eta. \tag{2.57}$$

Consequently, the initial equation for the time-averaged dipolar coupling (Eq. 2.50) can be rewritten as follows:

$$\overline{D} = D_a\left\{(3\cos^2\vartheta - 1) + \eta\sin^2\vartheta\cos 2\varphi\right\}, \tag{2.58}$$

where D_a is the so called 'magnitude of the residual dipolar coupling tensor' which equals $\kappa A_a/3r^3$.

In most practical applications the alignment tensor $\mathbf{A}$ is not known and has to be determined from the measured RDCs. For this purpose a minimum number of five *independent* couplings is needed as the alignment

tensor consists of five independent parameters. A corresponding fit of the experimental data is mostly based on *singular value decomposition* (SVD) and can be performed with programs such as PALES[21] or MODULE.[22] In addition, it is often possible to predict residual dipolar couplings from first principles, if the three-dimensional structure is known (e.g., PALES, TRAMITE,[23] or COSMOS[24]).

So far, molecules were assumed to be rigid, which is by no means true for unfolded proteins, for example. But also small molecules or well defined proteins and nucleic acids reveal some internal dynamics. Consequently, the dipolar coupling is scaled by the order parameter S_{RDC} which is not identical to the squared order parameter presented in Sec. 2.3.6. Nowadays, a lot of effort is spent on the interpretation of RDCs in terms of molecular dynamics. This is especially interesting as most of the timescales accessible by NMR techniques are covered (cf. Sec. 2.3) and therefore a thorough picture of the molecule of interest can be given,

$$\overline{D} = S_{RDC}\left(D_a\left\{(3\cos^2\vartheta - 1) + \eta\sin^2\vartheta\cos 2\varphi\right\}\right). \tag{2.59}$$

2.2.2 Alignment Media

For the measurement of anisotropic parameters like RDCs, RCSA, or RQCs the correct choice of the alignment medium is essential. It should reintroduce some degree of anisotropy but retain the benefits of the liquid state, i.e., small linewidths and undistorted lineshapes. The right alignment strength is of course depending on the parameter and the molecule to be observed. Alignment media can be divided into three categories according to the physical origin responsible for partial alignment. These classes will be discussed briefly in the following and advantages and disadvantages are pointed out.

Liquid Crystalline Media

Liquid crystalline (LC) phases have been the first media reported to partially align solute molecules for NMR measurements. Already in 1963 SAUPE and ENGLERT[18] acquired a ^{1}H-spectrum of benzene dissolved in a *p*-azoxyanisole derivate – a thermotropic LC. Many further examples followed not only with nematic phases[25,26] but also with smectic[27–29] and cholesteric[26,30,31] liquid crystals. Nowadays, mostly lyotropic mesophases instead of the thermotropic media are used. In both cases the alignment results from a spontaneous orientation of the liquid crystal in the strong external magnetic field. This in turn provides an anisotropic surrounding

for the solute which consequently gets aligned. However, liquid crystals exhibit a first order phase transition which sets a lower boundary for the minimum alignment strength. This limit is often already too high to obtain high resolution spectra, e.g., the spectrum of benzene in the above mentioned example spreads over 2500 Hz. Moreover, lyotropic mesophases are only stable in very defined concentration and temperature ranges placing severe limitations on their applicability. On the other hand, the solute does not have to diffuse into the liquid crystal as it is the case for stretched polymer gels (*vide infra*), which is especially advantageous for unstable samples. A large variety of different liquid crystalline phases for different solvents has been published and only a few can be mentioned here. For organic solvents such as dichloromethane, chloroform, or dimethylformamide poly-γ-benzyl-L-glutamate[31, 32] and poly-γ-ethyl-L-glutamate[33] have proven to be beneficial, whereas filamentous phage,[34] purple membrane bicelles,[35] and other liquid crystals[36–38] are suitable for aqueous solutions.

Paramagnetically Induced Alignment

This approach is based on the self-alignment of paramagnetic ions in an external magnetic field. Thus metal-binding molecules, e.g., metallo-proteins can be partially aligned if the bound metal ion is replaced by a paramagnetic ion like Tb^{3+}, Tm^{3+}, or Dy^{3+}.[39, 40] But also non-metal-binding molecules can be oriented if a sufficient *paramagnetic tag* is attached, although this has only been described for proteins and oligonucleotides.[41, 42] There are different techniques to fix the paramagnetic tag to a protein,[43] either a metal binding peptide is fused to the C/N-terminus or a metal binding ligand is fused to a solvent exposed cysteine residue or a complete paramagnetic protein is added. However, the synthetic addition of a tag often involves some preparative expenses, which is a major drawback of this technique. Moreover it turned out that some of the proposed metal binding tags exhibit different binding modes for the paramagnetic ion[44, 45] which result in different alignment tensors obscuring data analysis. All paramagnetic tags only result in a fairly small alignment, e.g., $\overline{D}_{max} \approx 14$ Hz for a ^{1}H-^{15}N spin pair in a protein.[46] This alignment can be scaled by the external magnetic field, as the alignment strength is field dependent. But paramagnetic tags also offer some unique advantages which are difficult to achieve by other means. Once the tag is attached to the molecule under investigation, the alignment tensor can be modified simply by changing the paramagnetic ion. The introduction of a paramag-

netic ion not only facilitates the observation of RDCs, RCSA, and RQCs, but will also lead to *pseudo contact shifts*.[47] These can also be used for structural investigations[48–50] or fast assignment strategies.[51] In contrast to other orienting media paramagnetic tags align *internally* and not *externally*, i.e., the source for alignment stems from the inside of the molecule (the paramagnetic ion) and is not due to an anisotropic interaction with the surrounding. This enables the detection of interdomain motions in proteins as different alignment tensors are observed for different domains of one protein.[43, 52]

Stretched Polymer Gels

The field of stretched polymers gels for alignment was pioneered by DELOCHE and SAMULSKI[53] in 1981, but it took until 2000 that the approach of 'strain induced alignment in a gel' (SAG) found broader acceptance.[54, 55] For this purpose a polymer gel is stretched *mechanically* to give an anisotropic environment for the solute which renders the alignment strength field independent. There are many different ways to achieve stretching in a polymer, like the use of Shigemi plungers,[56] teflon funnels,[57] the drying of the gel on a glass capillary before reswelling,[58] or simply anisotropic swelling.[59] However, one technique stands out from the others which was published by KUCHEL *et al.*[60] Alignment is achieved via a rubber tube with a gel inside that can be stretched, thus allowing an interactive adjustment of the alignment strength. This can be utilized for an increased precision of the RDC measurement as the coupling can be extracted from a linear fit and is not relying on a single point measurement. Moreover, this allows for tracing of solvent effects on the conformation of the solute. The class of stretched polymer gels is probably the most flexible and a variety of alignment media have been published for all types of solvents and molecules, e.g., polystyrene (PS),[59, 61] polydimethylsilane (PDMS)[62] for apolar organic solvents, polyacrylamide,[63] polyvinylacetate (PVA),[64] polyacrylnitrile (PAN),[65] polyurethane (PU)[66] for polar organic solvents and polyacrylnitrile[65] for aqueous solutions. Gelatine gels[67, 68] have to be pointed out here as they are chiral, thus enabling the discrimination of enantiomeres.

2.3 Relaxation and Dynamics

2.3.1 General Considerations

Relaxation in spectroscopical terms is defined as the ambition of the quantum mechanical system to return to its ground state, which is characterized by a maximum of entropy and a minimum of enthalpy. In principle, three fundamentally different pathways have to be distinguished - *spontaneous emission*, *coherent stimulated emission*, and *incoherent stimulated emission*. The first two processes are well-known from optical spectroscopy. Spontaneous emission determines the natural linewidth of optical systems via the Heisenberg uncertainty relationship, while the coherent stimulated emission is exploited in LASER applications. However, when calculating the probability for a spontaneous emission of an isolated magnetic dipole only small transition rates are obtained. For example, a transition probability of $\approx 10^{-18}$ Hz results for a proton in the excited state when placed in a static magnetic field of 14.1 T. In addition, it can be shown that also coherent stimulated emission is negligible as source for nuclear spin relaxation.[69]

Actually, nuclear spins relax as a consequence of the coupling to the *lattice*. The term lattice describes all surroundings, i.e., the complete microscopic environment, including other molecules as well as other degrees of freedom of the relaxing molecule itself - this comprises vibrational or rotational modes, for example. The energy levels of the lattice can be regarded as quasi-continuous, with their populations determined by the Boltzmann distribution. Moreover, the lattice can be assumed to be in permanent thermal equilibrium ensuring the relaxation of the spin system at any time.[8] The lattice acts as source of electromagnetic fields which alter the magnetic field strength at the location of the nucleus. As a result of the stochastic Brownian motion of the nucleus relative to the lattice these electromagnetic fields become time-dependent. These time-dependent electromagnetic fields induce emissions in the spin system and hence lead to relaxation. Obviously, these processes are not coherent as they inherently depend on the random motion of the molecule relative to the lattice.

The distribution of the occurring frequencies caused by the Brownian motion (and internal motions) is described by the *spectral density* $J(\omega)$ (see

8 Although this assumption is perfectly correct, local deviations from this condition can be found. In proteins this observation led to the invention of techniques like 'longitudinal TROSY',[70] 'SOFAST-HMQC',[71] or the 'extended flip-back scheme'.[72]

Sec. 2.3.4). A high spectral density at a certain frequency ω is equivalent to an enhanced stimulation of a transition in the spin system at the same frequency, hence the stimulated relaxation rate R is proportional to the intensity of the spectral density $J(\omega)$. Therefore the spectral density is linking the macroscopically observable relaxation rates with the statistical microscopic motions.

If the fluctuating electromagnetic fields are decomposed into their components parallel and perpendicular to the external magnetic field B_0, the relaxation processes can be divided even further. Longitudinal components give rise to *adiabatic* or *entropic* relaxation, whereas transverse components are responsible for *non-adiabatic* or *enthalpic* relaxation.[69] The latter are causing transitions between energy levels in the spin system if their frequency matches the separation of the corresponding energy levels. This can lead to transitions from the energetically higher state to the energetically lower state and *vice versa*, though the probability for a 'downstream' transition is much higher as the lattice is in thermal equilibrium and therefore offers a larger quantity of low energy states. Accordingly, the lattice is absorbing the energy within the spin system and brings the system back to the Boltzmann distribution. Certainly, these transitions between eigenstates of the spin system are reducing the lifetime of the spin state and introduce uncertainties in energies which in turn result in a decrease of phase coherence. Thus, non-adiabatic processes are responsible for thermal equilibration and a loss of phase coherence.

Depending on their sign/direction, longitudinal components of the fluctuating electromagnetic fields may add or subtract to/from the external magnetic field, which causes a dispersion of the magnetic field strength across the sample. Hence, the spins precess with different Lamor frequencies about the z-axis, which leads to a variation of energies of the nuclear spin states. As pointed out above, this variation is the origin of phase decoherence.

2.3.2 NMR Timescales

Beside the structure of a biomacromolecule, its dynamics is of critical importance for its function. Molecular motions play an important role in many biological processes like the recognition of binding partners, folding and unfolding events,[73,74] regulatory effects[75] or enzymatic conversion.[76,77] Moreover, they can make significant entropic contributions to the free energy.[78–80] These motions cover a wide range of timescales and

NMR spectroscopy is especially well suited to monitor these processes as it can access all timescales at an atomic resolution. Therefore, a brief overview to NMR timescales is given in the following, and the NMR observables encoding the corresponding motion are indicated.

- The *Larmor timescale* is characterized by the precession frequency of the nuclear spin in the static magnetic field. Therefore motions in the nanosecond or sub-nanosecond range are monitored which define the relaxation rate constants. Several processes occur on this timescale and may be sampled. For example, the interaction of a ligand with a target protein will change the molecular weight of the two. If this change is significant, the rotational diffusion rate will change as well and result in altered relaxation rates. For biomacromolecules especially internal motions and their change upon binding is of fundamental importance, as these contain information about enthalpy and entropy of the interaction. Internal motions are often faster than the rotational diffusion and are responsible for modifications of the relaxation rates. It has to be pointed out that these motions are commonly associated with small amplitudes of motions (< 1 Å) with small energy barriers. But also large scale motions may be responsible for altered relaxation rates, if smaller effects accumulate over several residues. Finally, a simple mathematical example should illustrate the relationship between the timescale and the Larmor frequency. As $\tau_{Larmor} = 1/\omega_{Larmor}$ the Larmor timescale will be approximately 0.17 ns, if a Larmor frequency of 600 MHz is assumed.

- The *spectral timescale* is determined by the inverse of the chemical shift difference of the conformational states adopted during the motion, i.e., $\tau_{spect} = 1/\left|\Omega_1 - \Omega_2\right|$. Considering a ^{15}N-nucleus in two different conformations with the chemical shifts 120 ppm and 122 ppm would correspond to a timescale of ≈ 8 ms. The μs-ms timescale is especially interesting as folding and unfolding events occur on this timescale as well as allosteric effects.[81, 82] Enzymes often have dissociation rate constants on the same order, leading to the assumption that certain motional processes are responsible for the catalytic activity.

- Finally, the *relaxation timescale*, which is defined by the spin-lattice relaxation time of the molecule. Hence, it is on the order of milliseconds to seconds. Because these motions are slower than the

spectral timescale, individual signals can be observed for each state. Exchange rates between the states can be extracted by ZZ-exchange spectroscopy.[83, 84] Furthermore, newer developments in pulse sequence design, like the 'SOFAST-HMQC'[71] open up the possibility to monitor very slow folding or unfolding events in real time.[74]

The NMR timescales are summarized in Fig. 2.6 together with the underlying molecular process and the affected NMR parameter. Two techniques have to be highlighted in this respect, as both are not relying on relaxation and therefore take an exceptional position among the others. Macroscopic diffusion can be determined using refocussing pulsed field gradients and the corresponding translatorial diffusion constant D_t is extracted by quantification of the resulting magnetization loss. However, this translational motion is independent of the internal motion which is assumed to be responsible for most functions of the biomacromolecule. In contrast, residual dipolar couplings are sensitive to a wide range of internal motions and permit a comparably simple geometrical interpretation of their ensemble average. Therefore, they facilitate the measurement of 'supra-τ-motions'[85][9] and the investigation of intrinsically unfolded proteins with large degrees of conformational freedom.[86]

2.3.3 Molecular Sources of Relaxation

In the preceding section fluctuating electromagnetic fields were identified as sources for relaxation. However, the molecular origins of these electromagnetic fields have not been discussed so far. In this section the main relaxation mechanisms are discussed and corresponding equations are presented.

Every magnetic dipole inherently exhibits a dipole field, which is axially symmetric around its principal axis. In the case of a nuclear spin in an external static magnetic field this axis is identical with the z-axis of the magnetic field. The components parallel and perpendicular to this axis can be described by

$$\begin{aligned} B^S_{x,y}(t) &= \tfrac{\mu_0 \hbar \gamma_S}{8\pi r_t^3} P_2^{(1)}(\cos\theta_t) \\ B^S_z(t) &= \tfrac{\mu_0 \hbar \gamma_S}{8\pi r_t^3} P_2^{(0)}(\cos\theta_t), \end{aligned} \tag{2.60}$$

9 These are motions on the ns-μs timescale.

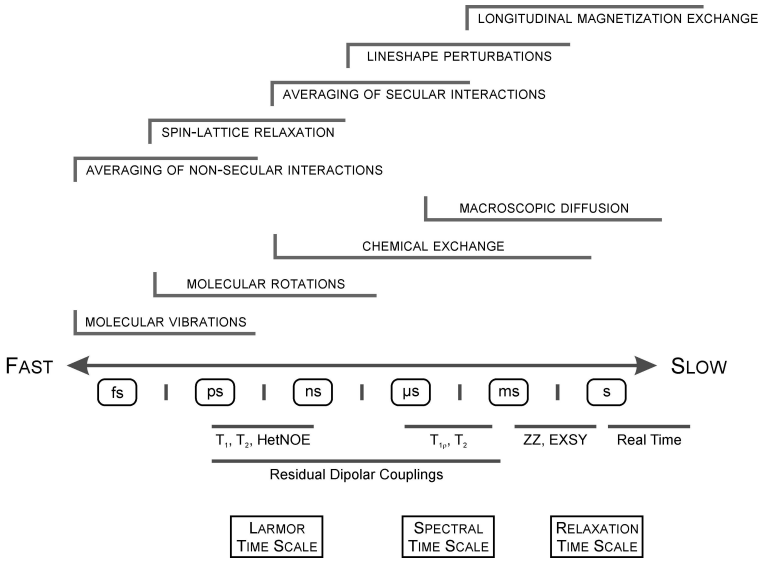

Figure 2.6: Motional timescales related to the corresponding NMR phenomenon (Top) and the associated NMR observable (Bottom). The NMR timescale is indicated at the bottom.

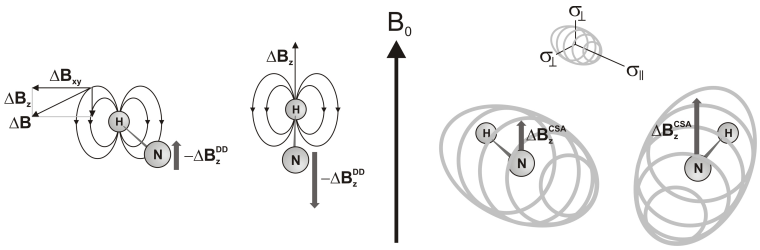

FIGURE 2.7: Dominant relaxation mechanisms for spin-$\frac{1}{2}$ nuclei. LEFT: The dipolar field of a nucleus may be seperated into components parallel and perpendicular to the external magnetic field. Due to Brownian motion these components fluctate at the site of an adjacent nucleus. RIGHT: Modulation of the local magnetic field components due to chemical shift anisotropy. For convenience only the z-component is given. Note that the local dipolar fields of ^{1}H and ^{15}N have opposite sign, due to the differing gyromagnetic ratio ($\gamma_H > 0$ and $\gamma_N < 0$).

with the corresponding second order associated Legendre polynomials

$$\begin{aligned} P_2^{(0)}(\cos\theta_t) &= \tfrac{3}{2}\sin(2\theta_t) \\ P_2^{(1)}(\cos\theta_t) &= \tfrac{1}{2}(3\cos^2\theta_t - 1). \end{aligned} \tag{2.61}$$

Considering a directly bonded ^{1}H-^{15}N spin pair in a protein each dipole will exhibit its own magnetic dipole field centered at the location of the corresponding nucleus. Depending on the orientation of the bond vector with respect to the external magnetic field the components of the dipole fields will add or subtract (cf. Fig. 2.7). As the molecule tumbles in solution due to stochastic Brownian motion, fluctuations in the magnetic field are induced, which in turn will lead to relaxation. The dipolar coupling constant, characterizing the magnetic energy operating for example on the ^{15}N-spin, can be obtained by multiplying the field contribution in Eq. 2.60 with the gyromagnetic ratio of the interacting spin γ_I

$$D_{IS} = \frac{\mu_0 \hbar \gamma_S \gamma_I}{8\pi r_{IS}^3}. \tag{2.62}$$

The chemical shift is a consequence of the shielding effect of the electrons surrounding the nucleus. Due to the external magnetic field these electrons are circulating around the nucleus and induce secondary magnetic fields, which may enhance or weaken the static magnetic field. As a result of

the deviating electron sheath for each nucleus, different Larmor frequencies result for different nuclei. In general, these shielding effects are orientation-dependent, resulting in an anisotropic shielding tensor. This shielding tensor is mathematically related to the *chemical shift anisotropy* tensor (CSA) with the principal axis σ_{xx}, σ_{yy}, σ_{zz}. In solution, usually only the isotropic chemical shift σ_{iso} is observed as the molecule tumbles fast enough to average all values ($\sigma_{iso} = \mathrm{Tr}\{\sigma\} = (\sigma_{xx} + \sigma_{yy} + \sigma_{zz})$). Of course, these tumbling motions will lead to fluctuations of the magnetic field as well and hence to relaxation. Just as the dipolar coupling constant, the coupling constant for the chemical shift anisotropy C quantifies the magnetic energy acting on spin I

$$C = \frac{\gamma_I B_0 \Delta\sigma}{3}\sqrt{1 + \frac{\Delta\eta^2}{3}}. \tag{2.63}$$

In this equation $\Delta\sigma$ is the anisotropy and $\Delta\eta$ the rhombicity of the CSA tensor.[10] For the ^{15}N-nucleus the CSA tensor is axially symmetric and the anisotropy becomes $\Delta\sigma = \sigma_{ax} = \sigma_{\parallel} - \sigma_{\perp}$, while the rhombicity simplifies to zero. In most cases the principal axis of this CSA tensor is assumed to be parallel to the ^{1}H-^{15}N bond vector, although it has been pointed out by Fushman and Cowburn that the two vectors share an angle of $\approx 17^\circ$ on average in proteins.[87]

Further sources of fluctuating magnetic fields exist in molecules but are not relevant for the relaxation processes in proteins and especially the ^{15}N nucleus which has been investigated in Chapter 4. Therefore, these sources will be just given for completeness, but will not be discussed in detail. This group includes for example scalar coupling interactions, quadrupolar interactions, paramagnetic interactions, and spin rotations. The corresponding coupling constant for each of these interactions is specified in Tab. 2.2.

2.3.4 Correlation Function and Spectral Density

So far, the discussion of relaxation phenomena presented here has focused on the origin of the fluctuating electromagnetic fields, but was lacking a description of the molecular motions underlying these processes. This, however, is an essential piece for a quantitative description of relaxation and will be presented in this section. In mathematical terms the motional processes of a molecule are commonly described by the *correlation function*

10 The anisotropy is defined as $\Delta\sigma = \sigma_{xx} - \frac{\sigma_{yy}+\sigma_{zz}}{2}$ and the rhombicity as $\Delta\eta = \frac{\sigma_{yy}-\sigma_{zz}}{\sigma_{xx}-\sigma_{iso}}$.

Table 2.2: Overview of the spin-lattice interactions along with the corresponding coupling constants and effective correlation times.

Interaction	Coupling Constant	Effective Correlation Time
dipolar[a]	$D = \sqrt{\frac{4}{3}} \left(\frac{\mu_0 \gamma_I \gamma_S \hbar}{8\pi r_{IS}^3} \right) \sqrt{s(s+1)}$	$\tau_c = \frac{1}{6D_R}$
CSA	$C = \left(\frac{\gamma_I B_0 \Delta\sigma}{3} \right) \sqrt{1 + \frac{\Delta\eta^2}{3}}$	$\tau_c = \frac{1}{6D_R}$
scalar	$K_{SC} = \sqrt{\frac{1}{3}} J \sqrt{s(s+1)}$	$\tau_c = \frac{1}{6D_R}$
spin rotation[b]	$K_{SR} = \sqrt{\left(\frac{C_{ax}^2 + 2C_{rhom}^2}{3} \right) \left(\frac{I_m kT}{2\hbar^2} \right)}$	$\tau_{impulse} = \frac{I_J}{6kT\tau_{rot}}$
quadrupolar[c]	$Q = \frac{\sqrt{3}}{8} \left(\frac{e^2 \mu_q q}{\hbar} \sqrt{1 + \frac{\Delta\eta_e^2}{3}} \right)$	$\tau_c = \frac{1}{6D_R}$

[a] I = relaxing spin; S = coupled spin; s = spin quantum number.

[b] I_m= moment of inertia; C_{ax}, C_{rhom} = axial and rhombic components of the spin-rotation coupling tensor.

[c] μ_q= nuclear quadrupole moment; q = electric field gradient; η_e = asymmetry parameter of the electric field.

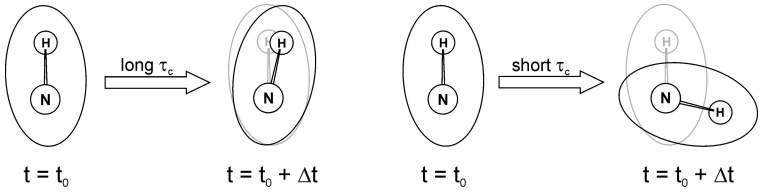

Figure 2.8: Illustration of the rotational correlation time τ_c. The orientations of a molecule at two different time points ($t = t_0$ and $t = t_0 + \Delta t$) is indicated for large values of τ_c (Left) and small values (Right). In both cases the ^{1}H-^{15}N bond vector is fixed with respect to the molecular frame of reference.

$C(t)$, which characterizes the correlation of orientations at two different timepoints. It is best visualized when considering a ^{1}H-^{15}N spin pair whose orientation is fixed relative to the molecular frame of reference. When the molecule tumbles in solution the bond vector between the two atoms will change its direction and the magnitude of the change will depend on the tumbling rate. Obviously, large molecules will tumble significantly slower than small molecules. Therefore, the ^{1}H-^{15}N bond vector will be found in almost the same orientation after a small time step Δt and consequently, both orientations are highly correlated. But the bond vector will reorient much faster if the molecule tumbles fast in solution and only a small degree of correlation is obtained between the two orientations; both cases are illustrated in Fig. 2.8. The rate of reorientation is characterized by the rotational correlation time τ_c and is related to the correlation function of a rigid, spherical molecule by

$$C(t) = \frac{1}{5} \exp\left(-t/\tau_c\right). \tag{2.64}$$

The correlation time can also be imagined as the average time interval required by a molecule to rotate by one radian.[88] It can be calculated for the above assumed case of a spherical molecule via Stoke's law

$$\tau_c = \frac{4\pi\eta_w r_{hydro}^3}{3k_B T}, \tag{2.65}$$

where η_w is the viscosity of the solvent, r_{hydro} the hydrodynamic radius of the solute, k_B the Boltzmann constant, and T the temperature. Even with this simple assumption of a spherical molecule fundamental principles

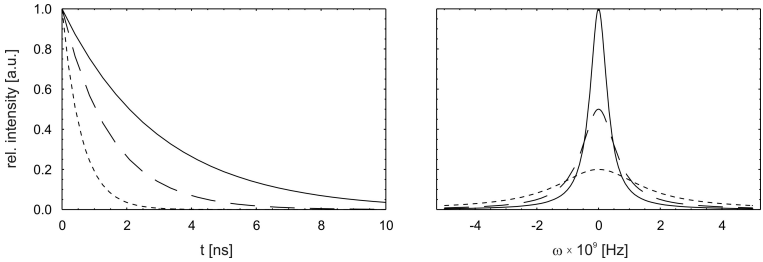

FIGURE 2.9: Correlation functions (LEFT) and spectral densities (RIGHT). Both plots have been normalized to 1 and overall correlation times of $\tau_c = 3, 1.5,$ and 0.6 ns have been used for simulations of the solid, long dashed, and short dashed curve, respectively.

can be disclosed. An increase of temperature will lead to a decrease of the correlation time, while an increase of the viscosity of the solvent will result in a rise of the correlation time. In general, these are the only macroscopic handles offered to the spectroscopist to modify the relaxation parameters of the molecule under investigation. For example, WAND *et al.* conducted experiments with proteins encapsulated in reverse micelles dissolved in low-viscosity solvents to reduce the correlation time entailing optimized relaxation parameters.[89]

Commonly, the motional parameters are not analyzed in time space, but in frequency space. Therefore, the correlation function is Fourier transformed and results in the corresponding *spectral density function* $J(\omega)$:

$$J(\omega) = \frac{\tau_c}{1 + \omega^2 \tau_c^2}. \tag{2.66}$$

Apparently, the spectral density function adopts the shape of a Lorentzian function. But it has to be pointed out that the spectral density function does not always have this simple mathematical form. If a more complex motional model is assumed, the correlation function will have a more sophisticated form as well and will also give rise to more complex spectral density functions (see Sec. 2.3.6). However, the model of the rigid, spherical rotator already reveals that short correlation times will lead to broad spectral densities and *vice versa* (cf. Fig. 2.9). As different nuclei have different gyromagnetic ratios and correlation times (see Sec. 2.3.6), the magnitude and frequency of the corresponding magnetic dipole will vary

as well. Therefore, each nucleus of the tumbling molecule will create its own dipolar field with its own spectral density function. In addition, superpositions of motions will be generated leading to spectral density functions centered around the sum or the difference of the nuclei.

2.3.5 Selected Relaxtion Mechanisms

As already pointed in Sec. 2.1.3, the time course of an NMR experiment can be calculated with the Liouville- von Neuman equation (Eq. 2.16), where $\widehat{\Gamma}$ is the relaxation superoperator. How is this operator related to the equations derived above? The relaxation superoperator is a $4^n \times 4^n$ matrix, where n is the number of spins, and the entries of the matrix are the relaxation rates between all basis operators. If the basis operators are arranged in a fashion that the populations are on the top left followed by zero-quantum operators, single-quantum operators and so forth, the relaxation superoperator adopts the form of the *Redfield kite*. Hence, the diagonal elements are the *auto-relaxation* rates and the off-diagonal elements are the *cross-relaxation* rates. In general, no transitions between operators of different coherence order occur, i.e., a single-quantum is not able to relax into a double-quantum operator, for example. In addition, heteronuclear spin systems commonly exhibit non-zero cross-relaxation rates only for the submatrix of populations. This may change if cross-correlated relaxation is gaining significance. In contrast, cross-relaxation in homonuclear spin systems may also occur between operators apart from z-magnetization (populations). This effect is exploited in ROESY experiments. The general construction scheme of the Redfield kite in the Cartesian operator basis is illustrated in Fig. 2.10. Notably, the submatrix indicated in Fig. 2.10 equals the relaxation matrix commonly analyzed for NOESY experiments (see Sec. 2.3.7).

The elements of the relaxation superoperator are composed of the contributions (*partial relaxation rates*) of each relaxation mechanism relevant for the corresponding operator. The sum of all these partial relaxation rates will give the correct entry for the relaxation superoperator and hence the superoperator itself

$$\widehat{\Gamma} = \sum_{w,w'} \Gamma^{w,w'}. \tag{2.67}$$

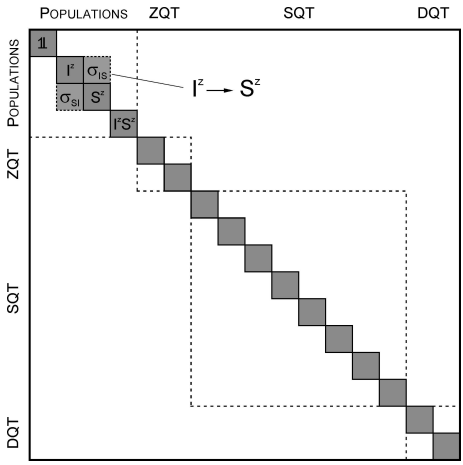

FIGURE 2.10: Schematic representation of the Redfield kite for a two-spin system. The entries are the relaxation rates between the corresponding operators with the auto-relaxation rates along the diagonal. Off-diagonal elements correspond to cross-relaxation rates, whereby cross-relaxation rates σ between the operators I_z and S_z are highlighted. ZQT = zero-quantum transition; SQT = single-quantum transition; DQT = double-quantum transition.

Partial relaxation rates can be calculated via

$$\Gamma_{\delta}^{w,w'} = \frac{1}{2} \left| K^{w} K^{w'} \right| \sum_{i(\delta)} a_i^{w,w'} J^{w,w'}(\omega_i), \tag{2.68}$$

where the index w specifies the relaxation mechanism, e.g., dipolar relaxation, K^w indicates the corresponding coupling constant, and $J(\omega)$ the spectral density function. The index i denotes the transition frequency and depends on δ specifying the transition under investigation. Prefactors $a_i^{w,w'}$ for the spectral density functions can be calculated by solving the corresponding double commutator[69] for the relaxing operator I_δ

$$[I_w, [I_{w'}, I_\delta]] \tag{2.69}$$

with the operator I_w characterizing the relaxation mechanism. Some prominent examples for partial relaxation rates are listed in Tab. 2.3.

With the coupling constants reported in Tab. 2.2 and the additional entries in Tab. 2.3 relaxation rates can be calculated by substitution into Eq. 2.68. In the following sections some relevant cases are discussed in more detail. All examples are concerned with the relaxation of the ^{15}N-nucleus in a ^{1}H-^{15}N spin pair, as these foundations are used in a later chapter. Only the paragraph on the transient NOE (*vide infra*) examines two adjacent proton spins.

Longitudinal Relaxation

Longitudinal relaxation or misleadingly called *spin-lattice* relaxation is the process by which nuclear spins are returning to their equilibrium state, characterized by the Boltzmann distribution. Commonly, it is quantified by the time constant T_1 or the reciprocal value, the longitudinal relaxation rate constant R_1. Using the equations described above, the following expression can be derived for R_1:

$$\begin{aligned} R_1 &= \Gamma_1^D + \Gamma_1^{CSA} \\ &= \frac{1}{2} D^2 \left[6J(\omega_N) + 2J(\omega_N - \omega_H) + 12J(\omega_N + \omega_H) \right] + \frac{1}{2} C^2 6J(\omega_N). \end{aligned} \tag{2.70}$$

If R_1 is plotted versus the correlation time of a spherical molecule (cf. Fig. 2.11) it becomes apparent that R_1 relaxation is significantly slowed down for small and large correlation times τ_c. These two cases are denoted as *extreme narrowing* ($|\omega\tau_c| \ll 1$) and *slow tumbling* limit ($|\omega\tau_c| \gg 1$).

Table 2.3: Partial relaxation rates $\Gamma(I)$ in the IS-spin system.

Auto-relaxation rates		$K^w K^{w'}$	$J(0)^a$	$J(\omega_I)$	$J(\omega_I-\omega_S)$	$J(\omega_S)$	$J(\omega_I+\omega_S)$
T_1-type	$\Gamma^D(I_z)$	D^2		6	2		12
	$\Gamma^{CSA}(I_z)$	C^2		6			
	$\Gamma^{SC}(I_z)$	J^2			2		
	$\Gamma^{Q}(I_z)$	Q^2		2			8
T_2-type	$\Gamma^D(I_x)$	D^2	4	3	1	6	6
	$\Gamma^{CSA}(I_x)$	C^2	4	3			
	$\Gamma^{SC}(I_x)$	J^2	1		1		
	$\Gamma^{Q}(I_x)$	Q^2	3	5			2
T_1-type	$\Gamma^D(2I_zS_z)$	D^2		6		6	
	$\Gamma^{CSA}(2I_zS_z)$	C^2		6			
T_2-type	$\Gamma^D(2I_xS_z)$	D^2	4	3	1		6
	$\Gamma^{CSA}(2I_xS_z)$	C^2	4	3			
	$\Gamma^D(2I_xS_x)$	D^2		3	1	3	6
	$\Gamma^{CSA}(2I_xS_x)$	C^2		3			
Cross-correlation rates[b]							
	$\Gamma^{D_1,D_2}(I_z)$	$\pm S^{D_1,D_2} D_1 D_2$		6			
	$\Gamma^{D_1,D_2}(I_x)$	$\pm S^{D_1,D_2} D_1 D_2$	4	3			
	$\Gamma^{D,CSA}(I_z \rightarrow 2I_zS_z)$	$\pm S^{D,CSA} DC$		6			
	$\Gamma^{D,CSA}(I_x \rightarrow 2I_xS_z)$	$\pm S^{D,CSA} DC$	4	3			
Cross-relaxation rates							
	$\Gamma^{D_1,D_2}(I_z \rightarrow S_z)$	D^2			-2		12
	$\Gamma^{SC_1,SC_2}(I_z \rightarrow S_z)$	J^2			-2		

[a] When R_2 is measured under spin locking conditions $J(0)$ has to be replaced by $J(\omega_{SL})$.

[b] The sign of the cross-correlation rate depends on the spin state of spin S (α or β). For isotropic molecular tumbling the order parameter $S^{w,w'}$ is identical with the second order Legendre polynome P_2 where θ equals the fixed angle between the IS dipole-dipole interaction and the CSA tensor.

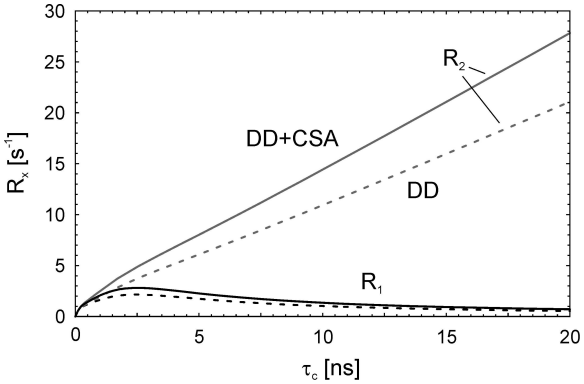

Figure 2.11: Longitudinal (black) and transverse (grey) relaxation rates for the isolated ^{1}H-^{15}N spin system. A bond length of $r_{NH} = 1.02$ Å and a static magnetic field of $B_0 = 14.1$ T was used for calculations. Furthermore, the CSA tensor was assumed to be axially symmetric with an asymmetry parameter of $\Delta\sigma = -160$ ppm. Dashed lines indicate simulations neglecting CSA contributions.

Transverse Relaxation

The loss of coherence is denoted as *transverse* or *spin-spin* relaxation. Analogously to the spin-lattice relaxation it can be characterized by the time constant T_2 or the relaxation rate constant R_2:

$$\begin{aligned} R_2 =& \Gamma_2^D + \Gamma_2^{CSA} + R_{ex} \\ =& \frac{1}{2} D^2 \left[4J(0) + 3J(\omega_N)\omega_N - \omega_H) + 6J(\omega_H) + 6J(\omega_N + \omega_H)\right] \\ &+ \frac{1}{2} C^2 \left[4J(0) + 3J(\omega_N)\right] + R_{ex}. \end{aligned} \tag{2.71}$$

In comparison with longitudinal relaxation, transverse relaxation exhibits a dependence on the spectral density function at zero frequency $J(0)$ and contains an additional exchange contribution which accounts for chemical exchange processes. Unlike longitudinal relaxation rates, R_2 relaxation rates increase monotonically with increasing correlation time (see Fig. 2.11).

Heteronuclear NOE

If a nucleus is irradiated with a weak radio frequency field for a sufficient long time, this will effect the populations of the energy levels of an adjacent spin. For example, irradiating the proton spin in a ^{1}H-^{15}N spin pair will lead to a change of the population difference of the ^{15}N-nucleus. This phenomenon is termed *steady state nuclear Overhauser effect* or in short *steady state NOE*. It can be described as the ratio between the cross-relaxation rate and the longitudinal relaxation rate

$$\begin{aligned}\mathrm{N\{H\}} =& 1 + \frac{\gamma_H}{\gamma_N}\frac{\Gamma^{D_1,D_2}(I_z \rightarrow S_z)}{\Gamma_1^D + \Gamma_1^{CSA}} \\ =& 1 + \frac{\gamma_N}{\gamma_H} D^2 \left[12J(\omega_N + \omega_H) - 2J(\omega_N - \omega_H)\right] \\ & \frac{1}{D^2\left[6J(\omega_N) + 2J(\omega_N - \omega_H) + 12J(\omega_N + \omega_H)\right] + C^2 6J(\omega_N)}.\end{aligned} \tag{2.72}$$

Recalling the extreme narrowing and the slow tumbling limit discussed in the context with the longitudinal relaxation rate, these two cases can be distinguished also for the heteronuclear NOE. When τ_c adopts very small values ($|\omega\tau_c| \ll 1$) Eq. 2.72 simplifies to

$$\lim_{\tau_c \rightarrow 0} \mathrm{N\{H\}} = 1 + \frac{\gamma_N}{\gamma_H}\frac{10D^2}{20D^2 + 6C^2}, \tag{2.73}$$

whereas it takes the following form in the slow tumbling limit ($|\omega\tau_c| \gg 1$)

$$\lim_{\tau_c \rightarrow \infty} \mathrm{N\{H\}} = 1 + \frac{\gamma_N}{\gamma_H}\frac{D^2(12\omega_0^2\omega_N^2 - 2\omega_2^2\omega_N^2)}{D^2(12\omega_0^2\omega_N^2 + 2\omega_2^2\omega_N^2 + 6\omega_2^2\omega_2^2) + 6C^2(\omega_0^2\omega_2^2)}. \tag{2.74}$$

Here, the substitutions $\omega_0 = \omega_N - \omega_H$ and $\omega_2 = \omega_N + \omega_H$ have been incorporated. This results in the two limits of -3.93 and 0.78 for extreme narrowing and slow tumbling, respectively, when only dipolar relaxation is assumed. Notably, the heteronuclear NOE changes its sign when moving from short correlation times to long correlation times. A corresponding plot of the heteronuclear NOE versus the correlation time is shown in Fig. 2.12.

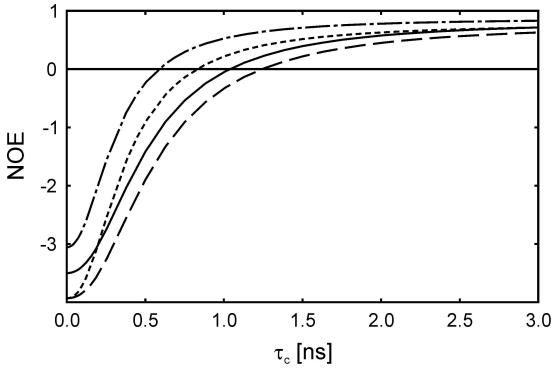

Figure 2.12: Plot of the heteronuclear NOE in dependence of the molecular correlation time. Curves are calculated with the same parameters as for Fig. 2.11. $B_0 = 14.1$ T, only DD (——); $B_0 = 14.1$ T, DD + CSA (- - -); $B_0 = 21.1$ T, only DD (-·-·-); $B_0 = 21.1$ T, DD + CSA (·····).

Transient NOE

The *transient NOE* describes the time course of I_z-magnetization, if spin S is selectively inverted. This one-dimensional experiment forms the foundation for the analysis of molecular structures by NMR spectroscopy. Distance information can be gained by analyzing the initial rate of the I_z-magnetization change, which is proportional to the cross-relaxation rate. By acquiring a series of experiments with varying mixing times to quantify the initial rate, distances can be extracted via the r^{-6} dependence of the cross-relaxation rate. Usually, cross- and auto-relaxation rates are abbreviated as follows: $\sigma_{IS} = \Gamma^{D_1,D_2}(I_z \rightarrow S_z)$ and $\rho = \Gamma^{D}(I_z)$, resulting in

$$\mathrm{I\{S\}{-}NOE} = 1 + \exp\left\{(\sigma_{IS} - \rho)\, t_{mix}\right\}\left[1 - \exp\left\{-2t\right\}\right]. \tag{2.75}$$

Obviously, more complex structures cannot be analyzed with simple 1D techniques, hence 2D or higher dimensional experiments have to be conducted to resolve the spectral overlap. Therefore, the following equations for the diagonal and cross-peak intensities are presented:

$$\begin{aligned} S_{diag} &= \cosh\left(\rho t_{mix}\right) \exp\left(-\sigma_{IS} t_{mix}\right) \\ S_{cross} &= \sinh\left(\rho t_{mix}\right) \exp\left(-\sigma_{IS} t_{mix}\right). \end{aligned} \tag{2.76}$$

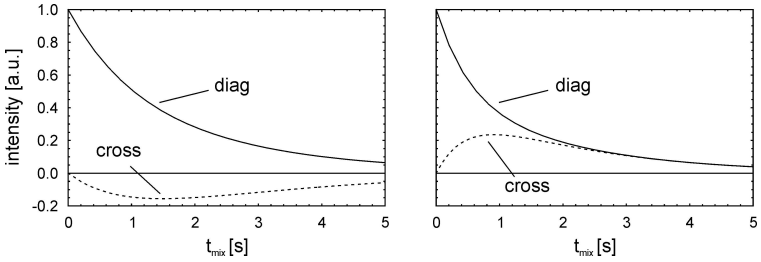

FIGURE 2.13: Signal intensities in the 2D-NOESY spectrum of a ^{1}H-^{1}H spin pair with small (LEFT, $\tau_c = 0.1$ ns) and large (RIGHT, $\tau_c = 1$ ns) correlation times. Cross- and diagonal-peak intensities are drawn as dashed and solid lines, respectively.

Corresponding illustrations for the signal intensities of two protons sharing a distance of $r_{HH} = 2$ Å are shown in Fig. 2.13. Likewise the heteronuclear NOE, the transient NOE is negative for small correlation times and positive for long correlation times. Cross-peaks in homonuclear 2D-NOESY spectra are also negative in the extreme narrowing limit and positive in the slow tumbling limit.

Cross-Correlated Relaxation

The probably most famous application of *cross-correlated relaxation* (CCR) is the *TROSY* experiment[90] (transverse relaxation optimized spectroscopy). Here, cross-correlation is used to attenuate the effects of transverse relaxation to yield sharp signals in a ^{1}H-^{15}N correlation spectrum, even if the molecule exhibits large correlation times. Cross-correlation denotes the interference of two relaxation mechanisms, i.e., relaxation due to the dipolar interaction and CSA interaction in the case of TROSY. Interference of the relaxation mechanisms leads to the addition or subtraction of the magnetic field components and hence, results in the attenuation or enhancement of the local magnetic field. Therefore, cross-correlated relaxation alters the relaxation behavior of the nucleus under investigation. The molecular origin of cross-correlation is the synchronism of the correlation function for two different relaxation mechanisms. This usually stems from a fixed geometry between the two sources of the local magnetic field. For example, the CSA tensor and the ^{1}H-^{15}N bond vector share a well defined

orientation relative to each other. Therefore, cross-relaxation occurs in this case.

The linewidth in TROSY spectra at half height along the ^{15}N-dimension can be calculated by multiplying the transverse relaxation rate R_2 with the factor π^{-1}

$$\begin{aligned}\Delta\nu_N =&\pi^{-1}\left[\Gamma_2^D+\Gamma_2^{CSA}+\Gamma^{D,CSA}(I_x\rightarrow 2I_xS_z)\right]\\ =&\frac{1}{2\pi}D^2\left[4J(0)+3J(\omega_N)+J(\omega_N-\omega_H)+6J(\omega_H)+6J(\omega_N+\omega_H)\right]\\ &+\frac{1}{2\pi}C^2\left[4J(0)+3J(\omega_N)\right]\pm\pi^{-1}S^{D,CSA}DC\left[4J(0)+3J(\omega_N)\right].\end{aligned} \tag{2.77}$$

As can be seen from this equation, the order parameter $S^{w,w'}$ describing the *cross-correlation* between the two correlation functions for the molecular relaxation mechanisms may adopt positive or negative values, representing a positive (constructive) or negative (destructive) interference between the two sources of relaxation. Actually, different spectral densities should be used in Eq. 2.77 for a precise description of the phenomenon. However, identical functions may be used when a rigid molecule is assumed, which has been done for convenience here.

For proteins tumbling slowly in solution, the high frequency contributions of $J(\omega)$ can safely be neglected ($|\omega\tau_c|\gg 1$). Hence, Eq. 2.77 can be recasted as follows[91]

$$\begin{aligned}\Delta\nu_N =&\frac{1}{2\pi}\left(D^2+C^2\pm P_2(\cos\theta)DC\right)\left[4J(0)+3J(\omega_N)\right]\\ =&\frac{1}{2\pi}\left(D^2+C^2\pm\left(3\cos^2\theta-1\right)DC\right)\left[4J(0)+3J(\omega_N)\right].\end{aligned} \tag{2.78}$$

Here, $P_2(\cos\theta)$ is the second order Legendre polynomial as already specified in the caption of Tab. 2.3. θ gives the angle between the principal axis of the CSA tensor and the ^{1}H-^{15}N bond vector. Interestingly, this angle has not been considered in the original work of Pervushin *et al.*,[90] which led to the wrong conclusion that the 'TROSY effect' is most pronounced at a magnetic field strength of ≈ 24.8 T. For proteins, an average angle of $\theta = -17^\circ$ is found[87] resulting in an 'optimal' field strength of ≈ 21.7 T. The dependence of the ^{15}N-linewidth on the magnetic field and the molecular correlation time τ_c is shown in Fig. 2.14.

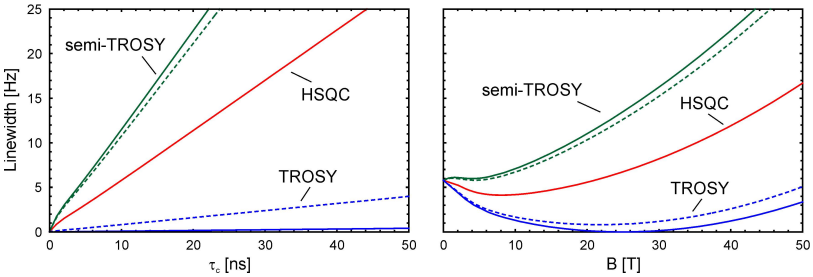

FIGURE 2.14: Dependence of the TROSY effect on the correlation time τ_c (LEFT) and the magnetic field strength B_0 (RIGHT). Simulations have been performed using Eq. 2.78 and the parameters stated in Fig. 2.11. No additional relaxation sources like remote protons have been assumed, hence linewidths are underestimated. For the correlation time dependence a magnetic field strength of $B_0 = 21.14$ T was used, while the B_0-dependence was calculated with a correlation time of $\tau_c = 10$ ns. Green lines correspond to a constructive interference of relaxation mechanisms (broad TROSY line) while blue lines correspond to a destructive interference (narrow TROSY line). For curves in red cross-correlation has been neglected (linewidth in HSQC). Solid lines indicate a vanishing angle θ between the principal axis of the CSA tensor and the ^{1}H-^{15}N bond vector, whereas an angle of $\theta = -17°$ has been assumed for dashed lines.

2.3.6 Model-Free Analysis

By analyzing relaxation data the NMR spectroscopist usually wants to gain information about the dynamics of a molecule. Relaxation and dynamics are related by the correlation function or spectral density, respectively. Therefore, the objective is to derive a correlation function out of the relaxation data which is suitable to explain the observed relaxation parameters. For this purpose, several approaches have been described. For example, one may assume a certain model for the motion of interest and test it against the relaxation data.[92–94] This, however, has the drawback that relaxation data might be over-interpreted.[95–97] Actually, in many cases the limited amount of relaxation data does not allow for the distinction between various models. The use of molecular dynamic (MD) simulations can be regarded as an extension of this approach as a certain 'model' is incorporated.[98, 99] Another approach is the *spectral density mapping* which has proven to be especially suitable for partially unfolded proteins.[97] Here, the analysis is based on the fact that relaxation rates are linear combinations of corresponding spectral density functions, each with its own, characteristic frequency. Hence, spectral densities can be extracted by solving the system of linear equations for relaxation rates. By far the most frequently used method to analyze relaxation rates in terms of dynamical parameters is the *model-free* approach which was proposed by Lipari and Szabo[95, 96] in 1982 and was extended by Clore *et al.*[100] This procedure makes use of the *generalized squared order parameter* S^2 and the *internal correlation time* τ_i to characterize the NMR relaxation parameters. As no explicit model of the molecular motion is assumed, it is referred to as 'model free'. The model-free approach is capable of analyzing motions faster than the overall correlation time. This approach was used in the analysis of the dynamical properties of BMPR-IA$_{\mathrm{ec/sf}}$ and is therefore discussed in more detail here.

Correlation Functions and Spectral Densities

Consider again a ^{1}H-^{15}N spin pair in a protein where the overall tumbling can be described by the correlation function in Eq. 2.64. In contrast to Sec. 2.3.4 the ^{1}H-^{15}N bond vector is now changing its orientation relative to the molecular fixed frame of reference. In the model-free approach it is postulated that this *internal* motion of the ^{1}H-^{15}N bond vector is *independent* of the overall tumbling of the protein. Therefore, it can be described

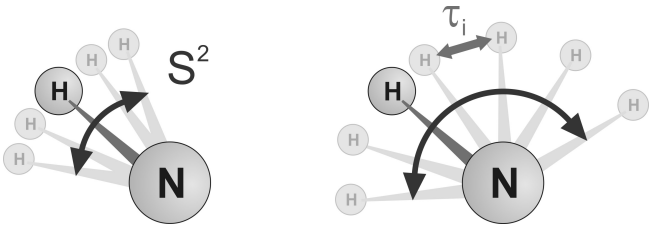

FIGURE 2.15: Illustration of the squared order parameter S^2 and the internal correlation time τ_i for the example of a ^{1}H-^{15}N spin pair. While the squared order parameter characterizes the 'amplitude' of the motion, the internal correlation time characterizes the 'rate of reorientation'.

by its own correlation function $C_i(t)$ and the complete correlation function for this spin pair can be written as the product of the two correlation functions

$$C(t) = C_o(t)C_i(t), \tag{2.79}$$

where the indices o and i refer to the overall and the internal motion, respectively. The correlation function for the internal motion $C_i(t)$ is defined as

$$C_i(t) = S^2 + \left(1 - S^2\right) e^{-\frac{t}{\tau_i}}. \tag{2.80}$$

Here, τ_i indicates the internal correlation time and S^2 the squared order parameter. The physical meaning of the two parameters is illustrated in Fig. 2.15. While the order parameter describes the spatial restriction of the motion of the ^{1}H-^{15}N bond vector, the internal correlation time quantifies the *rate* of reorientation of this vector. Two limiting cases can be distinguished. The orientation of the ^{1}H-^{15}N bond vector may be rigidly fixed relative to the molecular frame of reference, then S^2 adopts a value of 1. Hence, $C_i(t)$ simplifies to 1 and relaxation is governed by the overall correlation function and the corresponding correlation time τ_c. If the motion of the ^{1}H-^{15}N bond vector is completely unrestricted, a squared order parameter of 0 results and therefore internal motions become dominant for relaxation. Substituting Eq. 2.80 and Eq. 2.64 into Eq. 2.79 results in

$$C(t) = \frac{1}{5} e^{-\frac{t}{\tau_c}} \left[S^2 + \left(1 - S^2\right) e^{-\frac{t}{\tau_i}} \right]. \tag{2.81}$$

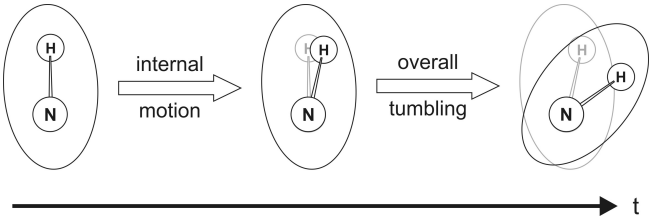

Figure 2.16: Illustration of the overall rotational correlation time τ_c and the internal correlation time τ_i. The orientation of the ^{1}H-^{15}N bond vector relative to the molecular frame of reference and the orientation of the molecule itself in solution at three different time points is indicated. While for short time periods the molecule does not change its orientation within the solution reorientation occurs for longer periods. In contrast, the ^{1}H-^{15}N bond vector already changes its orientation at short time periods, if τ_i is significantly shorter than τ_c.

By Fourier transformation the spectral density function is obtained

$$J(\omega) = \frac{2}{5}\left[\frac{S^2\tau_c}{1+\omega^2\tau_c^2} + \frac{\left(1-S^2\right)\tau'}{1+\omega^2\tau'^2}\right], \tag{2.82}$$

where τ' is related to the overall correlation time and the internal correlation time by $\tau'^{-1} = \tau_c^{-1}\tau_i^{-1}$. This equation clarifies again the two cases already discussed above. If the internal motion is slow relative to overall tumbling ($\tau_i \gg \tau_c$) then $\tau' \approx \tau_c$ and the spectral density function takes the form of Eq. 2.66. On the other hand, if the internal motion is faster than the rotational correlation time ($\tau_i \ll \tau_c$), τ' is approximately equal to τ_i and the spectral density function in Eq. 2.66 is scaled by the factor S^2. As a result the correlation function decays rapidly with a rate of τ_i^{-1} until it drops below the value of S^2 (see Fig. 2.17 and expansion therein). Then the slope of the correlation function changes and it decays with a time constant of τ_c. This indicates that overall motion becomes more decisive with increasing time what is illustrated in Fig. 2.16.

It has been recognized very early that the simple assumption of two uncorrelated motions is sometimes not sufficient to analyze all experimental relaxation data.[100] Therefore, the model-free approach was extended by an additional parameter set. The correlation function $C_i(t)$ is divided into a product of two separate functions, namely $C_s(t)$ and $C_f(t)$. These represent a slow internal motion and a fast internal motion, where the time

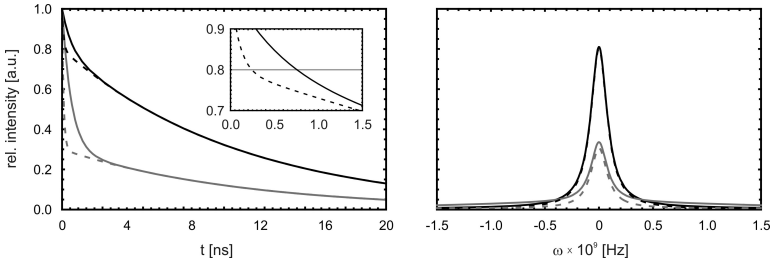

FIGURE 2.17: Correlation functions (LEFT) and spectral densities (RIGHT) consisting of internal and overall motions. For the black curves a squared order parameter of $S^2 = 0.8$ was assumed, while for grey curves S^2 was set to 0.3. The dashed graphs were simulated with an internal correlation time of $\tau_i = 0.1$ ns, while for solid lines τ_i was assumed to be 0.6 ns. In all cases the overall correlation time was $\tau_c = 11$ ns. It becomes apparent, that if internal motions govern the relaxation process, the correlation function drops rapidly with a rate of τ_i^{-1} but changes its slope significantly if a value of S^2 was reached (see enlargement).

constant for the two internal motional modes have to differ by more than one order of magnitude to be physically relevant. Then the new internal correlation function can be written as

$$C_i(t) = C_f(t) \cdot C_s(t) = S^2 + \left(1 - S_f^2\right) e^{-\frac{t}{\tau_f}} + \left(S_f^2 - S^2\right) e^{-\frac{t}{\tau_s}} \qquad (2.83)$$

with $S^2 = S_f^2 S_s^2$. Here, the two squared order parameters refer to fast (S_f^2) and slow internal motion (S_s^2), respectively. The corresponding correlation times are τ_f and τ_s. As before, the spectral density function can be obtained by Fourier transformation

$$J(\omega) = \frac{2}{5}\left[\frac{S^2\tau_c}{1+\omega^2\tau_c^2} + \frac{\left(1 - S_f^2\right)\tau_f'}{1+\omega^2\tau_f'^2} + \frac{\left(S_f^2 - S^2\right)\tau_s'}{1+\omega^2\tau_s'^2}\right] \qquad (2.84)$$

where the correlation times τ_f' and τ_s' are defined as $\tau_f'\tau_c/(\tau_f + \tau_c)$ and $\tau_f'\tau_c/(\tau_f + \tau_c)$, respectively, and obey the condition $\tau_f \ll \tau_s \ll \tau_c$.

It has to be emphasized that, for the derivation of the equations stated above, a spherical molecule was assumed. The form of Eq. 2.84 changes dramatically if an axially symmetric diffusion tensor (*vide infra*) is assumed

$$J(\omega) = \frac{2}{5}\sum_{j=1}^{3} A_j \left[\frac{S^2\tau_j}{1+\omega^2\tau_j^2} + \frac{\left(1 - S_f^2\right)\tau_f'}{1+\omega^2\tau_f'^2} + \frac{\left(S_f^2 - S^2\right)\tau_s'}{1+\omega^2\tau_s'^2}\right]. \qquad (2.85)$$

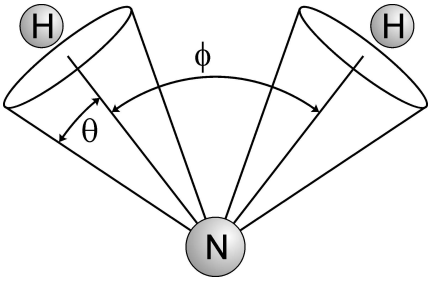

Figure 2.18: The 'two-site-jump' model for the ^{1}H-^{15}N bond vector. For the bond vector two *independent* motional modes are assumed, where the amplitudes of both modes are characterized by the angles θ and ϕ. While the angle θ corresponds to the faster of the two motional modes, the angle ϕ refers to the slower mode of the motion.

The convenience of the model-free approach is based on the fact that no assumption on the physical nature of the motion is made. However, the fitting parameters which are the outcome of a model-free analysis can still be related to a specific motional model. Typical models are the 'rotation-on-a-cone' model or the 'Gaussian-axial-fluctuation' model[98] and have been reviewed by Daragan *et al.*[94] For example, S^2 is related to the semi-cone angle θ of the 'wobbing-in-a-cone' model by $S^2 = [0.5\cos\theta\,(1+\cos\theta)]^2$.[101, 102] When a second internal motional mode is introduced to the fitting function of the model-free approach, the 'two-site-jump' model can be used to interpret the microscopic behavior of the ^{1}H-^{15}N bond vector. It is illustrated in Fig. 2.18 and assumes two motions apart from overall tumbling. One refers to the slower internal motion and is described by a jump of the bond vector between two sites. The other motion corresponds to the fast internal motion and represents free diffusion within an axially symmetric cone. If this model is used for interpretation and both sites are populated equally, S_s^2 translates into the angle ϕ between both cones via $S_s^2 = \left[1 + 3\cos^2\phi\right]/4$.

Diffusion Tensors

As pointed out in the previous section, the properties of the diffusion tensor have a dramatic effect on the mathematical form of the spectral density function. While for an isotropic diffusion tensor Eq. 2.82 can be used, the

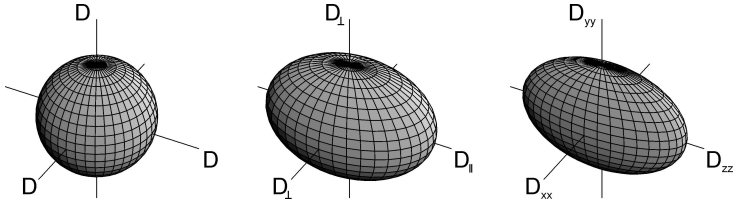

FIGURE 2.19: Illustration of different rotational diffusion tensor symmetries. LEFT: Isotropic diffusion tensor with $D_{xx} = D_{yy} = D_{zz} = D$. MIDDLE: Axially symmetric diffusion tensor with $D_{xx} = D_{\parallel} > D_{yy} = D_{zz} = D_{\perp}$. RIGHT: Fully anisotropic diffusion tensor with $D_{xx} > D_{yy} > D_{zz}$.

lengthy definition of Eq. 2.85 has to be applied for an axially symmetric diffusion tensor. Consequently, knowledge about the rotational diffusion tensor is essential for the analysis and interpretation of relaxation data.

The diffusion tensor quantifies the rate of rotation around the three principal axis of the molecular fixed frame of reference. This frame of reference is rotated so that the principal axis of the molecular frame coincide with the principal axis of the diffusion tensor. In a pictorial way, the diffusion tensor can be understood as some measure for the shape of the molecule and is related to the tensor for the moment of inertia. For example, a perfectly spherical molecule with uniform density will exhibit an *isotropic diffusion* tensor. Although proteins in solution usually do not obey these conditions they can be treated as globular molecules to a good approximation as well. Obviously, the diffusion tensor will adopt a different characteristic if the molecule deviates strongly from the spherical geometry and may become even fully *anisotropic*. Then all three principal components of the diffusion tensor (D_{xx}, D_{yy}, D_{zz}) exhibit different values, in which D_{xx} is defined to be the largest and D_{zz} the smallest element ($D_{xx} > D_{yy} > D_{zz}$). If two eigenvalues of the diffusion tensor are equal, the tensor is said to be *axially symmetric* where two cases can be distinguished. Either the molecule exhibits a *prolate* shape with $D_{xx} > D_{yy} = D_{zz}$ or the molecule has an *oblate* shape where $D_{xx} = D_{yy} > D_{zz}$. Different symmetries of the diffusion tensor are illustrated in Fig. 2.19.

Model Definitions

Extracting the motional parameters from relaxation data requires least-square fitting of the corresponding equations (Eq. 2.70-2.72) to the experimental relaxation rates. For a model-free analysis, typically three experimental parameters are available, i.e., the longitudinal (R_1), the transverse (R_2), and the cross-relaxation rate (heteronuclear NOE). Following the expressions given above for the spectral densities the model-free approach invokes a maximum of three parameters to interpret the experimental data. Therefore, the analysis must be based on strict statistical criteria to avoid over-interpretation, as N observables are fitted to N parameters. This problem can be partly overcome by measuring relaxation rates at more than one static magnetic field strength. Using Eqs. 2.79-2.85 five 'models'[11] can be distinguished and are summarized in Tab. 2.4.

- **Models 1 and 3** These two models are the most simple in the model-free approach. For model 1 only one parameter, the squared order parameter S^2, is needed. Internal motions characterized by the internal correlation time τ_i are assumed to be very fast (< 20 ps) and hence the spectral density function reduces to

$$J(\omega) = \frac{2}{5}\left(\frac{S^2\tau_c}{1+\omega^2\tau_c^2}\right). \tag{2.86}$$

  If an additional exchange process contributes to relaxation, the parameter R_{ex} is introduced and the model is referred to as model 3.

- **Models 2 and 4** In the classic Lipari-Szabo model (model 2) the internal correlation time is said to be 'relaxation active'. It is much slower than in model 1 but still faster than the overall tumbling time. The spectral density function can be expressed with the help of Eq. 2.82. Analogously to model 3, an additional exchange contribution is introduced via R_{ex} for model 4.

- **Model 5** This is the extended Lipari-Szabo model, which includes a very fast and a slower internal motion. As pointed out above, the two correlation times τ_f and τ_s differ at least by one order of magnitude. The spectral density function is given by Eq. 2.84.

11 The term 'model' is misleading in this context though commonly used in literature. Here, the term 'model' just describes the complexity of the correlation function or spectral density, respectively. It does *not* assume any specific motional model.

TABLE 2.4: Models in the model-free approach and their corresponding fitting parameters.

model	1	2	3	4	5
	S^2	S^2, τ_f	S^2, R_{ex}	S^2, τ_f, R_{ex}	S_f^2, S^2, τ_s

2.3.7 Back-Calculation of NOESY Spectra

Typically, structures of proteins and other biomacromolecules are determined either by X-ray crystallography or NMR spectroscopy. While X-ray crystallography uses the complex diffraction pattern produced by the molecular crystal in the beamline, the structure determination by NMR spectroscopy is mainly based on the analysis of experimental NOE data. However, X-ray crystallography offers the invaluable advantage to allow a validation of the generated structure simply by using it as input for predicting the expected diffraction pattern and comparing it with the experimental diffraction pattern. A comparable procedure is seldomly employed when NMR spectroscopy is used for structure determination, even though it is feasible, in theory as well as in practice. As the protein structure of the extracellular domain of BMPR-IA$_{ec}$ presented in Chapter 4 has been validated with the in-house written software NMRSPIRIT a short overview on NOE back-calculation is given.

The basis for back-calculating NOESY spectra is the relaxation matrix discussed in Sec. 2.3.5. The submatrix of the Redfield kite indicated in Fig. 2.10 contains the information needed to quantify cross-peak intensities and is denoted as $\mathbf{R}$ in the following. Along the diagonal of the matrix auto-relaxation rates can be found ($R_{kk} = \rho_k$), whereas off-diagonal elements represent cross-relaxation rates ($R_{kj} = \sigma_{kj}$). Consequently, the time course of z-magnetization can be written as

$$\frac{\mathrm{d}\Delta\mathbf{M}_z(t)}{\mathrm{d}t} = -\mathbf{R}\Delta\mathbf{M}_z(t). \tag{2.87}$$

The column vector $\Delta\mathbf{M}_z(t)$ is of dimension $1 \times n$ where n equals the number of spins in the spin system under investigation.[12] Therefore, large matrices have to be computed for molecules such as proteins comprising more than 500 relevant spins. Nevertheless, calculations are comparably fast requiring

12 Δ indicates the deviation from equilibrium magnetization.

less than 5 min for a 100 amino acid protein on a standard PC. The entries of the vector $\Delta\mathbf{M}_z(t)$ are the expectation values for the corresponding z-magnetization ($\Delta\mathbf{M}_{kz}(t) = \langle\Delta I_{kz}(t)\rangle$).

The differential equation in 2.87 has the formal solution

$$\Delta\mathbf{M}_z(t) = e^{-\mathbf{R}t}\Delta\mathbf{M}_z(0), \tag{2.88}$$

with $\Delta\mathbf{M}_z(0)$ corresponding to the initial magnetization.

An interesting property of NOESY transfer can be elucidated with this equation. Consider a homonuclear three spin system, where spin ① is in close proximity to spin ② and spin ② is additionally close to spin ③, but spin ① and ③ are too far apart to share a significant dipolar coupling ($\sigma_{13} = 0$). Hence, the following relaxation matrix can be set up for the spin system:

$$\mathbf{R} = \begin{pmatrix} \rho_1 & \sigma_{12} & 0 \\ \sigma_{12} & \rho_2 & \sigma_{23} \\ 0 & \sigma_{23} & \rho_3 \end{pmatrix}. \tag{2.89}$$

Solving Eq. 2.88 for this special case includes calculation of the matrix exponential of $\mathbf{R}$ which can be found by expanding it into a Taylor series. Consequently, the first entry of $\Delta\mathbf{M}_z(\tau_m) = \langle I_{1z}\rangle(\tau_m)$ represents the magnetization transfer from spin 1 to the other spins and takes the following form

$$\begin{aligned}
\langle I_{1z}\rangle(\tau_m) &= \sum_{k=1}^{3}\{e^{-\mathbf{R}\tau_m}\}_{1k}\langle I_{kz}\rangle(0) \\
&\approx \sum_{k=1}^{3}\{E_{1k} - R_{1k}\tau_m + \frac{1}{2}R_{1k}^2\tau_m^2 - \frac{1}{6}R_{1k}^3\tau_m^3\}\langle I_{kz}\rangle(0) \\
&= \langle I_{1z}\rangle(0)\{1 - \rho_1\tau_m + \frac{1}{2}(\rho_1^2 + \sigma_{12}^2)\tau_m^2 \\
&- \frac{1}{6}(\rho_1^3 + 2\rho_1\sigma_{12}^2 + \underline{\rho_2\sigma_{12}^2})\tau_m^3\} \\
&+ \langle I_{2z}\rangle(0)\{\underline{-\sigma_{12}\tau_m} + \frac{1}{2}(\rho_1 + \rho_2)\sigma_{12}\tau_m^2 - \frac{1}{6}(\rho_1^2 + \sigma_{12}^2)\sigma_{12} \\
&+ (\rho_1 + \rho_2)\rho_2\sigma_{12} + \sigma_{12}\sigma_{23}^2)\tau_m^3\} \\
&+ \langle I_{3z}\rangle(0)\{\frac{1}{2}\underline{\sigma_{12}\sigma_{23}\tau_m^2} - \frac{1}{6}(\rho_1 + \rho_2 + \rho_3)\sigma_{12}\sigma_{23}\tau_m^3\}.
\end{aligned} \tag{2.90}$$

Each term in this equation corresponds to a physical process, but only underlined terms will be discussed in more detail. Direct transfer from spin ① to spin ② is described by the term $-\sigma_{12}\tau_m$ and is the origin of 'regular' cross-peaks in the NOESY spectrum. The term $\rho_2\sigma_{12}^2$ specifies the *back-transfer* between two adjacent spins, i.e., the process $I_1 \rightarrow I_2 \rightarrow I_1$ and causes a reduction of cross-peak intensity. Furthermore, the term $\sigma_{12}\sigma_{23}\tau_m^2$ is the source of a process called *spin diffusion*, which often hampers the analysis of NOESY spectra. It characterizes the transfer from spin ① through spin ② to spin ③, i.e., $I_1 \rightarrow I_2 \rightarrow I_3$. As a result this process causes a cross-peak between spin ① and spin ③, although they are not close enough in space to cause a 'regular' cross-peak. Notably, the sign for the direct transfer and spin diffusion have opposite sign. Hence, cross-peak intensities for the two processes may have opposite signs as well if σ adopts *positive* values. This, however, is not the case for large macromolecules, where σ is generally *negative*.

As can be seen from these equations, spin diffusion and back-transfer depend strongly on the mixing time and the correlation time (via σ). Therefore, these effects can only be neglected if short mixing times are used, which is the reason why especially short mixing times (< 150 ms) are used for protein spectroscopy.

Chapter 3

Towards the Measurement of ^{1}H-^{1}H-RDCs

3.1 Introduction

The discovery of weakly aligning media for the use in NMR spectroscopy in 1995[103] facilitated a multitude of applications and emerged as a versatile tool, not only in structural biology,[104–106] but also in materials science,[107–109] medicine,[110, 111] and chemical research.[112, 113] It offers a broad spectrum of applications which ranges from the determination of structures and dynamics of biomacromolecules,[104, 105, 114–122] through the analysis of stereochemistry of small compounds[123, 124] and their enantiomeric ratio[67, 68, 125] to the elucidation of point groups.[126, 127] All these applications are mainly based on the precise determination of residual dipolar couplings (RDCs). For biomacromolecules, nowadays, defined labelling schemes are introduced by default, which allow the facile and rapid measurement of distinct couplings due to the increased sensitivity and resolution (cf. Sec. 4.5). Small organic compounds like peptides, oligosaccharides, nucleotides, lipids, or natural products, however, commonly lack this advantage. In addition, sufficient NMR active spin labels usually cannot be incorporated as corresponding synthesis are not straightforward or cost-intensive. Therefore, RDC measurements of small organic molecules predominantly rely on the determination of $^{1}D_{CH}$-couplings which can be extracted from coupled HSQC spectra as described in Sec. 5.2. Still, for

compounds like saccharides this only results in a maximum of six couplings for a sugar ring. Considering the fact, that a minimum of five couplings is essential to determine the alignment tensor, which usually forms the basis for any further investigations, the underlying ambiguity becomes evident. The situation even worsens if CH bond vectors are collinear and hence are degenerate,[128] leading to the impossibility to determine the alignment tensor at all. To overcome this problem measurement of couplings different to the $^1D_{CH}$-couplings is desirable. Several different approaches exist to access $^nD_{CH}$-couplings at natural abundance,[129,130] however, most of these techniques still face the problem that they are inherently insensitive, complicating a corresponding measurement. The most abundant and most sensitive spin in organic compounds usually is the ^{1}H-nucleus and hence, the measurement of ^{1}H-^{1}H-RDCs appears reasonable. But, analyzing ^{1}H-^{1}H-couplings in weakly aligned media is often hampered by the large linewidth and only in selected cases their extraction is feasible and has been solved satisfactory, as for $^2D_{HH}$-coupling in CH_2-moieties, for example.[131]

In principle, ^{1}H-^{1}H-RDCs can be measured with the same experimental techniques as commonly applied to $^nJ_{HH}$-couplings in isotropic solution, i.e., COSY or J-modulated techniques.[132] However, these techniques fundamentally rely on the separation of lines within the multiplet and any signal overlap will at least complicate if not fully prevent the extraction of the corresponding couplings. Obviously, this situation is commonly met when aligning organic compounds in stretched polymer gels or other media, as can be seen from Fig. 3.1. Here, strychnine is aligned in a PS/$CDCl_3$ gel and, apparently, no distinct lines can be observed for any multiplet. Consequently, it must be concluded that techniques basing on line separations are not sufficient to extract ^{1}H-^{1}H-RDCs and therefore, techniques exploiting the cross-peak volume as a measure for the coupling constant, like the H^NH^α experiment by VUISTER *et al.*,[133] are favourable.

As pointed out by THIELE *et al.*,[134] knowledge about the sign of the residual dipolar coupling is highly desirable, too. However, extraction of the sign of ^{1}H-^{1}H-RDCs is strongly hindered because of the fairly small scalar coupling. For example, consider two coupled ^{1}H-spins which are separated by 10 Hz in a 1D-spectrum in isotropic solution and subsequent alignment leads to a splitting of 20 Hz. As only 'effective' coupling constants $\Delta_s = |J+D|$ can be observed, the splitting might result either from a dipolar coupling of $D = +10$ Hz or from a coupling of $D = -30$ Hz, even if the *absolute* sign of the scalar coupling is available. Usually, the alignment

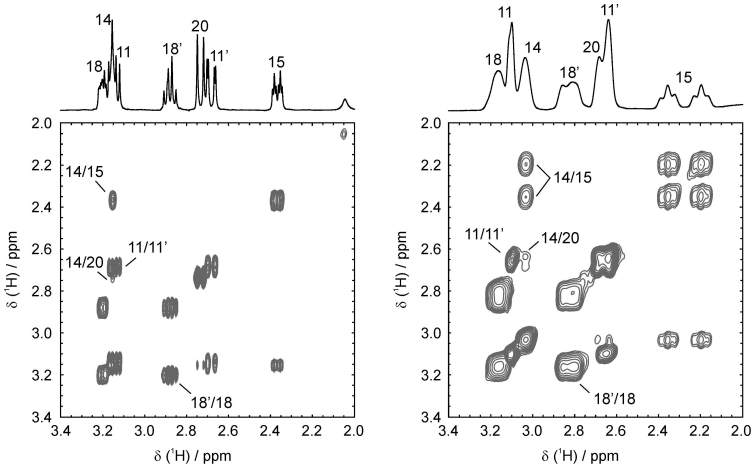

Figure 3.1: Line broadening and reassignment of ^{1}H-resonances in a strychnine sample. Reassignment of strychnine aligned in a PS/$CDCl_3$ gel was achieved using the JESTER-XY16 mixing sequence (*vide infra*). Left: Region of the 1D spectrum of strychnine dissolved in $CDCl_3$ with the assignment corresponding to Luy *et al.*[61] Right: The same region of the 1D spectrum of strychnine in a stretched PS/$CDCl_3$ gel with a quadrupolar deuterium splitting of $\Delta\nu_Q = 121$ Hz and the assignment derived from the *J*-ONLY-TOCSY.

strength is not known *a priori* and hence, ambiguities arise in the *sign* and *size* of the dipolar coupling. Typically, the sign of ^{1}H-^{1}H-couplings is determined using the E.COSY principle[135] and this technique has also been applied to the measurement of ^{1}H-^{1}H-RDCs.[134,136] Still, as described above, line broadening will severely deteriorate any measurement and thus E.COSY spectra cannot be regarded as a general solution to this problem. As a result of these principal considerations one can state that a technique for the measurement of ^{1}H-^{1}H-RDCs should meet the following requirements: first, it should be sign-sensitive; second, it should be volume-based, and third, the experimental effort should be as small as possible.

Homonuclear Hartmann-Hahn or TOCSY experiments are among the most important techniques in liquid state NMR spectroscopy[1,3] but they have seldomly been applied to the measurement of homonuclear coupling constants.[137–140] The majority of their applications concerns the assignment of scalar coupled spin systems, for which the resulting isotropic mixing Hamiltonian leads to very efficient coherence transfer.[141–145] The advantage of homonuclear Hartmann-Hahn transfer is the pure in-phase cross-peak pattern. Compared to COSY-type techniques, where broad lines will lead to a complete cancellation of the anti-phase cross-peaks, TOCSY spectra do not suffer from this drawback and exhibit intense cross-peaks even under strong line broadening effects[146] – a first prerequisite for the measurement of ^{1}H-^{1}H-couplings. In addition, the cross- and diagonal-peak volume is related unambiguously to the *relative* sign and size of the coupling constants within the spin system. Mostly, also the absolute sign of the scalar coupling constants can be extracted, as three-bond couplings are typically positive and two-bond couplings are negative.[1] Therefore a second prerequisite is fulfilled as well. Finally, TOCSY spectra are easy to setup and can be routinely measured without any further effort, rendering them a well-suited alternative for the determination of ^{1}H-^{1}H-couplings.

The transfer processes through scalar couplings in homonuclear Hartmann-Hahn experiments are very well understood,[3,144,145] but also for combinations of RDCs and scalar couplings suitable equations have been derived.[147–149] In contrast to purely scalar coupled spins with an isotropic coupling Hamiltonian, the symmetry of the interaction is reduced to an axially symmetric or cylindrical coupling Hamiltonian if dipolar couplings are present. As a consequence, coherence transfer can result in either positive

1 In the case of olefines and other seldom cases deviations from this rule are observed – in these cases the $^2J_{HH}$ coupling becomes positive.

or negative cross-peaks, depending on the orientation of the initial magnetization with respect to the principal axis of the effective Hamiltonian of a given multiple pulse sequence.[139, 146, 150]

Among the multitude of existing isotropic mixing sequences the properties change significantly with respect to coherence transfer through dipolar couplings. Most importantly, the offset dependence of the transfer efficiency of existing multiple pulse sequences differs for scalar and dipolar couplings[151] and the effective dipolar coupling constant is significantly scaled for the different sequences.[146, 150]

The latter argument enables the design of a set of pulse sequences that facilitate the sign sensitive measurement of residual dipolar couplings. Picking up the above example with two coupled proton spins, an additional experiment would be available now, where the splitting of the multiplet components now refers to $\Delta_s = |J + 0.5 \cdot D|$, for example. Obviously, the two cases, $D = 10$ Hz and $D = -30$ Hz, can be distinguished easily now, as one would lead to a splitting of $\Delta_s = 15$ Hz and the other one to a splitting of $\Delta_s = 5$ Hz.

Interestingly, homonuclear RDCs can be scaled even to zero by the use of the JESTER-1 multiple pulse sequence, which was originally designed for heteronuclear isotropic Hartmann-Hahn transfer (HIHAHA). This not only facilitates the reassignment of scalar coupled spin systems in presence of RDCs, but also allows the determination of scalar coupling constants even if the molecule under investigation is aligned. This might emerge as beneficial as alignment media might slightly influence the conformation of the solute[152] and hence, will alter the underlying scalar couplings. This effect will be probably most profound for ^{1}H-^{1}H-scalar couplings, especially $^3J_{HH}$, as these are very sensitive for any conformational change.

In this study the scaling of residual dipolar couplings within TOCSY mixing sequences is analyzed theoretically and is shown in experiment. In addition, the obtainable transfer amplitudes are used for the determination of ^{1}H-^{1}H scalar couplings in isotropic solution and for the determination of ^{1}H-^{1}H-RDCs within the alignment medium.

3.2 Modifying the Dipolar Coupling Tensor

3.2.1 Theory

Consider a homonuclear spin system with two spin-$\frac{1}{2}$ nuclei, termed I_1 and I_2. Then the cylindrical coupling Hamiltonian in an anisotropic medium

is given by[148,149]

$$\mathcal{H}_{cyl} = \mathcal{H}_J + \mathcal{H}_D, \tag{3.1}$$

where the isotropic coupling Hamiltonian is described by

$$\mathcal{H}_J = 2\pi J\{I_{1x}I_{2x} + I_{1y}I_{2y} + I_{1z}I_{2z}\} = 2\pi J\mathbf{I}_1\mathbf{J}\mathbf{I}_2 \tag{3.2}$$

with

$$\mathbf{J} = \begin{pmatrix} 1 & 0 & 0 \\ 0 & 1 & 0 \\ 0 & 0 & 1 \end{pmatrix} \tag{3.3}$$

and the anisotropic dipolar component with the definition according to KRAMER *et al.*[151] is of the form

$$\mathcal{H}_D = 2\pi D\{-\frac{1}{2}I_{1x}I_{2x} - \frac{1}{2}I_{1y}I_{2y} + I_{1z}I_{2z}\} = 2\pi D\mathbf{I}_1\mathbf{D}\mathbf{I}_2 \tag{3.4}$$

with

$$\mathbf{D} = \begin{pmatrix} -\frac{1}{2} & 0 & 0 \\ 0 & -\frac{1}{2} & 0 \\ 0 & 0 & 1 \end{pmatrix}. \tag{3.5}$$

In both cases the coupling tensors $\mathbf{J}$ and $\mathbf{D}$ are real and diagonal matrices which can be treated separately since all appearing product operators commute as long as chemical shift contributions are neglected. The orientational component of the scalar interaction $\mathbf{J}$ is proportional to the identity matrix, independent of the choice of reference system. In a toggling frame defined by a non-selective rf-irradiation, the isotropic scalar coupling tensor $\mathbf{J}$ therefore is constant, whereas the anisotropic coupling tensor $\mathbf{D}$ is modulated by the irradiation of pulses. Since $\mathrm{Tr}(\mathbf{D}) = 0$, the dipolar interactions can be averaged to zero. If the pulse sequence is cyclic (with cycle time τ_{cycl}), i.e., if the orientation of the toggling frame is identical to the orientation of the rotating frame at the beginning and at the end of the pulse sequence (which is for example the case for all TOCSY-sequences, as they have an effective flip angle that corresponds to multiples of 360°), the effect of a pulse sequence can be described by the average coupling terms[3,153,154]

$$\overline{\mathcal{H}_{cyl}} = \mathcal{H}_J + \overline{\mathcal{H}}_D \tag{3.6}$$

with the corresponding average dipolar coupling Hamiltonian

$$\overline{\mathcal{H}_D} = 2\pi D\mathbf{I}_1\overline{\mathbf{D}}\mathbf{I}_2. \tag{3.7}$$

As long as rf-pulses dominate all other interactions, the average Hamiltonian can be derived straightforwardly in the toggling frame[3] where the isotropic and dipolar interactions are modulated as a function of time. The integration over all orientations adopted by the tensor $\mathbf{D}'(t)$ during the pulse sequence divided by the 'residence time' at the corresponding orientations yields the average coupling tensor $\overline{\mathbf{D}}$,

$$\overline{\mathbf{D}} = \frac{1}{\tau_{cycl}} \int_0^{\tau_{cycl}} \mathbf{D}'(t) \mathrm{d}t. \tag{3.8}$$

The time-dependent coupling tensor $\mathbf{D}'$ is again a real 3×3 matrix. As shown by Glaser *et al.*,[3,151] its elements $d_{\alpha\beta}$ $(\alpha, \beta = x, y, z)$ can be calculated via three-dimensional rotation matrices according to

$$\mathbf{D}' = \begin{pmatrix} d_{xx}(t) & d_{xy}(t) & d_{xz}(t) \\ d_{yx}(t) & d_{yy}(t) & d_{yz}(t) \\ d_{zx}(t) & d_{zy}(t) & d_{zz}(t) \end{pmatrix} \tag{3.9}$$

with

$$d_{\alpha\beta}(t) = -\frac{1}{2} a^1_{x\alpha}(t) a^2_{x\beta}(t) - \frac{1}{2} a^1_{y\alpha}(t) a^2_{y\beta}(t) + a^1_{z\alpha}(t) a^2_{z\beta}(t), \tag{3.10}$$

where the coefficients $a^i_{\alpha\beta}(t)$ $(\alpha, \beta = x, y, z$ and $i = 1, 2$ for the two spins I_1 and $I_2)$ denote the elements of the real, three-dimensional rotation matrix $\mathbf{C}^i_{rot}$ at a given time t. This matrix in turn is composed of individual rotation matrices for the flip angles β, phases φ, and tilt angles θ[10,151] and can be written as

$$\mathbf{C}^i_{rot} = \mathbf{R}^i_{phase}(-\varphi) \mathbf{R}^i_{tilt}(-\theta) \mathbf{R}^i_{flip}(\beta) \mathbf{R}^i_{tilt}(\theta) \mathbf{R}^i_{phase}(\varphi) \tag{3.11}$$

where the matrices $\mathbf{R}^i_{flip}(\beta)$, $\mathbf{R}^i_{phase}(\varphi)$, and $\mathbf{R}^i_{tilt}(\theta)$ are defined as follows

$$\mathbf{R}^i_{flip}(\beta) = \begin{pmatrix} 1 & 0 & 0 \\ 0 & \cos(\beta_i) & -\sin(\beta_i) \\ 0 & \sin(\beta_i) & \cos(\beta_i) \end{pmatrix}$$

$$\mathbf{R}^i_{phase}(\varphi) = \begin{pmatrix} \cos(-\varphi_i) & -\sin(-\varphi_i) & 0 \\ \sin(-\varphi_i) & \cos(-\varphi_i) & 0 \\ 0 & 0 & 1 \end{pmatrix} \tag{3.12}$$

$$\mathbf{R}^i_{tilt}(\theta) = \begin{pmatrix} \cos(\frac{\pi}{2} - \theta_i) & 0 & \sin(\frac{\pi}{2} - \theta_i) \\ 0 & 1 & 0 \\ -\sin(\frac{\pi}{2} - \theta_i) & 0 & \cos(\frac{\pi}{2} - \theta_i) \end{pmatrix}.$$

These equations can be used to get a first impression of the dipolar transfer properties of a certain mixing sequence. An illustrative example is the offset dependence of the elements of the average dipolar coupling tensor $\overline{\mathbf{D}}$ for cw-irradiation as the most simple representative of 'TOCSY' sequences (see Fig. 3.2). Here, all elements average to zero if the effective fields for both spins are aligned along the *magic angle*: $\theta_{MA} = \arctan\sqrt{2} \approx 54.7°$. This is exactly the condition described by LEE and GOLDBURG[155] to reduce the dipolar coupling interaction in solids for line narrowing. Obviously, terms along the anti-diagonal do not completely vanish for any offset and hence, the dipolar interaction cannot be removed from the dipolar coupling tensor for any combinations of offsets. However, more sophisticated pulse sequences have been created to achieve a homonuclear decoupling.[153, 154, 156, 157]

Purely Phase-Alternating Pulse Sequences

The above described cw-irradiation can be regarded as the most simple representative of a special class of mixing sequences which are denoted as purely phase-alternating pulse sequences. These sequences have in common, that all pulses are applied along the same axis which includes a 180° shift of the pulse phase (e.g., x, −x), as this can simply be represented by negative flip angles. The most popular sequence of this type is DIPSI-2[158] which is commonly applied along the x-axis.[2] Within the framework

2 DIPSI-2 consists of nine pulses with alternating phase (x,−x). The basis cycle ($320^\circ_x\ 410^\circ_{-x}\ 290^\circ_x\ 285^\circ_{-x}\ 30^\circ_x\ 245^\circ_{-x}\ 375^\circ_x\ 265^\circ_{-x}\ 370^\circ_x$) is expanded by MLEV-4.

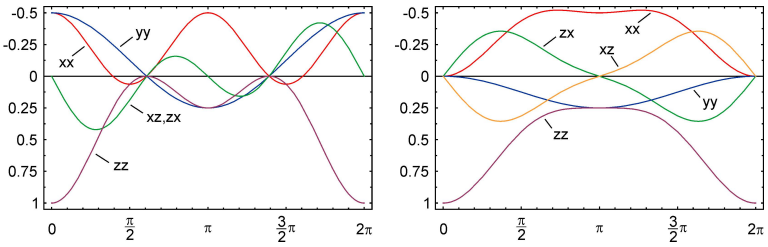

FIGURE 3.2: Offset dependence of components $\overline{d_{xx}}$, $\overline{d_{xz}}$, $\overline{d_{yy}}$, $\overline{d_{zx}}$, and $\overline{d_{zz}}$ of the average dipolar coupling tensor $\overline{\mathbf{D}}$ under cw-irradiation. The graphic is adapted from KARMER *et al.*[151] LEFT: Offset dependence along the diagonal of a 2D-spectrum ($\theta = \theta_1 = \theta_2$). RIGHT: Offset dependence along the anti-diagonal of a 2D-spectrum ($\theta = \theta_1 = \pi - \theta_2$).

derived in Eqs. 3.1-3.12 the dipolar transfer properties of these mixing sequences can be analyzed globally assuming two on-resonant spins, i.e., neglecting any chemical shift offsets ($\theta = \frac{\pi}{2}$).

Without loss of generality, it can be assumed that all pulses are applied along the x-axis ($\phi = 0$) with a flip angle of β_i, where the index i indicates the first, second, ... n^{th} pulse. Hence, the rotation matrix $\mathbf{C}^i_{rot}$ can be written as the product of single rotations $\mathbf{C}^j_{rot}$ with $j = 1 \ldots i$ and has the simple form[3]

$$\begin{aligned}\mathbf{C}^i_{rot} &= \begin{pmatrix} 1 & 0 & 0 \\ 0 & \cos\beta_i & \sin\beta_i \\ 0 & -\sin\beta_i & \cos\beta_i \end{pmatrix} \cdot \ldots \cdot \begin{pmatrix} 1 & 0 & 0 \\ 0 & \cos\beta_1 & \sin\beta_1 \\ 0 & -\sin\beta_1 & \cos\beta_1 \end{pmatrix} \\ &= \begin{pmatrix} 1 & 0 & 0 \\ 0 & \cos\sum_{j=1}^{i}\beta_j & \sin\sum_{j=1}^{i}\beta_j \\ 0 & -\sin\sum_{j=1}^{i}\beta_j & \cos\sum_{j=1}^{i}\beta_j \end{pmatrix}.\end{aligned} \tag{3.13}$$

3 The index j indicates that the pulse is already completed and has reached its maximum value. E.g., a pulse β_1 is applied to a spin which performs a $\frac{\pi}{2}$ rotation upon its application. This rotation can be described by $\mathbf{C}^1_{rot}$. The value of the pulse varies between $\beta_{1,b} = 0^\circ$ at the beginning and $\beta_{1,e} = 90^\circ$ at the end of the pulse. If a second pulse β_1 is applied now, the magnetization has to be rotated to the correct position so that the rotation matrix $\mathbf{C}^2_{rot}$ can be used. Obviously, this can be described by inserting the value for $\beta_{1,e}$ into the equation for the first rotation matrix $\mathbf{C}^1_{rot}$.

Using the definition of the tensor elements $d_{\alpha\beta}$ in Eq. 3.10 the time-dependent coupling tensor $\mathbf{D}'$ for the i^{th} pulse can be expressed as

$$\mathbf{D}'_i = \begin{pmatrix} 1 & 0 & 0 \\ 0 & \frac{1}{4}\left(1 - 3\cos 2\sum_{j=1}^{i}\beta_j\right) & -\frac{3}{4}\sin 2\sum_{j=1}^{i}\beta_j \\ 0 & -\frac{3}{4}\sin 2\sum_{j=1}^{i}\beta_j & \frac{1}{4}\left(1 + 3\cos 2\sum_{j=1}^{i}\beta_j\right) \end{pmatrix}. \tag{3.14}$$

The overall average dipolar coupling Hamiltonian $\overline{\mathbf{D}}$ therefore results as the weighted sum over all time-dependent coupling tensors $\mathbf{D}'_i$. Assuming that all pulses are applied with the same, constant rf-amplitude, the time τ_i for each pulse is linearly depending on the pulse angle ($\tau_i = f_i \cdot \beta_i$) of the pulse[4] and hence, the time-dependent and also the overall average dipolar coupling tensor can be normalized by division by the overall pulse angle. Consequently, the overall average dipolar coupling Hamiltonian $\overline{\mathbf{D}}$ can be written as

$$\overline{\mathbf{D}} = \frac{1}{\sum_{i=1}^{n}|\beta_{i,e}|}\left(\sum_{i=1}^{n}\int_0^{|\beta_{i,e}|}\mathbf{D}'_i\right). \tag{3.15}$$

Inserting the expressions for the rotation matrices $\mathbf{C}^i_{rot}$ results in

$$\overline{\mathbf{D}} = \begin{pmatrix} -\frac{\sum_{i=1}^{n}|\beta_{i,e}|}{2\sum_{i=1}^{n}|\beta_{i,e}|} & 0 & 0 \\ 0 & \frac{1}{4} - \frac{3\sin 2\sum_{i=1}^{n}|\beta_{i,e}|}{8\sum_{i=1}^{n}|\beta_{i,e}|} & -\frac{3\sin^2\sum_{i=1}^{n}|\beta_{i,e}|}{4\sum_{i=1}^{n}|\beta_{i,e}|} \\ 0 & -\frac{3\sin^2\sum_{i=1}^{n}|\beta_{i,e}|}{4\sum_{i=1}^{n}|\beta_{i,e}|} & \frac{1}{4} + \frac{3\sin 2\sum_{i=1}^{n}|\beta_{i,e}|}{8\sum_{i=1}^{n}|\beta_{i,e}|} \end{pmatrix}. \tag{3.16}$$

Recalling that TOCSY mixing sequences are cyclic, i.e., the toggling frame is aligned with the rotating frame at the beginning and at the end of the sequence the overall pulse angle is always a multiple of 360° in case of purely phase alternating pulse sequences. Hence, Eq. 3.16 simplifies to

$$\overline{\mathbf{D}}_{\text{PA}} = \begin{pmatrix} -\frac{1}{2} & 0 & 0 \\ 0 & \frac{1}{4} & 0 \\ 0 & 0 & \frac{1}{4} \end{pmatrix}. \tag{3.17}$$

This derivation clarifies, that all purely phase alternating pulse sequences have a dipolar scaling factor of $s_D = -\frac{1}{2}$.

4 By using this definition, negative flip angles encounter a negative correlation factor f_i as τ_i is obviously always positive. Therefore, the absolute value of the flip angle has to be used for the integration boundary.

Eliminating the Dipolar Coupling Interaction in TOCSY spectra – the J-ONLY-TOCSY

As seen above, the presented framework of the time averaged dipolar coupling tensor is very flexible in analyzing multiple pulse sequences for their transfer properties. So far, the application was restricted to purely phase alternating pulse sequences. Another very interesting class of pulse sequences are the heteronuclear isotropic Hartmann-Hahn sequences (HI-HAHA). Only few sequences have been described in literature for this application so far[3, 159–161] and their homonuclear mixing properties have not been studied in detail yet. One representative is the JESTER-1[3, 161] multiple pulse sequence which shows by far the largest active bandwidth, at least for heteronuclear transfer. Assuming again two on-resonant, homonuclear spins the time evolution of the tensor elements $d_{\alpha\beta}$ for the JESTER-1 pulse sequence can be derived and is given in Fig. 3.3. Here, the shortest possible supercycle (RR, with R being the basic multiple pulse sequence element $90^\circ_x\, 270^\circ_y\, 450^\circ_x$) is chosen which aligns the toggling frame with the rotating frame at the beginning and at the end of the pulse sequence. As can be seen in Fig. 3.3, all tensor elements average to zero apart from d_{xy} and d_{yx}. This result remains valid for more sophisticated MLEV-type supercycles[162] like MLEV-4, MLEV-8, MLEV-16, or MLEV-32 and the average dipolar coupling tensor has the form

$$\overline{\mathbf{D}}^{\mathrm{MLEV}}_{\mathrm{JESTER}-1} = \begin{pmatrix} 0 & -\frac{1}{6\pi} & 0 \\ -\frac{1}{6\pi} & 0 & 0 \\ 0 & 0 & 0 \end{pmatrix}. \tag{3.18}$$

In this case, the diagonal elements are zero and the effective dipolar coupling Hamiltonian is reduced to the double quantum term $\mathcal{H}_D^{\mathrm{MLEV}} = a_{DQ}\{I_{1x}I_{2y} + I_{1y}I_{2x}\}$ with $a_{DQ} = (1/3)D$ and vanishing a_{ZQ} which, according to[3]

$$T_z^{12} = \frac{1}{2}\{\cos(a_{DQ}t) - \cos(a_{ZQ}t)\} \tag{3.19}$$

leads to negative coherence transfer between two isolated spins. The double quantum transfer is very weak, resulting in only 2.75% transferred in-phase magnetization compared to ideal transfer at a mixing time of $1/(2D)$. The suppression of dipolar coupling evolution is already very good, but it can be suppressed even further if supercycles of the XY-type[163, 164] (XY-8 or higher) are used for the expansion of the JESTER-1 basic sequence, as has previously been explored for the creation of clean TOCSY transfer.[165]

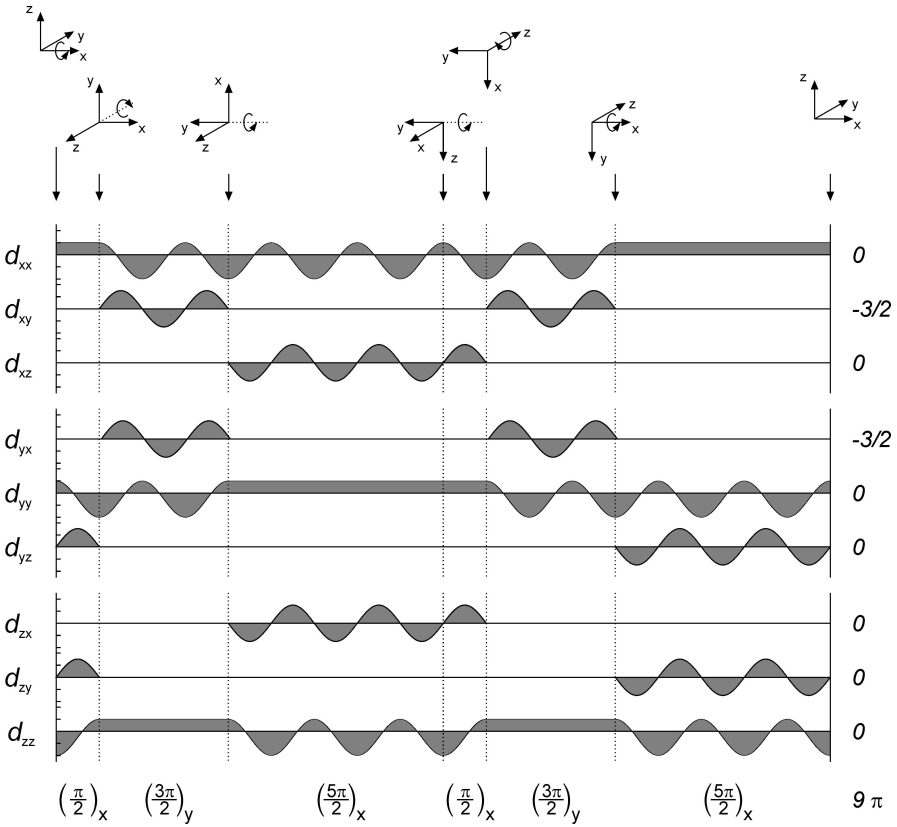

FIGURE 3.3: Evolution for the tensor elements $d_{\alpha\beta}$ of the dipolar coupling tensor $\overline{\mathbf{D}}$. The tensor elements evolve under the basic JESTER-1 multiple pulse sequence element expanded by a RR supercycle. At the top of the plot the rotations of the toggling frame as a result of the applied pulses are drawn. The integrals over the complete supercycle for each tensor element are shown at the very right.

In this case the dipolar coupling tensor for two on-resonant spins fully averages to zero

$$\overline{\mathbf{D}}^{\mathrm{XY8}}_{\mathrm{JESTER}-1} = \begin{pmatrix} 0 & 0 & 0 \\ 0 & 0 & 0 \\ 0 & 0 & 0 \end{pmatrix}, \tag{3.20}$$

i.e., the dipolar interaction is completely suppressed allowing only transfer via scalar couplings. Equivalent results were found for the WIM-24 sequence,[160]5 which also fully suppresses the dipolar coupling interaction for two on-resonant spins. However, the WIM-24 mixing sequence has a much smaller band width compared to JESTER-1 and was therefore not considered further (*vide infra*)

$$\overline{\mathbf{D}}_{\mathrm{WIM}-24} = \begin{pmatrix} 0 & 0 & 0 \\ 0 & 0 & 0 \\ 0 & 0 & 0 \end{pmatrix}. \tag{3.21}$$

Offset Dependence of Various Mixing Sequences

A more detailed view on the transfer amplitudes including off-resonance effects can be achieved by quantum mechanical simulations of a two-spin system including chemical shift offsets in the overall Hamiltonian. The transfer amplitudes for in-phase transfer via scalar and dipolar couplings for four different pulse sequences (DIPSI-2,[158] MOCCA-XY16,[150, 166] JESTER-MLEV16, and JESTER-XY16) with the initial magnetization oriented along z have been calculated according to

$$T_z^{12}(\tau) = \frac{\mathrm{Tr}\{I_{2z}^{\dagger} U(\tau) I_{1z} U^{\dagger}(\tau)\}}{\mathrm{Tr}\{I_{2z}^{\dagger} I_{2z}\}}, \tag{3.22}$$

using the simulation program Simone[167] (Fig. 3.4). In the definition of the transfer amplitude I_{1z} and I_{2z} represent the initial and the target state, respectively and U(τ) the propagator

$$U(\tau) = \exp\left(-\mathrm{i}\, \mathcal{H}_{\mathit{eff}} \tau\right), \tag{3.23}$$

with the overall effective Hamiltonian $\mathcal{H}_{\mathit{eff}}$ of the corresponding pulse sequences. From these simulations it is apparent that all tested pulse sequences show comparable transfer properties for scalar coupled spins (cf.

5 The WIM-24 pulse sequence consists of 12 pulses ($90^{\circ}_{x}\, 90^{\circ}_{y}\, 90^{\circ}_{x}\;\; 90^{\circ}_{x}\, 90^{\circ}_{y}\, 90^{\circ}_{x}\;\; 90^{\circ}_{-x}\, 90^{\circ}_{y}\, 90^{\circ}_{-x}\;\; 90^{\circ}_{-x}\, 90^{\circ}_{y}\, 90^{\circ}_{-x}$.) and is expanded by an $S\overline{S}$ supercycle, where $\overline{S}$ indicates time reversion and phase shifting by 180°

Fig. 3.4), but very different properties for purely dipolar coupled spins. While the MOCCA-XY16 multiple pulse sequence shows strong zero-quantum based positive transfer amplitudes for dipolar coupled spins, the DIPSI-2 sequence results in negative amplitudes. The JESTER-1 sequence with MLEV-16 supercycle yields dipolar transfer amplitudes generally below 3%. The JESTER-1 sequence with XY16 expansion, finally, fully suppresses dipolar coupling contributions over the whole bandwidth calculated, while retaining the beneficial transfer properties of an isotropic Hartmann-Hahn sequence for scalar coupled spins.

3.2.2 Experimental

To verify the findings in practice, homonuclear ^{1}H-^{1}H-TOCSY experiments have been recorded for the cyclic undecapeptide cyclosporin A (CsA) in isotropic and partially oriented samples. Using the pulse sequence shown in Fig. 3.5, four experiments with the multiple pulse sequences used in Fig. 3.4 and a conventional ROESY[168, 169] for comparison (pulse sequence not shown) were recorded for the aligned CsA sample. For all TOCSY sequences the magnetization for in-phase transfer was positioned along z before the mixing period. The differences for the various sequences can best be seen in the N-methyl to aliphatic region shown in Fig. 3.6. The DIPSI-2 sequence produces positive as well as negative cross-peaks depending on whether scalar or dipolar couplings dominate the transfer. In the region where transfer is only expected via dipolar transfer (2.6 - 3.7 ppm of the indirect dimension), all cross-peaks are negative and signals expected from scalar coupling transfer, as e.g., peaks along 3.83 ppm, are significantly reduced (Fig. 3.6 A). The MOCCA-XY16 sequence, instead, results in positive cross-peaks throughout the spectrum (Fig. 3.6 B). Its cross-peaks are generally most intense because of the very efficient transfer via dipolar couplings[150] and its favourable relaxation properties.[166] A distinction between scalar and dipolar mediated cross-peaks is generally not possible in this case. The TOCSY spectra with the two JESTER-1 derived mixing periods are shown in Fig. 3.6 C,D with generally positive cross-peaks. As expected from the simulations in Fig. 3.4 practically no transfer is visible in the region from 2.6 to 3.7 ppm, clearly demonstrating the suppression of coherence transfer via dipolar couplings. Residual negative cross-peaks in the selected region for the JESTER-1 sequence with MLEV-16 expansion are very weak (note the factor 10 used for selected slices in Fig. 3.6). Since none of the multiple pulse sequences are compensated

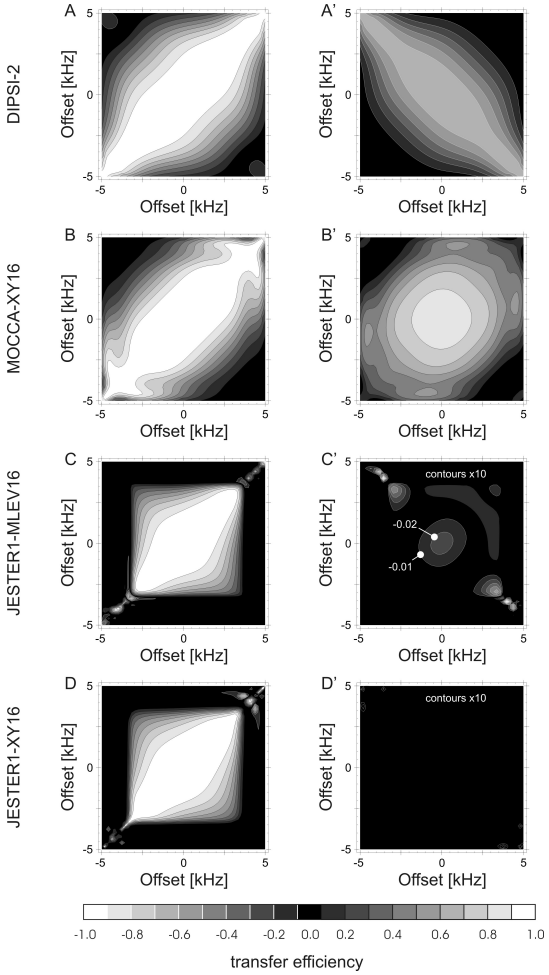

Figure 3.4: Simulated offset profiles of the transfer amplitudes using Simone[167] via scalar and dipolar couplings for various TOCSY multiple pulse sequences: MOCCA-XY16 (A, A'), DIPSI-2 (B, B'), JESTER-1 with MLEV16 expansion (C, C'), and JESTER-1 with XY16 expansion (D, D'). In all cases the transfer between two coupled spins was analyzed with I_{1z} as the initial and I_{2z} as the target state. On the left hand side offset profiles for the transfer via scalar couplings are shown (A, B, C, D), while the right hand side (A', B', C', D') represents the corresponding dipolar transfer profiles. For details of the simulation see App. A.3.1.

TABLE 3.1: Maximum on-resonance scaling factors s_D and active bandwidths of TOCSY sequences. The active bandwidth BW is determined along the anti-diagonal[a] and is limited by a transfer efficiency larger than 0.5. For a better characterization of the dipolar transfer properties a second bandwidth ($BW_D^{0.3}$) is given. In addition, 'blind spots'[e] are tabulated as well as the principal axis z' of the effective dipolar coupling tensor. Parts of the table are adopted from KRAMER *et al.*[146]

Sequence[a]	s_D	$BW_J^{0.5}[B_1]$	$BW_D^{0.5}[B_1]$	$BW_D^{0.3}[B_1]$	$(D/J)_P^0$	$(D/J)_L^{0\,e}$	z'
DIPSI-2	−0.5	0.77	0.39	0.60	−4	2	x
MOCCA-XY16	0.74	0.59	0.63	0.75	2	−1	z
MLEV-16[b]	0.25	0.57	–	0.50	8	−4	y
JESTER-XY16[c]	0.0	0.83	–	–	–	–	–
WIM-24[cd]	0.0	–	–	–	–	–	–

[a] For DIPSI-2 and MLEV-16 the bandwidth for dipolar transfer has been determined along the diagonal for a transfer efficiency of −0.5 and −0.3 as these are the limiting parameters.

[b] The dipolar transfer efficiency for MLEV-16 does not exceed ≈ 0.32; therefore no value is given for $BW_D^{0.5}$.

[c] As JESTER-1 and WIM-24 suppress dipolar transfer fully, no bandwidth and 'blind spots' are given for these sequences.

[d] The transfer efficiency for WIM-24 does not constantly exceed a value of ≈ 0.20; therefore no value is given for $BW_J^{0.5}$.

[e] 'Blind spots' $(D/J)_{P,L}^0$ denote ratios of D and J that will lead to no net transfer in the spectrum.

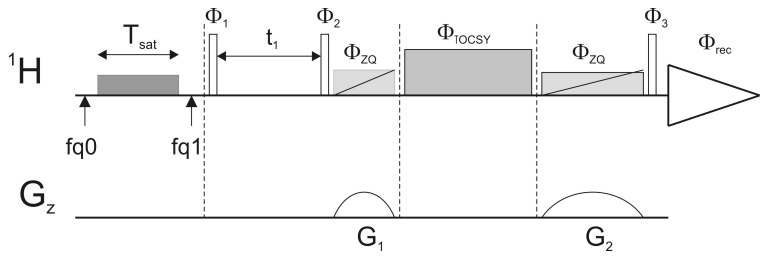

Figure 3.5: The basic pulse sequence for the acquired TOCSY spectra. Presaturation of unwanted signals originating from the PDMS/$CDCl_3$-gel as alignment medium[62, 114] was achieved by a frequency jump to the corresponding signal (fq0), subsequent cw-irradiation, and finally a frequency jump back to the original position (fq1). Zero-quantum artifacts were suppressed by the method described by Thrippelton *et al.*[15, 170] For further experimental details see App. A.2 and article by Klages *et al.*[171]

for cross-relaxation transfers, cross-peaks for both JESTER-1 variants as well as DIPSI-2 and MOCCA-XY16 experience contributions from nuclear Overhauser enhancement in the rotating frame (ROE). The corresponding ROESY spectrum is shown in Fig. 3.6 E for comparison. Residual cross-peak intensities in the slices for the JESTER-1 sequences in Fig. 3.6 that are not explained by scalar coupling transfer or ROE contributions can be attributed to t_1-noise.

The applicability of the *J*-ONLY-TOCSY approach is demonstrated in Fig. 3.7, where the JESTER-1 TOCSY spectrum acquired on the aligned CsA sample (Fig. 3.7 A) is compared with a conventional DIPSI-2 TOCSY recorded on an isotropic sample of CsA dissolved in $CDCl_3$ (Fig. 3.7 B). Although cross-peak intensities vary slightly because of variations in the multiplet patterns due to dipolar couplings being present in the aligned sample, the appearance of the two spectra is basically identical and the assignment of scalar coupled spin systems in the partially oriented sample is possible.

3.3 Measuring ^{1}H-^{1}H Residual Dipolar Couplings

So far, it could be shown, that different TOCSY sequences have the ability to scale the dipolar coupling Hamiltonian differently and will thereby also

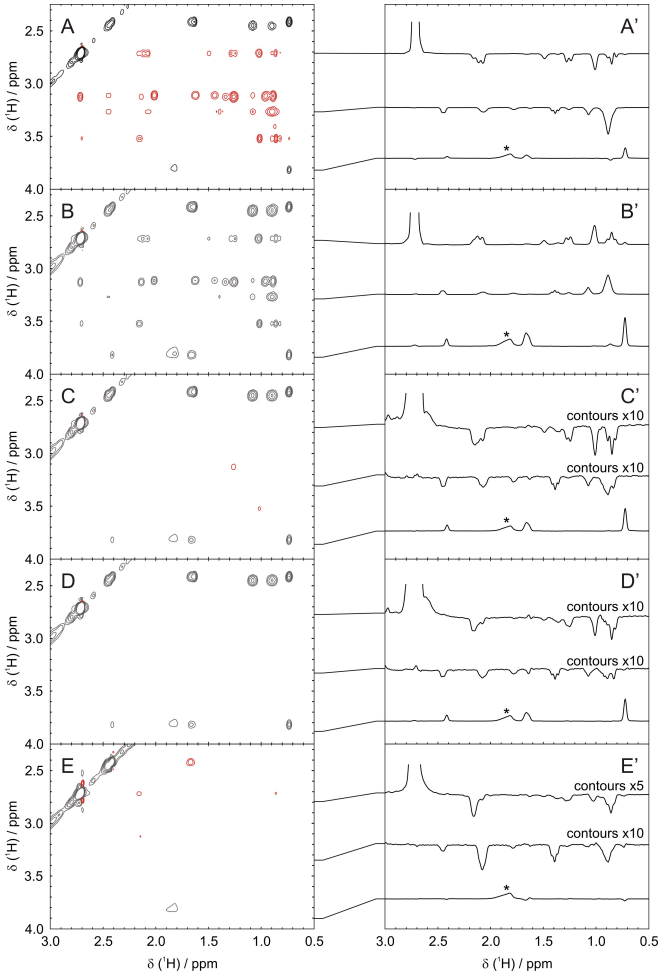

FIGURE 3.6: Enlargement of the N-methyl to aliphatic region of TOCSY and ROESY spectra acquired on cyclosporin A partially aligned in a PDMS/$CDCl_3$ gel. DIPSI-2 (A, A'), MOCCA-XY16 (B, B'), JESTER-1 with MLEV16 expansion (C, C'), and JESTER-1 with XY16 expansion (D, D'), as well as a cw spin-lock for ROESY transfer (E, E') were applied during the mixing period. For better visualization example traces (two traces with purely dipolar transfer and one trace with expected transfer via scalar couplings) are shown on the right with scaling by a factor of 5 or 10 whenever annotated. Signals marked with an asterisk originate from chemical exchange with residual water.

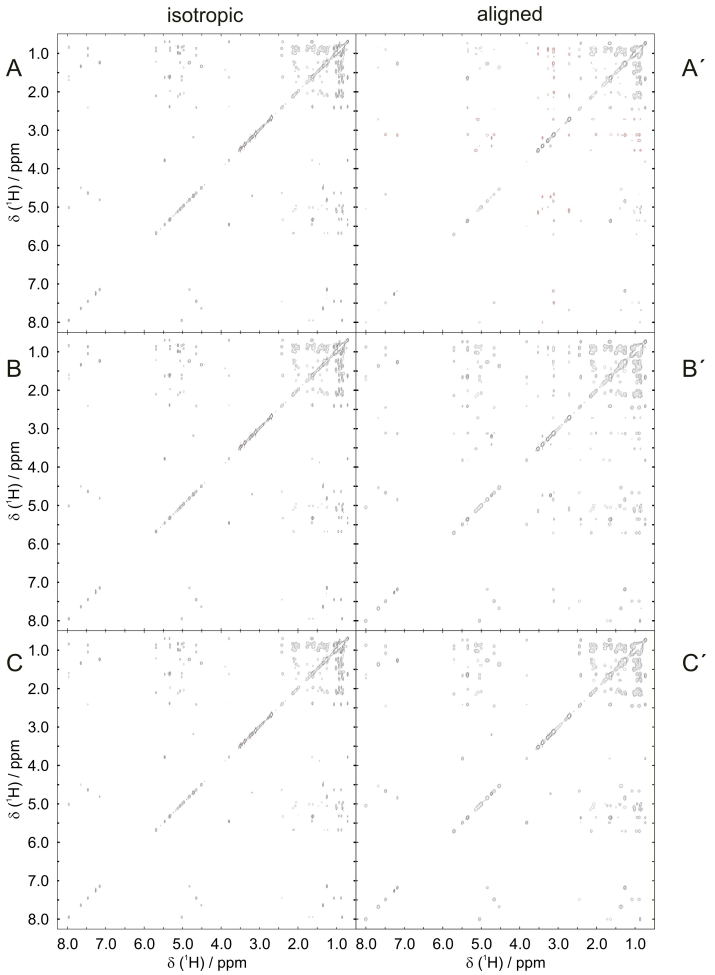

Figure 3.7: Experimental TOCSY spectra of isotropic cyclosporin A (A, B, C) and cyclosporin A aligned in a stretched PDMS/$CDCl_3$ gel (A', B', C'). Spectra were acquired using DIPSI-2 (A, A'), MOCCA-XY16 (B, B'), and JESTER-XY16 (C, C') multiple pulse sequences. While the TOCSY spectra using DIPSI-2 and MOCCA-XY16 are very different in the isotropic and aligned cases, they are virtually identical for JESTER-XY16.

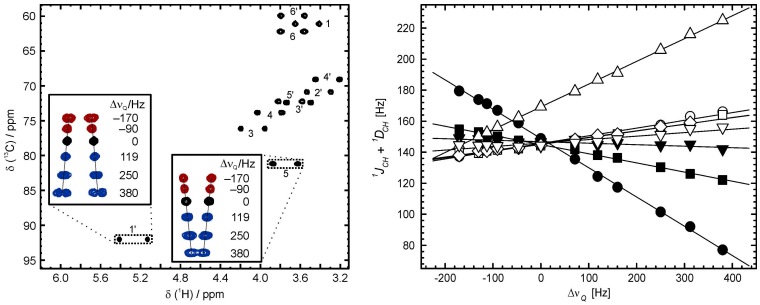

FIGURE 3.8: Scaling of the dipolar coupling using a rubber-based 'stretching apparatus'. LEFT: Cutout from the ^{1}H-^{13}C-HSQC spectrum of sucrose aligned in gelatine. Splitting of the resonances is depending on the alignment strength tuned by the stretching apparatus. RIGHT: Plot of the observed splitting $^1J_{CH} + ^1D_{CH}$ in the ^{1}H-^{13}C-HSQC spectrum versus the alignment strength quantified by the quadrupolar splitting of D_2O. Figures were adopted from KUMMERLÖWE *et al.*[172]

scale the effective dipolar coupling constant differently. As already pointed out in Sec. 3.1, this can be exploited for the sign sensitive measurement of residual dipolar couplings. The underlying principal concept was described by KUMMERLÖWE and LUY who scaled the alignment strength of a polymer gel *mechanically* by the use of a rubber tube.[60] Hence, dipolar couplings are scaled accordingly, allowing the extraction of couplings by linear least square fitting leading to an increased precision of the RDC measurement. The procedure is illustrated in Fig. 3.8 where sucrose is aligned using a gelatine/H_2O gel.[67,68] A disadvantage of this technique are the inherently broad lines as shimming is perturbed due to the stretching apparatus within the NMR sample tube. Even intensive adjustment of the shim coil currents can only partially compensate for this deficiency. However, future developments might enable an optimized setup and an improved spectral quality. Still, scaling of dipolar coupling constants using different TOCSY mixing sequences appears superior, as no 'stretching apparatus' is needed and shimming is only required once. Hence, a similar approach can be used where the coupling constants are scaled 'software' wise.

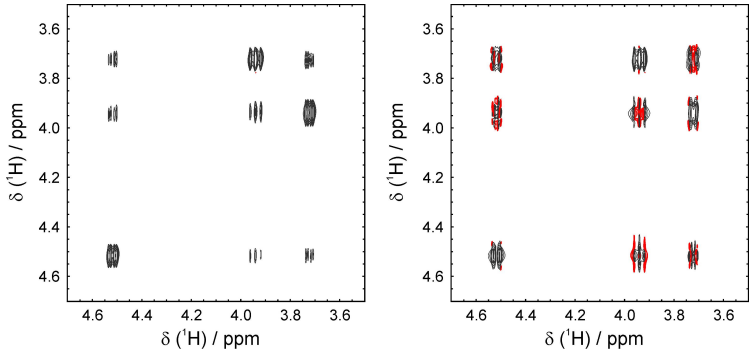

Figure 3.9: Influence of the ZQ suppression scheme on the spectral quality. Left: TOCSY spectrum acquired with a DIPSI-2 mixing sequence and the zero-quantum suppression scheme. Right: Same as before, but acquired without zero-quantum filter. Peak volumes for several spectra of both types have been compared and resulted in a small deviation of generally below 1.5% for the small molecule DBPA.

3.3.1 Zero-Quantum Suppression

For a quantitative evaluation of TOCSY transfer amplitudes it has to be ensured that the zero-quantum suppression scheme used in the TOCSY spectra is not or only negligible influencing the experimental transfer amplitudes. Therefore, TOCSY spectra with and without zero-quantum suppression have been recorded for a sample of 2,3-dibromopropionic acid (DBPA) dissolved in $CDCl_3$. A quantitative comparison of normalized volume integraals (Sec. 3.3.2) resulted in a deviation of below 1.5%. As can be seen in Fig. 3.9 strong zero-quantum artifacts occur if no suppression scheme is utilized. However, it remains unclear if spectra *with* zero-quantum suppression scheme may probably give more 'correct' transfer amplitudes, while peak volumes in spectra *without* suppression scheme give 'worse' results, though NOE contributions increase the longer the suppression scheme gets. Anyway, deviations are small for small molecules and can savely be neglected.

In addition, the influence of miscalibration on the zero-quantum suppression scheme and hence, on the experimental transfer amplitudes was tested. Therefore, the first zero-quantum filter was adjusted carefully according to Thrippleton *et al.*[15] The second zero-quantum filter, however, which

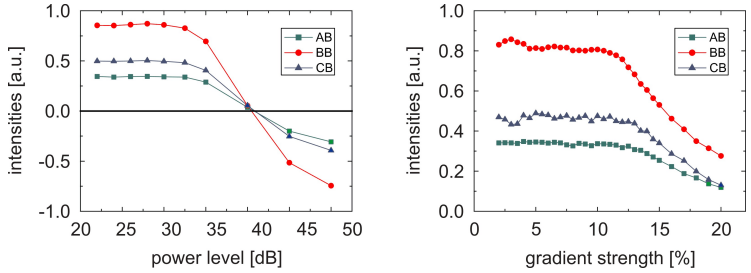

FIGURE 3.10: Dependence of zero-quantum suppression scheme on miscalibration. LEFT: Influence of the rf-amplitude of the adiabatic inversion pulse, where B_1 field strengths are given in dB attenuation. RIGHT: Variation of the gradient strength G_2 in % of the maximum gradient field strength.

is placed directly after the mixing sequence and shortly before acquisition, was deliberately mis-set. Two parameters (cf. Sec. 2.1.8) determine the quality of zero-quantum suppression, i.e., the gradient strength (G_1 and G_2 in Fig. 3.5) and the rf-amplitude of the frequency swept adiabatic inversion pulse. Both parameters were successively varied over a broad range and absolute peak volumes were compared. The results are shown in Fig. 3.10 and indicate that the zero-quantum suppression scheme is a very robust building block, allowing a large degree of miscalibration. Even when the *absolute* intensities of the peaks drop, their *relative* intensity still remains constant for an even broader range. However, as zero-quantum artifacts start to increase again under these conditions and might interfere with resonances of neighboring peaks when spectra become more crowded, it should be avoided to choose those condition. Recapitulatory, it has to be concluded that the zero-quantum suppression scheme published by THRIPPLETON *et al.*[15, 170] represents an excellent tool, for the quantitative analysis of TOCSY transfer amplitudes.

3.3.2 Extracting Transfer Amplitudes

To test the applicability of TOCSY spectra as a tool for the determination of ^{1}H-^{1}H-RDCs, experimental transfer amplitudes had to be extracted. Therefore, a series of spectra with increasing mixing times were recorded for an isotropic and an aligned sample of DBPA in $CDCl_3$. DBPA was aligned using a PS/$CDCl_3$ gel and was chosen as a first test sample because of

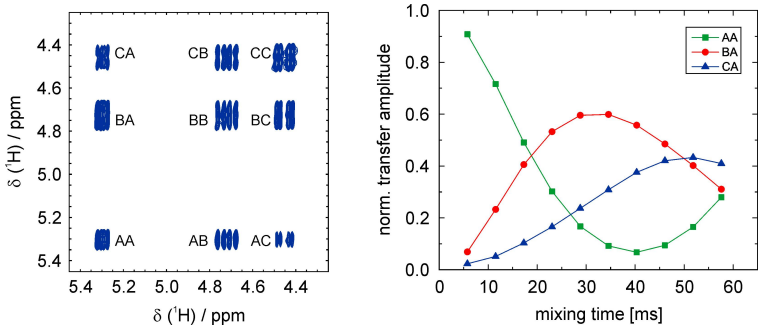

Figure 3.11: Left: Annotated ^{1}H-^{1}H-TOCSY spectrum of 2,3-dibromopropionic acid acquired with JESTER-XY16 mixing sequence in $CDCl_3$. Right: Extracted transfer amplitudes with increasing mixing times using JESTER-XY16 mixing. For convenience transfer amplitudes are only shown for one 'strip' of the TOCSY spectrum.

its very simple spin system. It consists of three spins which are mutually coupled and exhibits scalar coupling constants of 11.3 Hz, 4.3 Hz, and −10.1 Hz, respectively (*vide infra*). Mixing times were varied between ≈ 4 ms and ≈ 55 ms using different mixing sequences, i.e., MOCCA-XY16, DIPSI-2, and JESTER-XY16. This resulted in spectra as shown in Fig. 3.11. Volume integrals of cross- and diagonal-peaks were extracted by using the Sum over Box module of Sparky,[173] though several other settings have been tested as well. However, other methods gave rise to equivalent results, while being more complex at the same time and were therefore not considered further.

An essential piece in the determination of TOCSY transfer amplitudes is normalization. Obviously, when simulating TOCSY spectra, no peak amplitudes larger than 1 can be observed as illustrated in Fig. 3.12. Therefore, amplitudes, or more precisely, peak volumes have to be scaled or normalized. Assuming solely scalar coupled spins and neglecting relaxation effects due to ROE transfer, only positive transfer amplitudes are expected for DBPA. As the magnetization within the spin system remains constant in this case, peak volumes can be normalized for each 'strip' in each spectrum separately by summation over all transfer amplitudes of one strip and subsequent division of the corresponding individual peak volumes by this sum. The condition of vanishing transfer through ROE is well satisfied

for DBPA and also transverse and longitudinal relaxation due to autorelaxation are expected to be small, due to the low molecular weight and short experimental mixing times. Therefore, all spectra of isotropic samples can be evaluated using this procedure. However, the situation changes, when inspecting spectra of anisotropic samples or spin systems of five or more spins. In those cases transfer amplitudes may become negative (see Fig. 3.12, blue curves) and will deteriorate any normalization according to the above described method. Also normalization using only the *absolute* value of the transfer amplitude will fail as can also be seen from Fig. 3.12. At a mixing time of 200 ms, assuming a two spin system coupled by by a dipolar coupling of 10 Hz, transfer amplitudes are zero for both spins. Hence, normalization has to be achieved using reference spectra, which are acquired with zero mixing time. If not available, transfer amplitudes can also be normalized to spectra with the shortest possible mixing time, i.e., only one repetition of the basis element including supercycles. Certainly, this introduces *systematic* errors, which however, are small and can be partially compensated by renormalization after the first fitting run (*vide infra*).

3.3.3 Fitting TOCSY Spectra

The Optimization Algorithm

Initially, a program had to be implemented that enables the quantitative calculation of TOCSY transfer amplitudes of spin systems with more than two spins. This was achieved using the software package MATLAB.[174] This allowed for the implementation of an easy and clear source code though an inplementation in a different programming language might have been faster. However, simulations never exceeded a time span of ≈ 15 min even for the most complicated spin systems calculated during the course of this work.

For the calculations a full quantum mechanical treatment of the spin system was used. However, chemical shift offsets were neglected and effective Hamiltonians were used

$$\mathcal{H}_{\mathit{eff}} = \mathcal{H}_J + \overline{\mathcal{H}_D}. \tag{3.24}$$

Here, the overall scalar coupling Hamiltonian $\mathcal{H}_J$ is the sum over all mutual

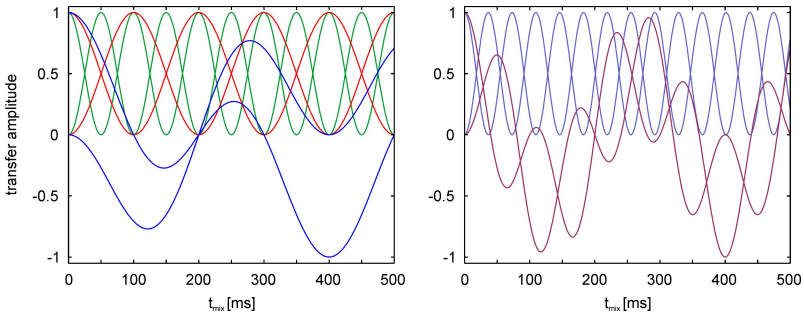

Figure 3.12: Simulated TOCSY transfer amplitudes for a two-spin system. Left: Time evolution of transfer amplitudes under a purely isotropic mixing Hamiltonian (green), under a purely dipolar mixing Hamiltonian (red), and under the effective coupling Hamiltonian created by the DIPSI-2 mixing sequence assuming only a dipolar coupling (blue). Only in case of DIPSI-2 mixing negative transfer amplitudes are expected. In all cases a coupling constant of 10 Hz was assumed. Right: Superimposition of transfer through dipolar and scalar couplings, where both are assumed to be 10 Hz. Curves assuming the superimposition of an isotropic and a dipolar coupling Hamiltonian, as comparably found for MOCCA-XY16 mixing sequence are shown in blue. Transfer amplitudes resulting from a DIPSI-2 mixing sequence are shown in violet.

coupling Hamiltonians $\mathcal{H}_J^{i,j}$

$$\mathcal{H}_J = \sum_{i<j}^{n} \mathcal{H}_J^{i,j} \qquad \mathcal{H}_J^{i,j} = 2\pi J \mathbf{I}_i \mathbf{J} \mathbf{I}_j \tag{3.25}$$

where i and j refer to spin i and j and n denotes the maximum number of spins. As spin i does not couple to itself and each interaction has to be included only once, the conditions $i \neq j$ and $i < j$ have to be obeyed. Furthermore, the scalar coupling tensor is the identity matrix. For the overall dipolar coupling Hamiltonian equivalent equations apply, but using the dipolar coupling tensor instead. Here, the results obtained in Sec. 3.2 and listed in Tab. 3.1 have to be included.

$$\overline{\mathcal{H}_D} = \sum_{i<j}^{n} \mathcal{H}_D^{i,j} \qquad \overline{\mathcal{H}_D^{i,j}} = 2\pi D \mathbf{I}_i \overline{\mathbf{D}} \mathbf{I}_j \tag{3.26}$$

The observable transfer amplitudes then simply result from calculation of the propagator U_{eff} at time point t (see Eq. 3.23)

$$U(t) = \exp\left(-i\mathcal{H}_{eff}t\right) \tag{3.27}$$

and subsequent determination of the transfer amplitude[6] analogously to Eq. 3.22

$$T_z^{ij}(\tau) = \frac{\mathrm{Tr}\{I_{jz}^{\dagger} U(\tau) I_{iz} U^{\dagger}(\tau)\}}{\mathrm{Tr}\{I_{jz}^{\dagger} I_{jz}\}}. \tag{3.28}$$

As magnetization in all experiments was positioned along the z-axis before the mixing period, the above equation was restricted to I_z magnetization.

The obtained transfer amplitudes can then be compared to the experimental ones and by adjusting the individual coupling constants for simulations the theoretical transfer amplitudes can be fitted to the experimental data. In principle, several algorithms exist to solve this optimization problem. However, MATLAB readily provides some algorithms for this type of problem and three of these were tested more thoroughly. This comprised a simulated annealing protocol (SA), a genetic algorithm (GA), and a gradient-based linear least square fitting routine (LSQ).[7]

6 Please note, that for calculation of the transfer amplitudes T_z^{ij} the above conditions ($i \neq j$ and $i < j$) do not apply, as e.g., $i = j$ represents diagonal peaks.

7 More precisely the algorithm is based on the interior-reflective Newton method.[175]

When spin systems get larger and more spins are included, it is very likely that a potential surface is created that consists of several minima. Therefore, global fitting algorithms (SA and GA) were favoured initially. However, to test the convergence time of each algorithm, theoretical transfer amplitudes were calculated for a seven spin system using the set of seven experimental coupling constants reported for methyl-α-D-glucopyranoside.[176] Subsequently, all three algorithms were tested by setting the initial guess for all $^3J_{HH}$-couplings to a value of $+1$ and to a value of -1 for $^2J_{HH}$-couplings and eventually measuring the time until convergence was reached, i.e., the deviation between 'experimental' and 'back-calculated' transfer amplitudes drops below a certain threshold. It turned out, that the LSQ algorithm was by far the quickest and was therefore used during further investigations. Though, it is still possible, that SA and GA algorithms become favourable if spin systems exceed a number of $n = 7$.

Furthermore, the quality or robustness of the algorithm against experimental errors was tested. Therefore, random noise of up to 20% was added to the theoretically calculated transfer amplitudes and renormalization finally resulted in the 'experimental' input data. Fitting using the afore selected LSQ algorithm resulted in deviations smaller than 1.5 Hz on average (see Tab. 3.2). This clearly shows, that the algorithm is well-suited to extract coupling constants from experimentally obtained transfer amplitudes, even if the data is 'noisy'. However, optimization results for smaller couplings deviate stronger from the theoretical value than for larger couplings. This can be rationalized by considering the transfer profile for spins with small couplings. It is much less 'pronounced' compared to large couplings, i.e., the transfer amplitudes do not vary strongly over time if only short mixing times are encoutererd. Hence, restricting the maximum mixing time to < 100 ms to avoid relaxation effects, inevitably results in a larger error for smaller couplings.

Fitting Experimental Transfer Amplitudes

After extensive testing of the fitting algorithm, real experimental data were fitted against the quantum mechanical equations for TOCSY transfer. As described in Sec. 3.3.2 data was obtained from an isotropic and an aligned sample of DBPA in $CDCl_3$. After normalization, initially only data of the isotropic sample, extracted from spectra using the JESTER-XY16 mixing sequence at ten different mixing times, were fitted. In principle, a maxi-

TABLE 3.2: Theoretical and back-calculated coupling constants in an artificial 7 spin system. Noise of 20% was added to the theoretically predicted transfer amplitudes and were subsequently fitted with the LSQ routine, starting from values of $J_{i,j} = 1$ Hz.

Coupling	J_{theo}	J_{fit}	ΔJ	J_{start}
$^3J_{H_1,H_2}$	8.00	8.02	0.02	+1.00
$^3J_{H_2,H_3}$	9.40	9.67	0.27	+1.00
$^3J_{H_3,H_4}$	9.20	9.28	0.08	+1.00
$^3J_{H_4,H_5}$	9.70	9.68	0.02	+1.00
$^3J_{H_5,H_{6R}}$	6.00	5.20	0.80	+1.00
$^3J_{H_5,H_{6S}}$	2.30	3.68	1.38	+1.00
$^2J_{H_{6R},H_{6S}}$	−12.30	−12.09	0.21	−1.00

mum of three scalar couplings is observable in this spin system and starting values of +1 and −1 for the optimization procedure were used for $^3J_{HH}$- and $^2J_{HH}$-couplings, respectively. To verify the fit results of the isotropic sample, a 1D-^{1}H-spectrum was recorded at high resolution (cf. Fig. 3.13). Results are reported in Tab. 3.3 and reveal an excellent agreement between coupling constants obtained with the different techniques. Deviations are generally small (< 0.5 Hz) where the largest deviation is again observed for the smallest experimental coupling.

In the next step, transfer amplitudes obtained from an aligned sample using JESTER-XY16 mixing were analyzed. Again data sets of ten different mixing times were used as input. In theory, the JESTER-XY16 mixing sequence should fully suppress any transfer through dipolar couplings and therefore should give identical transfer amplitudes which consequently would translate into equal coupling constants. Indeed, fitting the experimental data resulted in virtually the same coupling constants as reported above for the isotropic sample (see Tab. 3.3). This verifies again the concept of the *J*-ONLY-TOCSY and clearly reveals its applicability to determine scalar coupling constants under weakly aligned conditions.

Finally, also data of the anisotropic sample acquired with TOCSY spectra using DIPSI-2 and MOCCA-XY16 mixing was evaluated. For the fitting procedure scalar couplings were kept fixed at the value obtained from the above fitting process, i.e., 11.3 Hz, 4.5 Hz, and −10.1 Hz, respectively.

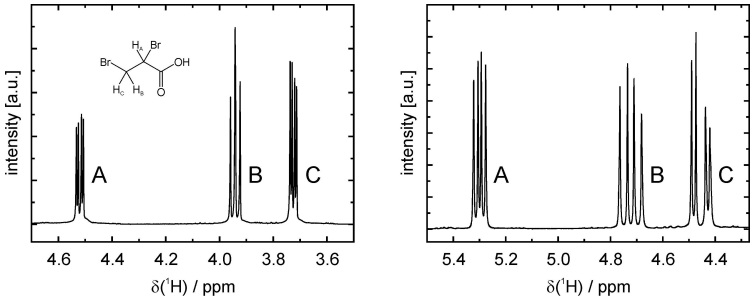

Figure 3.13: 1D-^{1}H-spectra of 2,3-dibromopropionic acid. The chemical shift offset between the two spectra originates from a mis-set lock. Left: Spectrum in isotropic solution. The molecular structure of 2,3-dibromopropionic acid is given with the resonance assignment. Right: Annotated spectrum of DBPA aligned in PS/$CDCl_3$.

Table 3.3: Experimental scalar coupling constants of 2,3-dibromopropionic acid obtained in isotropic and aligned samples. All coupling constants are given in Hz.

Coupling[a]	^{1}H-spectrum	$\text{TOCSY}_{\text{iso}}$[b]	TOCSY_{al}[c]	ΔJ_{iso}
J_{AB}	11.3	11.2	11.3	−0.1
J_{AC}	4.3	4.6	4.5	+0.3
J_{BC}	−10.1	−10.2	−10.1	−0.1

[a] Assignments for the couplings refer to those given in Fig. 3.11.

[b] Obtained from fitting TOCSY spectra acquired with JESTER-XY16 mixing in isotropic solution.

[c] Obtained from fitting TOCSY spectra acquired with JESTER-XY16 mixing in an aligned sample.

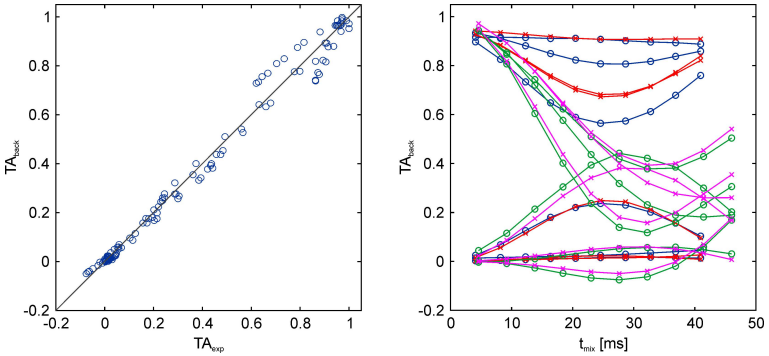

FIGURE 3.14: Results from fitting experimental transfer amplitudes. LEFT: Experimental versus back-calculated transfer amplitudes. The good correlation between the values indicates the high quality of the fit. RIGHT: Time evolution of experimental (circles, blue and green) and back-calculated (crosses, red and pink) transfer amplitudes. The evolution is shown for both mixing sequences, i.e., MOCCA-XY16 (blue and red) and DIPSI-2 (green and pink). For convenience transfer amplitudes using JESTER-XY16 mixing are not shown.

Simultaneous fitting of transfer amplitudes from DIPSI-2 and MOCCA-XY16 mixing gave the coupling constants listed in Tab. 3.4. The quality of the fit is depicted in Fig. 3.14 where the experimental versus the back-calculated transfer amplitudes are plotted. In addition, the experimental and 'back-calculated' transfer curves are shown. For verification of the optimization results, a 1D-^{1}H-spectrum was recorded for the DBPA sample aligned in PS/$CDCl_3$ (see Fig. 3.13). Here only the absolute value of the splitting $\Delta_s = |J + D|$ could be extracted, which is also shown in Tab. 3.4.

As can be seen from the data, experimental data obtained from fitting TOCSY spectra is again in excellent agreement with the splittings observed in simple 1D-^{1}H-spectra. However, extracted coupling constants are less precise as for the isotropic case, but deviations are generally smaller than 2 Hz. When inspecting the back-calculated transfer amplitudes, it becomes apparent, that especially the transfer curves for the diagonal signals of MOCCA-XY16 mixing deviate strongly from the back-calculated ones. Therefore, only data using DIPSI-2 mixing was fitted for test reasons (see Tab. 3.4). Indeed, the results resemble the data obtained from the 1D-^{1}H-

Table 3.4: Fitted residual dipolar coupling constants of 2,3-dibromopropionic acid obtained in a PS/$CDCl_3$ gel. In addition, the scalar coupling constant in the aligned sample is given along with the splitting $\Delta_s = |J + D|$ observed in a 1D-^{1}H-spectrum.

Spin pair[a]	J [Hz][b]	Δ_s [Hz][c]	D [Hz][d]	D [Hz][e]	$J + D$ [Hz][f]	$\Delta_{s,dev}$ [Hz][g]
AB	11.3	17.4	4.5	4.7	15.8	1.6
AC	4.5	10.0	4.3	4.9	8.8	1.2
BC	−10.1	31.8	−21.2	−21.2	−31.3	0.5

[a] For assignments see Fig. 3.13.

[b] Obtained from fitting TOCSY spectra acquired with JESTER-XY16 mixing in aligned sample.

[c] Obtained from 1D-^{1}H-spectrum.

[d] Obtained using all experimental TOCSY transfer amplitudes.

[e] Obtained using only transfer amplitudes from TOCSY spectra with DIPSI-2 mixing.

[f] Calculated using residual dipolar couplings when fitting all experimental data.

[g] Deviation of the splitting observed in the 1D-^{1}H-spectrum from the fitting result ($\Delta_s - |J + D|$).

spectrum better and deviated in maximum by 1.4 Hz. Compared to the previous fitting results this implies a drop of 0.2 Hz in the error. Hence, the influence of the deviating transfer amplitudes in spectra using MOCCA-XY16 can be neglected.

Systematic Errors and Starting Values

As pointed out in Sec. 2.1.7 TOCSY transfer is inevitably connected to ROESY and NOESY transfer. By the development of the invariant trajectory approach[6] a tool was created that allows the quantification of these contributions with respect to the actual TOCSY transfer. Therefore, offset profiles for the transverse and longitudinal weights as defined in Eq. 2.40 and Eq. 2.41 have been calculated using the program SIMONE.[167] Simulations were conducted for the mixing sequences DIPSI-2, MOCCA-XY16, and JESTER-XY16 and results are shown in Fig. 3.15.

It is apparent from the simulations that all three mixing sequences exhibit very different weight profiles. While for DIPSI-2 and JESTER-XY16 magnetization is predominantly positioned along a transverse axis, in MOCCA-XY16 magnetization is mainly stored along the z-axis. Hence, longitudinal relaxation is the dominating[8] relaxation source in MOCCA-XY16 and transverse relaxation is dominating DIPSI-2 and JESTER-XY16. To obtain the actual NOE and ROE contributions, the weight has to be multiplied by the cross-relaxation rate σ_{ij} between the two spins. In the case of small molecules (extreme narrowing limit), the longitudinal and the transverse cross-relaxation rates are negative and hence will subtract from the observed transfer amplitudes in the TOCSY spectra. This effect is smallest for the MOCCA-XY16 sequence, as longitudinal cross-relaxation rates are smaller than the corresponding transverse cross-relaxation rates. On the other hand, when investigating large molecules (slow tumbling limit), a negative contribution to the overall transfer amplitude is expected for DIPSI-2 and JESTER-XY16, but a small positive contribution is expected for the MOCCA-XY16 sequence.[9] In both cases the contributions to the experimental transfer amplitudes increase with increasing mixing time.

How do these findings affect the results of the fitting procedure? In prin-

8 The term 'dominates' refers to the time during which the corresponding relaxation mechanism is active and not to the actual size.

9 In the slow tumbling limit the transverse cross-relaxation rate is twice as large as the longitudinal cross-relaxation rate, but with opposite sign.

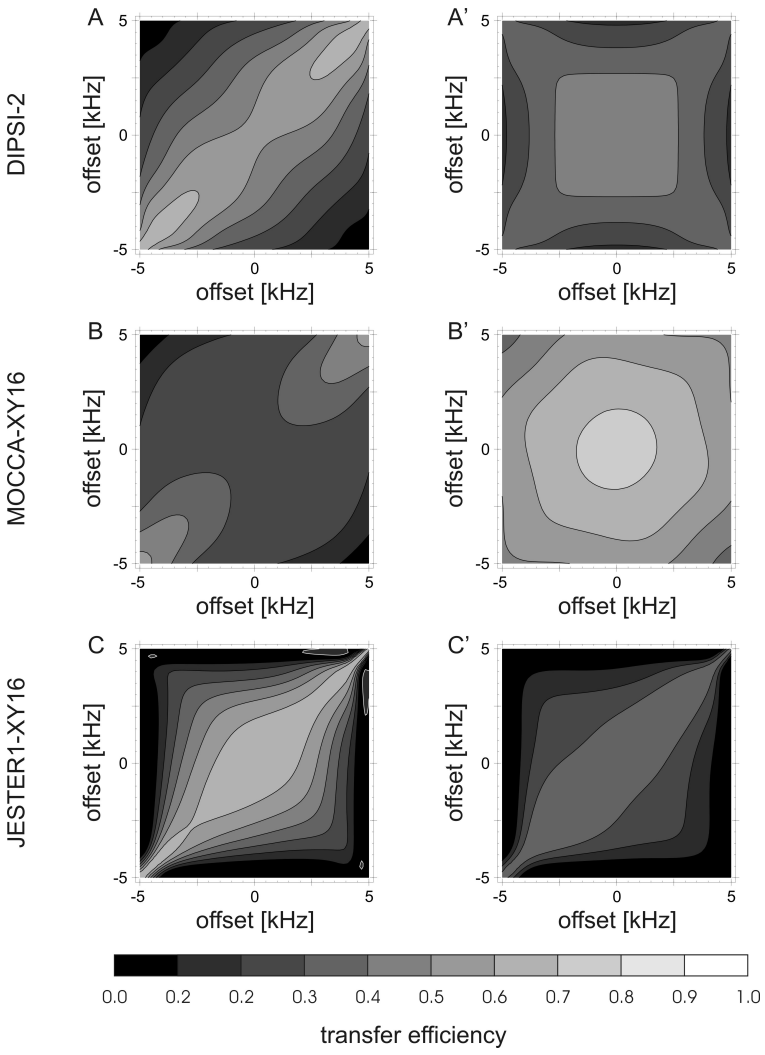

Figure 3.15: Offset dependence of transverse (A, B, C) and longitudinal (A', B', C') weights for several TOCSY mixing sequences. Invariant trajectories have been calculated using the program Simone for DIPSI-2 (A, A'), MOCCA-XY16 (B, B'), and JESTER-XY16 (C, C') and and were converted into weight profiles using Eqs. 2.40-2.41.

ciple, all these effects can be neglected if the strips in the TOCSY spectra are normalized in each spectrum separately (see Sec. 3.3.2), as all peaks (cross- and diagonal-peaks) are affected to the same extent if sufficiently strong rf-pulses are applied, i.e., if offset effects are negligible. However, if this assumption is not valid, cross-peaks distant from the diagonal will exhibit smaller NOE and ROE contributions, hence they will appear larger than they actually are in the extreme narrowing limit. This is also true for the DIPSI-2 and the JESTER-XY16 sequence in the slow tumbling limit, whereas cross-peaks in the MOCCA-XY16 sequence remote from the diagonal will appear smaller. A relative increase in the transfer amplitude will commonly lead to an overestimation of the corresponding coupling constant and *vice versa*.

Things get even more complicated when normalization cannot be carried out strip-wise, i.e., if spin systems of more than 5 spins are inspected or if negative transfer amplitudes are expected due the residual dipolar couplings in DIPSI-2 spectra, for example. Normalization is then carried out with a reference spectrum. Hence, relaxation effects are not eliminated by normalization in any case. The effects on the obtained coupling constants are not straightforward, but simulations show that again smaller couplings are affected more strongly. Furthermore, the simulations revealed that deviations are generally below 0.6 Hz taking into account a global, unrealistic high relaxation rate of $R_{1,2} = 5\ \mathrm{s}^{-1}$.[10]

Another essential problem, when fitting TOCSY transfer amplitudes with the LSQ algorithm is the *initial guess*, i.e., the starting point for optimization. As the LSQ algorithm is gradient-based, it only finds a local minimum during the optimization process and could get easily stuck on the potential surface. As discussed above, this was the reason why a 'global' optimization routine like SA or GA was favoured initially. However, these algorithms face the same problems in principle though not as pronounced as for gradient-based algorithms. Still, this problem can be overcome if a 'good' initial guess is available.

When inspecting the equations that quantitatively describe TOCSY transfer, it becomes apparent that transfer amplitudes of cross-peaks at short mixing times are proportional to $\sin^2(2\pi Jt)$. This observation can be used to estimate a value for the coupling constant which is then inserted into the fitting protocol. To test the quality of this guess and how well it re-

10 Transverse and longitudinal relaxation rates are much smaller for small molecules ($\tau_c < 0.5$ ns).[88]

sembles the actual coupling constant simulations were conducted for a three spin system, where the mixing time was set to 10 ms and one coupling was kept fixed at $J_{23} = 10$ Hz. Subsequently, transfer amplitudes (T_z^{11}, T_z^{12}, and T_z^{13}) were calculated using, on the one hand, the $\sin^2$-approximation and, on the other hand, the full quantum mechanical equations while varying the remaining two coupling constants within boundaries of ± 25 Hz. Then the difference between the two simulations was calculated and the deviation in transfer amplitudes was converted into errors of the coupling constant. Results are shown in Fig. 3.16 and reveal that errors by using the $\sin^2$-approximation are generally below 1 Hz for mixing times smaller than 10 ms. Only for extreme settings, i.e., $|J_{1j}| > 23$ Hz or $|J_{1j}| \approx 0$ Hz, stronger deviations were found. Still, all initial guesses were sufficient to find the correct minimum in the conducted simulations. It has to be pointed out that Glaser *et al.* have proven that zero transfer might occur in a three spin system for any value of J_{23} if a certain relation between J_{12} and J_{13} is met.[3] Obviously the $\sin^2$-approximation will give wrong results for these conditions.

As described by Fogolari *et al.*[137,138] the coupling constant could also be estimated with the equation

$$J_{ij} = \frac{\sqrt{4T^{ij}}}{2\pi t}. \tag{3.29}$$

However, it turned out that this approximation results in far worse results and represents only good guesses for small couplings $|J_{1j}| < 5$ Hz. Hence, it was not considered during the experiments.

3.4 Discussion

3.4.1 Modifying the Average Dipolar Coupling Tensor

Isotropic mixing conditions, as present in homonuclear TOCSY experiments in liquid state samples, typically result in positive transfer amplitudes.[1,144,145] Exceptions are only known for heteronuclear spin systems containing a spin-1 nucleus[177] and for homonuclear spin systems consisting of five or more spins-$\frac{1}{2}$.[4] In planar coupled two-spin systems the transfer amplitude is also generally positive,[178–180] but three or more planar coupled spins are known to undergo negative transfer under certain conditions.[181] The situation in dipolar coupled spin systems is fundamentally different, as TOCSY-type multiple pulse sequences can give rise to

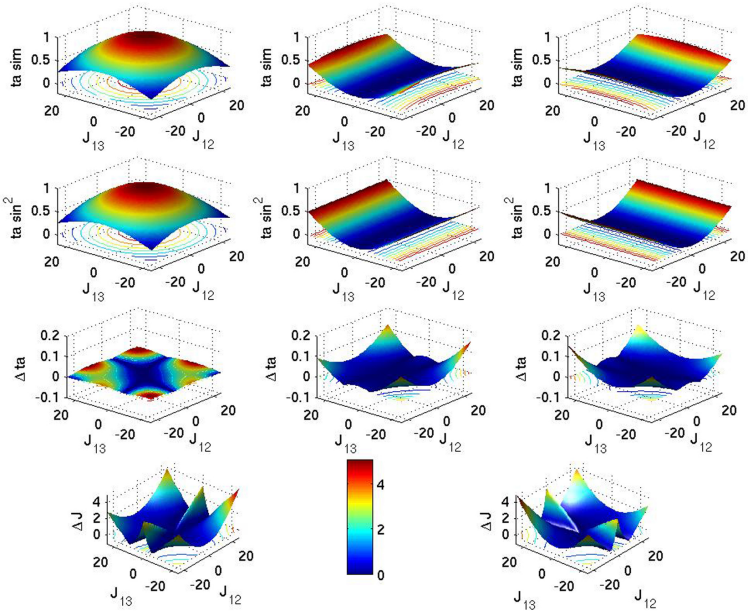

FIGURE 3.16: Simulations comparing the 'sin^2-approximation' to the full-quantum mechanical treatment of the spin system. In the top panel simulations were conducted on a three spin system using the complete set of quantum mechanical equations. Below the sin^2-approximation was used to estimate the transfer amplitude. In the third panel from the top, the deviations between both simulations are depicted. In all cases transfer amplitudes T_z^{11}, T_z^{12}, and T_z^{13} are shown from left to right and the scalar couplings J_{12} and J_{13} are varied between ± 25 Hz, while J_{23} was kept fix at 10 Hz. In the bottom panel the difference in transfer amplitude is translated into a deviation of the J_{12}-coupling (LEFT) and J_{13}-coupling (RIGHT). The colour bar (MIDDLE) indicates the deviation of the J_{12}-/J_{13}-coupling from the theoretical value in Hz.

ZQ-based positive transfer as well as DQ-based negative transfer between any two coupled spins, as is shown in Eq. 3.19 and was reported previously.[147–149,151] The derivation of the vanishing average dipolar coupling Hamiltonian for the JESTER-1 sequence with XY16 expansion is given in Sec. 3.2.1, but a simplified view would be that the sequence produces equal amounts of ZQ- as well as DQ-based transfer, therefore leading to zero net transfer.

JESTER-1 as a simple multiple pulse sequence initially designed for heteronuclear isotropic Hartmann-Hahn (HIHAHA) transfer with a relatively large bandwidth (cf. Tab. 3.1)[3,161] expectedly removes all diagonal elements in the average homonuclear dipolar interaction tensor $\overline{\mathbf{D}}$ (see Eq. 3.18) since HIHAHA sequences obey the condition of an isotropically distributed principal interaction axis. As has been shown in Sec. 3.2.1, off-diagonal elements also disappear by the expansion in XY-type supercycles.[163,164]

The bandwidth along the anti-diagonal of JESTER-1 with XY16 expansion for its use in *J*-ONLY-TOCSY experiments is approximately $0.8 \cdot B_1$, which is on the same order as for conventional TOCSY sequences like MLEV-16,[162] DIPSI-2,[158] or MOCCA-XY16[150,166] (cf. Tab. 3.1). However, other multiple pulse sequences with improved bandwidths might be constructed out of HIHAHA sequences or optimized using techniques like optimal control of spin dynamics, which in the last few years has been applied successfully to a number of problems concerning pulse and pulse sequence design.[182–189]

For a number of multiple pulse sequences like e.g., DIPSI-2, polarization transfer purely based on dipolar couplings in isolated two-spin systems results in negative cross-peaks, which, in principle, can easily be distinguished from transfer via scalar couplings. However, one should always be aware in this case that the transfer is a *combination* of scalar and dipolar couplings[149] (see Fig. 3.12) and the identification of covalently bound spin systems is not unambiguously possible. This is especially the case for large spin systems with very complex transfer functions and also applies to multiple pulse sequences designed for clean TOCSY transfer through RDCs.[165]

The usual limitations of zero order average Hamiltonian theory apply for the suppression of dipolar interactions, i.e., RDCs must be considerably smaller than the inverse basic cycle time. Since the JESTER-XY16 sequence has a minimum expansion in XY8 in order to fully suppress the dipolar interactions, the basic cycle time corresponds to the time needed

for a 6480° pulse, i.e., at an rf-amplitude of 7 kHz all residual dipolar couplings should be significantly smaller than ≈ 400 Hz. The multiple pulse sequences presented here therefore are fully applicable in combination with most of the recently developed alignment media. Applied with correspondingly increased rf-amplitudes, they might well be applicable also in solid state experiments.

The JESTER-1-based multiple pulse sequences are not clean TOCSY sequences in the sense that they do not suppress transfer via transverse or longitudinal dipolar relaxation in the spin diffusion limit.[7–9] Such sequences require magnetization to be oriented twice as long along the z-axis as in the transverse xy-plane to compensate negative ROE and positive NOE relaxation contributions for large molecules in the spin diffusion limit. Especially for small to medium-sized molecules, however, the ROE-contribution will be very weak and corresponding negative cross-peaks of low intensity can easily be distinguished from positive TOCSY peaks via scalar couplings (*vide infra*).

An aspect which has not been discussed so far, is the value of the JESTER-XY16 pulse sequence for reassigning spin systems in the alignment medium. Solute molecules dissolved in liquid crystalline media as well as paramagnetically tagged molecules will experience chemical shift changes due to the medium acting as co-solvent,[61] residual chemical shift anisotropy, or pseudocontact shifts.[47] This phenomenon is shown in Fig. 3.1 where signals of the protons 11 and 14 change their positions upon alignment. In addition, signals for resonances for proton 20 and 11′ do overlap in the alignment medium. Using conventional techniques for reassigning the spin system, like HMBC-type, COSY-type or TOCSY-type experiments, cannot generally be used, since coherence transfer also occurs via dipolar couplings through space. Heteronuclear correlations via scalar and/or residual dipolar couplings can generally not be distinguished by any pulse sequence, since they have coupling Hamiltonians of identical form. The same situation applies for homonuclear correlation experiments that are based on weakly coupled spins like COSY-type experiments. Only in the strong coupling limit the scalar and dipolar interactions differ in their effective Hamiltonian and a general distinction of their contribution is possible. The newly designed JESTER-XY16 is able to suppress transfer through residual dipolar couplings and allows an unambiguous reassignment.

3.4.2 Measuring ^{1}H-^{1}H Residual Dipolar Couplings

Residual dipolar couplings have proven to be a valuable and versatile tool in many research areas, especially for the structural and dynamical characterization of organic molecules. While for large- and medium-sized molecules measurement of $^1D_{CH}$- and $^1D_{NH}$-couplings is mostly sufficient for further investigations, small molecules suffer from the fact, that only few of these couplings are available. Furthermore, these couplings are often redundant due to the co-linear orientation of the underlying bond vectors and hence, the alignment tensor remains under- or sparsely determined. This creates the need for the measurement of new, independent coupling constants.

Measurement of ^{1}H-^{1}H residual dipolar couplings appears as the logical consequence since these couplings are widely abundant and very sensitive even across larger distances due to the high gyromagnetic ratio (cf. Eq. 2.49). However, their extraction is often complicated by the large experimental linewidth, which renders any method based on line separations inadequately. Analyzing transfer amplitudes in TOCSY spectra, in principle allows the measurement of ^{1}H-^{1}H-RDCs independent of the actual linewidth, as only peak volumes are inspected. This approach is not new,[137,138] though it has never been applied for the determination of ^{1}H-^{1}H-RDCs. A center piece in the analysis of residual dipolar couplings with TOCSY spectra is the use of different mixing sequences, which have the ability to modify the dipolar coupling tensor differently. This allows not only the measurement of the size of the dipolar coupling, but also for the sign of the dipolar coupling relative to the corresponding scalar coupling (*vide infra*).

As described in Sec. 3.1 the sign of the D_{HH}-coupling bears valuable information. But only in cases were the dipolar coupling D is much smaller than the J-coupling, e.g. in case of $^1D_{NH}$-couplings, the absolute sign of the dipolar coupling can be extracted without knowledge of the absolute sign of the J-coupling. Typically, measuring the sign of D_{HH}-couplings inevitably requires knowledge of the *absolute* sign of the corresponding J_{HH}-coupling as only the *relative* sign is available for dipolar couplings. The *absolute* sign of J_{HH}-couplings can be extracted from E.COSY-type spectra in isotropic solution or can be safely guessed in cases of $^2J_{HH}$- and $^3J_{HH}$-couplings. But complications arise when residual dipolar couplings are measured for spin pairs that are separated by more than three bonds, e.g. two axially protons in a six-membered ring. The underlying J_{HH}-coupling is commonly very small (< 1 Hz) and cannot be extracted safely. Consequently, only the size

of the dipolar coupling can be extracted in those cases, but not the sign, due to a lack of information on the J_{HH}-coupling.

As pointed out above, measuring the sign of ^{1}H-^{1}H-RDCs requires scaling of the dipolar coupling Hamiltonian and is achieved using different mixing sequences. But, as described in Sec. 3.1, this can also be achieved by simply changing the alignment strength mechanically and hence scaling the dipolar coupling constant. Though this technique still exhibits some practical imperfections it may be beneficially combined with the scaling on the quantum mechanical level. This would also allow the generation of complementary data sets, that would increase the precision of the determined coupling constants.

Measuring ^{1}H-^{1}H-RDCs within a series of TOCSY spectra reproduced the coupling constants found for the test system DBPA within a 1D-^{1}H-spectrum very well. The general deviation was found to be below 0.5 Hz for scalar couplings and below 2 Hz for residual dipolar couplings. Comparing this result to errors commonly obtained in measurements of $^1D_{CH}$-couplings in HSQC spectra reveals the quality of this method. For $^1D_{CH}$-couplings the error is usually estimated to be 1 Hz but precise measurements revealed revealed that the errors are typically underestimated.[172] Hence, errors for ^{1}H-^{1}H-RDCs obtained by the 'TOCSY method' are on the same order as for $^1D_{CH}$-couplings, especially when considering the fact, that errors were generously rounded up.

Signal overlap between resonances of different spin systems might turn out to be one of the bottlenecks using the 'TOCSY method' as well. In the case of considerable line broadening or simply in case of large spin systems, cross-peaks may be not resolved and hence transfer amplitudes cannot be extracted. But, in principle, as can be seen from the name – TOCSY = *TOtal Correlation SpectroscopY* – all coupling constants are already encoded in only one strip of the spectrum. Therefore, only *one* resolved strip should be sufficient to extract *all* coupling constants. A subsequent test for the three spin system of DPBA indeed revealed the possibility of this approach without a significant loss of accuracy. However, in practice, when spin systems consist of more spins, this approach would include the measurement of spectra with impracticable long acquisition times. Therefore, the statement has to be weakened so that the analysis of only *few* resolved strips should be sufficient to extract the desired coupling constants.

A further limitation of the 'TOCSY method' is the inevitable need for the calculation of theoretical transfer amplitudes during the fitting pro-

cess. Though tests have been conducted on a seven spin system which still required an acceptable amount of time (< 15 min), it is easily imagined that calculations will exceed any practicable range, when considering the fact that the calculated matrices scale exponentially with the number of spins within the spin system. For this purpose, an interesting approach was described by Fogolari *et al.* for purely scalar coupled spins,[137, 138] using Liouvillian superoperators.[190] In principle, the evolution of the density matrix σ_0 at time point $t = 0$ is expanded into a Taylor series and hence, the expectation value of a certain target operator can be calculated by simply multiplying the corresponding prefactors which depend on the scalar and dipolar couplings. This approach is very powerful and is only limited by the order of the terms which have been included from the Taylor expansion. So far, only terms and prefactors up to 4^{th} order have been published, which limits the analyzable mixing times and couplings. Moreover, suitable equations have to be derived for the transfer through dipolar couplings, as the coupling Hamiltonian is altered.

3.5 Conclusion

In Sec. 3.2 the so-called *J*-ONLY-TOCSY experiment was introduced, which suppresses transfer via residual dipolar couplings. The key step of the experiment is the use of JESTER-1-derived multiple pulse sequences that eliminate the effective dipolar coupling Hamiltonian while retaining good transfer properties via scalar couplings. In addition, it allows the unambiguous identification of scalar coupled spin systems in partially aligned samples. Hence, the assignment for a spin system can be easily reestablished using the *J*-ONLY-TOCSY.

Furthermore, the foundations for the determination of ^{1}H-^{1}H-RDCs using TOCSY spectra were derived theoretically and experimentally. A general route for the extraction and normalization of TOCSY transfer amplitudes was described and a suitable optimization algorithm for fitting the experimental data was selected. The proposed method allows the measurement of ^{1}H-^{1}H-RDCs independent of the actual linewidth and to a precision of below ≈ 2 Hz. Systematic influences on the precision of the measurement have been described and quantified and were found to be less than 0.5 Hz in the case of small molecules ($\tau_c < 1$ ns). In crowded spectra, the extraction of coupling constants for the complete spin system can be reduced to an analysis of only few well-separated TOCSY strips. The

increased ambiguity of a reduced set of cross-peaks can probably partly be compensated by the use of other RDC scaling techniques like the rubber-based stretching apparatus to increase the amount of experimental data points. A loophole for the inevitable increased computational efforts for large spin systems for the fitting procedure is described but not yet implemented in practice.

Chapter 4

The Bone Morphogenetic Protein Receptor Ia

This project was conducted in cooperation with the group of Prof. T. Müller, Lehrstuhl für Botanik I – Molekulare Pflanzenphysiologie und Biophysik, Universität Würzburg. Protein sample preparation, mutational studies, and measurements of binding affinities were performed by A. Kotzsch.

4.1 Introduction

4.1.1 BMPs and Related Proteins

Already in 1965 M. Urist discovered the activity of BMPs by observing that implantation of demineralized bone matrix at subcutaneous or intramuscular sites leads to bone formation in rats.[191] The osteogenic potential was attributed to a glycoprotein complex, which was called 'bone morphogenetic factor' and is the origin of the name of this class of proteins. In the late 1980s BMPs could be isolated for the first time and the gene sequence was reported.[192]

Despite their name, the function of BMPs is highly divers and not restricted to formation of bone and cartilage. From expression studies and mouse models it is known that BMPs show a very broad range of activities in many different cell types like monocytes, epithelial cells, mesenchymal

cells, or neural cells.[193] BMPs regulate cell proliferation and differentiation, chemotaxis, and apoptosis. Moreover BMPs have a central function in embryonic development, i.e., the establishment of the dorsal/ventral body axis and the formation of kidney, eye, limb, amnion, heart, and testis.[194–197] In the adult organism they are responsible for regeneration processes like bone and joint formation in osteogenesis.

The bone morphogenetic proteins (BMPs) belong to the protein superfamily of transforming growth factor-β (TGF-β). This group of multi functional growth factors can be divided into subgroups on the basis of sequence similarity.[198, 199] Along with the growth and differentiation factors (GDNF) the BMPs form the largest subgroup comprising 15 members. Other proteins like TGF-βs, activines, inhibins, nodal, myostatin, muellerian inhibiting substances (MIS), and glial-derived neurotrophic growth factors (GDNFs) are also associated to this superfamily. So far, the superfamily of TGF-βs comprises more than 30 members which have been identified in several organisms ranging from *C. elegans*, *D. melanogaster*, and *Xenopus laevis* to mammals.

Like all members of the TGF-β superfamily, BMPs are translated as precursor proteins. These are composed of a N-terminal signalling peptide, a prodomain, and a C-terminal mature domain. After cleavage of the signalling peptide the preproteins dimerize. The mature protein is finally formed by the proteolytic cleavage of a RXXR-motif by a furine-analogue protease.[200, 201]

The mature domain of a monomer comprises 100-140 amino acid residues and possesses a cysteine knot as characteristic motif.[202, 203] This consists of two disulfide bridges which form an eight membered amino acid ring. A third disulfide bridge is thread through this ring and forms the knot. This very stable structural motif not only occurs in the TGF-β family, but can also be found in other cytokines such as platelet derived growth factors and nerve growth factors, as well as in the comparably small ω-conotoxins.[204]

The basic structure of the monomeric subunit of the TGF-β family is shown in Fig. 4.1 on the basis of BMP-2[205] and is commonly described by the *open hand analogy*.[202] Each monomer is folded into nine β-strands ($\beta 1 - \beta 9$) and a long α-helix ($\alpha 3$ in BMP-2). The N-terminus represents the thumb and the two β-sheets are denoted as finger 1 and finger 2. Consequently, the convex surface is described as *knuckle* and the helical region as *wrist*. Most proteins similar to TGF-βs are homodimeric in their natural occurring form, though inhibines, activines, and some BMPs have been observed in a heteromeric form. The thenar of the monomer is buried

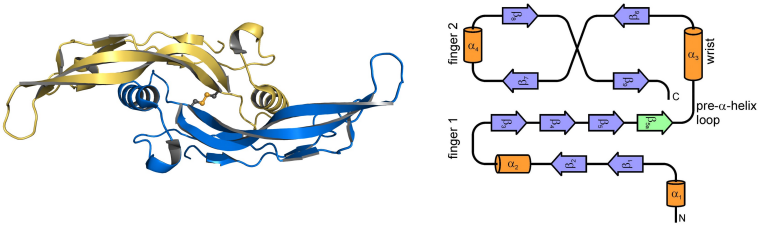

Figure 4.1: The 'open hand' analogy. Left: Cartoon representation of the BMP-2 dimer crystal structure, as a representative for ligands in the TGF-β superfamily. The dimer is linked by a disulfide bridge. Right: Schematic representation of the fold of the BMP-2 monomer, revealing the two central β-sheets denoted as finger 1 and finger 2 and the helix α_3 representing the wrist.

in the concave side of the fingers of the other monomer. The dimer is stabilized by hydrophobic interactions and in most cases by an additional intermolecular disulfide bridge (not within GDF-3, GDF-9/-9b, and Lefty-1/-2).

From the TGF-β superfamily the crystal structures of TGF-β_2,[202] TGF-β_3,[206] BMP-2,[205] BMP-3,[207] BMP-6,[207] BMP-7,[208] BMP-9,[209] GDF-5,[210] GDF-15,[211] GDNF[212] have been solved. In addition, the structure of TGF-β_1[213] has been solved by NMR spectroscopy. Though profound differences exist between the amino acid sequences of these proteins, all members of the TGF-β superfamily exhibit a highly similar fold of the protein backbone. For example BMP-2 and TGF-β_2 show only 32% identity in their amino acid sequence but the superimposition of the bachbone atoms reveals a RMSD of just 1 Å.[199] Minor differences can be observed only in loop regions at the 'finger tips', at the N-terminus and the N-terminal end of the helix.

4.1.2 Receptors of the TGF-β Superfamily

All characterized ligands of the TGF-β superfamily mediate their signal via a transmembrane serine/threonine-kinase. The only exceptions are GDNF whose signal is initiated via a receptor tyrosine-kinase[214] and ligands like MIC-1, where the signal mediating receptor is still unknown. In the human genome only 12 serine/threonine receptor kinases within the TGF-β system have been identified so far, which can be divided on the basis of sequence

homology and functionality into two subfamilies, the type I (7 members) and the type II (5 members) receptors Fig. 4.2.[215]

To the group of type I receptors belong the activine-like-kinase 1 and 7 (Alk-1 and Alk-7), the activin type-I and -IB receptors (ActR-I = Alk-2, ActR-IB = Alk-4), the BMP type-IA and -IB receptors (BMPR-IA = Alk-3, BMPR-IB = Alk-6), the TGF-β type I receptor (TβR-I = Alk-5). The group of type II receptors is composed of the TGF-β type II receptor (TβR-II), the BMP type II receptor (BMPR-II), the activin type II and IIB receptor (ActR-II, ActR-IIB), and the muellerian inhibiting substance receptor (MISR-II).[216]

Both receptor types consist of 500 to 570 amino acid residues and can be dissected into three domains, i.e., an extracellular, ligand binding domain, a transmembrane domain, and a intracellular domain with kinase function. The extracellular domains with around 120 to 150 residues share a comparably small sequence homology. However, a conserved pattern of 10 cysteines can be identified, which determines the structural stability.

With the help of the crystal structure of the activin type II receptor the fold underlying the extracellular domain of type II receptors could be solved.[217] The fold comprises three double stranded β-sheets and five disulfide bridges. Because of the structural homology to the physiologically unrelated neurotoxines the fold is specified as *three finger toxine fold*.

The characteristic attribute of the type I receptors is a sequence of 30 amino acids which is highly conserved and directly precedes the kinase domain. Due to the pattern of the amino acids (SGSGSG) this region is named GS-box. Phosphorylation of these amino acids activates the kinase for signal transduction (*vide infra*).[218, 219] Type II kinases are constitutively active while the type I receptors depend on ligand binding and on activation through the type II receptor.[220]

In addition to signal transducting receptor kinases some ligand proteins require cell surface proteins for binding which are denoted as type III receptors. For example, betaglycan, endoglin, and proteins from the EGF-CFC family belong to this class.[221]

4.1.3 Signal Transduction

The Smad-depending signal pathway is the best characterized signal cascade, and is initiated by the interaction of the TGF-β ligand with its receptor. In Fig. 4.3 this pathway is described schematically. Upon binding of the ligand to the extracellular domain of both receptors the intracellular

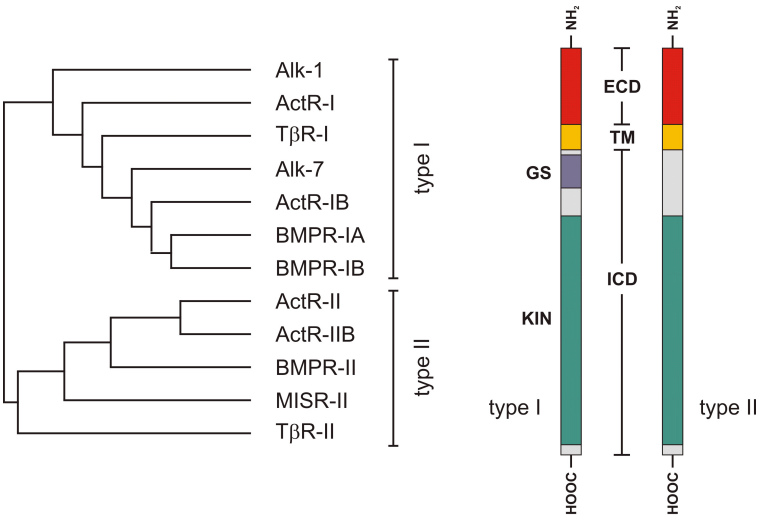

Figure 4.2: Tree representation of receptor sequence homologies within the TGF-β superfamily (Left) and a schematic representation of the type I and type II receptors (Right). ECD: extracellular domain; TM: transmembrane domain; ICD: intracellular domain; KIN: kinase domain; GS: GS-box (see text for details).[215]

kinase domains are brought into close proximity. This leads to transphosphorylation of the GS-box from the type I receptor by the constitutively active type II receptor resulting in conformational changes of this region.[219, 220, 222–224] The now activated type I receptor kinase passes on its signal via intracellular mediators, the Smad-proteins. Smads can be classified into three groups, i.e., receptor regulated Smads (R-Smads), common-mediator Smads (Co-Smads), and inhibitory Smads (I-Smads).[225]

R-Smads are directly phosphorylated and therefore activated by type I receptors.[226] R-Smads can be divided into two classes, depending on the receptor responsible for activation. Smad-2 and Smad-3 are termed *Activin/TGF-β activated Smads* which can be phosphorylated by TβR-I, ActR-IB, and Alk-7. In contrast, Smad-1, -5, and -8 are phosphorylated by BMPR-IA, BMPR-IB, ActR-I, and Alk-1 and are therefore called *BMP activated Smads*.[221] Phosphorylation of R-Smads leads to dissociation from the receptor complex and to formation of the heteromeric complex with Smad-4 being the only member in the class of Co-Smads. This complex accumulates in the cell nucleus where it might associate with various DNA-binding partners or different co-activators or co-repressors for transcription.[227] I-Smads (Smad-6 and Smad-7) compete for the interaction with the receptors or the Co-Smads and hence represent a negatively regulating signal cascade.[228, 229]

TGF-β ligands are also able to mediate their signal in a Smad independent signal cascade. As an example it is referred to the activation of the small GTPase Ras, the mitogen-activated protein kinases (MAP-kinase), ERKs, and c-Jun-terminal kinases.[230]

4.1.4 Ligand/Receptor Interactions - Specifity and Affinity

For the more than 30 ligands of the TGF-β superfamily only seven type I and five type II receptors are available. This disproportion and the necessity of the ligands to bind to both receptor chains for signal transduction requires an overlap in receptor specifity.[231] In Fig. 4.4 the different possibilities for ligand/receptor interactions within the TGF-β superfamily are illustrated. It reveals that on the one hand certain receptors may interact with several different ligands and on the other hand that ligands may also interact with different receptors. This promiscuity is not only restricted to ligands of the TGF-βs. In this context attention has to be drawn to the type II receptors of ActR-IIB and its close relative ActR-II. These receptors may bind to actvine and inhibine,[232, 233] as well as

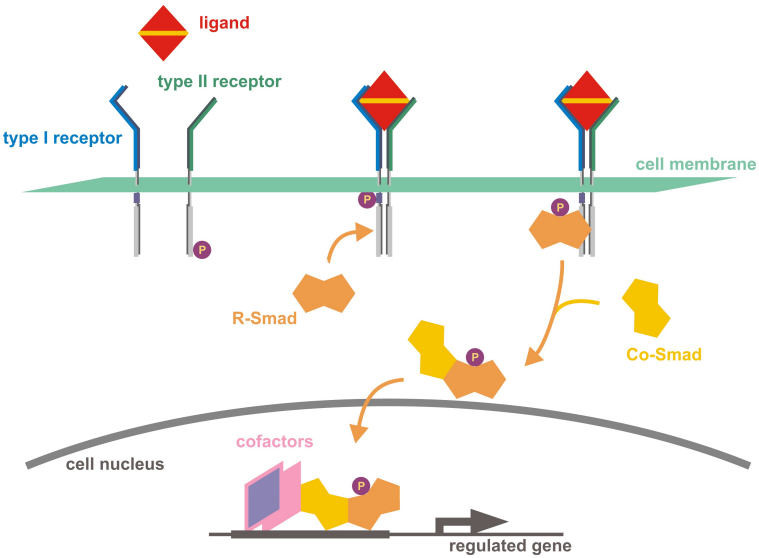

Figure 4.3: Schematic representation of the signalling pathway of the bone morphogenetic protein. The ligand dimer (red) binds to the receptor chains of the type I receptors (blue) and the type II receptor (green). This leads to phosphorylation of R-Smads (orange), which, together with Co-Smads (yellow), relay the signal into the cell nucleus. With the help of cofactors, a regulated gene is finally activated/deactivated.

GDF-1/-8/-11[234–236] and nodal[237] to initiate Smad-2/-3 gene expression via the type I receptors ActR-IB and Alk-7, respectively. Furthermore, the interaction between ActR-II/-IIB with BMP-2/-4,[238] GDF-5, BMP-6[239] and BMP-7[240] could be demonstrated. Together with the type I receptors BMPR-IA/-IB and ActR-I, respectively signalling occurs by the Smad-1/-5/-8 specific pathway.

On the basis of cross-linking experiments the ligand/receptor interactions within the TGF-β superfamily could be grouped into two classes.[214] The first is formed by actine and TGF-βs. These bind with high affinity to their constitutively active *type II receptors*.[241] This interaction represents a trigger factor as it enables the recruitment and transphosphorylation of the corresponding type I receptor.[242–245] An interaction of free TGF-β with the type I receptor in the absence of TβR-II has not been observed so far. Cross-linking experiments with ActA reveal an analogous cooperative progression. Here, a high affinity interaction with its type II receptors ActR-II and ActR-IIB can be diagnozed as well, while an interaction with the type I receptor alone cannot be observed.[219, 246] The second binding mode is best studied for the interaction of BMP-2, BMP-4, BMP-6, and GDF-5 with their corresponding receptors. Initially, BMP-2 binds with high affinity to the *type I receptor* BMPR-IA or BMPR-IB, whereas the affinity for the type II receptors BMPR-II, ActR-II, and ActR-IIB drops by a factor of 50-100 compared to type I receptors.[247] Binding experiments in entire cells also revealed varying binding affinities for the two receptors with a strong preference for the type I receptor.[223, 239, 248–250] In principle, BMP-7 exposes an equivalent cooperative binding mechanism, as a high affinity for BMPR-IB and a low affintity for type II receptors (ActR-II/ActR-IIB) can be observed.[240, 248] However, BMP-7 does not signal via BMPR-IB, but through ActR-I, to which it exhibits a very low affinity.[251] In this case the presence of a coreceptor is discussed, which assists the binding event to the signal transducting receptor.

For some members of the TGF-β superfamily participation of coreceptors that assist the formation of active ligand/receptor complexes has been proven (Fig. 4.4). For example, betaglycan acts as *type III receptor* for TGF-βs[252, 253] and inhibin, while cripto is essential for the interaction of nodal and GDF-1 with their signal mediating receptors.[236, 254]

Beside signal transducting receptors and coreceptors a further receptor type for the TGF-β members can be found in the cell membrane which are denoted as *pseudo-receptors*. Pseudo-receptor BAMBI (BMP and activin receptor membrane bound inhibitor) is composed only by a membrane

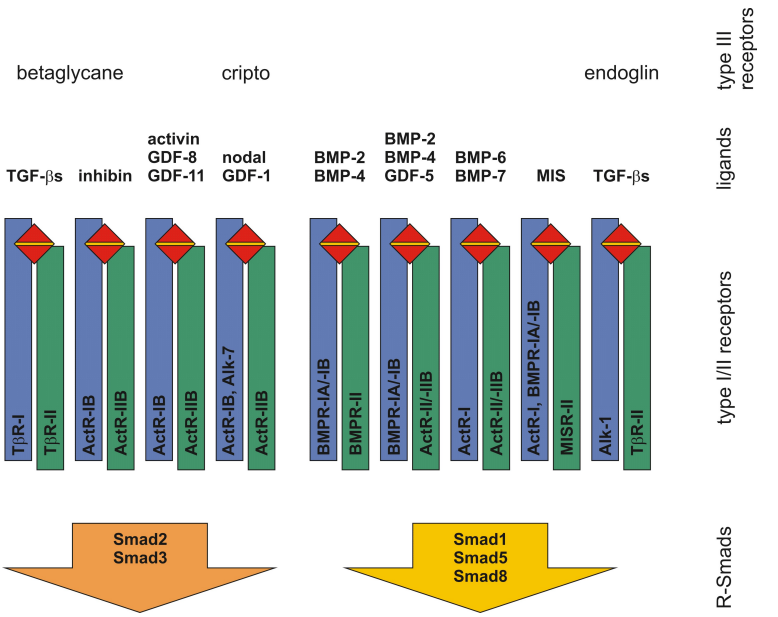

Figure 4.4: Schematic representation of the receptor/ligand interactions within the TGF-β superfamily. Shown is the selectivity of the ligands for the receptor pairs (type I and type II) and the specifity of R-Smads for signal transduction.[226] At the top of the illustration possible type III receptors are indicated.

spanning domain and a ligand binding extracellular domain. Consequently, it competes for the formation of signal active ligand/receptor complexes representing a down-regulating mechanism.[255, 256]

Apart from receptor binding TGF-β ligands may interact with a manifold of soluble modulator proteins.[193, 257, 258] Upon binding to these factors, access to the receptors is inhibited. For instance decorin and α-makroglobulin bind to free TGF-β, follistation binds activines and BMPs, whereas the members of the noggin, chordin/SOG, and DAN/cerberus families are potent inhibitors of BMPs.

4.1.5 Structural Basis for the Ligand/Receptor Interaction

The Binary Complex BMP-2:BMPR-IA$_{ec}$ and the Ternary Complex BMP-2:BMPR-IA$_{ec}$:ActR-II

Signal transduction within the TGF-β superfamily is initiated upon binding of the ligands to a total of four receptor chains; namely two type I receptors and two type II receptors. Here the type II receptor represents the *trigger* chain while the type I receptor is the *signal* chain. Both receptors have strongly different affinities for the ligand though the assignment as high-, low-affinity receptor does not correspond with the receptor type and is not conserved for a specific receptor chain (see Sec. 4.1.4). In the case of BMP-2 interacting with BMPR-IA$_{ec}$ and ActR-II, BMPR-IA$_{ec}$ represents the high affinity receptor and ActR-II the low affinity receptor.

In Fig. 4.5 the three dimensional structure of the heteromeric complex formed by BMP-2 and the receptor ecto domain of BMPR-IA is shown.[259, 260] It exhibits the interaction of one type I receptor with the BMP-2 dimer where one receptor chain is binding both monomers of the ligand. BMPR-IA$_{ec}$ is interacting with the cleft formed by the finger epitope of one BMP-2 monomer and the wrist epitope of the other monomer. This interaction does not alter the two-fold symmetry of the unbound ligand[205] and is preserved within the binary complex and ternary complex (*vide infra*). The N-termini of the type I receptors are pointing away from the membrane while the C-termini are directed towards the membrane but are not in contact with each other.

The binding epitopes of the receptor are large (1130 Å^2)[259] and are mainly composed of hydrophobic sidechains. The buried surface area is formed by 25 amino acids from BMPR-IA$_{ec}$ and 15 residues from one BMP-2 subunit and 12 residues from the other subunit. A key role is adopted by F85 in BMPR-IA$_{ec}$[259] which forms a *knob-into-hole*-motif with a hydrophobic pocket of BMP-2 formed by a 3_{10}-helix of one BMP-2 (N59, I62, and V63) and the convex face of the second BMP-2 (W28, W31, M89, Y103, and M106). The second pocket is formed by residues F49 and P50 in the pre-helix loop of BMP-2 (Fig. 4.5 D) interacting with F60, I62, and I99 of BMPR-IA$_{ec}$ (Fig. 4.5 C). Beside the hydrophobic interactions 10 hydrogen bonds could be identified between BMP-2 and BMPR-IA$_{ec}$. By means of mutation/function experiments on BMPR-IA$_{ec}$ and BMP-2 the wrist epitope was validated as the type I binding epitope, but no major binding determinants were found.[259, 261]

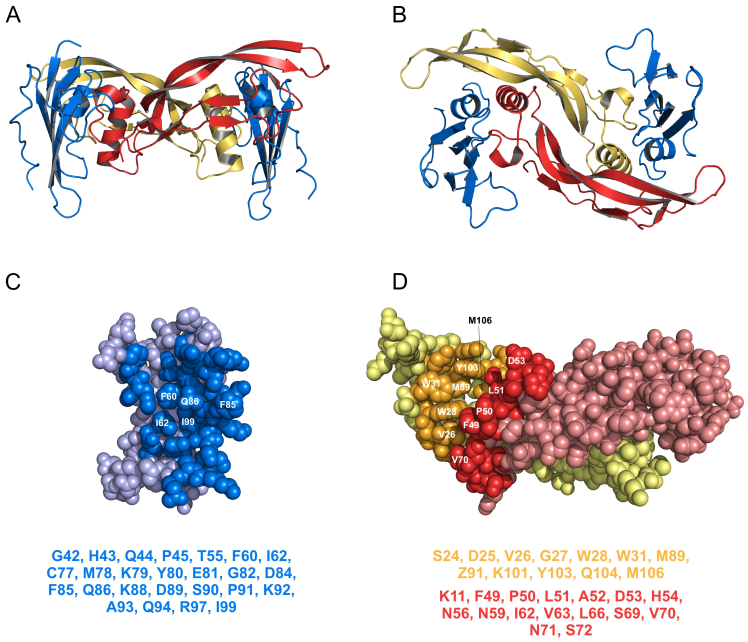

Figure 4.5: Structure of the binary complex BMP-2:BMPR-IA$_{ec}$ in cartoon representation (Pdb 1REW).[260] The ligand binding interfaces between BMP-2 and its type I receptor BMPR-IA$_{ec}$. (C) Peeled-away interface of BMP-2 and (D) of BMPR-IA$_{ec}$.

Only the determination of the high resolution structure of BMP-2:BMPR-IA_{ec} facilitated a precise characterization of the geometry of the hydrogen bond network.[260] Surprisingly, only three out of ten hydrogen bonds formed contribute significantly to the binding affinity. The functional groups of the ligand that are involved in this interaction are the amide proton of L51, the carbonyl group of L51 and the amide proton of D53. All these residues are located in the 'pre-helical' loop of BMP-2. A L51P mutation prevents binding to the type I receptor although the crystal structure of this mutant does not differ from that of wildtype BMP-2 within experimental error. These findings underline the importance of L51 as hydrogen bond donor and acceptor and identifies it as *binding hot spot*. The hydrogen bonds of L51 are formed with the sidechain carbonyl group of Q86, which therefore represents one of the major binding determinants on the receptor side.

With the help of mutation studies the binding interface of BMP-2 with its type II receptors could be investigated.[259] As a result, the convex face of finger 1 and 2 of BMP-2 ('knuckle epitope') was identified to interact with ActR-II and BMPR-II. Functional investigations revealed only a low affinity variation upon point mutations. The variant BMP-2 A34D led to the strongest changes decreasing the affinity for BMPR-II and ActR-II by a factor of 10 and 3, respectively.

On the basis of the crystal structure of the ternary complex BMP-2:BMPR-IA_{ec}:ActR-II[262] (Fig. 4.6) the interaction of BMP-2 with ActR-II could be studied in more detail. Like the interface between BMP-2 and its type I receptor, the binding interface of BMP-2 and ActR-II is mostly hydrophobic in nature. It is composed of 12 residues from BMP-2 and 10 residues from ActR-II and covers a total surface area of 670 $Å^2$. Previous studies have shown residues F42, W60, and F83 on ActR-II to be significant for the ligand/receptor interaction (Fig. 4.6 C). These residues interact with A34, P35, S88, M89, and L90 of BMP-2 (Fig. 4.6 D) which are identical among other ligands interacting with ActR-II (BMP-7 and activin). Only one polar contact is shared between the two binding partners, namely E109 on BMP-2 and K37 on ActR-II. However, this contact is not conserved among different ligands which might explain the interesting fact that ActR-II represents the high-affinity receptor for BMP-7 and activin, but the low affinity receptor for BMP-2. Mutation studies with BMP-2 to mimic the binding interface of BMP-7 and activin (S85R, L100K, and E109R) revealed higher binding affinities for the mutants. This can be ex-

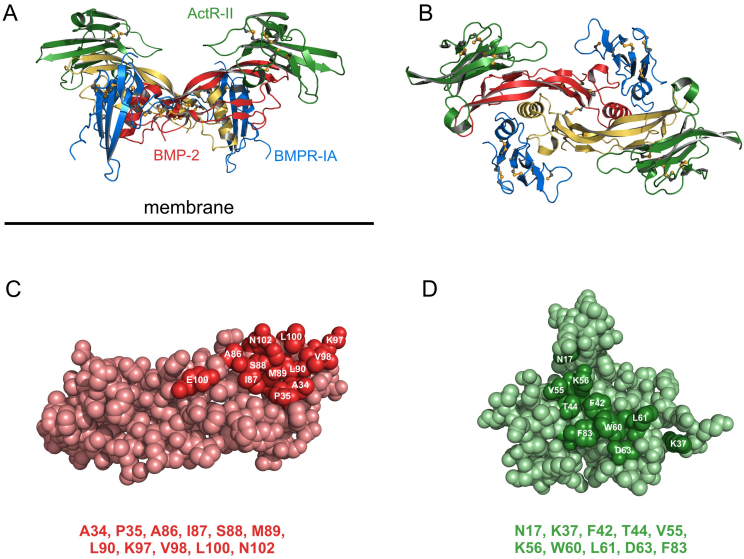

Figure 4.6: Structure of the ternary complex BMP-2:BMPR-IA$_{ec}$:ActR-II in cartoon representation. The ligand binding interfaces between BMP-2 and its type II receptor ActR-II. Peeled-away interface of BMP-2 and of ActR-II are shown in panel C and D, respectively.

plained by a reorientation of sidechains and an establishment of hydrogen bonds leading to local energetic gains.

Remaining Questions in the Interaction of BMP-2 with its Receptors.

So far, it is unknown if and how strong the structures for the receptor ecto domains (BMPR-IA$_{ec}$ and ActR-IIB) and BMP-2 change upon complex formation. Comparing the structure of the free form of BMP-2[205] and to the one bound to BMPR-IA and ActR-IIB,[262] differences are predominantly located in loop regions (pre-helical loop, finger I loop) and the 'finger regions'. The pre-helical loop which carries the main binding determinants for binding with BMPR-IA appears very flexible. In contrast to other structural regions of free BMP-2 it exhibits large temperature coefficients. This might also explain the small association rates ($k_{on} \approx 5 \cdot 10^5$ M^{-1}s^{-1}),

as has been observed for other representatives of the BMP-family (GDF-5 and BMP-6).[210, 263] Mutations in several positions of the loop region, especially the beginning and the end, result in a decreased association rate which suggests that the BMPs also use an induced fit mechanism.[247] But the amplitude of this conformational change is far smaller than the massive changes in the receptors Act-A and TGF-β_3. Possibly, the flexibility of the pre-helical loop is responsible for the discrimination in the interaction with different type I receptors. In a low resolution solution structure of the extracellular domain of BMPR-IA published in 2000 by a japanese group,[261] the complete α-helix is missing, which is clearly present in the complex structure.[1] But this helix is essential for the interaction with BMP-2 as it carries the main binding determinants, F85 and Q86 (BMPR-IA). For unknown reasons, both, structural assignment and coordinate data have been withdrawn from the RCSB (PDB) data base.

Investigations on the flexibility of the ligand structure via ^{15}N-relaxation studies have also been accomplished only for TGF-β_1 and TGF-β_3.[213, 264] In general, the analysis of protein-protein interactions mostly excludes the change in entropy. Structural and functional analysis often rely only on the correlation of a rigid complex structure with the binding data from a mutagenesis study. As a result of a mutation, it is often assumed that the change in free energy by an exchange of polar amino acids results from a change in enthalpy while for apolar amino acids this change is tracked back to a change in the hydrophobic interactions. Though the latter is regarded as an entropic effect as the binding energy results from a (re-)orientation of the solvent shell surrounding the proteins, this term is most often treated as an enthalpic contribution in binding experiments.

NMR investigations, as well as MD simulations have shown that the idea of a completely rigid protein is insufficient.[265] Even highly ordered regions exhibit at least a fast dynamical component in the ps-ns range in NMR relaxations studies.[266, 267] But this conformational entropy is mostly neglected in interaction studies. For a thorough understanding of protein-protein recognition and interaction, knowledge about all energy terms is essential.[268, 269] During the last decade major achievements have been made on the field of protein dynamics. These led to some surprising results, e.g., it would be expected that the flexibility of the residues decreases when a ligand binds to its receptor as the conformational degrees

1 The results of the structural analysis have never been published in an adequate journal, so far.

of freedom are restricted by additional interactions (hydrogen bonds, van der Waals contacts,...). This loss in *conformational entropy* must then be compensated by advantageous enthalpic interactions. Many examples are known for this mechanism where residues are immobilized within the binding epitope.[270, 271] But there are also contradicting examples where the binding process induces changes in the flexibility in a region of the protein *remote* from the actual binding epitope.[272, 273] An interpretation of this phenomenon is that the increased flexibility of the remote region compensates for the entropy loss in the binding epitope.[84, 274] Interestingly, some examples have also been reported where the flexibility increases *within* the binding epitope upon complex formation.[84] This was described especially for hydrophobic protein-protein binding interfaces comparable to the interfaces between the BMP's and their receptors.[264] On the background of the large conformational changes of the TGF-β ligands TGF-β_3 and Act-A but not BMP-2, it is of major interest whether the flexibility of the ligands differs within the TGF-β family and as a consequence different activation mechanism result.

For the ligands TGF-β_1, TGF-β_2, and TGF-β_3 dynamical investigations via NMR relaxation studies have been accomplished and emphasize that TGF-β ligands are highly flexible molecules.[213, 264] Even though the three TGF-β ligands exhibit high sequence homologies, large differences are observed in the three isoforms.[264] Therefore a ligand induced unfolding and reorientation seems possible. It is worth noting that the interaction epitopes range among the most flexible and dynamical parts of the molecules, raising the question how these regions might possibly carry the main binding determinants. On the other hand, structural investigations on the BMP receptor complexes BMP-2:BMPR-IA and BMP-2:BMPR-IA:ActR-IIB reveal clearly that only minor changes in the ligand architecture are observable upon receptor binding.[259, 260, 262] Consequently, the investigation of the dynamical parameters seems essential for a thorough understanding of the binding mechanism of the BMP and TGF-β proteins to their receptor.

For a quantitative description of the protein-protein recognition and interaction, knowledge about the flexibility of protein mainchain and sidechain atoms is desirable. The high receptor promiscuity within the BMP family might result from a high flexibility of the residues in the binding epitope which leads to a plastic adaption to different receptor interfaces.

4.2 Resonance Assignment

For the structure determination and the adjacent analysis of the protein dynamics, conditions had to be found that assure a stable and a spectroscopically 'well-behaving' sample. Initially, the complete extracellular domain of BMPR-IA (134 AA) was prepared. The ^{1}H-^{15}N-HSQC spectrum at 25°C revealed a folded protein but also some highly flexible amino acids clustering in the middle (8.0 − 8.5 ppm) of the spectrum, which is characteristic for unstructured residues. It is already known from the binary complex BMP-2:BMPR-IA$_{ec}$ that the N-terminal residues do not give a defined electron density. Therefore a deletion mutant was expressed where 27 N-terminal amino acids were omitted. This resulted in the short form of BMPR-IA$_{ec}$, named BMPR-IA$_{ec/sf}$ hereafter. A series of spectra with varying temperature exhibited well resolved spectra at 25°C, while an increased temperature enhanced the exchange with protons of water and led to the disappearance of some resonances. The comparison of the NMR spectra with the full-length protein showed no significant differences, indicating the preservation of the structure in BMPR-IA$_{ec/sf}$. Consequently, these conditions were chosen as the default measurement conditions (see Sec. B.1), unless otherwise indicated.

4.2.1 Backbone Assignment

Sequential assignment of the backbone resonances of BMPR-IA$_{ec/sf}$ was accomplished semi-automatically with the software package PASTA.[275] To create the required list of 'pseudo-residues' a highly resolved, folded ^{1}H-^{15}N-HSQC spectrum (Fig. 4.7) served as a basis. Theoretically, 124 cross-peaks are expected in the spectrum, including 28 sidechain resonances.[2] The original peaklist was reduced by resonances originating from Gln and Asn sidechains, which were identified in a ^{1}H-^{15}N-HSQC with inverted NH_2-groups. Sidechain resonances of Arg were also removed from the pseudo-residue list. Finally, a list of 105 cross-peaks served as initial input for PASTA.

The consecutive analysis of the HNCO, HN(CA)CO, CBCA(CO)NH, HNCA, and the HNCACB spectra led to the assignment of most C', C^{α}, and C^{β} i and $i-1$ resonances for each pseudo-residue. A subsequent PASTA

2 The protein comprises 102 AA including 8 proline residues. It is assumed that the N-terminus and Lys sidechains are not observable but that Gln, Asn, His will give rise to two and Arg to one cross-peak.

run resulted in the assignment of ≈ 80% of the non-proline residues. With the combined use of a HNHA and a HN(CA)HA spectrum and the extracted H^{α}-resonances, the assignment could be promoted further. During the course of structure determination, the associated analysis of NOESY spetra yielded further assignments, such that 88 out of 94 non-proline residues could be assigned. The remaining residues are predominantly located between residue C40 and C44 and could not be assigned probably due to high water exchange rates of the amide proton or chemical exchange.

4.2.2 Sidechain Assignment

As a start a CC(CO)NH and a HBHA(CO)NH spectrum were recorded to create pairs of assigned H^{α}-C^{α} and H^{β}-C^{β} pairs along the protein backbone. From these anchor points the assignment was started using a (H)CCH-COSY and a H(C)CH-TOCSY spectrum. Due to the large abundance of proline (8) and leucine (7) residues signal overlap became an issue for these amino acids. To overcome this problem a highly resolved (H)CCH-TOCSY was acquired which on the one hand exploits the higher chemical shift dispersion of the ^{13}C-nucleus and on the other hand renders the complete spin system observable. Therefore only one resolved ^{13}C-resonance along the sidechain enables the distinction between two residues of the same type. This strategy resulted in the full assignment of 92 residues, while most of the remaining residues are assigned at least partially (Tab. B.2).

In general, aromatic resonances escape the assignment procedure described above. However, these resonances are highly beneficial for structural investigations as they are often located in the hydrophobic core. To connect the aromatic protons with the aliphatic sidechains several techniques have been proposed in the past.[276–279] Attempts to carry out assignments using HBCB(CGCD)HD and HBCB(CGCDCE)HE experiments failed due to poor signal-to-noise and thus aromatic assignments were made by linking aromatic spin systems to the respective $C^{\beta}H_2$-protons in a HCH-NOESY spectrum. The aromatic spin system itself was then analyzed with the concerted use of an *IP*-COSY,[280] a ^{1}H-^{1}H-TOCSY,[3] and a *DQ*-COSY[282, 283] (see Fig. 4.8).

Finally, sidechain protons originating from asparagine and glutamine

3 Amide protons were suppressed in this spectrum with a BIRD-filter.[281]

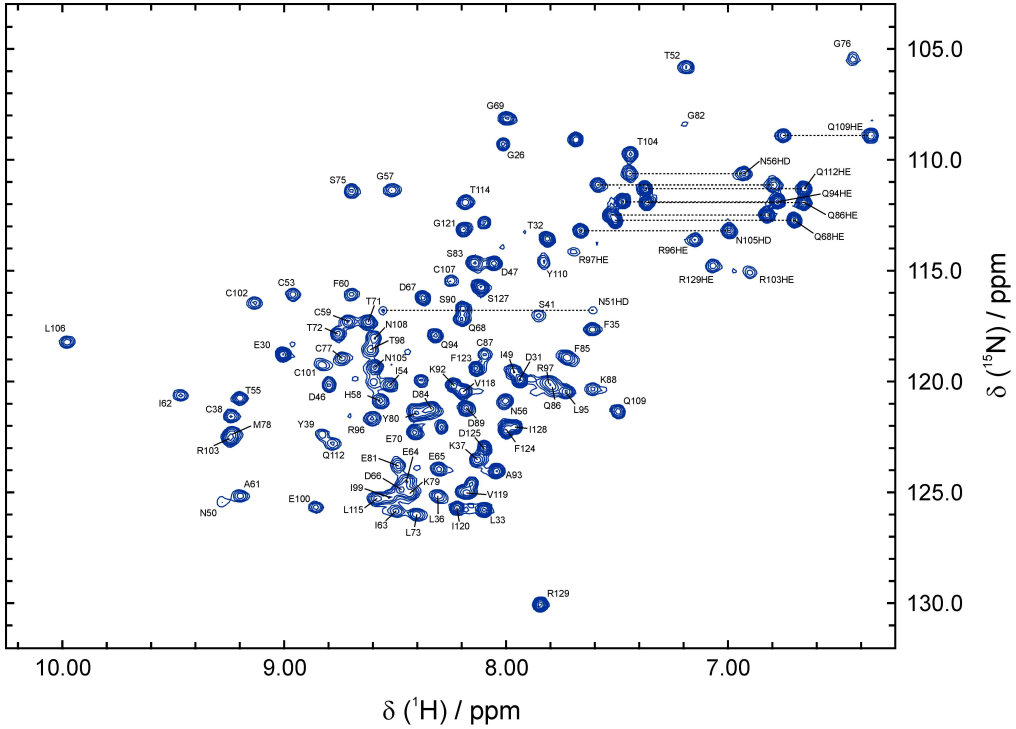

Figure 4.7: Annotated ^{1}H-^{15}N-HSQC spectrum of BMPR-IA$_{ec/sf}$ recorded at a temperature of 25°C and a proton frequency of 600 MHz. Amide sidechain resonances of Asn and Gln are connected by dotted horizontal lines. Cross-peaks resulting from Arg sidechains (indicated by the ending 'HE') are aliased due to the States acquisition scheme.

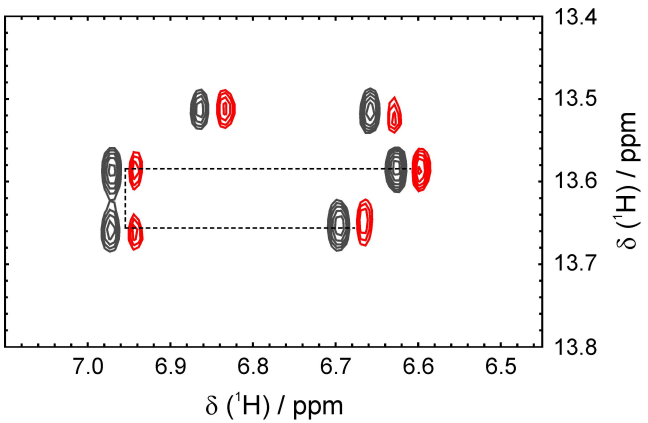

FIGURE 4.8: ^{1}H-^{1}H-double quantum spectrum for aromatic sidechains. Here a phenylalanine residue is shown whose resonances are conneted by dotted lines. The double-quantum frequency (sum of the single-quantum ferquencies) is given on the ordinate whereas the resonance frequency of the single aromatic protons is given on the abscissa.

residues were connected by the use of the CBCA(CO)NH. Furthermore, arginine H^{ϵ}-resonances were linked to the corresponding sidechain with the aid of the HCH-NOESY.

4.3 Secondary Structure, Dihedral Angles, and Hydrogen Bonds

A further central step in the structure determination of a protein is the identification of secondary structure elements. There are different NMR spectroscopic parameters indicating the tendency towards a certain geometry. However, only the combination of several of these parameters allows an unambiguous characterization. Commonly used secondary structure indicators are the NOE pattern, characteristic chemical shifts, and ^{3}J-couplings, although ^{1}J-, ^{2}J-couplings have been discussed as well. Recent developments also make use of so-called *dipolar waves*[284–286] or *PISEMA wheels*[287, 288] where the $^{1}D_{NH}$-coupling is either plotted versus the sequence position or the ^{15}N-CSA, respectively. The resulting pattern allows

for the prediction of the shape and orientation of a certain secondary structure element. Below the techniques utilized for the structure of BMPR-$IA_{ec/sf}$ are discussed in more detail.

4.3.1 TALOS

One of the most easily accessible NMR parameters to predict the secondary structure is the chemical shift as it is readily available after the assignment process. It has been known for many years that the observed chemical shift is closely related to the local geometry of the protein backbone. This concept has been systematized by WISHART *et al.*[289–291] and is commonly known as the *chemical shift index*, CSI. The software package TALOS represents an extension of this idea.[292] While the CSI only distinguishes qualitatively between α-helices and β-strands TALOS offers the opportunity to quantitatively predict the Φ/Ψ-combination of a residue.

TALOS is a database system that is based on empirical chemical shift data of proteins with known structure.[4] It includes the chemical shifts of H_i^{α}, C_i^{α}, C_i^{β}, C'_i, and N_i and additionally data from the precessor and successor resulting in a total of 15 shifts for the analysis of each residue. The idea is to find an amino acid triplet with known structure that consists of similar amino acids and exhibits similar chemical shifts. If this is the case, the Φ- and Ψ-angles are used for a prediction of the backbone geometry.

A disadvantage of the TALOS software is its comparably small database. This leads to erroneous predictions especially for sparsely populated Φ/Ψ-combinations such as positive Φ-angles. In addition, TALOS inherently generates 1.8% wrong assignments. To avoid these complications the recently released software package SIMSHIFT uses much larger databases but in return chemical shifts are based on back-calculation, i.e., not real, experimental shifts,[293] but predicted ones. Also the underlying search algorithm deviates from the one used in TALOS. A comparision of the two programs revealed similar results for both (Fig. 4.9), therefore SIMSHIFT might be valuable to validate data obtained from TALOS.

In practice, TALOS searches its database for the 10 best-fitting triplets. If all of these exhibit a consistent Φ/Ψ-angle distribution their averages and standard deviations are used for a prediction (see Fig. 4.9). These values were directly used as dihedral angle restraints in the structure calculation

4 The database has been restricted to crystal structures with a resolution higher than 2.2 Å. Moreover, solely residues located in 'well-defined' regions are include, i.e., residues with high B-factors or known to be flexible in solution are discarded.

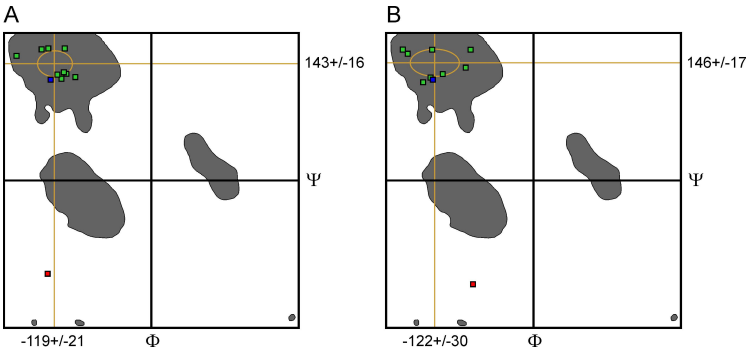

Figure 4.9: Typical output from a Talos (Left) and a SimShift (Right) analysis, where both show an equivalent tendency. Residue M78 is shown as a representative example where not all predictions cluster in equal regions of the Ramachandran map. As characteristic NOE contacts (e.g., $H_i^N \rightarrow H_{i-1}^{\alpha}$) and ${}^3J_{H^N H^{\alpha}}$-couplings indicate an extended structure the prediction was still used.

with an additional tolerance of $\pm 5^{\circ}$. Nevertheless, also predictions with deviating Φ/Ψ-values were used if at least 8 out of 10 predictions cluster in the same area of the Ramachandran map and other secondary structure indicators display an equivalent behavior. If no consistent conclusion was possible the predictions were discarded. Eventually, 58 pairs of Φ/Ψ-angles could be extracted and were used in the structure calculation (see App. B.3).

It is essential for an accurate analysis of secondary chemical shifts to reference the observed chemical shifts correctly. This was achieved by an external reference (trisilyl-d4-propionate acid, TSP) for the ^{1}H-dimension and subsequent indirect referencing for the other dimensions.[294] It has to be pointed out that 2.6 ppm have to be added to the ^{13}C-chemical shift values to match the chemical shift referencing used to compile the Talos databank, i.e., direct referencing to the ^{13}C-shift of the TMS methyl groups. To verify the correct referencing the program CheckShift can be used.[295]

4.3.2 $^3J_{H^N H^\alpha}$-Couplings

Another frequently used NMR parameter to investigate the secondary structure are ^3J-couplings as they offer a straightforward dependence between the observed coupling and the corresponding dihedral angle. This correlation is called *Karplus relation* and is a generally observed phenomenon in NMR spectroscopy. Even for very uncommon combinations of nuclei these correlations exist, e.g., $^3J_{^{119}\mathrm{Sn},^{13}\mathrm{C}}$.[296] The Karplus relation is an ordinary fourier series truncated after the second term where each term has an empirical prefactor. Since the Karplus relation depends on the molecular environment, different Karplus parameters are reported for different atoms and substituents involved.[176,297,298] In protein spectroscopy especially the $^3J_{H^N H^\alpha}$-coupling is of major interest due to its pronounced dependence on the backbone angle Φ and the easy accessibility. This coupling is on the order of a few Hz, ranging from 3.9 Hz for an ideal α-helix to 8.9 Hz for antiparallel β-sheets. The Karplus equation for $^3J_{H^N H^\alpha}$-couplings can be expressed as follows:

$$^3J_{H^N H^\alpha}(\Phi) = 6.98\cos^2(\Phi - 60^\circ) - 1.38\cos(\Phi - 60^\circ) + 1.72. \qquad (4.1)$$

Many different experiments have been proposed for the measurement of $^3J_{H^N H^\alpha}$-couplings.[133,140] In this work the commonly used experiment by VUISTER *et al.* was applied. Here the coupling constant can be estimated from the ratio of the diagonal-peak (H^N-H^N) and the cross-peak (H^N-H^α). Subsequently the coupling can be calculate via the equation:

$$^3J_{H^N H^\alpha} = \frac{\arctan\sqrt{-(S_{cross}/S_{diag})}}{2\pi\zeta e}. \qquad (4.2)$$

In this equation 2ζ denotes the delay in which the homonuclear H^N-H^α-coupling evolves and was set to 13.05 ms in the experiment. S_{cross} and S_{diag} are the signal intensities of the cross-peak and diagonal-peak, respectively. Because the *in-phase* operator giving rise to the diagonal-peak relaxes more slowly than the *anti-phase* operator responsible for the cross-peak, a compensating factor e is introduced into the equation. The final set of 60 $^3J_{H^N H^\alpha}$-couplings used in the structure calculation were evaluated with a value of $e = 0.9$ (see App. B.3).

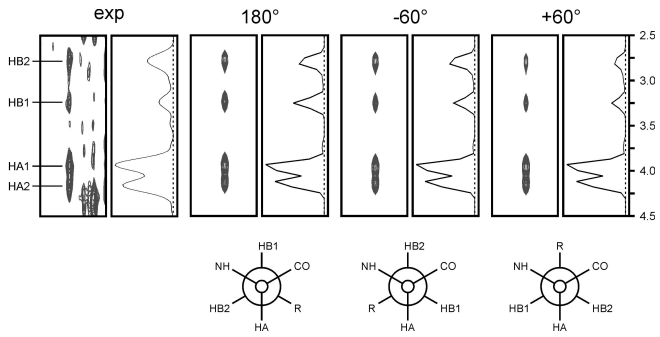

Figure 4.10: Back-calculation of NOESY spectra for the assignment of the χ^1-angle. Shown are HNH-NOESY strips of the residue H58. On the left hand side the experimental spectrum is given and alongside the back-calculated HNH-NOESY spectra for the χ^1-angles 180°, −60°, and 60°, respectively. It is apparent that the simulation for $\chi^1 = -60°$ matches the experimental data best. Resonance assignments are given for HB1 and HB2 of residue H58 and additionally for HA1 and HA2 of G57. The nomenclature follows the convention used in the software package Xplor and not the IUPAC conventions.

4.3.3 χ^1- and χ^2-Angle Restraints

The analysis of the χ^1-angle rotamer is closely related to the diastereotopic assignment of H^β-resonances. This was achieved using a combination of HNHB, HNH-NOESY, and HCH-NOESY spectra. From the HNHB spectrum the $^3J_{NH^\beta}$-couplings were extracted in a qualitative manner. This allowed for the distinction between the ±60° and the +180° rotamer. Subsequently, the HNH-NOESY/HCH-NOESY was used to assign the correct χ^1-rotamer and the corresponding prochirality of each H^β by investigating the $H^\alpha \rightarrow H^{\beta_{1,2}}$ and the $H^N \rightarrow H^{\beta_{1,2}}$ cross-peaks. If this procedure was deteriorated by overlapping H^β-resonances, the assignment strategy was changed and intra-residue H^β to H^α and H^N cross-peaks were analyzed in the HCH-NOESY, though this technique may be perturbed by spin-diffusion. To verify the assigned rotamer NOESY spectra were simulated for the local structure and compared semi-quantitatively with the experimental spectrum (Fig. 4.10). This resulted in 48 χ^1-angle assignments which where used in the structure calculations by applying dihedral angle restraints with a tolerance of ±30°.

The determination of the χ^2-rotamer for leucine, isoleucine, and proline[5] was accomplished with the HCH-NOESY as well. Characteristic patterns for intra-residue NOE connectivities led to assignments for 5 of 7 leucine residues and 5 of 7 isoleucine residues. The proline pucker could be assigned for 4 out of 8 residues. The corresponding dihedral restraints were also applied with a tolerance of $\pm 30^\circ$ with exception of proline residues where the χ^2-rotamer was restrained to $\pm 45^\circ$ with a tolerance of $\pm 5^\circ$ (see App. B.3).

4.3.4 Hydrogen Bonds

The identification of hydrogen bonds is an essential step in the structure determination process, as they are one of the major components that define the fold of the protein. So far, only one practicable method has been reported to *directly* observe hydrogen bonds in proteins. This technique makes use of the very small ${}^2J_{H^N C'}$- and ${}^3J_{NC'}$-scalar couplings[6] across the hydrogen bond.[299–301] The latter can be extracted from a HNCO spectrum optimized for small coupling constants which includes a prolonged evolution delay and suppression of the direct ${}^1J_{NC'}$-coupling. Nevertheless, experiments mostly suffer from poor sensitivity, as they are prone to relaxation during the long evolution delay (≈ 133 ms). Unfortunately, spectra for BMPR-IA$_{ec/sf}$ also revealed poor signal-to-noise ratios and could not be analyzed. Only the use of a perdeuterated sample might enable the acquisition of long-range-HNCO spectra.

Information about the hydrogen bond network can still be gained by NMR spectroscopy, however, only *indirectly*. An arsenal of different techniques has been designed that utilize the different properties of the hydrogen bonded amide proton compared to the unbonded one. Mostly these are based on the variation of the water exchange rate. Hydrogen exchange takes place on different timescales ranging from milliseconds to months where slow exchange is commonly attributed to the participation in a hydrogen bond. Hence, different experiments can be performed to sample the different timescales. Most easily water exchange is observed in H/D-exchange experiments where the protonated protein is lyophylised and redissolved in D_2O. A time resolved series of fast ^{1}H-^{15}N-HSQC spectra can then be used to monitor the decay in signal intensity.[302,303] This approach is obviously limited by the time for acquiring a single 2D-spectrum

5 Here the χ^2-angle was used to define the proline pucker.
6 Couplings are: ${}^2J_{H^N C'} = 0.2$ - 0.6 Hz and ${}^3J_{NC'} = -0.2$ - -0.9 Hz

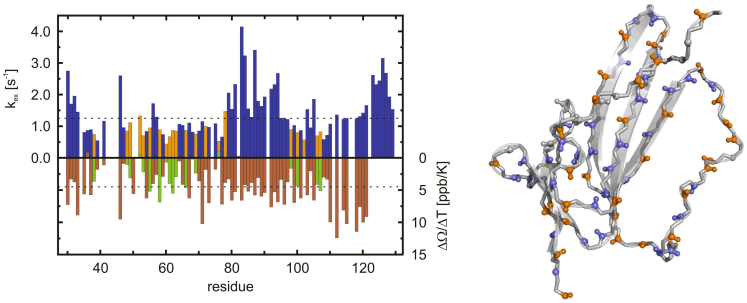

Figure 4.11: Experimental water exchange rates (blue) and temperature coefficients (red) for BMPR-IA$_{ec/sf}$ (Left). Amide protons for which H-bond restraints have been included in the structure calculation are indicated in yellow (water exchange) and green (temperature coefficient). Temperature coefficients have been mapped on the final structure of BMPR-IA$_{ec/sf}$ (Right) where orange indicates temperature coefficients smaller than -4.5 ppb $\cdot$ K^{-1} and blue indicates larger coefficients.

which restricts the accessible exchange rates to $k_{ex} < 10^{-2}$ s^{-1}. Faster exchange rates can be analyzed when the amide magnetization is selectively saturated and its recovery due to exchange with the bulk water is recorded.[304–307] A typical representative of this class of experiments is the Mexico experiment,[304,305] which expands the range of observable hydrogen exchange rates to $k_{ex} = 0.05 - 50$ s^{-1}. Even faster exchange rates have been unaccessible for NMR spectroscopy for a long time, but only recently Kateb *et al.* proposed an interesting experiment to monitor this time regime by exploiting the contribution of the scalar coupling to the relaxation of the ^{15}N-nucleus, that depends on the exchange rate.[308]

In the present study, the Mexico experiment was used to quantify water exchange rates. Signal intensities were recorded at different mixing times (50 ms, 100 ms, 150 ms, 200 ms, and 250 ms) and subsequently fitted to an exponential build-up curve. Water exchange rates could be extracted for most amide protons (84) and exchange rates k_{ex} between 0.44 s^{-1} and 4.14 s^{-1} were observed (see Fig. 4.11). Clearly visible are the diminished water exchange rates for amide protons located in secondary structure elements already found by means of other parameters.

In addition to water exchange rates, temperature coefficients[309] have

been analyzed for a large fraction of the protein, i.e. the dependence of amide proton chemical shifts on the sample temperature was determined. The temperature coefficient is also a classical parameter to obtain information about hydrogen bonding and has frequently been used. In general, amide proton chemical shifts are shifted towards lower frequencies due to chemical exchange with the bulk water magnetization. As chemical exchange is significantly slowed down for amide protons participating in hydrogen bonding these protons are less affected, resulting in more positive temperature coefficients. Even positive temperature coefficient can be observed for highly 'protected' protons. As a rule of thumb, amide protons with a coefficient larger than -4.5 ppb $\cdot$ K^{-1} are assumed to be hydrogen bonded.

Amide proton chemical shifts have been measured between 10°C and 40°C and linear least square fitting resulted in temperature coefficients between -12.4 ppb$\cdot$K^{-1} and 1.0 ppb$\cdot$K^{-1}. Results are shown in Fig. 4.11 and reveal similar trends like the water exchange rates.

It has to be pointed out, that water exchange rates or temperature coefficients are no proof for hydrogen bonds, and can only be regarded as indicators. For example, small water exchange rates may also result if amide protons are deeply buried in the protein core but do not participate in a hydrogen bond[310] and equivalent arguments also apply for temperature coefficients. Moreover, only the *hydrogen bond donor* can be observed, while the *hydrogen bond acceptor* remains 'invisible'. Therefore, defining hydrogen bonds for a protein is always a concerted process with the actual structure calculation (*vide infra*). Hydrogen bonds have only been introduced for amide protons that consistently produced geometries that justified corresponding constraints and, in addition, exhibited temperature coefficients and water exchange rates indicating slow exchange with water. Hydrogen bond geometries were inspected using the procedure of KABSCH and SANDER[311] where the energy of the hydrogen bond is calculated using a simple electrostatic approach via

$$E_{Hbond} = q_1 q_2 (r_{ON}^{-1} + r_{C'H}^{-1} - r_{OH}^{-1} - r_{C'N}^{-1}) f. \tag{4.3}$$

In this equation $q_1 = 0.42e$ and $q_1 = 0.20e$ are the partial charges on C',O and N,H respectively, with e being the unit electron charge. The interatomic distance between atoms A and B is denoted r_{AB} and is given in units of Å. To convert E_{Hbond} into units of kcal $\cdot$ mol^{-1} the factor $f = 332$ is used. For hydrogen bonds showing energies below 1.5 kcal $\cdot$ mol^{-1} and

exhibiting acceptor- and donor-angles of smaller than 30° and 40° respectively, hydrogen bonds restraints were included. Hydrogen bonds have been treated as pseudo-covalent bonds following the approach by Truffault *et al.*[312]

4.4 Tertiary Structure

The central building block for structure determination using NMR techniques is the evaluation of NOESY cross-peak intensities and the subsequent translation into distance restraints. Though much effort has been put into the design of automated tools to circumvent this time-consuming and tedious process,[313,314] these programs are still vulnerable to produce locally distorted structures.[315] While automated assignment programs are well-suited to extract the global fold they perform poorly in the determination of local geometries. Therefore, in cases where the global fold is known (as for example for BMPR-IA$_{ec}$) and local geometry is important, they appear unfeasible. To compare structures in their *apo*- and *holo*-form the local geometry has to be determined as accurate as possible, which requires extra data compared to current automated techniques. Hence, the following 3D-NOESY spectra were recorded and analyzed manually: HNH-NOESY, NNH-NOESY, CNH-NOESY,[316] and HCH-NOESY. For this purpose, observed NOESY cross-peaks have been converted into distance ranges after rescaling of intensities in the 3D-spectra according to corresponding HSQC intensities. Cross-peaks were divided into four classes, strong, medium, weak, and very weak, which resulted in restraints on upper distances of 2.7 Å, 3.2 Å, 4.0 Å, and 5.0 Å, respectively. Lower bounds were also included for very weak or absent sequential H^N-H^N cross-peaks using a minimum distance of 3.2 Å.

As a start it was assumed that the fold of the BMPR-IA receptor ecto domain in its *apo*-form adopts a similar conformation as within the crystal structure of the binary complex with BMP-2.[259,260] This allowed for the design of a model structure which served as initial coordinate file for structure calculations. Starting from this model, sequential H^N_i-H^α_{i-1} and H^N_i-$H^N_{i\pm1}$ NOESY cross-peaks were assigned. Additionally, H^N_i-$H^\alpha_{i'}$ and H^N_i-$H^N_{i'}$ contacts across β-sheets were extracted if the assignment was unambiguous.[7] This led to a new model that was used for the next step.

7 The prime indicates that no sequential information connects the two signals under investigation.

Here H_i^α-$H_{i'}^\alpha$ cross-peaks were evaluated to define the dimensions of the β-sheets. These contacts are very characteristic for *anti*-parallel β-sheets since opposing H^α-atoms are only ≈ 2.2 Å apart and result in very intense cross-peaks. Consequently, absent or reduced signal intensities indicate termination of the secondary structure element. Afterwards, the resulting model structure was refined iteractively by the successive addition of distance restraints derived from HNH-NOESY and HCH-NOESY spectra. *Intra*-residual distance restraints were only added if no unambiguous χ^1-rotamer could be identified. The resulting average structure and the corresponding restraint list was submitted to the program AQUA[317, 318] to check for the completeness and redundancy, leading to further assignments. Refinement was carried out by comparison of experimental and back-calculated HNH-, CNH-, and NNH-NOESY spectra (see Sec. 4.3.3). This process resulted in the adjustment of lower and upper bounds, where necessary.

In total 699 NOE distance restraints were extracted, resulting in approximately nine per structured residue. Thereof, 167 were intra-residual, 249 sequential, 57 medium range, and 182 long range NOEs (cf. Tab. 4.1 A). These numbers are comparably small compared to other reprted NOE-based structures of equivalent sized proteins, because most local NOEs have been replaced with dihedral restraints. Still, the yielded structures are well-defined for most parts (*vide infra*) showing a RMS deviation of 0.78 Å over all structured heavy atoms (Tab. 4.1 B) and only a RMS deviation of 0.32 Å over structured backbone atoms.

From the final ensemble of 20 simulated annealing structures an average structure was calculated ($\langle SA \rangle$) and refined again with the experimental restraints to yield the regularized average structure ($\langle SA \rangle_r$, see Fig. 4.12).[8] This and the structure ensemble was validated with PROCHECK,[320] WHATCHECK,[321] and MOLPROBITY.[319] The results from the MOLPROBITY output are summarized in Tab. B.4. In Fig. 4.13 a Ramachandran map for the regularized average structure is shown. This reveals that around 12% of all residues are not located in the most favoured regions of the Ramachandran plot. However, most of these 'misplaced' residues are located in unstructred parts, i.e. the N- and C-termini and the large binding loop for BMP-2 (F80-R96). Only three resdiues, namely F35, L36, and R103 are located in structured regions exhibiting less frequently popu-

8 The regularized average structure was used for all plots in this thesis if not indicated differently.

Table 4.1: *apo*-BMPR-IA$_{ec/sf}$ solution structure statistics and atomic RMS deviations.[a]

A. Structural statistics		
RMSD from distance restraints[b] (Å)	SA	$\langle SA \rangle_r$
all (699)	0.022 ± 0.002	0.011
intra-residue (167)	0.011 ± 0.004	0.016
inter-residue sequential (249)	0.021 ± 0.003	0.020
medium range (57)	0.039 ± 0.004	0.037
long range (182)	0.025 ± 0.006	0.023
H-bond (44)	0.000 ± 0.000	0.000
RMSD from dihedral restraints (deg)(168)	0.194 ± 0.002	0.162
RMSD from $^3J_{H^N H^\alpha}$-restraints (Hz)(60)	0.889 ± 0.042	0.975
H-bond restraints; averages (Å/deg)[c] (22)	2.18 ± 0.15/ 15.2 ± 6.6	2.18 ± 0.15/ 15.2 ± 6.6
H-bond restraints; min-max (Å/deg)(22)	1.94-2.44/ 5.9-26.6	1.91-2.52/ 2.8-30.8
Deviations from ideal covalent geometry		
Bonds(Å $\times 10^{-3}$)	7.42 ± 0.14	7.27
Angles(deg)	0.80 ± 0.02	0.78
Impropers(deg)	2.72 ± 1.69	1.63
Structure quality indicators[d]		
Ramachandran map regions (%)	87.2/100/0	88/100/0
Steric clashes > 0.4Å per 1000 atoms	0.0	0.0

B. Atomic RMSD (Å)[e]				
	SA vs. $\langle SA \rangle$		SA vs. $\langle SA \rangle_r$	
	Backbone	All	Backbone	All
Structured residues	0.32 ± 0.11	0.78 ± 0.11	0.59 ± 0.12	1.05 ± 0.14
Secondary structure[f]	0.25 ± 0.07	0.46 ± 0.11	0.40 ± 0.08	0.78 ± 0.07
$\langle SA \rangle$ vs. $\langle SA \rangle_r$[g]	0.49	0.81		

[a] Structures are labeled as follows: SA, set of 20 final simulated annealing structures; $\langle SA \rangle$, the mean structure calculated by averaging the coordinates of SA structures after fitting over secondary structure elements; $\langle SA \rangle_r$, the structure obtained by regularising the mean structure under experimental restraints.

[b] Numbers in brackets indicate the number of restraints of each type.

[c] Hydrogen bonds were restrained by treating them as pseudo-covalent bonds.[312] Deviations are expressed as the average distance/average deviation from linearity for restrained hydrogen bonds.

[d] Determined using the program MolProbity.[319] Percentages are for residues in favoured (98%), allowed (99.8%) and disallowed regions of the Ramachandran map.

[e] Based on heavy atoms superimposition.

[f] Defined as residues L36-Y39, T52-T55, H58-E65, T71-M78, R97-C102.

[g] RMS deviation for superimposition over ordered residues.

lated Φ/Ψ-combinations.[9] These residues were again validated carefully by back-calculation of the corresponding NOESY spectra, but revealed no inconsistency with the experimental data.

BMPR-IA$_{ec/sf}$ adopts a fold similar to the three finger toxines[322] typical for type I and type II receptors. However, while in type II receptors, like ActR-II indeed three fingers are formed by three anti-parallel two stranded β-sheets ($\beta_1\beta_2$, $\beta_3\beta_4$, and $\beta_5\beta_6$), in type I receptors actually only two fingers are observed. This holds also true for BMPR-IA$_{ec/sf}$, which forms only two β-sheets due to the lack of a strand corresponding to β-strand 6 in ActR-II (PDB 1BTE; see Fig. 4.12). Hence, the fold of BMPR-IA$_{ec/sf}$ comprises a two stranded β-sheet (β_1 and β_2) and a three stranded β-sheet (β_3, β_4, and β_5).

The secondary structure elements are well established and are stabilized by a network of 22 hydrogen bonds. In addition, five disulfide bridges are formed that significantly increase the rigidity of the molecule, as they connect the loops as well as the N- and C-terminus. Two disulfide bridges are linking strand β_1 and β_3 and strand β_2 and β_4 fixing the orientation between the two β-sheets. Noteworthy, the long C-terminal loop comprising residues L111 to P117 is well-defined, although it does not participate in the formation of the β-sheet. This might be attributed to the hydrophilic character of the residues (L111, P113, L115, and P116) which pack against the hydrophobic residues of the three stranded β-sheet (A61, I63, and L73). The rigidity of the secondary structure elements is also reflected by the very small RMSD over backbone atoms of 0.19 Å $\pm$ 0.07 Å (heavy atoms: 0.46 Å $\pm$ 0.11 Å). Even most loop regions are well-established with a RMSD of 0.32 Å $\pm$ 0.11 Å over all backbone atoms of structured elements.

Though large parts of the protein are highly defined, some loops exhibit a strongly unstructured nature. In particular, the loop interconnecting strand β_4 and β_5 is highly flexible. Interestingly, the helix, present in the crystal structure (PDB 1REW)[260] seems to be absent in the solution structure (*vide infra*).

9 For a protein of this length, about 1-2 residues are expected to be located outside of the most favoured region of the Ramachandran map, i.e. 2% of all residues are expected to lie outside the inner cyan contour of the Ramachandran map shown in Fig. 4.13.

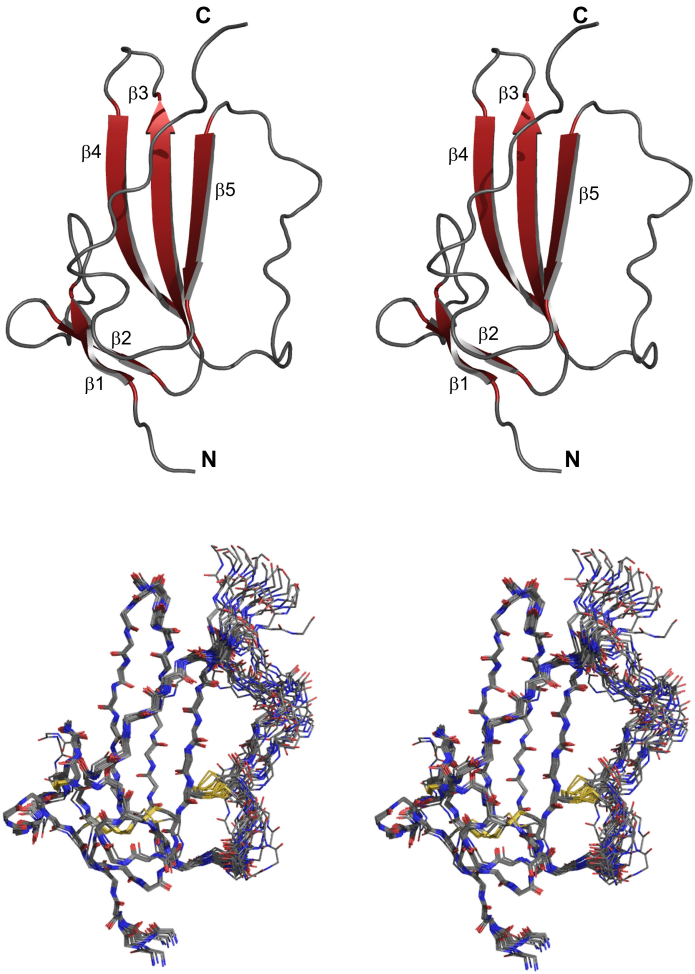

Figure 4.12: Stereoview of the final solution structure of BMPR-IA$_{ec/sf}$. Top: Cartoon representation of the regularized average structure ($\langle SA \rangle_r$), secondary structure elements are highlighted in red. Bottom: Ensemble of the 20 lowest energy structures after structural refinement. Structures are superimposed over secondary structure elements.

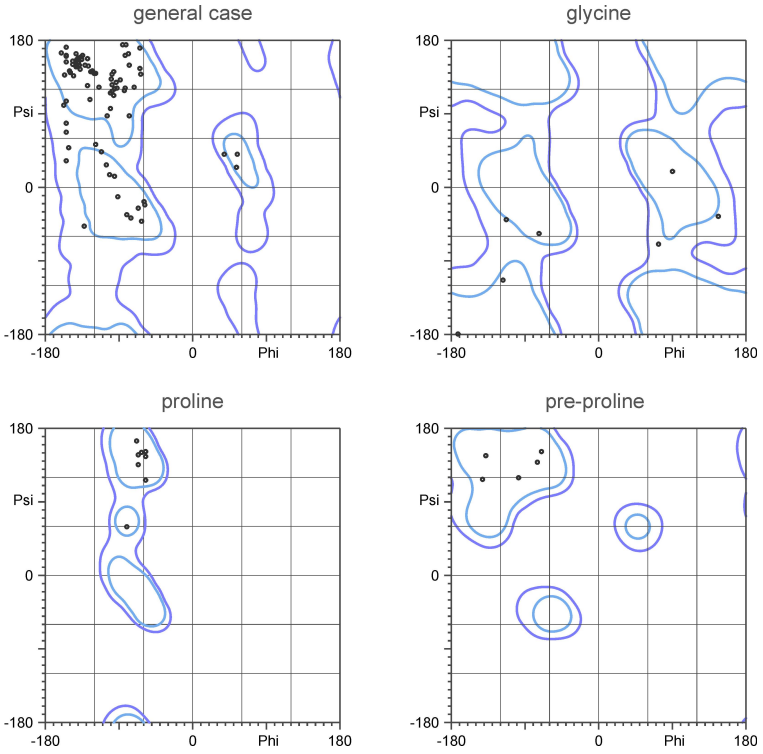

FIGURE 4.13: Ramachandran map of the regularized average structure ($\langle SA \rangle_r$) of BMPR-IA$_{ec/sf}$ taken from the software MOLPROBITY. Most residues are located in favoured regions of the Ramachandran plot (cyan, 98% contour $\hat{=}\ 2\sigma$) whereas outlieres are still joining the allowed regions (purple, 99.8% contour $\hat{=}\ 3\sigma$).

4.5 Residual Dipolar Couplings

In recent years, residual dipolar couplings have become a routinely measured parameter for biomacromolecules, and offer a wealth of structural information. For example, they can be used for structural refinement of proteins[105] and nucleic acids[323] as well as smaller molecules like peptides,[114] as described in Chapter 5. Moreover, structural information about inherently unfolded proteins can be gained. An even more interesting application is the elucidation of dynamical properties of molecules, as RDCs are uniquely suited to sample a very broad range of timescales (Fig. 2.6). This has been demonstrated for proteins as well as for RNA fragments. In the present study, however, RDCs have been used to validate the final structure obtained from structure calculations using predominantly NOE distance restraints. In contrast to *statistical* parameters implemented in programs such as ProCheck,[320] WhatCheck,[321] and MolProbity,[319] RDCs represent an *independent*, *experimental* parameter.

RDCs have been measured for the neighboring spins ^{1}H-^{15}N and ^{13}C'-$^{13}C^{\alpha}$ in a poly-(acrylamide) gel strained by a Shigemi plunger upon swelling (see App. B.1).[56] While ^{1}H-^{15}N-RDCs have been obtained from *IPAP*-^{1}H-^{15}N-HSQC spectra[324,325] ^{13}C'-$^{13}C^{\alpha}$-couplings were extracted from a simple HNCO spectrum without $^{13}C^{\alpha}$-decoupling in the indirect dimension.[106,326] Altogether 151 RDCs (72 ^{1}H-^{15}N, 79 ^{13}C'-$^{13}C^{\alpha}$) could be determined in the range of -16.9 Hz to 17.7 Hz and -4.4 Hz to 4.0 Hz for ^{1}H-^{15}N and ^{13}C'-$^{13}C^{\alpha}$ spin pairs, respectively. Renormalization of ^{13}C'-$^{13}C^{\alpha}$-RDCs to ^{1}H-^{15}N-RDCs resulted in the histogram depicted in Fig. 4.14, which indicates a fairly strong rhombicity.

The extraction of the alignment tensor by singular value decomposition using the software Pales[21] resulted in poor correlations between the experimental and back-calculated RDCs ($R = 0.63$ and $Q = 0.75$).[10] Subsets of ^{1}H-^{15}N- and ^{13}C'-$^{13}C^{\alpha}$-RDCs alone led to even worse correlations (^{1}H-^{15}N: $R = 0.60$ and $Q = 0.73$; ^{13}C'-$^{13}C^{\alpha}$: $R = 0.41$ and $Q = 0.91$). However, when loop regions and terminal amino acids of the N- and C-terminus were excluded from fitting the correlation factor improved to $R = 0.92$ and the quality factor to $Q = 0.39$. This clearly proves the correctness of secondary structure elements of the structure determined for BMPR-

10 The quality factor Q is defined as $Q = \mathrm{RMS}(D_{exp} - D_{back})/\mathrm{RMS}(D_{exp})$ according to Cornilesu *et al.*[327]

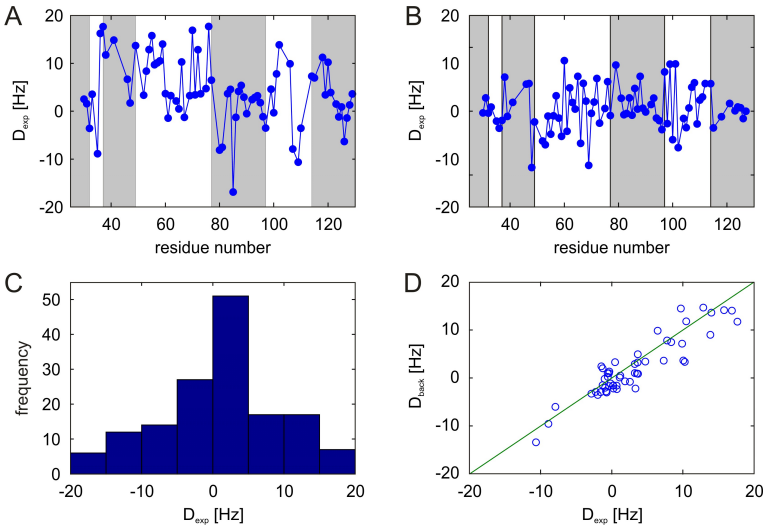

FIGURE 4.14: Resdiual dipolar couplings for BMPR-IA$_{ec/sf}$. A, B: RDCs plotted by sequence position (A: D_{NH}-couplings, B: $D_{C'C^\alpha}$-couplings), where residues shaded in grey are located in unstructured regions. C: Histogram of the ensemble of normalized D_{NH}- and $D_{C'C^\alpha}$-couplings. The distribution of the couplings indicates a significant rhombicity, as the most abundant coupling is located in the center of the histogram.[328] D: Experimental versus back-calculated RDCs (not normalized). RDCs for unstructured regions have been omitted.

IA$_{ec/sf}$ as both indicators resemble values expected for structures based solely on NOE- and dihedral angle restraints.[106] Moreover, as already indicated by the histogram, values of $A_{\hat{x}} = 1.72 \cdot 10^{-4}$, $A_{\hat{y}} = 6.82 \cdot 10^{-4}$, and $A_{\hat{z}} = -8.54 \cdot 10^{-4}$ have been obtained for the alignment tensor, resulting in a rhombicity of 0.4 (cf. Eq. 2.55 and Eq. 2.57), confirming the initial assumption of a significant rhombic component.

4.6 Titration Studies

4.6.1 Titration with TFE

As apparent from the solution structure (Fig. 4.12) and previous studies from Hatta *et al.*,[261] the α_1-helix of BMPR-IA$_{ec/sf}$ present in the crystal structure is missing in the unbound form. To further investigate this finding, titrations with increasing concentrations of trifluorethanol (TFE) were conducted. The cosolvent TFE is known to induce helix formation on peptides and proteins with a corresponding helical propensity.[329]

The concentration of TFE was increased in steps of 2.5% v/v and average chemical shift changes were calculated using the empirical formula 4.4 which compensates for the reduced spectral width in the ^{1}H-dimension compared to the ^{15}N-dimension.

$$\Delta\delta_{av} = \sqrt{\frac{\Delta\delta_{H^N}^2 + (\Delta\delta_N/5)^2}{2}}. \tag{4.4}$$

Here, δ_{H^N} and δ_N indicate the amide proton and the amide nitrogen chemical shift, respectively. The titration revealed significant shifts in the region of the former α_1-helix of up to 130 ppb upon addition of 10% v/v TFE (cf. Fig. 4.15). Residues C87 and K88 are most strongly affected, indicating major conformational changes. But also residues S83, F85, and D89 show significant shifts, although their reorientation seems much less pronounced. Unfortunately, amino acid Q86, as one of the binding hot spots in the binary complex with BMP-2, could not be observed due to signal overlap. Not surprisingly, some residues in other regions of the protein are also strongly affected, but indicating only their solvent exposed nature. It can be excluded that chemical shift changes in the former α_1-helix are merely based on solvent effects, as amino acids neighbouring these residues are also solvent exposed but are much less affected, hence, indicating a distinct conformational change in this region.

4.6.2 Titration with ActR-IIb and cyclo-(FPRFPa)

Before 2006, when Allendorph *et al.* released the crystal structure of the ternary complex BMP-2:BMPR-IA$_{ec}$:ActR-II,[262] it remained unclear if the receptor ecto domains of the type I receptor and the type II receptor interact *before* the ligand is bound. To test this hypothesis, BMPR-IA$_{ec/sf}$

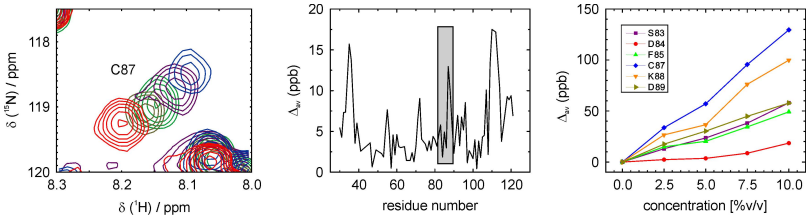

FIGURE 4.15: Titration of BMPR-IA$_{ec/sf}$ with trifluorethanol (TFE). LEFT: Detail of the ^{1}H-^{15}N-HSQC spectra recorded to monitor chemical shift changes. MIDDLE: Sequence plot of average chemical shift changes. Shifts have been normalized to 1.0% v/v TFE. RIGHT: Chemical shift changes of residues located in the 'α_1-helix' of BMPR-IA$_{ec/sf}$ upon addition of TFE.

was titrated with increasing amounts of ActR-IIB (0.5, 1.0, and 2.0 equivalents), but no significant chemical shift changes were observed in the ^{1}H-^{15}N-HSQC spectra. Hence, it must be concluded that the two receptors do not interact with each other supporting the results of ALLENDORPH *et al.* Moreover, BMPR-IA$_{ec/sf}$ was also titrated with the cyclic peptide *cyclo*-(FPRFPa). This peptide was designed by AXEL MEYER to mimic parts of the binding interface of BMP-2, and was intended to bind to BMPR-IA$_{ec}$ preventing an interaction with the natural counterpart BMP-2. However, also this titration did not reveal any chemical shift perturbations within the spectra.

4.7 Dynamical Investigations

As evident from the BMPR-IA$_{ec/sf}$ structure ensemble, substantial regions of the protein are poorly defined (Fig. 4.12). Especially loop $\beta_4\beta_5$ appears to be largely unstructured, showing the largest RMSD over C$^{\alpha}$-atoms within the ensemble, apart from the C- and N-termini (*vide infra*). To investigate the origin of this observation BMPR-IA$_{ec/sf}$ was subjected to dynamical studies. Interestingly, all backbone amide resonances of loop $\beta_4\beta_5$ within the ^{1}H-^{15}N-HSQC spectrum do not reveal a significant line broadening. This indicates that either no or negligible conformational exchange is present on slow (μs-ms) timescales (Fig. 2.6) or, rather likely, that relaxation is exclusively (or predominatly) governed by motions that occur on the ps-ns timescale leading to a decrease of R_2 and therefore to

sharp lines. This phenomenon is commonly observed for the C-termini of proteins where resonances show particularly narrow and intense resonances, and is also observed for BMPR-IA$_{ec/sf}$. Hence, the investigation of the dynamical properties of BMPR-IA$_{ec/sf}$ was restricted to a model-free analysis to monitor motions *faster* than the overall correlation time.

Consequently, spectra to quantify, T_1-, T_2-relaxation and the heteronuclear ^{15}N-{^{1}H} NOE of the ^{15}N-nucleus were acquired at two different magnetic field strengths (14.1 T and 17.6 T). Unfortunately, two different samples had to be used for the two data sets that did not stem from the same batch of protein preparation. Although the temperature and all other relevant experimental parameters were identical at both field strength, the two data sets could not be fitted simultaneously to the corresponding equations, but had to be analyzed separately. This might be attributed to slight changes in the buffer conditions, such as the pH. However, the extracted dynamical parameters were similar for both samples, and therefore only data from measurements at 600 MHz (14.1 T) are presented in the following sections for brevity.

4.7.1 Diffusion and Hydrodynamic Calculations

Initially, the overall, rotational diffusion tensor was estimated from the R_2/R_1 ratio. Assuming the simplest model in the model-free approach (model 1), this ratio becomes independent of the squared order parameter, as all contributions apart from the spectral density function cancel out and hence allow the determination of the rotational correlation time.[330–333] Obviously, only selected residues fulfilling this prerequisite may be used, and a cutoff larger than 0.8 for the heteronuclear NOE was used to select appropriate residues. The subsequent fitting of the tensor parameters is readily achieved using programs such as R2R1_Diffusion or Quadric_Diffusion.[334]

The analysis revealed that the molecule is best described by an axially symmetric diffusion tensor as can be seen from Tab. 4.2. An F-test, comparing the fit for the axially symmetric diffusion tensor and the isotropic diffusion tensor reveals that the use of the axially symmetric diffusion model significantly improves the fit results ($F = 10.15$). In contrast, assuming a fully anisotropic diffusion tensor appears not to be statistically relevant ($F = 1.39$). The final results from diffusion tensor optimization lead to an overall correlation time of $\tau_c = 7.97$ ns which is comparable with the results from hydrodynamic calculations. However, the ratio $D_{\parallel}/D_{\perp}$

TABLE 4.2: Diffusion tensor analysis for BMPR-IA$_{ec/sf}$.

Tensor[a]	τ_c [ns][b]	D_{ratio}[c]	F
isotropic	8.06 ± 0.01	–	–
axial-sym.[d]	7.80 ± 0.02	2.93 ± 0.01	10.15
anisotropic[e]	7.17 ± 0.01	2.51 ± 0.09	1.39
optimized-MF[f]	7.97 ± 0.06	2.12 ± 0.12	–

[a] Anisotropy of the diffusion tensor.
[b] Rotational correlation time obtained from $\tau_c = 1/(6D_{iso})$.
[c] Ratio of the components of the diffusion tensor.
[d] $D_{ratio} = D_{\parallel}/D_{\perp}$.
[e] $D_{ratio} = 2D_{zz}/(D_{xx} + D_{yy})$.
[f] Optimized model-free results.

changed dramatically, probably due to the large amplitude of the motion of loop $\beta_4\beta_5$ as well as the long C- and N-termini. These alter the shape of the molecule and hence affect $D_{\parallel}/D_{\perp}$. This hypothesis is supported by measurements of the *translational* diffusion constant D_t which is related to the *rotational* diffusion constant D_r via[97]

$$D_r = \frac{27\pi^2\eta_w^2 D_t^3}{k_B^2 T^2}, \tag{4.5}$$

if a rigid spherical molecule is assumed. Definitions in this equation are equivalent to Eq. 2.65. From an experimental, translational diffusion constant of $D_t = 1.474 \cdot 10^{10}$ m^{2}s^{-1} the correlation time τ_c was estimated to 4.22 ns which compares rather well with experimental values from other proteins of equivalent size like ubiquitin (4.1 ns).[335] However, this value deviates strongly from the results obtained by the model-free analysis, indicating a strong influence of the flexible parts on overall molecular tumbling. As the model-free approach is designed to analyse fast motions relative to a fixed conformation with fixed geometry, the analysis of BMPR-IA$_{ec/sf}$ surely represents a limiting case and results should be handled with care.

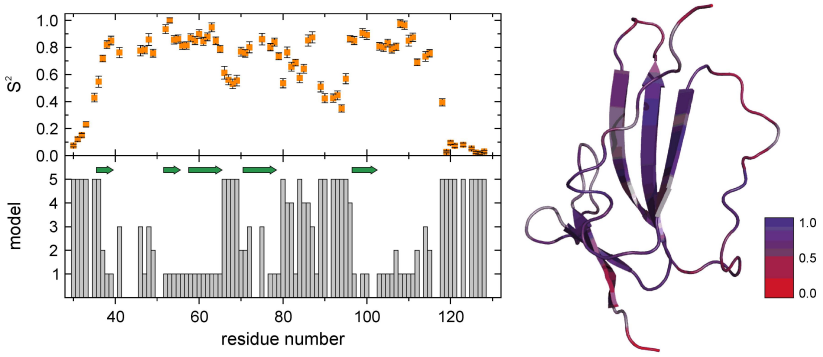

Figure 4.16: Left, upper panel: Sequence plot of the squared order parameter S^2 for BMPR-IA$_{ec/sf}$. Left, lower panel: Model selection for model-free analysis of experimental relaxation data. Right: S^2 mapped onto the solution structure of BMPR-IA$_{ec/sf}$ according to the colour bar. Grey residues could not be analyzed.

4.7.2 ps-ns Dynamics

Squared order parameters of 77 residues could be extracted for BMPR-IA$_{ec/sf}$ using the model-free approach. These are plotted in the upper panel of Fig. 4.16 while in the lower panel the corresponding model used for analysis is indicated. Motions in the secondary structure elements of BMPR-IA$_{ec/sf}$ are largely restricted with an average squared order parameter of $\langle S^2 \rangle = 0.84 \pm 0.02$. This corresponds to a semi-cone angle θ of $19.5^\circ \pm 1.1^\circ$ if the 'wobbing-in-a-cone' model is assumed (Sec. 2.3.6). Furthermore, almost all residues within secondary structure elements could be fitted with model 1 apart from strand β_4 where a few residues exhibit an exchange contribution (model 3). Residues of higher flexibility on the ps-ns timescale are located in loop regions or at the C- or N-terminal end of the protein chain.

The region with the smallest order parameters apart from the C- and N-terminus is located between strand β_4 and β_5 where nearly all residues are assigned to model 5. In addition, the small loop $\beta_3\beta_4$ also shows a significantly increased flexibility, though less pronounced as for loop $\beta_4\beta_5$. Model 5 indicates two distinct motional modes – one on the picosecond timescale corresponding to fast librations of the H-N bond vector and a second mode

on the nanosecond timescale corresponding to dihedral transitions. Hence, both loops feature a complex motional behaviour.

Fast motions within the two loops are rather restricted and adopt similar values as the the secondary structure elements, with squared order parameters of $\langle S^2 \rangle = 0.76 \pm 0.01$ and $\langle S^2 \rangle = 0.73 \pm 0.02$ for loop $\beta_3\beta_4$ and loop $\beta_4\beta_5$, respectively. Consequently, their semi-cone angles θ are also similar ($24.9° \pm 1.1°$ and $26.7° \pm 1.0°$) if a 'two-site-jump' model is assumed. However, inspecting the contribution of the slower motion for these loops to the overall dynamics reveals a significant increase in the semi-cone angles ϕ for amino acid D89-Q94 but only a moderate increase for D66-G69. While in loop $\beta_4\beta_5$ semi-cone angles of up to 54.4° are observed, slower motions in loop $\beta_3\beta_4$ are much more restricted, with a maximum angle of 37.3°. The elevated dynamics of the two loops is accompanied by an increase of the water exchange rates (see Fig. 4.11).

4.8 Discussion

4.8.1 Comparison of Free and Bound BMPR-IA$_{ec}$

The solution structure of the free form of BMPR-IA$_{ec/sf}$ is highly similar to the structure of BMPR-IA$_{ec}$ observed in the crystal structure of the binary complex with BMP-2 (PDB 1REW).[260] This is reflected in the comparably small RMSD of 1.35 Å when all secondary structure elements and loop regions are considered apart from loop $\beta_4\beta_5$. Of the secondary structure elements, only strand β_1 appears shorter than in the complex. Differences are mainly located in loop regions in which loop $\beta_1\beta_2$ undergoes clear but not strong conformational changes. The highest RMS deviations for C^α-atoms of the free and bound forms of BMPR-IA$_{ec}$ are 2.4 Å to 3.9 Å for residues S41, G42, and H43 (cf. Fig. 4.17). For these residues, however, only few NOE contacts could be extracted as C40, G42, H43, and C44 could not be assigned, presumably due conformational exchange. Absence of these signals due to water exchange is also possible, but still unlikely as S41 exhibits only modest water exchange rates (Fig. 4.11). Similar arguments apply to residue N50 and N51 as well, which are also located in loop $\beta_1\beta_2$ and reveal broad or non-observable resonances in the ^{1}H-^{15}N-HSQC spectrum. Moreover, residues in this loop, if observable and analyzable, are predominantly fitted with model 3 in the model-free approach, which indicates an exchange contribution to the relaxation rates. The assumption of conformational exchange is supported further by the observation that

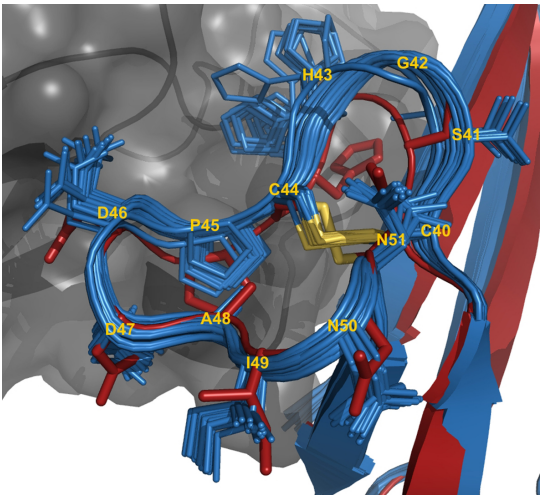

Figure 4.17: Comparison of loop $\beta_1\beta_2$ in the bound (red) and unbound (blue) form of BMPR-IA$_{ec/sf}$. Only small amplitude rearrangements occur in the transition from the unbound to the bound form.

the complexed loop $\beta_1\beta_2$ makes contact to the pre-helical loop of BMP-2. Hence, the changes in the structure probably represent a small induced fit to adapt for ligand binding. Previous reports suggest that loop $\beta_1\beta_2$ is relevant in determining ligand-specifity towards different BMP ligands.[210] Nickel *et al.* have shown, that GDF-5 (see Sec. 4.1.1) binds very specifically to the BMP receptor IB, revealing a 15-fold higher affinity compared to BMPR-IA$_{ec}$. Sequence analysis between BMPR-IA$_{ec}$ and BMPR-IB reveals that multiple amino acids differ in loop $\beta_1\beta_2$, e.g. S41 and G42 are substituted by histidines. In fact, exchanging these residues in BMPR-IA$_{ec}$ indeed modifies the binding properties for GDF-5, indicating the importance of this loop in ligand recognition. Interestingly, C40 and C44 are linked by a disulfide bridge, reducing potential conformational flexibility significantly. However, no mutations studies have so far investigated the influence of this disulfide bridge on binding activity.

As pointed out above, large parts of the C-terminus (L111-P117) are well-defined, though they adopt a different conformation in the solution structure compared to the crystal. Differences in C$^{\alpha}$-atom positions range

between 1.5 Å (Q112) and 3.0 Å (P116) but similar differences are also observed between the binary complex (PDB 1REW) and the tertiary complex (PDB 2GOO). A detailed investigation of the crystal structure reveals, that the loop maintains several crystal-lattice interactions suggesting that crystalisation artifacts cause the deviations between the two structures.

Loop $\beta_3\beta_4$, which lacks well-defined electron density in the crystal structure, appears rather defined in the solution structure of BMPR-IA$_{ec/sf}$. This view however has to be revised if the dynamical data is considered. All four residues at the tip of this loop (D66-G69) were fitted with model 5 and exhibit decreased order parameters associated with enlarged semi-cone angles for the slow as well as the fast component of the motion. Hence, the solution structure of BMPR-IA$_{ec/sf}$ seems to be over-determined in the region but obviously still represents the correct, time-averaged structure.

The most apparent difference between the crystal structure of BMPR-IA$_{ec}$ in the complex with BMP-2 and the unbound form of BMPR-IA$_{ec/sf}$ is the absence of the α_1-helix (cf. Fig. 4.18). The $\beta_4\beta_5$-loop exhibits the strongest deviations between the bound and the unbound form with a RMSD of 4.1 Å and a maximum deviation of 10.3 Å between F85-C$^{\alpha}$ in both structures. This can also be seen in Fig. 4.19 were the RMSD within the ensemble and compared to the crystal structure in the binary complex is plotted. This data compares rather well with results from the model-free analysis, which also indicates loop $\beta_4\beta_5$ to be highly flexible. The two turn helix (G82-D89) is located in the $\beta_4\beta_5$-loop of BMPR-IA$_{ec}$ in the crystal structure right at the binding interface with BMP-2 and carries two of the major binding determinants, namely F85 and Q86. While in the binary (PDB 1REW) and in the ternary complex (PDB 2GOO) the helix exhibits an identical shape with respect to backbone and sidechain orientation, this helix is completely missing in the NMR structure of the unbound receptor. Though only few NOE contacts are observable for this region, they unambiguously proof that the helix is not formed in the solution structure (*vide infra*). The residue revealing the smallest RMSD and largest order parameter in this loop is C87 which is linked by a disulfide bridge to strand β_5. Although this is located at the C-terminal end of the helix in the complex, this does not lead to a stabilization of the helix in solution.

Furthermore, a ^{1}H-^{15}N-HSQC spectrum of BMPR-IA$_{ec/sf}$ in complex with BMP-2 could be obtained allowing a direct comparison of the two structures (Fig. 4.20). Due to the very low concentration of the sample (81 μM) and the large size of the complex for NMR standards ($\approx$ 55.1 kDa) the spectral quality is very poor and no assignment could be achieved. In

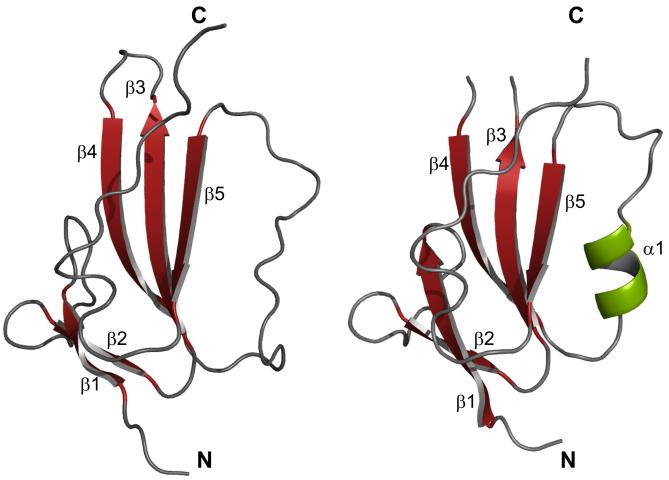

Figure 4.18: Comparison of solution structure (Left) crystal structure (Right) of BMPR-IA$_{ec/sf}$. The most apparent difference is the missing helix α_1 in loop $\beta_4\beta_5$ but minor changes can also be observed for loop $\beta_1\beta_2$.

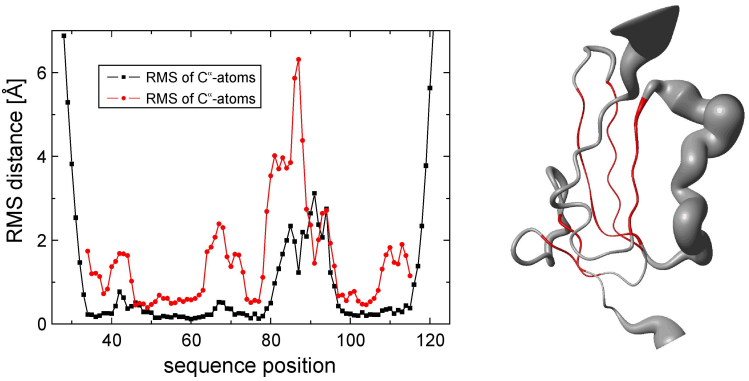

FIGURE 4.19: RMSD of C^{α}-atoms in the solution structure (PDB 1REW) of BMPR-IA_{ec}. LEFT: In black the RMSD of C^{α}-atoms within the ensemble is shown. In red the solution structure of BMPR-$IA_{ec/sf}$ is compared to the structure of BMPR-IA_{ec} within the binary complex to BMP-2 (PDB 1REW) by fitting successively fragments of five residues to each other. RIGHT: 'Sausage' plot of BMPR-$IA_{ec/sf}$, where the diameter represents the RMSD within the ensemble.

addition, the complex required strongly deviating buffer conditions from those used for the unbound form of BMPR-IA_{ec} and therefore chemical shift differences must be interpreted with caution. Still, at first glance, both spectra (bound and unbound BMPR-IA_{ec}) appear very similar, reflecting the equivalent fold observed for both structures. However, closer inspection reveals *relative* chemical shift differences for most peak positions. This supports the observation of large conformational rearrangements upon ligand binding, but might also be attributed to the deviating buffer conditions.

4.8.2 α_1-Helix Exists in a Nascent Form

A central question raised from the observations was whether the α_1-helix in the $\beta_4\beta_5$-loop, though not persistent in solution in the ligand-unbound state, still exists in a nascent form. To answer this question the carbon chemical shifts and ${}^{3}J_{H^N H^{\alpha}}$-couplings for the corresponding residues (G82-D89, shaded grey in Fig. 4.21) were inspected. While sequence plots for C^{α}- and C^{β}-chemical shifts indicate a random-coil structure, H^{α}-chemical

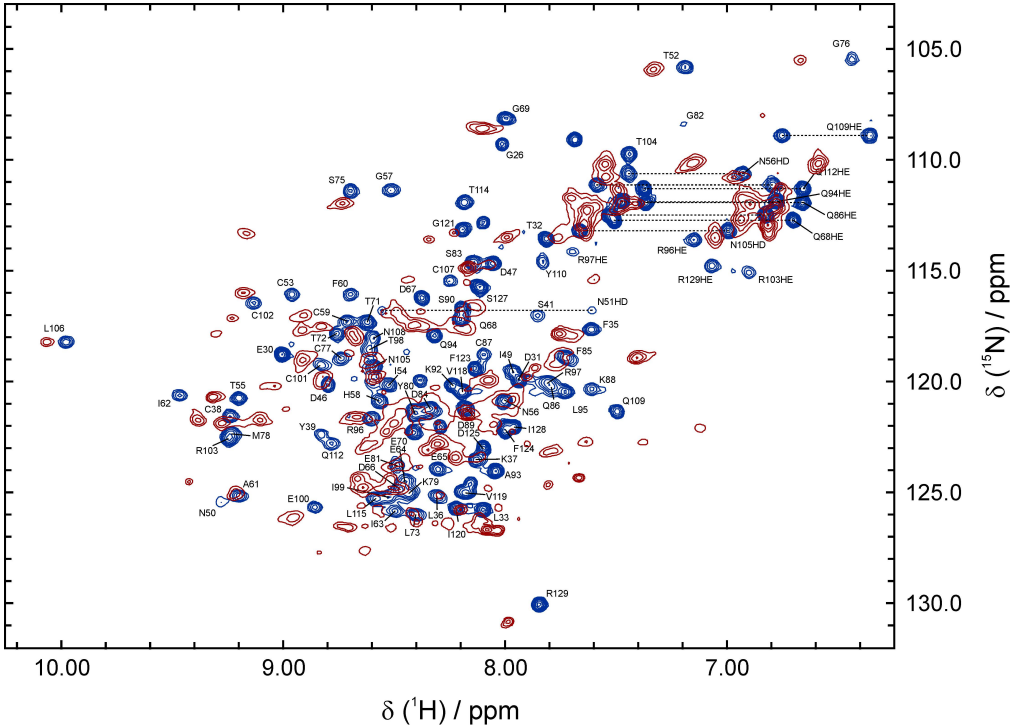

FIGURE 4.20: ^{1}H-^{15}N-HSQC spectrum of BMPR-IA$_{ec/sf}$ in complex with BMP-2 (red) recorded at a temperature of 25° and a proton frequency of 900 MHz. For comparison the annotated ^{1}H-^{15}N-HSQC spectrum of BMPR-IA$_{ec/sf}$ in the unbound form is also shown (blue). For convenience the ^{1}H-^{15}N-HSQC spectrum of the bound form is aligned with the ^{1}H-^{15}N-HSQC spectrum of the uncomplexed form of BMPR-IA$_{ec/sf}$ sin the nitrogen dimension at residue L106.

shifts display a bias from values indicative for random coil structures towards a helical secondary structure. The H^{α}-chemical shifts in this region deviate on average by -0.31 ppm$\pm$0.15 ppm from values typical for random coil with a deviation larger than $\pm$0.1 ppm being regarded as significant. Moreover, the $^{3}J_{H^{N}H^{\alpha}}$-coupling constants are also systematically lower than values expected for random coil structures. This hypothesis has been validated by the titration study with TFE described in Sec. 4.6.1. As all residues located in the region of the α_1-helix exhibit significant chemical shift changes upon titration with TFE it must be concluded that though the helix is neither partially present in the unbound form of BMPR-$IA_{ec/sf}$ nor presents a small population in the NMR structure ensemble. Still, a helical propensity is observable, that is easily stabilized to a helix upon titration with TFE, suggesting that it exists in a nascent form.

4.8.3 Rigid Scaffold for BMPR-IA_{ec} Activation

Recent studies by KOTZSCH *et al.*[336] on the interaction of BMPR-IA_{ec} with BMP-2 showed that two mutations (Y39D and T55I) outside the main interaction surface lead to complete unfolding of BMPR-IA_{ec} and consequently to loss of activity. This finding seems somewhat surprising, especially for Y39, since it is part of the solvent accessible surface and is not located in the hydrophobic core where an equivalent result could be explained more easily. Y39 is located in a cleft surrounded by N51 and T52 of strand β_2 and L106 and Q109 in the 3_{10}-turn in the C-terminal loop. It is possible that N51 and Q109 form stable π-π-stacking interactions with Y39 which could stabilize the adjacent β-strands and loops during folding. In the primary sequence Y39 is surrounded by two cysteines which are both part of the disulfide bridge network of the folded protein. C38 forms a disulfide bridge to C59, thereby linking strand β_1 and strand β_3, while C40 is connected to C44 in the folded protein. Disulfide bridges are known to form late during folding,[337] hence, Y39 might act as hydrophobic seed linking residues N51 and Q109 via a π-π-stacking sandwich enabling the establishment of the correct disulfide bond network. Consequently, a mutation from tyrosine to aspartate leads to an absence of the π-π-stacking interaction and folding cannot progress. This hypothesis is supported on the one hand by the observation that the aromatic residue Y39 is oriented in a favourable position to form π-π-stacking interactions with N51 and Q109. Its orientation within the ensemble is well-defined and is fixed by a multitude of long-range NOEs, showing contacts to all aforementioned residues,

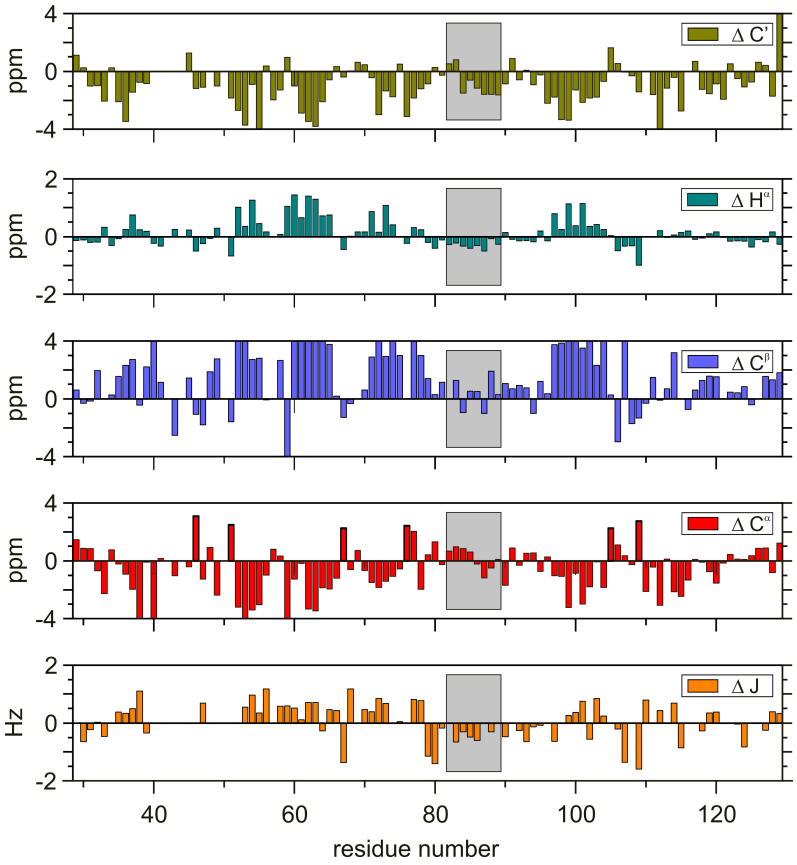

Figure 4.21: Sequence plot of secondary structure indicators for BMPR-IA$_{ec/sf}$. Shown are the chemical shift differences between experimental and random coil chemical shifts for C'-, H^{α}-, C^{β}-, and C^{α}-atoms. In addition, the deviation of $^{3}J_{H^{N}H^{\alpha}}$-couplings from the random coil value (6 Hz) is given.

e.g., Q109H$^{\alpha}$ → Y39H$^{\delta}$, T52H$^{\gamma}$ → Y39H$^{\delta}$, or L106H$^{\mathrm{N}}$ → Y39H$^{\mathrm{N}}$. This hypothesis is supported further by the finding that hydrophobic residues such as phenylalanine, leucine, valine as well as polar residues with long hydrophobic sidechains like lysine (as in BMPR-IB) are tolerated. Though no direct NOE cross-peaks between the aromatic protons of Y39 and the sidechain amide protons of N51 and Q109 could be observed due to signal overlap, π-π-stacking can still be observed indirectly, at least for Q109, by the influence of the aromatic ring of Y39 on its chemical shifts. As apparent from Fig. 4.7, resonances for the sidechain amide group of Q109 are significantly shifted *upfield* in both, the proton dimension and the nitrogen dimension compared to random coil values tabulated in the BMRB database[338] ($\Delta\delta_N = -2.0$ ppm and $\Delta\delta_{H^N} = -0.57$ ppm). Even more evident is the effect for the H$^{\gamma}$-protons of Q109; they are shifted by 1.3 ppm on average to higher fields. An upfield shift is only expected if the corresponding atom is located *above/below* the ring plane of the aromatic moiety whereas a position *beside* the aromatic ring would lead to a downfield shift. This results from the (de)-shielding effect of the aromatic π-electron system, which causes an anisotropic magnetic susceptibility with the shape of a double cone. For N51 the opposite effect is observed, a downfield shift for the amide group. This does not necessarily indicate that the complete moiety is oriented beside the aromatic ring. It is quite possible that only parts of the amide group, i.e. the carbonyl group are located above the ring plane while the nitrogen with the two attached protons protrude out from the double cone. However, chemical shifts of the sidechain amide group of N51 also argue for participation in a hydrogen bond, which would also be expected to shift the resonances downfield. This might overcompensate the upfield shift evoked by deshielding by means of the aromatic residue.

The other mutation causing unfolding of the complete receptor ecto domain is T55I. T55 is located at the C-terminal end of strand β_2 and forms a hydrogen bond with the carbonyl group of M78 via its sidechain hydroxyl group. In addition, M78 forms a second hydrogen bond with its carbonyl group to the backbone amide proton of H58 and thereby stabilizes the C-terminal end of strand β_4 as well as the tight turn between strand β_2 and β_3. Like Y39, the close proximity of T55 to the disulfide bridge network might explain the strong impact upon mutation into a leucine residue. Mutational studies of T55 reveal a tolerance only for isosteric substitutions, whereas the disruption of the hydrogen bond network appears not to be relevant (cf. Tab. 4.3). Not surprisingly, only residues as bulky as isoleucine lead to a complete loss of activity whereas substitution by isosteric valine

Table 4.3: Binding constants for the interaction of BMPR-IA$_{ec}$ T55 variants and BMP-2.

Receptor protein[a]	k_{on} [$10^5 M^{-1}s^{-1}$]	k_{off} [$10^{-3}s^{-1}$]	K_D [nM]
wild type[b]	3.3	0.5	1.5
T55A[b]	3.3	4.6	14.0
T55S[b]	3.6	1.2	3.2
T55V[b]	2.6	1.1	4.3
T55I[c]	0.028	7.2	2570

[a] Receptor variant ecto domains (except the T55I variant) were immobilized on the biosensor surface and perfused with dimeric BMP-2. The BMPR-IA$_{ec}$ T55I variant was measured with BMP-2 immobilized on the biosensor surface because kinetic rate constants could not be obtained with the reverse setup.

[b] The dissociation binding constant K_D was derived using $K_D = k_{off}/k_{on}$.

[c] The dissociation binding constant K_D was obtained from a setup with the ligand BMP-2 immobilized on the biosensor surface. This setup yields binding affinities for the so-called 1:1 interaction, which does not include avidity effects of the dimeric BMP-2.

or serine do not alter the binding constant K_D significantly. However, substitution by alanine also shows a remarkable effect leading to a 10-fold drop of affinity due to an increased dissociation rate constant, k_{off}. This supports the hypothesis that T55 takes a key role for the retention of the BMPR-IA$_{ec}$ fold. Obviously, despite the flexibility in the solution structure of BMPR-IA$_{ec}$, a rigid scaffold in a core region is required to maintain the BMPR-IA$_{ec}$ fold.

4.9 Conclusion

In this chapter the high-resolution structure of the receptor ecto domain of the human BMP receptor IA was determined and its dynamical properties were presented. Although numerous structures of BMPR-IA$_{ec}$ have been determined in the form bound to its natural counterpart BMP-2,[259, 260] or even with the additional type II receptor,[262] no structural data on the free, unbound form of BMPR-IA$_{ec}$ has been available so far. Comparing BMPR-IA$_{ec}$ in its *apo*- to its *holo*-form reveals that the five β-strands characteristic for the three finger toxin like fold are rigid and well-conserved,

partially due to the network of five disulfide bridges. Major conformational differences are located in loop $\beta_1\beta_2$ as well as loop $\beta_4\beta_5$ and indicate substantial conformational rearrangements in the sense of a disorder-to-order transition, especially for loop $\beta_4\beta_5$. These large scale conformational rearrangements with retention of the principal fold also manifest in the ^{1}H-^{15}N-HSQC spectrum of BMPR-IA$_{ec}$ in complex with BMP-2 compared to unbound BMPR-IA$_{ec}$, where most resonances experience a significant shift, though they are not fully displaced. Interestingly, two of the main binding determinants for the interaction with BMP-2 are located in this loop, namely F85 and Q86, which are part of a region that transforms into a helix (α_1) upon ligand binding. Since the interactions with BMP-2 can only be established when the helix is fully formed, substantial parts of the binding free energy are obviously generated by an induced fit of loop $\beta_4\beta_5$. In contrast, the structurally related type II receptors, like ActR-IIB, ActR-II or BMPR-II indeed undergo much less pronounced conformational changes. Here the A-loop,[11] which corresponds to loop $\beta_4\beta_5$ in BMPR-IA$_{ec}$, also forms a helix-like structure upon ligand binding, but with a much smaller conformational amplitude. In addition, the M-loop of ActR-II which has no true equivalent in BMPR-IA$_{ec}$[12] reveals some minor conformational differences.

The deviating magnitude of rearrangement for the type I and type II receptors upon ligand binding should result in differing association rates, with BMPR-IA$_{ec}$ expected to be slower than for the aforementioned ActR-II. Indeed, this can be observed when comparing the BMPR-IA$_{ec}$:BMP-2 system to previous binding studies of other protein-protein complexes. In systems like IL4:IL4Rα[339] or barnase-barstar,[340] association rate constants of $k_{on} \approx 1.3 \cdot 10^7$ M^{-1}s^{-1} and $k_{on} \approx 6 \cdot 10^8$ M^{-1}s^{-1} have been observed, respectively – rendering them diffusion-limited.[341] For the binary complex BMPR-IA$_{ec}$:BMP-2 however, the association rate in considerably smaller ($k_{on} \approx 5 \cdot 10^4$ M^{-1}s^{-1}). Furthermore, the association rate constant for BMPR-IA$_{ec}$ with BMP-2 is more than one order of magnitude smaller compared to the rate of complex formation for ActR-II:BMP-2 ($k_{on} \approx 7.2 \cdot 10^5$ M^{-1}s^{-1})[251] and other complexes of the TGF-β superfamily such as β3:TβRII.[342] This observation can be attributed to the fact that about 80% of the binding interface, including the main binding determinant, W60, are pre-formed in type II receptors allowing faster

11 The nomenclature follows that of GRENNWALD *et al.*[251]

12 While in ActR-II this loop comprises altogether nine amino acids, in BMPR-IA$_{ec}$ it consists of only three amino acids linking strand β_2 and β_3

association rates. Obviously, the mobile loops A and M of the type II receptors do not contribute significantly to binding affinity but rather to binding specifity.[262, 343]

This situation changes dramatically for BMPR-IA$_{ec}$ with its mobile loops $\beta_1\beta_2$ and $\beta_4\beta_5$. The results suggest that these loops not only determine binding specifity but also binding affinity. Conformational rearrangements in loop $\beta_4\beta_5$, including the formation of helix α_1 upon ligand binding, facilitate the activation of the main binding determinants and simultaneously provide the required shielding of these polar moieties from solvent. This clearly indicates that an induced fit is obligatory for any interaction of BMPR-IA$_{ec}$ with BMP-2. Moreover, this explains the ease with which residues G82-K88 form helix α_1 upon slight changes of the environment, like the presence of low concentrations of TFE. Correspondingly, the surface properties of free BMP-2 could mirror those of TFE. This hypothesis is supported by the finding, that mimicking only the local molecular environment of BMP-2 for the interaction with BMPR-IA$_{ec}$ (F48, P50, and L51) using the peptide *cyclo*-(FPRFPa)[344] does not result in any chemical shift changes and hence, any conformational changes. Not surprisingly, 'larger scale' modifications of the molecular environment are necessary for an induced fit.

A central question in receptor-ligand recognition within the BMP system is the binding promiscuity, i.e. how can so few receptors (seven type I receptors and five type II receptors) account for so many (≈ 30) ligands. This question is readily answered when the dynamical data for the binding interface is analyzed. As mentioned earlier BMPR-IA$_{ec/sf}$ interacts via loop $\beta_1\beta_2$ and $\beta_4\beta_5$, both of which exhibit an elevated dynamical behavior. In loop $\beta_4\beta_5$ a clear drop in the squared order parameters relative to the secondary structure elements is observed that is accompanied by increased semi-cone angles. In addition, predominantly model 4 or 5 was selected within the model-free approach, indicating a complex dynamical behavior. The comparably narrow lines in this loop suggest that exchange contributions to the dynamics do not dominate the transverse relaxation rate and therefore might play only a minor role. The large amplitude of the motion which is apparent from the large RMSD within the structure ensemble and the ^{1}H-^{15}N-RDCs of this loop, which are nearly averaged to zero, therefore must be attributed to assembled fast motions on the ps-ns timescale. In contrast, loop $\beta_1\beta_2$ exhibits clear motional modes on the μs-ms timescale, opposing the initial assumption that all motions occur on a timescale faster than the overall correlation time. While quantification of these motional

modes would be desirable, dynamical analysis performed here still offers an explanation for the binding promiscuity within the BMP receptor family; receptors adapt to different ligands by their inherent flexibility and divers dynamics on different timescales. Taking into account the high structural homology between type I and type II receptors and an equivalent conformational rearrangement for ActR-II, BMP-7, and BMPR-IA$_{ec}$ BMP-2 interactions, the modular design of the receptor structures becomes apparent.

The studies revealed that the dynamic interface is presumably the origin for the promiscuous nature of BMP ligand-receptor interactions. Nevertheless, a rigid scaffold for the core structure of BMPR-IA$_{ec}$ is still required to maintain its activity.[336] The mutation of single residues, as observed for the disease Juvenile Polyposis Syndrome (JPS)[345] can lead to inherently unfolded BMPR-IA$_{ec}$, which apparently looses the ability to bind ligands. Two common point mutations observed in JPS are located either at the periphery or very remote from the actual binding interface, but exert severe effects on the folding of BMPR-IA$_{ec}$. Mutagenesis studies revealed that distinct chemical or steric properties are required at these positions to maintain the overall fold. The aromatic ring of Y39 stabilizes the surrounding residues in the C-terminal 3_{10}-turn and strand β_2 (N51 and Q309) by π-π-stacking interactions. The close proximity of Y39 and N51 to disulfide bridges (C40-C44 and C38-C53) might indicate a possible role of Y39 for the correct formation of the disulfide network and the stabilization of loop $\beta_2\beta_3$. The other mutation that leads to a complete loss of function of BMPR-IA$_{ec}$ is T55I, where only isosteric mutations are tolerated.

Analogously to the above described mutations, single point missense mutations for type II receptors like BMPR-II and ActR-IIb are also located outside the accepted binding epitope.[346–348] Moreover, the affected residues seem to be conserved among various species, though the molecular origin of these mutations remain unknown. However, one may hypothesise that equivalent molecular mechanisms are responsible for deactivation of type II receptors. The idea of a rigid core structure with defined secondary structure elements is supported by the dynamical investigations of BMPR-IA$_{ec}$.

Chapter 5

Structure Refinement of Peptides using RDCs

5.1 Introduction

Though peptides probably belong to one of the best investigated structural classes in organic chemistry, new and interesting aspects are frequently found, making them a living and fascinating research area. The broad interest may be partially attributed to the biological activity of many representatives like gramicidin S,[349–351] rifampicin,[355] vasopressin,[356, 357] oxytocin,[358] vancomycin,[358] insulin,[359] polymixin B and E,[352–354] integrelin,[360] or somatostatin.[361] Peptides have also proven to be valuable scaffolds for pharmaceutical research, as they serve as starting points for further investigations.[362] However, peptides are rarely used as drugs, because they are easily digested within the body and commonly show a reduced bioavailibility. Therefore one of the major tasks in medicinal chemistry is the rational modification of bioactive substances, first into lead structures and finally into drug candidates and drugs. These efforts are guided by certain criteria which have been summarized under the acronym 'ADMET', meaning absorption, distribution, metabolism, excretion, and toxicity.

Many efforts have been put into the design of bioavailable and 'resistant' peptide mimetics and several suggestions have been proposed. Mainly these modifications concern the peptide bond to 'obscure' enzymatic recognition

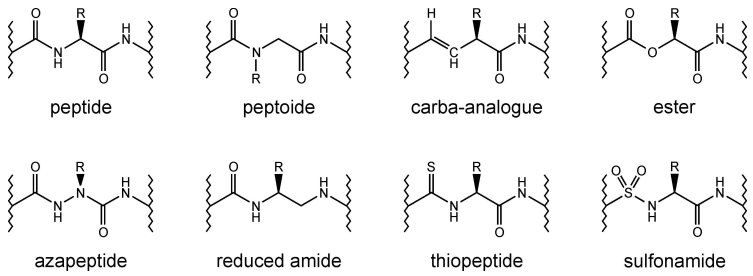

FIGURE 5.1: Peptide bond analogues commonly used to improve stability against degradation or to modify the conformational space occupied by the peptide.

and degradation. Beside the synthetic derivatives depicted in Fig. 5.1, cyclization and N-methylation are prominent alternatives to alter the ADMET profile.[363]

Obviously, the primary sequence of a peptide or peptide mimetic is of major importance for its bioactivity. Several target molecules show very pronounced selectivities for a certain amino acid motif, e.g., integrins for the sequences RGD and LDT.[364–366] However, sequence arguments alone may not explain different activities for linear and cyclic peptides as they were observed for the amino acid sequence RGDFV interacting with vitronectin.[367, 368] The strongly deviating activities actually result from different conformations adopted by the peptide, providing an opportunity for the medicinal chemist to start his search for an active compound. By cyclization the rigidity of the molecule is increased and as a consequence its conformational freedom is reduced. Starting from the original peptide a *spatial screening*[369] serves to identify the bioactive conformation and in turn enhances the activity. A frequently observed and sometimes wanted side effect is an improved selectivity of the active compound for its target molecule. In this context cyclic peptides have proven to be especially useful scaffolds, as correlations between sequence and conformation are comparably well understood.[363, 369–378]

Structures of organic molecules are most conveniently investigated by X-ray crystallography or NMR spectroscopy, as they are currently the only available techniques with a resolution at the atomic level. While for proteins X-ray crystallography gives virtually identical results as NMR spectroscopy, deviating results may be obtained for cyclic peptides where

crystal packing artifacts place severe limitations to any interpretation.[379] But also NMR techniques are facing problems as they often struggle with the limited information about long-range orientations, as classical NMR parameters like NOE intensities or J-couplings usually only monitor local geometries. Thus phenomenons such as twisted β-sheets or bended structures may be observed only indirectly. This problem may be overcome by the use of residual dipolar couplings, as they offer information about the relative orientation over virtually unlimited distances. As discussed above, detailed knowledge about the bioactive conformation enables a rational and streamlined drug development process. Consequently, structure refinement using RDCs may offer some interesting insights into the overall fold of small molecules. They may also open up the route for an improved understanding of structure-activity relationships. Therefore, the structure of cyclosporin A (CsA) was redetermined using RDCs as additional structural parameter beside the already published NOE and J-coupling restraints. Similar steps have already been described for proteins and nucleic acids,[105, 106, 323] but RDC aided structure determination or refinement of small molecules, especially peptides, is still uncommon.

5.1.1 Cyclosporin A - General Remarks

CsA is a homodetic, cyclic undeca-peptide, with the sequence *cyclo*-(MeBmt^1-Abu^2- Sar^3-MeLeu^4-Val^5- MeLeu^6-Ala^7-*D*-Ala^8 -MeLeu^9-MeLeu^{10}-MeVal^{11}) (see Fig. 5.2). It consists of three uncommon amino acids, namely MeBmt^1, Abu^2, and *D*-Ala^8; all other residues are naturally occuring amino acids or their N-methylated counterparts.

CsA is solely build of aliphatic amino acids, which renders it neutral and lipophilic. Hence, it is very soluble in apolar solvents like chloroform, THF, or benzene.[380–385] In addition, CsA is soluble in DMSO[380] and water, though the solubility in water is not sufficient to allow NMR spectroscopic investigations.[386] However, conformational studies have been conducted to cyclosporin derivatives in monoclonal antibodies in aqueous solution.[387]

CsA was discovered in 1970 by *Sandoz*[1] in the fungus *Tolypocladium inflatum GAMS*. It was isolated from soil samples collected near Hardanger Vidda (Norway), which also contained the analogue cyclosporin C.[388, 389] Nowadays, it is known that also other fungi, e.g., *Cyclindrocarpon lucidum BOOTH* are producing CsA and its analogues as secondary metabo-

1 now *Novartis*.

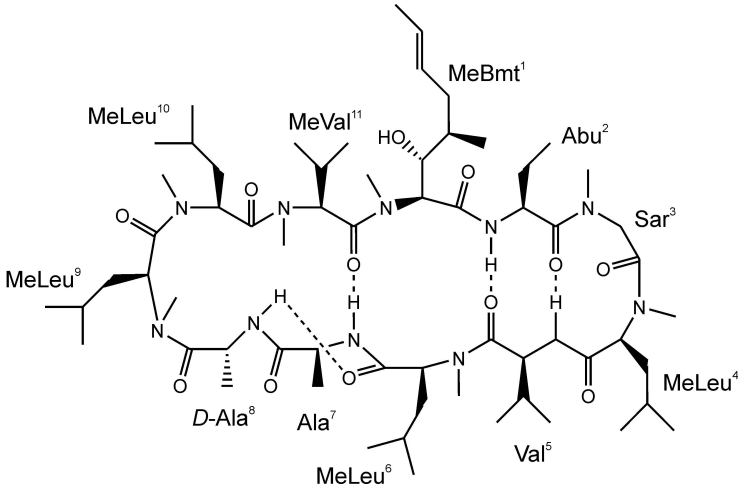

FIGURE 5.2: Constitution of the cyclic, homodetic undeca-peptide cyclosporin A. Residues are labeled with their abbreviation and sequence number. N-methylation is indicated in the residue name by the prefix 'Me' apart from the residue sarcosine (N-methylated glycine) which is typically abbreviated by 'Sar'. Hydrogen bonds are indicated by dashed lines.

lites.[390] The primary structure was solved in 1976 by Edmann degradation,[391] but it took until 1984 that the first total synthesis was accomplished by Wenger.[392] This synthesis facilitated the systematic investigation of structure-activity relationships, as modified structures became available. A central step in the total synthesis of CsA is the preparation of MeBmt.[2] It possesses three asymmetric carbon atoms and an *E*-configurated double bond, therefore representing an interesting target for organic chemists. The first synthesis was completed in 1983 and encompasses 24 steps starting from (*R*,*R*)-tartaric acid,[393, 394] but shorter and more elegant routes have been described in the following years.[395–401]

First hints that the biosynthesis of CsA occurs non-ribosomal are the occurrence of numerous natural derivatives and the presence of the non-proteogenic amino acids MeBmt and Abu. CsA is a secondary metabolite, which is assembled by multifunctional enzymes termed *non-ribosomal peptide synthases* (NRPS).[402–404] For the biosynthesis of CsA the key enzyme is cyclosporin synthase. In more than 40 steps CsA is assembled via elongation of a linear peptide chain starting from *D*-alanine.[405] For N-methylation the corresponding residue has to be activated by transformation into a thioester. It has been proven that all N-methyl groups and the γ-methyl group of MeBmt stem from methionine.[406] For this purpose, methionine was labeled with ^{3}H and ^{14}C and analyzed via ^{3}H-NMR spectroscopy. The other carbon atoms of MeBmt are introduced by head-tail-condensation of four acetate units.

First structural investigations have been performed on the iodo-derivative of CsA which gave a coarse view of the secondary structure.[407] The crystallographic analysis accomplished several years later could confirm the first assumptions and revealed a detailed view of the structure.[408] Extensive NMR investigations of CsA in chloroform, benzene, and THF have been carried out as well, including the resonance assignment and structure determination of the dominant conformer.[381, 385] While in these apolar solvents the main conformer is populated by more than 90%, in DMSO seven to eight conformers have been reported[380] which are in slow exchange with each other.[3] In apolar solvents amino acids 11 to 7 of CsA

2 MeBmt is the proposed abbreviation of *Wenger*[393] for 'Methyl-butenyl-methyl-threonine'. The chemically correct name of the MeBmt residue is (4*R*)-4-[(*E*)-2-butenyl]-4-N-dimethyl-*L*-threonine.

3 It is likely that in DMSO three peptide bonds are involved in a *cis*/*trans* isomerisation resulting in eight (2^3) possible conformers. However, it is not clear if all conformers are indeed populated.

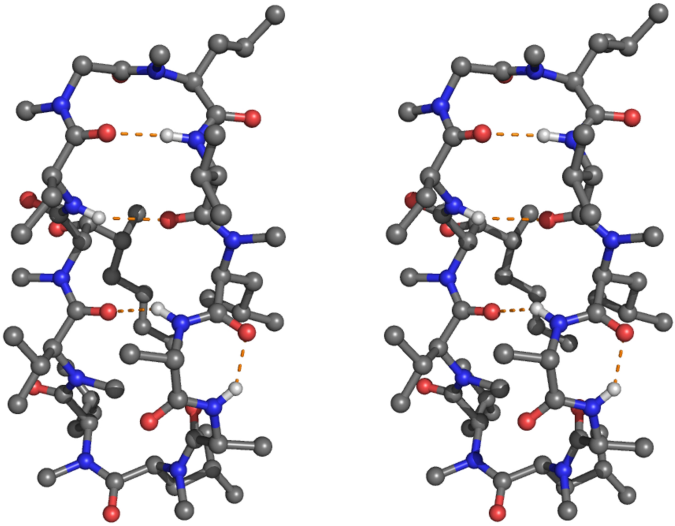

FIGURE 5.3: Stereoview of the solution structure of cyclosporin A recalculated with the dihedral angels given in the dissertation of M. Köck (see 'Tabelle 3.6' there).[385] Dashed lines indicate transannular hydrogen bonds in the cyclic peptide.

form a slightly twisted anti-parallel β-sheet with three transannular hydrogen bonds and a βII'-turn between Sar^3 and MeLeu^4 (cf. Fig. 5.3). Amino acids 7 to 11 also form a turn structure which accommodates the only *cis* peptide bond in the molecule between MeLeu^9 and MeLeu^{10}. This turn is structurally related to a βIVb-turn, though the Φ- and Ψ-angles do not resemble the theoretical values exactly, especially for amino acid $i+2$.[4] Moreover, a γ-turn is present in the molecule between amino acids 6 and 8 with the hydrogen bond formed between *D*-Ala^{8}NH and MeLeu^{6}C'.

In $CDCl_3$ solution CsA adopts nearly the same conformation as in the crystal structure. Minor differences concern the orientation of some side-chains and the intramolecular hydrogen bond between MeBmt^{1}OH and

4 Cyclosporin A: $i+1$ $\Phi = -125°$, $\Psi = 116°$; $i+2$ $\Phi = -131°$, $\Psi = 86°$; Theoretical values:[409] $i+1$ $\Phi = -135°$, $\Psi = 135°$; $i+2$ $\Phi = -75°$, $\Psi = 160°$

MeBmt^{1}C'. This hydrogen bond is not abundant in the crystal structure but could be verified by IR spectroscopy in solution. Noteworthy, MeBmt^{1}OH forms a hydrogen bond to the neighboring molecule in the crystal. CsA is one of the classical and probably the most prominent example for the difference between crystal structure and solution structure. This mainly refers to the observation that in the crystal structure the sidechain of MeBmt^1 is folded over the backbone while in solution the sidechain is pointing into the solvent. However, newer investigations revealed that even in solution the MeBmt^1 sidechain is folded over the backbone though it does not adopt the same conformation as in the crystal structure. Because of its comparably rigid and well-defined structure CsA has been used for methodological studies of NMR parameters.[382, 410–415] This was also one reason why CsA was chosen for the present study.

5.1.2 Pharmacological Effect of Cyclosporin A

CsA is one of the most successful peptidal drugs on the market. Under the trade name *Sandimmun*® it is distributed by *Novartis* since 1983 and currently has an annual turnover of about 1 bio. US dollars.[416] Its success can be attributed to the immunosuppressive effect which is exploited in transplantational surgery.

In the early days of organ and bone marrow transplantation graft rejection was the major obstacle. In the 1950's first approaches using corticosteroids, 6-mecaptopurin, or azathioprin led to poor results. Also the use of synergetic drug combinations in the 1960's did not show a satisfactory effect. A turning point was reached when in 1978, already 8 years after its discovery, a kidney transplantation was accomplished successfully with the help of CsA.[417, 418] As a consequence transplantations could be carried out on a larger scale with comparably low risks. Nevertheless, CsA also exhibits negative side effects like kidney damage or an increased risk for cancer.

CsA is a selective immuno suppressant with an additional fungicidal and anti-inflammatory effect. It leads to a drop of the immune barrier and hence to the suppression of the natural antibody formation by suppressing the activation of T-lymphocytes.[419] CsA does not act as cytostatic and its effect is reversible and selective for T-lymphocytes.

On a molecular basis, CsA binds to the 17.8 kDa protein cyclophilin A (CyPA), which is a peptidyl-prolyl isomerase catalyzing *cis*/*trans* isomerizations. This complex interacts with calcineurin, which in turn is

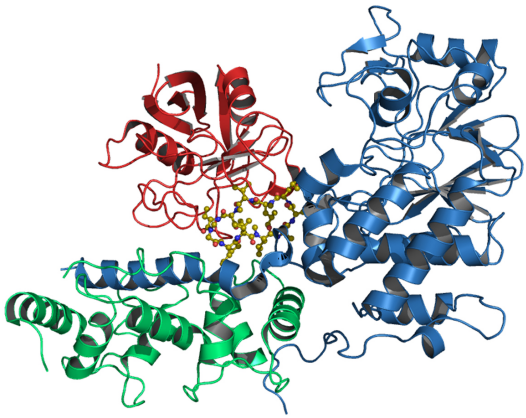

FIGURE 5.4: Cyclosporin A (dark yellow) complexed by calcineurin A (blue) and B (green) and cyclophilin A (red).[420] The CsA:CyPA binary complex lies at the base of the helical arm of the catalytic subunit of calcineurin A that binds the regulatory subunit calcineurin B.

responsible for the dephosphorylation of the transcription factor NFAT (nuclear factor of activated T-cells). NFAT effects a complete change in the transcription of the genome, leading to the activated state of the T-cell. Consequently, inhibiting dephosphorylation of NFAT results in a decreased immune response.

The crystal structure of the ternary complex of calcineurin interacting with CsA:CyPA has been investigated by KE *et al.* (Fig. 5.4) and was solved with a resolution of 2.8 Å.[420] This structure reveals no overall conformational changes in calcineurin when binding to CsA:CyPA. However, it confirms previous results that CsA adopts a totally different conformation in the bound form compared to the uncomplexed form.[421]5

5 Admittedly, the structure of CsA has not been solved in aqueous solution, but only in apolar solvents (see Sec. 5.1.1). Though, these are regarded as mimics for hydrophobic binding pockets.[422]

5.2 RDC Measurements

The measurement of partially oriented samples offers some curiosities which will be discussed briefly in the following. The most apparent problem is the occurrence of residual proton and/or carbon signals stemming from the alignment medium. For biomacromolecules this usually is not an issue as molecules are specifically labeled, mostly with ^{15}N, and therefore perturbing signals are inherently suppressed by any heteronuclear technique utilizing this label. However, small molecules like peptides, sugars, nucleotides, natural products, or synthetic derivatives are commonly unlabeled. Hence, heteronuclear spectra are recorded at natural abundance and special care has to be taken to suppress unwanted signals.

In principle, any scheme useful for solvent suppression in aqueous solution is also applicable to signals originating from alignment media. Admittedly, these techniques are mostly not convenient, as they have been optimized for comparably narrow water signals. In addition, residual signals from the alignment medium are often located in regions where also signals from the compound under investigation are abundant. As a consequence these signals would be suppressed too, when using WATERGATE[423, 424] suppression for example. Presaturation or 'flip-back' techniques are facing the same problem beside the difficulty to find pulses working selectively on the alignment medium, as these often show more than one distracting signal.[6] Thus it is unadvisable to exploit the chemical shift information to distinguish between signals of the alignment medium and the solute.

To separate the signals of the target molecule from signals of the alignment medium it is helpful to throw a glance at the physicochemical properties of the two. Commonly, the alignment medium has a much higher molecular mass than the solute, which translates into much smaller translational and rotational diffusion rates. Accordingly, suppression of residual signals in partially oriented samples is closely related to drug discovery using NMR methods, where the molecular weight difference is utilized to discriminate between binding and non-binding ligands.[341, 432–434] Typical techniques to suppress signals of the larger molecule are relaxation and diffusion filters. Both have been implemented for partially aligned samples.

Most commonly for heteronuclear experiments, a simple z-filter is intro-

6 Recent developments in pulse design[184, 185, 425–430] facilitate the selective inversion/excitation of defined spectral regions. Although these have also been applied for 'solvent suppression' more effort has been put into the selective excitation of defined spectral windows.[71, 431]

duced after the first INEPT step. Here, the different relaxation properties of the term $I_{1z}I_{2z}$ are utilized. While this term relaxes comparably slow for small molecules, its relaxes much faster for large molecules. This fact rests on the phenomenon that longitudinal cross-relaxation rates σ_{12} for protons are large for large molecules but are close to zero for small molecules. Usually a filter delay of 300 ms is sufficient to significantly decrease residual signals. Another approach makes use of the strongly deviating transverse relaxation rates R_2 for the alignment medium and the solute. Similar to the cross-relaxation rates exploited by z-filters, large molecules have large R_2 rates while small molecules relax much slower. Consequently, suppression of residual peaks from alignment media can be achieved by locking the magnetization along a transverse axis. These filters are usually incorporated prior to the actual pulse sequence and are also routinely applied for a duration of $\approx$ 300 ms. It has to be pointed out that some alignment media possess flexible sidechains rendering their relaxation properties similar to small molecules. Therefore these signals are difficult to suppress, as for instance in polystyrene.[59, 61]

This problem can be overcome by using diffusion filtered experiments. A *longitudinal eddy current delay* (LED)[435] building block is introduced right before the standard pulse sequence. As the solute has much higher diffusion rates than the alignment medium, which essentially does not diffuse at all, signals originating from the solute will be eliminated completely. Thus, difference spectroscopy is used and spectra are recorded with an interleaved sampling scheme acquiring spectra once with the LED sequence applied and once without. The difference of the two will leave only wanted signals observable.

Another problem hampering the measurement of RDCs is the lock signal. Due to the quadrupolar coupling of the deuterium nucleus the lock signal is split into a doublet. Only few alignment media exhibit quadrupolar splittings larger than several hundreds of Hertz, which would allow for selectively locking onto only one of the doublet components. Most media show quadrupolar splittings on the order of a few Hertz. Hence, the lock unit might accidentally alter its reference signal by changing from one component of the doublet to the other one between increments. Of course this will obscure the acquisition of spectra severely, leading to truncation artifacts in the indirect dimension. But also in the directly detected dimension artifacts will occur. Signals will be split into pseudo-doublets with a splitting corresponding to the quadrupolar splitting observed in the ^{2}D-spectrum. Therefore, 2D-spectra and long 1D-spectra are commonly

acquired *unlocked* though the linewidth might increase due to a slowly drifting static magnetic field B_0.

Closely related to the splitting of the lock signal is the tedious and time-consuming shimming process. Obviously the deuterium signal cannot be used for automated shimming, as the shim unit would try to maximize this signal and consequently produces a virtual singulet. For this reason, shimming has to be performed manually, either by maximizing the FID or by directly shimming on the spectrum. Only in solutions where protons are abundant, for example aqueous solutions, shimming can be performed automatically as protons do not show quadrupolar splittings. However, adding 'protons' in larger quantities is not a general solution, as these compounds usually interfere with observed spectra and force the receiver gain to be decreased. A possible solution to this problem might be the addition of perfluorinated compounds. As fluorine is a spin-$\frac{1}{2}$ nucleus, it will not show any splitting due to alignment, therefore singulets are expected allowing an automated shimming process. Moreover fluorine compounds are usually inert and do not appear in any commonly observed spectrum. However, perfluorinated compounds are also known to be poorly mixable with other solvents.[436]

While for proteins and nucleic acids one-bond D_{NH}-couplings ($^1D_{NH}$) are most frequently measured,[106] in case of small molecules D_{CH}-couplings are commonly determined because of their omnipresent character. Even under strong line broadening effects $^1D_{CH}$-couplings are comparably easy to measure (*vide infra*) due to the large chemical shift dispersion in the carbon dimension. As HSQC and HMQC techniques for observation of directly bonded, heteronuclear spin pairs are very sensitive, high signal-to-noise ratios are achievable that determine the precision of the measurement beside the spectral resolution. Furthermore, $^1D_{CH}$-couplings facilitate a simplified geometrical interpretation, as the interatomic distance is fixed and therefore one degree of freedom is eliminated from Eq. 2.48. This enables a streamlined structure determination process as ambiguities are removed and the conformational search-space is reduced.

A multitude of experiments has been proposed for the measurement of couplings between directly bonded heteronuclear spin-pairs. The majority utilizes IPAP techniques, where in-phase and anti-phase components are recorded in separate experiments and are added or subtracted to yield a single signal in each subspectrum. The spectral distance in the two subspectra finally yields the desired coupling constant. For biomacromolecules coupling evolution is commonly permitted in the *indirect* dimension be-

cause of the smaller linewidth along the ^{15}N-dimension compared to the ^{1}H-dimension. In contrast, for small molecules coupling evolution is directed to the *direct* dimension where a higher spectral resolution is obtainable. However, this advantage can be negated if anti-phase terms are present prior to detection that evolve into observable magnetization during acquisition and, hence, deteriorate the extraction of coupling constants. These anti-phase contributions stem from the inherent broader distribution of effective couplings constants ($^{1}D_{XH} + {}^{1}J_{XH}$) that inevitably lead to mismatched refocussing delays in the Re-INEPT of HSQC spectra. Anti-phase contributions can be eliminated by an additional 90° pulse on the X-channel just prior to acquisition.[437]

Special attention has to be paid to residual dipolar couplings of interchanging 'conformations'.[7] Here the observed RDCs clearly represent only averaged values and cannot be converted into geometrical information in a straightforward way. Nevertheless, if $^{1}D_{CH}$-couplings of methyl groups are considered, they can be converted into $^{1}D_{CX}$-couplings to the fourth attached atom via the formula:

$$D_{CX} = D_{CH_3}\left(-3\frac{\gamma_X r_{CH}^3}{\gamma_H r_{CX}^3}\right). \tag{5.1}$$

To obtain residual dipolar couplings for CsA it was partially aligned in a PDMS-gel cross-linked by accelerated electrons and swollen in chloroform. Measurement of D_{CH}-couplings was achieved by acquiring conventional sensitivity-enhanced coherence order selective ^{1}H-^{13}C-HSQC spectra without heteronuclear decoupling in the direct dimension. Most $^{1}J_{CH}$-coupling constants with the corresponding dipolar coupling could be measured from these spectra (see Fig. 5.5). For exact extraction of coupling constants the procedure described by YAN *et al.*[438] was used, where each component of the doublet is phased separately. Altogether 35 $^{1}D_{CH}$-couplings in the range of −22.3 to 27.9 Hz could be obtained.

RDCs were then fitted to the existing crystal and the NOE-derived structures using the program PALES.[21] In both cases, a scattering of back-calculated versus measured RDCs was observed with poor overall correlations of $R = 0.585$ and $R = 0.387$ for the crystal and NOE-derived structure, respectively (see Fig. 5.6). It must therefore be concluded that neither of the structures represents the time-averaged structure present in-

7 RDCs are sensitive to averaging processes on the ps-ns as well as the ms timescale (see Fig. 2.6).

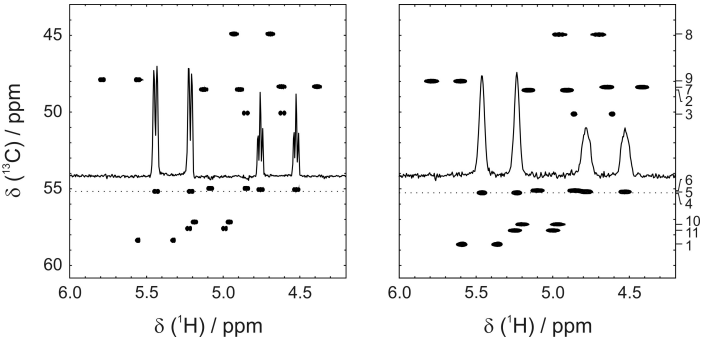

FIGURE 5.5: H^{α}-C^{α}-regions of the ^{1}H-^{13}C-HSQC spectra recorded on CsA in $CDCl_3$ (LEFT) and the PDMS/$CDCl_3$ gel (RIGHT) without heteronuclear decoupling during acquisition. Slices along the dotted lines are shown for an impression of the spectral quality. Residue assignment is given on the right-hand side.[385]

side the PDMS gel. For sidechains, the deviation of the $^{1}D_{CH}$-couplings can be explained by the inherent flexibility in the apolar solvent. For the backbone, however, it was previously found that a single, well-defined conformation is present in $CDCl_3$.[380, 383, 385] The correlations for the crystal and NOE-derived structures with only backbone RDCs considerably improves to $R = 0.900$ and $R = 0.779$, respectively, but the deviations between measured and fitted RDCs are still large. Hence, the measured RDCs were used for structural refinement.

5.3 Structure Calculation

Residual dipolar couplings can be incorporated into the structure calculation protocol just as other restraints, like scalar couplings or nuclear Overhauser enhancements. For this purpose, $D_i(\vartheta_i, \varphi_i)$ values (cf. Eq. 2.58) are converted to restraints by adding a computational potential energy term $E_i = K(D_{i,back} - D_{i,exp})^2$ to an overall penalty function. The scaling factor K is set in relation to other restraints and is of central importance and might be chosen differently for different molecules. If the ϑ_i-, φ_i-values of a computed structure fulfill the measured values within the experimental precision, then $E_i = 0$; otherwise, $E_i > 0$ and it will be added to the overall penalty. During simulated annealing, a random conformation is compared

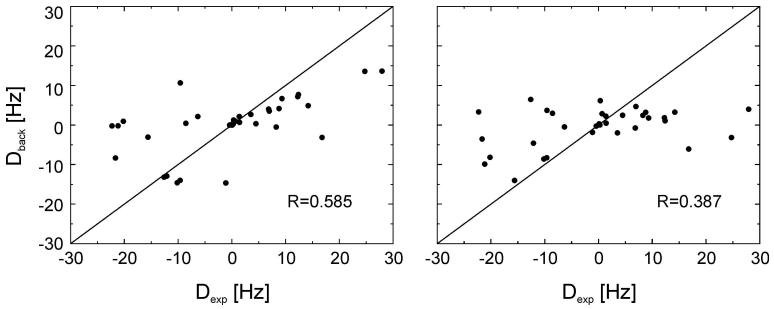

FIGURE 5.6: Experimental versus back-calculated D_{CH}-couplings for the crystal structure[408] (LEFT) and the NOE-derived structure[383] (RIGHT) of CsA. The correlation factors R indicate a poor correlation for both structural models. RDCs were back-calculated using the program PALES[21] with the BESTFIT-option.

with the experimental restraints and driven towards a structure by minimization of the penalty function. This approach has been implemented in the susceptibility anisotropy (SANI) potential of the software package XPLOR-NIH.[105, 323, 439, 440]

A more sophisticated approach is the incorporation of residual dipolar couplings as pair-wise defined coupling pairs, independent of the principal axis system (PAS).[441] A set of n RDCs is therefore transformed to a set of $n(n-1)$ pair-wise restraints by combining two RDCs $D_i(\vartheta_i, \varphi_i)$ and $D_j(\vartheta_j, \varphi_j)$ to a projection angle ϕ_{ij} (Fig. 5.7). The angle ϕ_{ij} is defined by the scalar product of two vectors **i** and **j** given in the common PAS frame

$$\cos\phi_{ij} = \begin{pmatrix} \sin\vartheta_i \cos\varphi_i \\ \sin\vartheta_i \sin\varphi_i \\ \cos\vartheta_i \end{pmatrix}^{\mathrm{T}} \begin{pmatrix} \sin\vartheta_j \cos\varphi_j \\ \sin\vartheta_j \sin\varphi_j \\ \cos\vartheta_j \end{pmatrix}. \qquad (5.2)$$

Since D_i and D_j specify ranges of (ϑ_i, φ_i) and (ϑ_j, φ_j), the pair-wise restraint is not particularly restrictive,[8] however, this indistinctness is compensated by the large amount of restraints (n vs. $n(n-1)$). The frame independent formulation conveniently allows for the incorporation of RDCs measured in several alignment media. In the software package XPLOR-NIH

8 A pair-wise defined restraint is inherently ambiguous, as the projection angle ϕ_{ij} is defined as the scalar product (*vide supra*).

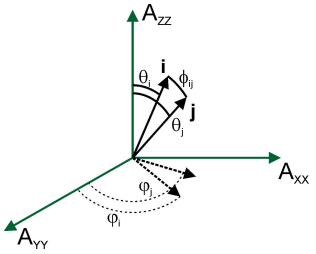

Figure 5.7: Projection angle ϕ_{ij} between two internuclear vectors in the principal axis system (A_{xx}, A_{yy}, A_{zz}) of the weakly aligned molecule.

this approach has been realized in the Vean potential.[9]

As D_{CH}-couplings have been measured in only one alignment medium, it was convenient to use the Sani potential of Xplor-nih to incorporate RDCs as angular restraints with respect to an introduced coordinate system representing the eigenvectors of the alignment tensor. It is important to note that the tensor orientation and magnitude (D_a and R, cf. Eqs. 2.57 and 2.58) do not change during the calculation for this potential. Therefore the choice of the initial alignment tensor is of critical importance for the further structure calculation process.

Several possibilities are known to obtain these sensitive data, even for unassigned RDCs. Most easily the tensor components D_a and R are extracted from a histogram of the experimental RDCs.[105,328,445] By consideration of Eq. 2.58 it is possible to correlate the observable extreme values to specific orientations in the alignment tensor. Hence, the possibly largest observable RDC corresponds to an orientation of the ^{1}H-^{13}C bond vector parallel to the z-axis of the alignment tensor ($\vartheta = 0°$), while for the smallest coupling the ^{1}H-^{13}C bond vector must coincide with the y-axis ($\vartheta = 0°$, $\varphi = 90°$). If the ^{1}H-^{13}C bond vectors are distributed isotropically, a histogram describing the probability of finding values of D_{CH} between these extremes will have the appearance of a chemical shift anisotropy (CSA) powder pattern. The highest probability dipolar coupling value, therefore, coincides with the magnitude of the bond vector aligned along the x-axis of the alignment tensor ($\vartheta = 90°$, $\varphi = 0°$). Since $D_{xx}^{CH} + D_{yy}^{CH} + D_{zz}^{CH} = 0$,

9 Several other potentials like 'Xdip'[442] or 'Tenso'[443] have been implemented in Xplor-nih, but will not be discussed here. For more detailed information the reader is referred to the online manual of this software package.[444]

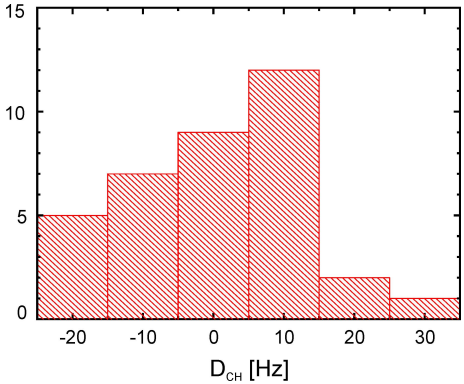

FIGURE 5.8: Histogram for RDCs of cyclosporin A. RDCs of methyl-groups have been normalized to D_{CH}-couplings, by scaling them with a factor of -3.

it follows from Eq. 2.58

$$\begin{aligned} D_{xx}^{CH} &= -D_a^{CH}(1 - \tfrac{3}{2}R) \\ D_{yy}^{CH} &= -D_a^{CH}(1 + \tfrac{3}{2}R) \\ D_{zz}^{CH} &= 2D_a^{CH}. \end{aligned} \tag{5.3}$$

In practice, the values of D_{zz} and D_{yy} are obtained by taking the high and low extreme values of the observed residual dipolar couplings, while the most populated value in the histogram corresponds to D_{xx} (cf. Fig. 5.8). With two unknowns and three observables (D_{xx}, D_{yy}, and D_{zz}), values for D_a and R can be obtained by least-square fitting. With this approach values of 12.85 and 0.60 have been extracted for D_a and R, respectively. However, as pointed out by CLORE *et al.*,[328] this approach is limited by the amount of observable couplings. If only a sparse amount of data is available (like for CsA), the extracted values should be used only as rough estimates. Still, in the present case the rhombicity does not deviate strongly (-5%) from the value used later for the structure calculation obtained by a different approach while D_a deviates by almost 50% (*vide infra*). This is a generally observed trend when a sufficient amount of data is analyzed; D_a usually deviates stronger ($\approx \pm 5\%$) and R less ($\approx \pm 0.1\%$) from the actual value when using this approach.[325]

As the assignment for CsA is known, the alignment tensor can be extracted with a program such as PALES[21] or REDCAT[446] by a least-square

fit of the experimental data versus a known structure. Obviously, as pointed out above, this procedure will fail if the input structure deviates from the actual structure, leading to bad correlation factors. Still, in the case of structured, cyclic peptides it can safely be assumed that the backbone conformation of the NOE-derived structure does not deviate strongly from the 'real' conformation present in solution, even if correlation factors are low. Therefore, values obtained by using, for example, the bestFit-module of Pales will represent good estimates and sufficient initial guesses, if only C^{α}-H^{α}-RDCs are considered. Equivalent results for D_a and R could be obtained using a grid search algorithm implemented in Xplor-nih (cf. Fig. 5.9). The grid search algorithm has the advantage that it directly offers the coefficients needed in the input script for Xplor-nih and values do not have to be converted from one software to the other, which is not necessarily straightforward.[10] Hence, relations needed to convert output data from Pales into Xplor format are presented below,

$$\begin{aligned} D_a^{Xplor} &= D_a^{Pales} D_{max} \\ R^{Xplor} &= D_r^{Pales} / D_a^{Pales}. \end{aligned} \tag{5.4}$$

Particular care has to be taken of atom naming when using Pales. As this software package is optimized for analyzing proteins, it assumes defined bond lengths for certain spin pairs and not the distances given in the structure file. This concerns the bonds between C^{α}-H^{α}, C'-N, N-H^{N}, and C^{α}-C'.[11] Consequently, deviating results are obtained for D_{max} according to Eq. 2.48-2.50 and therefore will obscure the input for Xplor-nih (see Eq. 5.4). These problems can be avoided when the corresponding atoms are renamed.

Since the implementation of the Sani potential is known to converge slowly, considerable effort was put into testing various procedures for including RDCs into structure calculations. Initially, all observable RDCs were included at once, which resulted in a multitude of distorted structures. Best results were obtained by grouping RDCs in classes of equivalent ^{1}H-^{13}C bond vectors on the basis of assumed flexibility and adding them successively to calculations (see App. C.3). Using this 'class' protocol, a set of highly defined structures could be obtained after only a few structure calculation cycles. In this set the best 10 out of 20 structures showed

10 Mistakes were found for the definition of the three coefficients in the help library of Xplor-nih, version 2.9.4a. The first coefficient should always equal 0, while the second coefficient is equal to D_a and the third coefficient equals R.

11 The distances for these spin pairs are taken from Ottiger and Bax.[447]

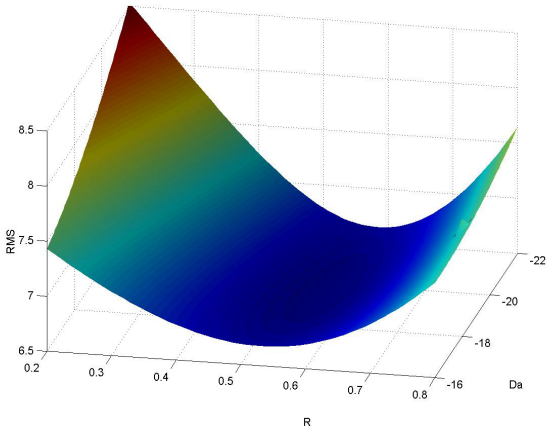

FIGURE 5.9: Grid search for the initial tensor used in structure refinement of CsA. While the value for the rhombicity R is well-defined, the energy surface is comparably shallow along the axis of D_a. However, the obtained initial values ($D_a = 19.2$ and $R = 0.56$) still represent sufficiently good estimates (*vide infra*).

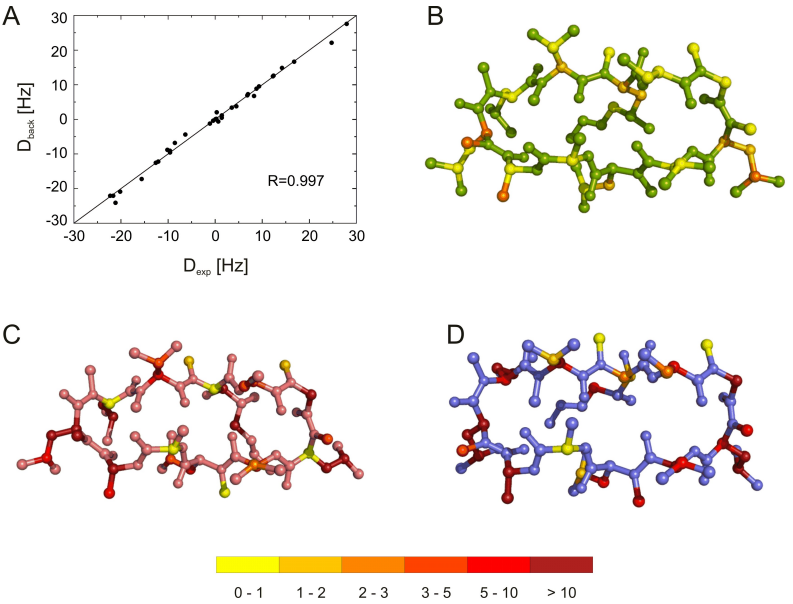

Figure 5.10: Experimental vs. back-calculated D_{CH}-couplings of CsA after structural refinement (A) and visualization of the differences between experimental and back-calculated RDCs in different structures (B-D). The crystal structure (C) and the NOE-derived structure (D) display strong deviations, while the RDC-refined structure (B) only exhibits minor deviations. Differences are colour coded as indicated at the bottom.

a very small RMSD of only 0.12 Å over all heavy atoms (see Tab. 5.1), and all RDC restraints are very close to being fulfilled within experimental errors, as shown in Fig. 5.10. The correlation between measured and back-calculated RDCs is $R = 0.997$. It is worth noting that, in addition to RDC restraints, the structure still fulfills all correct NOE-derived distance restraints used in the original solution structure.[12]

12 In the PhD thesis of M. Köck[385] the experimental NOE distances are compared to the distances obtained by MD simulation (see 'Tabelle 3.4' there). Here, some significant deviations between the two are revealed, e.g., Val^{5}H$^\beta$-MeLeu^{6}NMe (3.10 Å vs. 4.85 Å). The same deviations are also observed in the present study for both the NOE-derived structure and the RDC-refined structure.

TABLE 5.1: Structure statistics and atomic RMS deviations for RDC-refined cyclosporin A.[a]

A. Structural statistics	
RMSD from distance restraints[b] (Å)	SA
all (114)	0.062 ± 0.002
intra-residue (50)	0.079 ± 0.003
inter-residue sequential (36)	0.053 ± 0.001
medium range (28)	0.028 ± 0.003
RMSD from dihedral restraints (deg)(2)	0
RMSD from RDC restraints (Hz)(35)	0.49 ± 0.49
H-bond restraints; averages (Å/deg)[c] (4)	$2.25 \pm 0.35/19.2 \pm 4.6$
Deviations from ideal covalent geometry	
Bonds($Å \times 10^{-3}$)	0.010 ± 0.001
Angles(deg)	1.53 ± 0.04
Impropers(deg)	4.73 ± 0.41

B. Atomic RMSD (Å)[d]	SA vs. $\langle$SA$\rangle$	
	Backbone	Heavy
All	0.030 ± 0.026	0.120 ± 0.056
Residues 2-5	0.018 ± 0.020	0.041 ± 0.037
Residues 7-10	0.016 ± 0.013	0.041 ± 0.023

[a] SA, set of 10 final simulated annealing structures; $\langle$SA$\rangle$, the mean structure calculated by averaging the coordinates of SA structures.

[b] Numbers in brackets indicate the number of restraints of each type.

[c] Hydrogen bonds were restrained by treating them as pseudo-covalent bonds.[312] Deviations are expressed as the average distance/average deviation from linearity for restrained hydrogen bonds.

[d] Based on heavy atoms superimposition.

5.4 Discussion

5.4.1 Structural Influence of PDMS and General Remarks

When measuring RDCs in an anisotropic medium one always has to be aware that the alignment medium acts as cosolvent and might influence the dynamical and structural properties of the molecule. This phenomenon was shown previously for two oligosaccharides aligned in mineral liquid crystals.[152] It is well known that CsA adopts different conformations in different solvents, though the structures are highly similar in apolar solvents. Nevertheless, experimental RDCs are likely to be inaccurate as structural changes also comprise changes of the underlying scalar couplings. PDMS is an apolar alignment medium which exposes no functional groups to the solvent that might interact specifically with the solute. Even weak π-cation interactions observed for strychnine aligned in poly(styrene)[448] can be ruled out. Hence, PDMS purely works as 'steric' alignment medium and the probability of structural influences due to the alignment medium are diminished. Furthermore, the proton and carbon chemical shifts of CsA in chloroform and PDMS/chloroform gel have been compared. Only minor deviations can be observed, which are generally less than 0.3 ppm for carbon atoms and less than 0.07 ppm for protons (Tab. C.1). Taking into account that chemical shift changes are expected due to residual chemical shift anisotropy, potential structural changes can be neglected.

Within the program Pales, it is possible to predict the alignment tensor from a given structure based on a rod model (or plain wall model) for the stretched polymer gel. For a rigid spiroindene molecule, the agreement between predicted and experimentally determined RDCs is very good and results in a correlation factor of $R = 0.983$.[62] In contrast, the prediction for CsA with the crystal, lowest energy NOE-derived, and RDC-refined structural models yields correlation factors calculated for all 35 RDCs of $R = 0.414$, 0.034, and $R = 0.539$, respectively. Predictions from $D_{C^\alpha H^\alpha}$-couplings alone also only resulted in correlation factors of $R = 0.479$, 0.055, and $R = 0.601$, respectively. Even if the simulation parameters are varied far beyond any physically relevance, the correlation factors did not improve significantly. The poor correlations for CsA can easily be explained by the flexibility of the shape determining sidechains (*vide infra*). A prediction that only makes use of a single structural model and not of an ensemble of structures covering the whole conformational space of CsA must, of course, fail. This statement, though in an alleviated form, is also true for proteins

if large parts of the protein are subject to conformational exchange.

The RDC-supported structure calculations of CsA from a protocol as described above lead to a well-defined time-averaged structure. Several other protocols, however, failed to produce low-energy structures that obey the imposed restraints. Structure calculations starting from the NOE-derived structure using all distance and RDCs restraints at once resulted in an ensemble of strongly distorted structures. This can be explained by the slow convergence of the SANI potential, which obviously causes the structure calculation to get stuck in local minima of the potential hypersurface. It appears likely that if a sufficient amount of structures is calculated with all restraints included, the detour of grouping RDCs into classes is not necessary. However, using the SANI implementation, structure calculations converge fastest when using the 'class' approach, at least for smaller peptides.

To compare the results obtained from the structure calculations using only NOE distance restraints and using both NOE- and RDC-restraints to the crystal structure, all three structures have been superimposed in Fig. 5.11. For superimpositions well-defined regions have been chosen, i.e., residues 2-5 and residues 7-9. The difference in the backbone planarity is immediately obvious and explains the poor correlation of experimental versus back-calculated RDCs in the crystal and NOE-derived structure (0.585 and 0.387, respectively). For quantifying the *bend* of the structures a plane is defined through three atoms (Abu^2N, Abu^2C^{α}, Val^5C'), representing the begin and end of the βII'-turn, respectively. Subsequently, the distance of the atom $MeLeu^9C'$ above this plane is determined, as it represents the 'tip' of the structures if the βII'-turn is viewed as 'base'. Distances of 7.85 Å, 3.92 Å, and 5.76 Å have been measured for the crystal, the NOE-derived and RDC-refined structure, respectively. This clearly reveals that the crystal structure is the most bended structure, unlike the conclusions from previous investigations.[114, 449] However, the strong bend may still be attributed to crystal packing artifacts. The RDC-refined structure is found to be more bent than the NOE-derived structure, which supports the initial assumption that structure calculations solely based on NOE restraints might display long-range orientations not fully correct. As pointed out above, this stems from the fact that NOE distance restraints only monitor the nearest neighborhood (< 5 Å), while RDCs offer information over virtually unlimited distances.

An interesting question when using the 'class' approach to refine peptide structures with RDCs is how the different classes influence the struc-

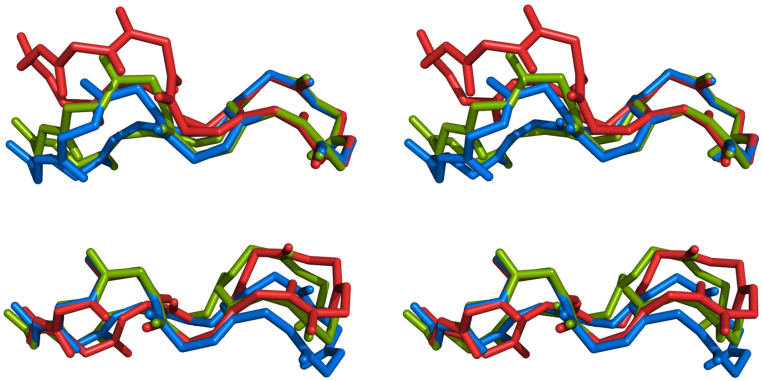

Figure 5.11: Stereoview of the backbone conformations of the crystal (red), the NOE-derived structure (blue) and the RDC-refined structure (green) superimposed onto the highly defined βII'-turn comprising residues 2-5 (Top) and residues 7-9 (Bottom).

ture during the course of structure determination, i.e., how the structure evolves. Therefore, structures after each refinement step have been superimposed at the βII'-turn between residues 2-5. The structure evolution is depicted in Fig. 5.12, where the NOE-derived structure is added for convenience (blue). Apparently, the structure changes in two successive, major steps. First, a significant bend is created when C^{α}-H^{α}-RDCs are added, while the further addition of backbone RDCs (C^{β}-methyl and N-methyl) only reveals minor influences. However, when C^{β}-H^{β}-couplings are used a second evolutionary step occurs that renders the structure close to the final RDC-refined structure. This indicates that C^{β}-H^{β}-couplings have a significant influence on the backbone conformation of the peptide and should be included into structure calculations if possible. This, however, is not a surprising finding, since the H^{β}-protons are still located close to the backbone.

Of crucial importance for the structure determination process is the initial guess of the alignment tensor or, in case of the Sani implementation, the values D_a and R. Therefore the initial values were deliberately misset to test the influence on the structure refinement process. The effect is illustrated in Fig. 5.13, where the final NOE energies of the structures

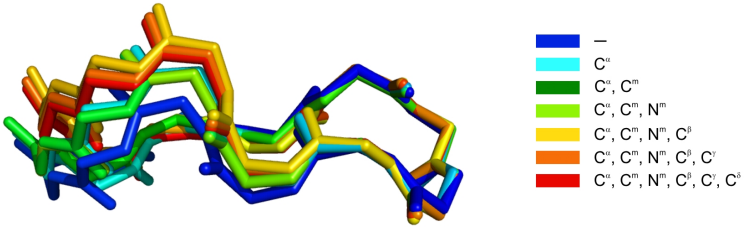

FIGURE 5.12: Evolution of the backbone fold of cyclosporin A by successive addition of RDCs. The RDCs are grouped into classes of assumed flexibility and are indicated on the right. While the structure is relatively 'flat' using only NOE restraints (blue) it becomes more bended when RDCs are added.

are plotted versus D_a and R. These plots reveal that equivalent energies are obtained for several combinations of tensor values, while extreme settings, deviating strongly from the original initial guess, lead to significantly higher energies. In addition, it can be observed that a discrimination between different tensor values is amplified if RDCs of C^{β}-H^{β} are included. This supports the statement that these RDCs are also very important for the backbone conformation, while the NOE-energy is not strongly increased. It was found that the tolerable deviation for D_a ($\approx \pm 10\%$) and for R ($\approx \pm 15\%$) are approximately equivalent. All low-energy structures (deep blue areas in Fig. 5.13, left) generated in this experiment were compared and found to be highly similar (RMSD over all backbone atoms: 0.19 Å $\pm$ 0.18 Å). This allows to conclude that the initial guess is not over-sensitive to incidental mis-settings. However, a full analysis, varying the tensor values over a sufficient broad range of D_a and R as described above, will result in more reliable results.

5.4.2 Sidechain Conformations

Previous studies using $^3J_{HH}$-coupling constants as indicators for χ_1-angles revealed that sidechains of CsA in chloroform are most likely averaged over several conformations.[385, 450] In contrast, in the RDC-refined structures the sidechains are all well defined, and practically no variations of dihedral angles are observed. However, the dynamic behavior of the CsA sidechains is also visible in the structure, since the hydrophobic tails all point straight into the solvent – a behavior typical of an averaged structure for flexible

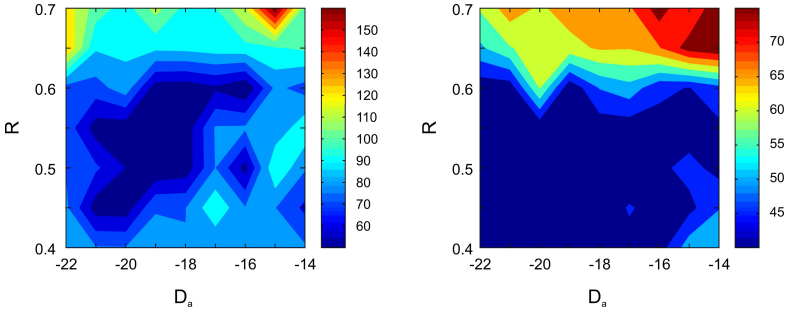

Figure 5.13: Influence of the alignment tensor on structure calculations of cyclosporin A. The NOE-energy in kcal $\cdot$ mol^{-1} is plotted in dependence of the values D_a and R describing the alignment tensor. Left: All classes of RDCs up to C^{γ}-H^{γ}-couplings (see App. C.3) have been included. Right: Only backbone RDCs (C^{α}-H^{α}, C^{β}-methyl, and N-methyl-couplings) are considered.

parts of a molecule in an apolar solvent.

It has to be pointed out that the final structure presented in this study is *over-restrained*, i.e., the conformational space occupied by the final structure ensemble is much smaller than the expected conformational variability in solution, especially for sidechains. Consequently, the resulting structure represents the time-averaged structure in solution. This, in fact, is true for all structures determined in solution, although rarely as precise and well-resolved as in this study. For a more complete structural model, additional data on local flexibility would be highly desirable.

Much effort is put into the interpretation of RDCs in terms of ensemble averages and dynamical parameters.[115–122] It has been shown that only one set of RDCs measured in a single alignment medium is not sufficient to display the dynamical behavior of the molecule correctly. This results from the fact that in principle *two* parameters, the angle between the interatomic vector and the external magnetic field *and* the squared order parameter S^2_{RDC} are fitted to only *one* observable, the experimental RDC. Therefore, additional sets of RDCs are necessary to define the structure and dynamics of the molecule simultaneously. However, this in turn introduces the difficulty to find alignment media that do not modify these parameters.

5.5 Conclusion

With this study it could be shown that PDMS gels cross-linked by accelerated electrons and swollen in $CDCl_3$ are especially well-suited to measure D_{CH}-RDCs at solute concentrations and natural abundance. The gels do not alter the structure of the molecule under investigation as probed by comparison of the chemical shifts and are therefore applicable to refine structures of apolar molecules. Altogether 35 reliable RDCs could be extracted that have been used for structure refinement. For the structure calculations the 'class' protocol has been developed that facilitates the efficient and time-optimized generation of undistorted structures. In contrast to the previously reported crystal structure and the NOE-derived structure, structures resulting from RDC-refinement fulfill both NOE and RDC restraints. The obtained structures show a significant stronger bend than the NOE-derived structure, though they are not as heavily bended as the crystal structure. The influence of different RDC classes was tested and revealed that the inclusion of C^{β}-H^{β} is necessary to expose the correct bend of the structure. The sidechains are found to point straight into the solvent, displaying the time-averaging of several conformation. Finally, the influence of the alignment tensor on the resulting structure was tested and disclosed that the alignment tensor might be mis-set by $\pm 10\%$ for D_a and $\pm 15\%$ for R and still give suitable results. However, a full analysis including the variation of the initial values by $\pm 30\%$ for both D_a and R seems reasonable, since not every molecule is as well-behaving as cyclosporin A in chloroform. The potential impact of RDCs, as angular restraints relative to an external coordinate system, on the precision of structural models of the time-averaged conformation in solution has been demonstrated. The possibility of measuring RDCs at natural abundance in a variety of solvents opens up a wide range of future applications. As already discussed in the introduction, medicinal chemists might be enabled to optimize the drug discovery process. For example, the increased activity of the mono-N-methylated VEBER peptide analogue might be explained by an increased bend of the structure.[451]

Chapter 6

Summary

The present thesis covers a comparably wide range in the field of solution state NMR spectroscopy, i.e., it comprises theoretical and methodological studies as well as applied investigations. This ranges from the design and simulation of new pulse sequences through the incorporation of residual dipolar couplings into the structure determination process of small molecules to the structural and dynamical characterization of a protein. While for the first two topics the focus lies on the extraction and application of residual dipolar couplings (RDCs) as NMR parameter, the analysis of the protein is based on more classical parameters like the chemical shift, scalar couplings, and nuclear Overhauser enhancements (NOEs).

In Chapter 3 a theoretical framework was described which allows the straightforward determination of the average dipolar coupling Hamiltonian $\overline{\mathbf{D}}$ of two on-resonant spins-$\frac{1}{2}$. The results were verified and extended to include off-resonance effects by the use of the full quantum mechanical equations. The idea to investigate mixing sequences originally designed for heteronuclear Hartmann-Hahn transfer (HIHAHA) led to the development of the *J*-ONLY-TOCSY, which fully suppresses transfer through residual dipolar couplings while retaining the favourable transfer properties for scalar coupled spins of classical Hartmann-Hahn sequences in homonuclear spin systems. In addition, it could be shown that any purely phase alternating pulse sequence exhibits identical dipolar transfer properties for two on-resonant spins. Using the newly designed *J*-ONLY-TOCSY together with the other results obtained from simulations, a procedure could

be established that enables the measurement of scalar and residual dipolar ^{1}H-^{1}H-couplings which are commonly difficult to obtain. A protocol for the correct extraction of transfer amplitudes from spectra was described and a suitable fitting algorithm was selected, that allows a rapid analysis of the data. Experiments on a small test system showed that couplings could be extracted with an error smaller than 2 Hz which is comparable to results obtainable with other methods. Systematic influences caused by longitudinal and transverse cross-relaxation as well as influences by experimental noise were extensively studied with simulations and were found to be small. Furthermore, a method for the extraction of a good initial guess for the fitting routine and criterions for its validity were given. Finally, possible drawbacks of this methods and potential ways to overcome these problems have been discussed.

In the second part of the thesis (Chapter 4) the structure of the extracellular domain of the human bone morphogenetic protein receptor IA (BMPR-IA) in its unbound form was investigated. This protein belongs to a class of receptors that, together with a second type of receptors, bind the so-called transforming growth factors-β. A central question studying the binding mechanism between this class of receptors and the corresponding ligands concerns the binding promiscuity, i.e. how so few type I receptors (seven) may account for so many (> 30) ligands. Therefore, structural and dynamical studies were conducted. Though central parts of the protein exhibit an identical fold compared to the crystal structure of the receptor in complex with BMP-2, significant differences are found for loop regions. Especially, the large binding loop, which carries some of the major binding determinants for BMP-2, reveals large conformational changes upon binding. Here, an α-helix is formed in the bound form, while this is missing in the unbound form, but still exists in a nascent form which could be proven by titration studies with TFE. In addition, small order parameters were found for this binding loop, suggesting an disorder-to-order transition upon binding for the receptor. Hence, binding promoscuity can be explained by the ability to adapt to different ligands via the 'soft' binding interface. Despite the high flexibility of large parts of the protein, a rigid scaffold is still required to preserve the receptor activity, as shown by mutational studies. Here, a π-π-stacking interaction appears to be responsible for stabilization during folding of the extracellular domain of the receptor.

The third project, described in Chapter 5, concers the structural refinement of cyclic peptides using RDCs. Although nowadays RDCs are analyzed by default for proteins and nucleic acids, their wealth for the

elucidation of structural information of small molecules still seems underestimated. Here, the structure of the well-characterized, cyclic, undecapeptide cyclosporin A was redetermined. Beside the previously published NOE distance restraints, angular restraints relative to an external coordinate system based on experimental RDCs were included. The resulting structure was compared to the previously determined crystal structure and a structure solely based on NOE distance restraints. The study revealed a significant stronger bend of the peptide backbone for the RDC-refined structure compared to the NOE-derived structure, but a much smaller bend than the crystal structure. While the stronger bend of the crystal structure can be attributed to crystal packing artefacts, the difference between NOE-derived and RDC-refined structure reveals the deficiency of NOEs to monitor long range information, as no NOE restraint was violated upon addition of RDCs. For the use of residual dipolar couplings in the structure determination process of peptides a protocol could be established that allows for the easy and time-efficient inclusion of RDCs which is usually prone to errors. In addition, influences of a mis-set initial alignment tensor were investigated and a procedure was described to avoid these errors.

Appendix A

J-ONLY-TOCSY

A.1 Sample Preparation

For testing the various transfer properties of TOCSY mixing sequences in isotropic solution 6.6 mg CsA have been dissolved in 600 μL $CDCl_3$. The aligned sample was prepared using a cross-linked poly(dimethylsiloxane) gel (PDMS, diameter = 3.0 mm, cross-linked with 200 kGy of accelerated electrons) which was equilibrated in $CDCl_3$ (1 mL) in an NMR-tube for several days. After one week the sample showed a constant $CDCl_3$ quadrupolar deuterium splitting of $\Delta\nu_Q = 33$ Hz. This results in ^{1}H-^{1}H dipolar couplings between -35 Hz and 39 Hz for geminal protons in CH_2 moieties when assuming the alignment tensor determined by Klages *et al.*[114] with a linear scaling factor. Supernatant solvent was removed and CsA dissolved in $CDCl_3$ was added to a final concentration of approximately 34 mM in the gel. The sample could be analyzed after 2 days of incubation.

For fitting experimental TOCSY transfer amplitudes to the correspondig quantum mechanical equations and for tests of the zero-quantum suppression scheme two samples were prepared, an isotropic sample and an anisotropic sample. For the isotropic sample 70 mg 2,3-dibromopropionic acid have been dissolved in 600 μL $CDCl_3$. The resulting solution was filtered to give the final sample. The aligned sample was prepared using a cross-linked poly(styrene) gel (PS, diameter = 3.4 mm, cross-linked with 0.75% v/v divinyl-benzene and 0.05% w/v AIBN) which was equi-

librated in $CDCl_3$ (1 mL) in a NMR-tube for several days. After one week the sample showed a constant $CDCl_3$ quadrupolar deuterium splitting of $\Delta\nu_Q = 109$ Hz. Supernatant solvent was removed and 70 mg 2,3-dibromopropionic acid dissolved in $CDCl_3$ was added. The sample could be analyzed after 2 days of incubation.

A.2 TOCSY Spectra

A.2.1 Experimental

The experiments were recorded on a Bruker 600 MHz DMX spectrometer equipped with a triple resonance probe head with actively shielded x,y,z-gradients. The DIPSI-2 and the JESTER-1 multiple pulse sequences were both applied with rf-amplitudes of 6.25 kHz while 180° pulses in the MOCCA-XY16 sequence were applied with an rf-amplitude of 12.5 kHz resulting in an average introduced rf-power equivalent to continuous wave irradiation of constant rf-amplitude of 6.99 kHz. Spin-locking in the ROESY experiments was achieved via a cw spin-lock with a rf-power of 6.25 kHz. Unwanted background signals, resulting from the alignment medium, were suppressed using presaturation with cw-irradiation after a corresponding frequency jump of the carrier frequency. Zero-quantum suppression was achieved by the combination of adiabatic CHIRP pulses (with durations of 30 ms before and 50 ms after the TOCSY mixing period) and simultaneously applied pulsed field gradients. The gradient strengths of the corresponding gradients were adjusted by the procedure described by THRIPPELTON *et al.*[15] (see supplementary information there).

For testing the transfer properties of various mixing sequences, spectra with mixing times of 82.88 ms for DIPSI-2, 81.92 ms for MOCCA XY16, 80.64 ms for JESTER-1 (with MLEV16 and JESTER-1 XY16 expansion), and 80 ms for the ROESY, respectively, were recorded with 8 scans per increment. The spectral widths for ^{1}H were 7184 Hz and 7205 Hz, sampled with 1024 and 512 complex points, respectively. All dimensions were apodized with a $\pi/2$-shifted squared sine-bell function after zero-filling to provide a processed spectrum of 2048×2048 complex points.

Transfer amplitudes for testing the linearity of the zero-quantum suppression scheme were obtained from TOCSY spectra using DIPSI-2 mixing and a mixing time of 18.42 ms. The spectral widths for ^{1}H were 2404 Hz and 1801 Hz, sampled with 1024 and 256 complex points, respectively. All dimensions were apodized with a $\pi/2$-shifted squared sine-bell function

after zero-filling to provide a processed spectrum of 1024×512 complex points.

TOCSY spectra for the quantification of ^{1}H-^{1}H-couplings were acquired with increasing mixing times. For DIPSI-2 multiples of 4.604 ms have been used while for JESTER-1 XY16 multiples of 5.760 ms and for MOCCA XY16 multiples of 4.096 ms have been used, respectively. The spectral widths for ^{1}H were 2404 Hz and 1801 Hz, sampled with 1024 and 256 complex points, respectively. All dimensions were apodized with a $\pi/2$-shifted squared sine-bell function after zero-filling to provide a processed spectrum of 1024×512 complex points.

Quantification of transfer amplitudes was achieved using the software Sparky.[173] Volume integrals were extracted from the spectra using the 'Sum over Box' module. Volumes were normalized to the sum over all integrals along a TOCSY strip for all mixing sequences in isotropic and anisotropic samples. Only for DIPSI-2 mixing in anisotropic samples volume integrals were normalized to the diagonal signal at a mixing time of 4.096 ms.

A.2.2 Pulse Programs

```
;jk2ZQjesterzXY16prsp
;avance-version (19.02.2008)
;homonuclear Hartman-Hahn transfer
;JESTER sequence for mixing
;2 ZQfilter before and after TOCSY mixing
;phase sensitive

#include <Avance.incl>
#include <Delay.incl>
#include <Grad.incl>

"d11=30m"

"d12=20u"

"d0=in0/2-p1*4/3.1416"

1 ze
2 d11
```

```
d12
d1
3 p18:sp6:f1 ph29:r
5u
lo to 3 times l4
d12 pl1:f1
p1 ph1
d0
p1 ph2

3u pl0:f1 ;1st ZQfilter
50u UNBLKGRAD
300u gron1
p11:sp11:f1 ph4
100u groff
4u pl10:f1

;begin JESTER with XY-16 Supercycle

4 p6*1 ph10
p6*3 ph11 ;X
p6*5 ph10

p6*1 ph11
p6*3 ph12 ;Y
p6*5 ph11

p6*1 ph10
p6*3 ph11 ;X
p6*5 ph10

p6*1 ph11
p6*3 ph12 ;Y
p6*5 ph11

p6*1 ph11
p6*3 ph12 ;Y
p6*5 ph11
```

```
p6*1 ph10
p6*3 ph11 ;X
p6*5 ph10

p6*1 ph11
p6*3 ph12 ;Y
p6*5 ph11

p6*1 ph10
p6*3 ph11 ;X
p6*5 ph10

p6*1 ph12
p6*3 ph13 ;Xbar
p6*5 ph12

p6*1 ph13
p6*3 ph10 ;Ybar
p6*5 ph13

p6*1 ph12
p6*3 ph13 ;Xbar
p6*5 ph12

p6*1 ph13
p6*3 ph10 ;Ybar
p6*5 ph13

p6*1 ph13
p6*3 ph10 ;Ybar
p6*5 ph13

p6*1 ph12
p6*3 ph13 ;Xbar
p6*5 ph12

p6*1 ph13
p6*3 ph10 ;Ybar
p6*5 ph13
```

```
p6*1 ph12
p6*3 ph13 ;Xbar
p6*5 ph12

lo to 4 times l1

;end JESTER

4u 300u gron2 ;2nd ZQfilter
p12:sp12:f1 ph4
100u groff
50u BLKGRAD
4u pl1:f1
p1 ph3
go=2 ph31
d11 mc #0 to 2 F1PH(ip1 & ip29, id0)
exit

ph1=0 2
ph2=0 0 0 0 2 2 2 2
ph3=0 0 2 2
ph4=0
ph10=0
ph11=1
ph12=2
ph13=3
ph29=0
ph31=0 2 2 0 2 0 0 2

;pl1 :  f1 channel - power level for pulse (default)
;pl9 :  f1 channel - power level for presaturation
;pl10:  f1 channel - power level for TOCSY-spinlock
;p1 :  f1 channel - 90 degree high power pulse
;p6 :  f1 channel - 90 degree low power pulse
;p11:  1st ZQfilter adiabatic inversion pulse Crp_5_50kHz_30m_10
;p12:  2nd ZQfilter adiabatic inversion pulse Crp_5_50kHz_50m_10
;p18:  f1 channel - pulse for presaturation
;d0 :  incremented delay (2D)
```

```
;d1 :  relaxation delay; 1-5 * T1
;d9 :  TOCSY mixing time
;d11:  delay for disk I/O [30 msec]
;d12:  delay for power switching [20 usec]
;d13:  short delay [4 usec]
;sp11:  power for 1st ZQfilter
;sp12:  power for 2nd ZQfilter
;gpz1:  gradient strength for 1st ZQ suppression
;gpz2:  gradient strength for 2nd ZQ suppression
;l1:  loop for JESTER cycle:  ((p6*144) * l1) = mixing time
;l4:  p18 * l4 = total duration of presaturation
;use 100 msec pulse of square shape defined by 1000 points

;in0:  1/(1 * SW) = 2 * DW
;nd0:  1
;NS: 8 * n
;DS: 16
;td1:  number of experiments
;FnMODE: States-TPPI, TPPI, States or QSEC

;Processing

;PHC0(F1):  90
;PHC1(F1):  -180
;FCOR(F1):  1
```

A.3 Simulations

A.3.1 Calculating the Dipolar Coupling Tensor

Time evolution of the tensor elements $d'_{\alpha\beta}$ within the dipolar coupling tensor were calculated using a script written in MATHEMATICA.[452] Therefore, 3×3 rotation matrices were defined for the phase, tilt, and flip angle. For each pulse of the supercycle the effect of preceeding pulses was calculated first. This included the calculation of the consecutive product of all rotation matrices as described in Eq. 3.11. Then, the effect of the 'current' pulse was calculated by integrating over the pulse angle β with fixed phase and tilt angle. Summation over the contributions of all pulses and deviding

by the overall 'pulse length' (sum over all flip angles) led to the complete, average dipolar coupling tensor.

A.3.2 TOCSY and ROESY Offset Profiles

Simulations of offset profiles (±5 kHz in both dimensions) of TOCSY spectra for two coupled spins-$\frac{1}{2}$ were performed using the program SIMONE.[167] 64 single offsets were calculated along each dimension and coupling constants of $J = D = 10$ Hz and a mixing time of 50 ms were used for all calculations. Maximum rf-amplitudes have been 12.5 kHz for the MOCCA-XY16 sequence (with an inter pulse delay of 88 μs) and 6.25 kHz for all other sequences. No B_1-field inhomogeneity was considered. For quantification of the longitudinal and transverse weights the invariant trajectory has been simulated and subsequently were calculated according to Eq. 2.40 and Eq. 2.41.

A.3.3 Fitting of Experimental Transfer Amplitudes

Fitting of experimentally obtained transfer amplitudes in TOCSY spectra was achieved using an in-house written program implemented using MATLAB. The key function of this program uses a standard fitting algorithm of MATLAB called 'LSQCURVEFIT'. This algorithm is based on the minimisation of squared differences between the input values and the back-calculated values. As input served the normalized transfer amplitudes extracted from diagonal- or cross-peaks in TOCSY spectra acquired with various mixing sequences (DIPSI-2, MOCCA-XY16, and JESTER-XY16) and different mixing times. The function to calculate the theoretical transfer amplitudes is based on Eq. 3.28, where U is taken from Eq. 3.27 with $\mathcal{H}_{eff}$ being $\overline{\mathcal{H}_{cyl}}$ from Eq. 3.6. $\mathcal{H}_J$ is the classical isotropic coupling Hamiltonian as described in Eq. 3.3 and Eq. 3.25 and $\mathcal{H}_D$ is the mixing sequence dependent coupling Hamiltonian for the dipolar coupling as described in Eq. 3.26 with $\mathbf{D}$ taken from Sec. 3.2.2 and KRAMER *et al.*[146] In detail the following coupling Hamiltonians for the dipolar coupling were used: $\mathcal{H}_D = \sum_{i<j}^{n} 0.74 \cdot 2\pi D(-0.5 I_{ix} I_{jx} - 0.5 I_{iy} I_{jy} + I_{iz} I_{jz})$ for MOCCA-XY16, $\mathcal{H}_D = \sum_{i<j}^{n} -0.5 \cdot 2\pi D(I_{ix} I_{jx} - 0.5 I_{iy} I_{jy} - 0.5 I_{iz} I_{jz})$ for DIPSI-2, and $\mathcal{H}_D = 0$ for JESTER-XY16. No offset dependence for the tranfer function was considered. Moreover scalar and dipolar couplings were limited to a range from -25 to $+25$ Hz and intial values for the fitting procedure were extracted from the experimental data via the '$\sin^2$-approximation'.

Appendix B

Structure and Dynamics of BMPR-IA$_{ec/sf}$

B.1 Sample Preparation

Protein Expression and Purification

The extracellular domain of BMPR-IA was expressed as thioredoxin fusion protein as described elsewhere.[453] To facilitate the production of active, monomeric BMPR-IA$_{ec}$ trigger factor was co-expressed (expression vector pTf16, Takara Bioscience). Isotopic labeling of the receptor ecto domains was achieved by expressing in *E. coli* BL21 (DE3) grown in M9 minimal medium according to published protocols.[454] For incorporation of ^{15}N the medium was supplemented with 0.5 g/L $^{15}NH_4Cl$ (98%, CK Gas Products Ltd., UK). For incorporation of ^{15}N and ^{13}C the medium was supplemented with 0.5 g/L $^{15}NH_4Cl$ and 3 g/L U-$^{13}C_6$-Glucose (99%, CK Gas Products Ltd., UK). Prior to induction of recombinant protein production with 1 mM IPTG another 1 g/L U-$^{13}C_6$-Glucose was added.

Because of the high degree of flexibilty for the N-terminal tail of BMPR-IA$_{ec}$ the first 27 N-terminal residues were removed to yield the BMPR-IA$_{ec/sf}$ variant which was used in all studies reported here. However, these N-terminal amino acids are essential for expression and purification of the protein. Therefore, a PreScission protease recognition sequence was introduced after the first 21 N-terminal residues of BMPR-IA$_{ec}$ (E22I, N23E,

G24V, V25L, T226F, L27Q, A28G).

E. coli BL21(DE3) cells harboring the expression and chapperone plasmid were cooled to 21°C after reaching an OD_{600} of 0.6. At 21°C expression of trigger factor was induced by adding 0.25 g/L arabinose (Fluka). Around 30 min later production of BMPR-IA$_{ec/sf}$ was triggered by adding 1 mg IPTG. Celles were grown over night, harvested, and disrupted by sonication. After centrifugation the supernatant solution was applied to a nickel affinity column (Ni-NTA, Qiagen). Cleavage of the BMPR-IA$_{ec/sf}$ thioredoxin fusion protein was achieved by adding 0.3 U thrombin (Sigma) per 1 g fusion protein. Thioredoxin and BMPR-IA$_{ec/sf}$ were seperated by anion exchange chromatography using EMD-TMAE material (Merck). PreScission protease cleavage of the N-terminal residues was carried out in the anion exchange chromatography elution buffer (20 mM TRIS, pH 8.0, 150 mM NaCl) using 10 U PreScission protease per 1 mg recombinant protein at 4°C over night. Active and monomeric BMPR-IA$_{ec/sf}$ was obtained after a BMP-2 affinity chromatography step. The protein yield of ^{15}N,^{13}C-BMPR-IA$_{ec/sf}$ was 0.6 mg/L minimal medium, ^{15}N-BMPR-IA$_{ec/sf}$ could be obtained in similar amounts (0.6 mg/L minimal medium). Protein homogeneity was analyzed by SDS-PAGE and ESI-FTIR-MS.

Mass spectrometric analysis of [^{15}N,^{13}C]-BMPR-IA$_{ec/sf}$ showed an m/z ratio of 1480.579 for the 8-fold charged ion which differs from the calculated m/z ratio (m/z = 1484.420 for 100% ^{13}C and 100% ^{15}N) by $\Delta m/z$ = 3.841. This difference can be attributed to incomplete incorporation of the isotopes. Most likely [^{15}N,^{13}C]-BMPR-IA$_{ec/sf}$ was yielded containing 98% ^{15}N and 94% ^{13}C.

The concentration of the [^{15}N,^{13}C]-BMPR-IA$_{ec/sf}$ sample used for NMR analysis was 0.5 mM in 10 mM potassium phosphate buffer pH 6.3, 0.2% w/v NaN_3, 5% v/v D_2O. The ^{15}N-BMPR-IA$_{ec/sf}$ sample was dissolved in the same buffer at a concentration of 1.1 mM.

Anisotropic Sample

Polyacrylamide gels were prepared using 200 μL of an acrylamide stock solution, 800 μL doubly destilled water, 10 μL 10% w/w APS, and 1 μL TMEDA. The acrylamide stock solution contained 30% w/w acrylamide and 0.8% w/w bisacrylamide. All components were mixed and pipetted into glass tubes with an inner diameter of 3.4 mm that were sealed at one end. Gels were polymerised over night and subsequently squeezed out. The obtained gels were cut into pieces of 2.6 mm length, washed over night by incubating them in doubly distilled water and finally dried at

room temperature.

To align BMPR-$IA_{ec/sf}$ the dried gel was put into a Shigemi tube and 300 μL of protein solution were added. Afterwards the Shigemi plunger was adjusted in a way that the gel was allowed swell to a maximum length of 1.8 mm. This resulted in a constant quadrupolar splitting of $\approx$ 2Hz of the residual D_2O signal after 2 days.

B.2 Experiments and Assignment of BMPR-IA$_{ec/sf}$

TABLE B.1: Experiments performed on *apo*-BMPR-IA$_{ec/sf}$.

Experiment	Nuclei	NS	Time domain	Data matrix
NHSQC	$^{1}H\times^{15}N$	4	512× 64	1024× 256
CHSQC	$^{1}H\times^{13}C$	4	512×128	1024×1024
HNCO	$^{1}H\times^{15}N\times^{13}C$	8	512× 36× 45	1024× 128× 256
CBCACONH	$^{1}H\times^{15}N\times^{13}C$	16	512× 36× 45	1024× 128× 256
HNCA	$^{1}H\times^{15}N\times^{13}C$	16	512× 36× 45	1024× 128× 256
HNCACB	$^{1}H\times^{15}N\times^{13}C$	16	512× 36× 50	1024× 128× 256
HNCACO	$^{1}H\times^{15}N\times^{13}C$	32	512× 36× 52	1024× 128× 256
HNCAHA	$^{1}H\times^{15}N\times^{1}H$	16	512× 28× 36	1024× 128× 128
CCCONH	$^{1}H\times^{15}N\times^{13}C$	16	512× 36× 70	1024× 128× 256
HNHA	$^{1}H\times^{15}N\times^{1}H$	16	512× 36× 64	1024× 128× 160
HBHACONH	$^{1}H\times^{15}N\times^{1}H$	16	512× 36× 61	1024× 128× 256
HNHB	$^{1}H\times^{15}N\times^{1}H$	32	512× 32× 54	1024× 256× 128
CCHcosy	$^{1}H\times^{13}C\times^{13}C$	8	512× 36× 45	1024× 128× 256
HCHtocsy	$^{1}H\times^{13}C\times^{1}H$	16	512× 32× 64	1024× 160× 256
CCHtocsy	$^{1}H\times^{13}C\times^{13}C$	16	512× 45× 95	1024× 256× 256
CNHnoesy	$^{1}H\times^{15}N\times^{13}C$	16	512× 36× 71	1024× 128× 128
HNHnoesy	$^{1}H\times^{15}N\times^{1}H$	16	512× 36× 80	1024× 128× 512
NNHnoesy	$^{1}H\times^{15}N\times^{15}N$	32	512× 32× 36	1024× 128× 256
HCHnoesy	$^{1}H\times^{13}C\times^{1}H$	8	512× 38× 64	1024× 128× 256
DQ 90	$^{1}H\times^{1}H$	16	512×400	1024×1024
IPCOSY	$^{1}H\times^{1}H$	16	512×400	1024×1024
TOCSY.noN	$^{1}H\times^{1}H$	16	512×400	1024×1024

Table B.2: Backbone and sidechain assignments of BMPR-IA$_{ec/sf}$. If diastereotopic assignments are available HX1 is written first.

Residue	HN (N)	CO	HA (CA)	HB (CB)	HG (CG)	HD (CD)
G28	–	–	–	–	–	–
P29	–	174.53	4.31 (64.38)	2.21, 1.83 (32.30)	1.95 (27.38)	3.59, 3.47 (49.90)
E30	9.01 (118.79)	173.73	4.17 (57.56)	1.86, 2.00 (29.40)	2.20 (36.36)	–
D31	7.94 (119.92)	173.60	4.56 (54.94)	2.62 (41.65)	–	–
T32	7.81 (113.57)	171.63	4.16 (62.41)	4.09 (70.04)	1.10 (21.87)	–
L33	8.10 (125.79)	172.44	4.49 (53.43)	1.41, 1.49 (41.90)	1.55 (27.15)	0.76 (25.40), 0.76 (23.46)
P34	–	173.65	4.13 (63.66)	1.99, 1.70 (31.97)	1.90 (27.62)	3.72, 3.53 (50.55)
F35	7.61 (117.67)	171.11	4.58 (57.69)	2.89, 2.93 (40.85)	–	7.13
L36	8.31 (125.15)	171.05	4.42 (54.77)	1.35, 0.90 (44.23)	1.20 (26.73)	0.56 (23.74), 0.59 (26.81)
K37	8.13 (123.55)	172.47	5.11 (54.73)	1.50 (35.01)	1.19, 1.29 (25.61)	1.53 (29.77)
C38	9.24 (121.58)	171.75	4.89 (51.95)	2.88, 2.94 (41.36)	–	–
Y39	8.83 (122.39)	172.26	4.78 (58.50)	2.32, 2.52 (40.90)	–	6.87, 6.66
C40	7.69 (–)	–	4.42 (53.85)	2.72 (48.92)	–	–
S41	7.85 (117.02)	–	4.16 (58.45)	3.68 (63.84)	–	–
G42	–	–	–	–	–	–
H43	–	–	4.88 (54.77)	2.80, 3.45 (29.49)	–	–
C44	8.56 (–)	–	–	–	–	–
P45	–	174.66	4.66 (62.50)	2.41, 2.22 (33.14)	2.25, 1.97 (27.65)	– (50.23)
D46	8.80 (120.17)	173.43	4.25 (57.19)	2.62, 2.67 (40.72)	–	–
D47	8.05 (114.67)	173.50	4.51 (52.84)	2.48, 2.90 (39.98)	–	–
A48	7.35 (122.66)	174.49	4.28 (53.43)	1.26 (20.87)	–	–
I49	7.96 (119.55)	173.30	4.24 (60.23)	1.62 (40.28)	0.97 (27.20), 0.77 (17.36)	0.74 (12.88)
N50	9.28 (125.47)	–	4.29 (54.66)	2.71, 2.91 (37.62)	–	–
N51	8.85 (–)	170.66	4.07 (56.08)	2.79, 3.06 (37.43)	–	7.61, 8.55 (116.80)
T52	7.19 (105.82)	169.91	5.37 (59.89)	3.89 (73.94)	1.02 (22.12)	–
C53	8.96 (116.07)	168.78	5.00 (52.56)	2.57, 3.59 (48.65)	–	–
I54	8.53 (120.17)	173.40	5.21 (59.20)	1.52 (40.22)	0.94, 1.33 (27.40), 0.67 (17.94)	0.63 (13.05)
T55	9.20 (120.75)	168.37	4.80 (60.06)	3.73 (70.49)	0.83 (19.62)	–
N56	8.00 (120.88)	172.88	4.92 (52.62)	2.90, 2.37 (38.92)	–	6.93, 7.44 (110.61)
G57	8.51 (111.38)	169.02	3.96, 4.14 (45.80)	–	–	–
H58	8.56 (120.87)	171.20	4.71 (56.14)	3.25, 2.79 (34.65)	–	–
C59	8.71 (117.29)	173.47	5.70 (52.34)	3.06, 2.96 (36.95)	–	–
F60	8.70 (116.07)	172.20	6.11 (56.63)	2.89, 2.99 (44.83)	–	6.69, 6.93, 6.80
A61	9.20 (125.17)	171.61	5.00 (52.32)	1.31 (23.95)	–	–
I62	9.47 (120.63)	170.85	5.35 (59.26)	1.61 (43.66)	0.83, 1.53 (28.92), 0.89 (17.22)	0.62 (14.67)
I63	8.50 (125.83)	170.51	5.24 (59.13)	1.50 (41.67)	1.46, 0.81 (29.18), 0.73 (17.00)	0.80 (14.38)
E64	8.45 (124.57)	171.41	5.01 (54.83)	1.88, 1.84 (34.32)	2.02, 2.05 (36.76)	–
E65	8.30 (123.96)	172.92	5.04 (54.76)	1.97, 1.76 (33.47)	2.42, 1.91 (36.52)	–
D66	8.47 (124.87)	174.94	4.75 (52.89)	2.64, 3.21 (41.99)	–	–
D67	8.38 (116.22)	174.21	4.31 (56.35)	2.64 (40.51)	–	–
Q68	8.20 (117.19)	173.74	4.38 (55.59)	2.28, 2.06 (29.78)	2.28 (34.70)	–
G69	8.00 (108.13)	171.65	4.14, 3.63 (45.73)	–	–	–

Table B.2: continued.

Residue	HN (N)	CO	HA (CA)	HB (CB)	HG (CG)	HD (CD)
E70	8.41 (122.30)	173.97	4.45 (56.02)	1.99, 2.03 (30.30)	2.07, 2.22 (36.43)	–
T71	8.62 (117.33)	172.16	5.21 (61.60)	3.91 (71.00)	1.04 (22.35)	–
T72	8.76 (117.84)	169.60	4.50 (61.27)	3.96 (72.32)	1.09 (21.83)	–
L73	8.40 (126.02)	173.15	5.25 (54.30)	1.65, 1.42 (44.86)	1.52 (28.05)	– (25.40), 0.85 (25.00)
A74	–	172.74	4.76 (51.44)	1.44 (23.35)	–	–
S75	8.70 (111.40)	171.59	4.50 (57.74)	3.86, 3.58 (65.70)	–	–
G76	6.44 (105.48)	167.89	3.73, 3.85 (47.42)	–	–	–
C77	8.74 (118.96)	170.67	4.95 (60.03)	2.77, 3.08 (46.00)	–	–
M78	9.24 (122.34)	171.99	4.76 (54.63)	1.88, 1.68 (35.81)	2.38, 2.38 (31.84)	–
K79	8.43 (125.03)	173.04	4.16 (57.12)	1.81 (33.72)	1.42 (24.75)	1.66 (29.74)
Y80	8.40 (121.42)	173.37	4.20 (59.91)	2.72 (39.00)	–	–
E81	8.49 (123.79)	173.24	4.17 (56.44)	1.72, 1.94 (30.86)	2.06 (36.21)	–
G82	7.20 (108.40)	171.52	3.69, 4.05 (45.68)	–	–	–
S83	8.14 (114.65)	171.90	4.28 (59.27)	3.78 (63.96)	–	–
D84	8.34 (121.23)	173.10	4.43 (54.95)	2.41, 2.48 (40.84)	–	–
F85	7.73 (118.92)	172.59	4.26 (58.52)	2.78 (39.84)	–	6.90, 7.00, 6.96
Q86	7.79 (120.28)	172.55	4.07 (56.00)	1.84, 1.67 (30.60)	2.12 (33.93)	–
C87	8.10 (118.79)	170.91	4.14 (56.81)	2.61, 2.94 (40.78)	–	–
K88	7.61 (120.33)	172.33	4.28 (56.21)	1.56, 1.67 (34.21)	1.21 (24.61)	1.53 (29.39)
D89	8.18 (121.19)	172.97	4.50 (54.20)	2.46 (42.09)	–	–
S90	8.19 (116.71)	170.24	4.64 (56.60)	3.74 (63.77)	–	–
P91	–	174.29	4.35 (63.80)	2.21, 1.85 (32.41)	1.93 (27.62)	3.69, 3.62 (50.98)
K92	8.24 (120.18)	173.33	4.21 (56.41)	1.64, 1.77 (33.23)	1.33 (25.08)	1.58 (29.31)
A93	8.04 (124.05)	174.58	4.21 (53.02)	1.33 (19.76)	–	–
Q94	8.32 (117.93)	172.78	4.19 (56.75)	2.08, 1.93 (29.10)	2.27 (34.28)	–
L95	7.73 (120.47)	174.27	4.36 (54.97)	1.55 (43.12)	1.49 (27.30)	0.78 (23.59), 0.81 (25.38)
R96	8.60 (121.67)	171.70	4.23 (56.57)	1.79 (30.66)	1.66 (27.32)	3.08, 3.12 (43.81)
R97	7.80 (120.13)	172.12	5.17 (55.26)	1.70 (34.04)	1.43 (26.65)	3.02 (44.44)
T98	8.61 (118.55)	169.25	4.60 (62.03)	3.77 (71.97)	1.18 (23.33)	–
I99	8.52 (125.23)	170.93	5.08 (59.37)	1.47 (42.14)	0.88, 1.47 (29.27), 0.74 (16.72)	0.44 (14.41)
E100	8.86 (125.68)	172.20	4.67 (55.84)	1.91, 1.68 (34.41)	2.14 (36.54)	–
C101	8.83 (119.26)	170.36	5.79 (55.01)	3.05 (45.32)	–	–
C102	9.13 (116.46)	170.67	5.00 (56.18)	3.40, 3.51 (46.09)	–	–
R103	9.24 (122.52)	172.12	4.80 (56.23)	1.49, 2.06 (32.61)	1.57 (29.76)	2.82, 3.03 (44.02)
T104	7.44 (109.73)	171.89	4.60 (61.27)	4.26 (72.49)	1.12 (22.35)	–
N105	8.59 (119.36)	174.15	4.79 (55.87)	2.70, 2.56 (39.26)	–	6.99, 7.66 (113.19)
L106	9.98 (118.23)	175.05	3.68 (56.79)	1.78, 1.92 (38.92)	1.38 (27.55)	0.83 (25.48), 0.54 (22.71)
C107	8.25 (115.46)	172.47	4.32 (58.37)	4.02, 3.18 (46.09)	–	–
N108	8.59 (118.04)	172.21	4.43 (53.32)	2.78, 2.27 (37.29)	–	–
Q109	7.49 (121.35)	172.30	3.38 (58.94)	1.35, 1.57 (28.77)	0.81, 1.03 (32.30)	–
Y110	7.83 (114.60)	–	4.59 (56.49)	3.24, 2.51 (38.40)	–	6.96
L111	6.61 (120.14)	172.88	4.17 (55.25)	1.33, 1.46 (43.40)	– (27.54)	0.70 (23.31), 0.68 (25.03)
Q112	8.78 (122.79)	169.48	4.57 (53.11)	1.78, 1.92 (3–)	2.14 (33.85)	–
P113	–	172.26	4.40 (63.04)	2.13, 1.70 (32.40)	– (27.56)	3.29, 3.39 (50.52)

Table B.2: continued.

Residue	HN (N)	CO	HA (CA)	HB (CB)	HG (CG)	HD (CD)
T114	8.18 (111.93)	172.18	4.40 (60.96)	4.00 (71.29)	1.12 (21.89)	–
L115	8.58 (125.29)	171.74	4.30 (53.23)	1.23, 1.49 (41.90)	– (26.74)	0.74 (26.28), 0.67 (24.56)
P116	–	–	4.63 (61.58)	1.85, 2.27 (30.98)	1.95, 2.03 (27.55)	3.30, 3.76 (50.53)
P117	–	174.10	4.35 (63.01)	2.21, 1.77 (32.30)	– (27.63)	– (50.53)
V118	8.19 (120.46)	173.27	3.90 (62.89)	1.90 (32.98)	–	–
V119	8.18 (125.03)	172.96	4.04 (62.25)	1.91 (33.28)	–	–
I120	8.22 (125.69)	173.44	4.11 (61.05)	1.76 (39.03)	– (27.36), – (17.69)	0.76 (12.82)
G121	8.19 (113.15)	169.08	3.94, 4.05 (44.85)	–	–	–
P122	–	173.92	4.27 (63.34)	2.09, 1.63 (32.16)	– (27.27)	3.47 (49.93)
F123	8.14 (119.41)	172.70	4.51 (58.04)	2.89 (39.71)	–	–
F124	8.00 (122.18)	172.14	4.49 (58.00)	2.97 (40.14)	–	–
D125	8.10 (123.00)	173.87	4.40 (54.47)	2.63, 2.55 (41.39)	–	–
G126	8.01 (109.28)	171.64	3.86 (45.86)	–	–	–
S127	8.11 (115.76)	171.52	4.32 (59.19)	3.76 (64.24)	–	–
I128	7.96 (122.05)	172.59	4.11 (61.80)	1.79 (38.82)	1.09, 1.39 (27.42), 0.82 (17.71)	0.77 (13.15)
R129	7.85 (130.07)	178.04	4.12 (57.54)	1.60, 1.73 (32.10)	1.46 (27.34)	3.05 (43.67)

B.3 Dihedral Angle Restraints for BMPR-IA$_{ec/sf}$

TABLE B.3: TALOS backbone dihedral angle restraints (ϕ & ψ) and sidechain (χ^1 & χ^2) dihedral angle restraints of BMPR-IA$_{ec/sf}$. In addition, $^3J_{H^N H^\alpha}$-couplings of BMPR-IA$_{ec/sf}$ are tabulated.

Residue	$\phi \pm \Delta\phi$ [°]	$\psi \pm \Delta\psi$ [°]	$\chi^1 \pm \Delta\chi^1$ [°]	$\chi^2 \pm \Delta\chi^2$ [°]	$^3J_{H^N H^\alpha} \pm \Delta J$ [Hz]
G28	–	–	–	–	–
P29	–	–	−25±5	45±5	–
E30	–	–	–	–	5.71±1.0
D31	–	–	–	–	6.54±1.0
T32	–	–	−60±30	0±0	–
L33	−103±39	135±16	0±0	180±30	6.07±1.0
P34	–	–	−25±5	45±5	–
F35	–	–	60±30	0±0	–
L36	–	–	180±30	60±30	7.68±1.0
K37	−123±23	137±22	–	–	7.98±1.0
C38	−98±23	121±19	–	–	9.21±1.0
Y39	−99±30	150±23	180±30	0±0	6.30±1.0
C40	−132±29	155±18	–	–	–
S41	−88±35	139±23	–	–	–
G42	–	–	–	–	–
H43	−99±25	131±19	–	–	–
C44	−103±35	126±39	180±30	0±0	–
P45	−59±12	141±15	–	–	–
D46	−59±15	−25±21	–	–	–
D47	−90±18	1±13	60±30	0±0	–
A48	−73±13	136±26	–	–	–
I49	−108±18	134±18	−60±30	180±30	–
N50	–	–	60±30	0±0	–
N51	53±11	45±19	–	–	–
T52	−132±23	159±20	60±30	0±0	–
C53	−135±19	142±23	60±30	–	8.11±1.0
I54	−118±23	131±19	−60±30	180±30	8.93±1.0
T55	−136±30	148±27	180±30	0±0	–
N56	–	–	60±30	0±0	9.34±1.0
G57	–	–	–	–	–
H58	−115±38	153±19	−60±30	0±0	8.15±1.0
C59	−101±17	125±14	−90±90	0±0	8.18±1.0
F60	−138±20	157±21	–	–	8.04±1.0
A61	−141±17	132±22	–	–	7.21±1.0
I62	−131±16	136±13	180±30	180±30	8.42±1.0
I63	−128±21	132±13	180±30	180±30	8.40±1.0
E64	−126±24	133±16	−60±30	0±0	6.45±1.0
E65	−127±25	134±19	180±30	−60±30	7.92±1.0
D66	−78±13	150±25	60±30	0±0	7.87±1.0
D67	−64±17	−19±31	–	–	4.24±1.0
Q68	−93±16	−5±18	−60±30	0±0	9.34±1.0
G69	87±14	10±11	–	–	–
E70	−81±21	140±17	–	–	7.92±1.0
T71	−119±24	139±18	120±90	0±0	7.77±1.0
T72	−121±23	131±18	60±30	0±0	8.69±1.0
L73	−121±30	141±19	−60±30	0±0	8.34±1.0
A74	−140±28	152±17	–	–	–
S75	−112±31	146±21	60±30	0±0	7.11±1.0
G76	–	–	–	–	–
C77	−83±30	132±16	−60±30	0±0	8.64±1.0
M78	−119±26	143±21	180±30	180±30	8.56±1.0
K79	−79±18	142±30	60±30	180±30	4.71±1.0
Y80	–	–	–	–	4.20±1.0
E81	–	–	–	–	–
G82	–	–	–	–	–
S83	–	–	–	–	5.68±1.0

Table B.3: continued.

Residue	$\phi \pm \Delta\phi$ [°]	$\psi \pm \Delta\psi$ [°]	$\chi^1 \pm \Delta\chi^1$ [°]	$\chi^2 \pm \Delta\chi^2$ [°]	${}^3J_{HNH\alpha} \pm \Delta J$ [Hz]
D84	–	–	–	–	6.38±1.0
F85	–	–	–	–	6.03±1.0
Q86	–	–	−60±30	0±0	5.79±1.0
C87	–	–	–	–	–
K88	–	–	–	–	6.40±1.0
D89	–	–	–	–	–
S90	–	–	–	–	6.04±1.0
P91	–	–	25±5	−45±5	–
K92	–	–	–	–	6.46±1.0
A93	–	–	–	–	5.71±1.0
Q94	–	–	–	–	–
L95	–	–	–	–	–
R96	−100±31	142±30	–	–	–
R97	−131±30	144±21	–	–	5.72±1.0
T98	−115±19	133±16	−60±30	0±0	–
I99	−125±18	137±19	180±30	180±30	7.52±1.0
E100	−133±27	144±18	−60±30	0±0	7.73±1.0
C101	−120±23	140±23	–	–	8.49±1.0
C102	−130±27	145±19	60±30	0±0	5.87±1.0
R103	–	–	–	–	8.70±1.0
T104	–	–	60±10	0±0	–
N105	–	–	60±30	0±0	–
L106	–	–	−60±30	180±30	6.58±1.0
C107	−72±16	−36±14	60±30	0±0	4.29±1.0
N108	−76±20	−41±18	−60±30	0±0	–
Q109	–	–	180±30	0±0	3.79±1.0
Y110	−106±23	6±10	−60±30	0±0	8.59±1.0
L111	−113±31	119±10	–	–	–
Q112	−94±24	141±20	180±30	0±0	7.88±1.0
P113	−64±12	149±15	–	–	–
T114	−112±27	127±23	60±30	0±0	8.39±1.0
L115	−102±32	132±23	−60±30	180±30	5.27±1.0
P116	−63±13	148±15	–	–	–
P117	−80±33	146±24	–	–	–
V118	–	–	180±30	0±0	6.44±1.0
V119	–	–	–	–	7.70±1.0
I120	–	–	–	–	7.76±1.0
G121	–	–	–	–	–
P122	–	–	−25±5	45±5	–
F123	–	–	–	–	6.93±1.0
F124	–	–	–	–	5.34±1.0
D125	–	–	–	–	6.96±1.0
G126	–	–	–	–	–
S127	–	–	–	–	6.49±1.0
I128	–	–	−60±30	0±0	7.79±1.0
R129	–	–	180±30	0±0	7.65±1.0

B.4 Structural Indicators

TABLE B.4: Results from MOLPROBITY for the final structure ensemble of 20 simulated annealing structures.

Model	Clash score[a]	Rot. outliers[b]	Ram. outliers[c]	Ram. allowed[d]	MolProbity score
1	0	0.0	0.0	90.0	1.05
2	0	0.0	0.0	88.0	1.10
3	0	0.0	0.0	87.0	1.12
4	0	0.0	0.0	86.0	1.14
5	0	0.0	0.0	90.0	1.05
6	0	0.0	0.0	88.0	1.10
7	0	0.0	0.0	91.0	1.02
8	0	0.0	0.0	86.0	1.14
9	0	0.0	0.0	90.0	1.05
10	0	0.0	0.0	86.0	1.14
11	0	0.0	0.0	85.0	1.16
12	0	0.0	0.0	87.0	1.12
13	0	0.0	0.0	87.0	1.12
14	0	0.0	0.0	86.0	1.14
15	0	0.0	0.0	87.0	1.12
16	0	0.0	0.0	88.0	1.10
17	0	0.0	0.0	86.0	1.14
18	0	0.0	0.0	89.0	1.08
19	0	0.0	0.0	83.0	1.19
20	0	0.0	0.0	84.0	1.18

[a] Number of atoms which share a distance with a neighbouring atom which is smaller than the sum of their van der Waals radii.

[b] Amount of residues (in percent) an uncommon combination of χ^1- and χ^2-angles ('rotamer outliers').

[c] Amount of residues (in percent) with a very uncommen combination of Φ- and Ψ-angles leading to a location in the Ramachandran map which is commonly not populated ('Ramachandran outliers').

[d] Amount of residues (in percent) with a less commen combination of Φ- and Ψ-angles leading to a location in the Ramachandran map which is commonly only sparsely populated though still observed ('Ramachandran allowed').

B.5 Dynamical Parameters of BRIA

Table B.5: Results of the model-free analysis for BMPR-IA$_{ec/sf}$. For each residue the corresponding model chosen is reported and the resulting squared order parameter S^2. In dependence of the model additional parameters are given, e.g., S_f^2, τ_i, and R_{ex}.

Residue	Model	S^2	S_f^2	τ_i [ps]	R_{ex} [s^{-1}]	Γ_i
E30	5	0.075±0.011	0.618±0.028	748±17	–	0.000
D31	5	0.122±0.016	0.741±0.032	738±22	–	0.000
T32	5	0.151±0.014	0.631±0.025	1092±19	–	0.000
L33	5	0.232±0.020	0.663±0.024	1288±45	–	0.000
F35	5	0.429±0.032	0.696±0.025	1883±239	–	0.000
L36	5	0.547±0.041	0.735±0.027	2046±805	–	0.000
K37	2	0.718±0.025	–	30±8	–	3.510
C38	1	0.820±0.029	–	–	–	0.335
Y39	1	0.851±0.032	–	–	–	0.977
S41	3	0.762±0.038	–	–	16.593±1.350	0.262
D46	3	0.776±0.039	–	–	16.690±1.316	0.026
D47	1	0.781±0.028	–	–	–	4.423
A48	3	0.858±0.044	–	–	8.013±1.112	0.791
I49	2	0.758±0.029	–	43±10	–	0.039
T52	1	0.935±0.033	–	–	–	2.244
C53	1	1.000±0.019	–	–	–	11.498
I54	1	0.857±0.031	–	–	–	0.167
T55	1	0.862±0.030	–	–	–	2.020
N56	1	0.813±0.028	–	–	–	2.913
G57	1	0.814±0.028	–	–	–	4.808
H58	1	0.871±0.029	–	–	–	0.666
C59	1	0.851±0.031	–	-	–	1.575
F60	1	0.899±0.032	–	–	–	3.747
A61	1	0.845±0.030	–	–	–	3.132
I62	1	0.878±0.029	–	–	–	3.773
I63	1	0.949±0.033	–	–	–	4.124
E64	1	0.849±0.028	–	–	–	3.087
E65	1	0.788±0.027	–	–	–	1.440
D66	5	0.613±0.047	0.791±0.032	1782±632	–	0.000
D67	5	0.561±0.036	0.727±0.027	1276±219	–	0.000
Q68	5	0.531±0.035	0.707±0.026	1530±221	–	0.000
G69	5	0.555±0.040	0.767±0.030	1433±218	–	0.000
E70	2	0.769±0.033	–	68±25	–	0.481
T71	2	0.757±0.028	–	37±10	–	0.006
T72	3	0.801±0.041	–	–	5.336±0.883	0.122
S75	3	0.861±0.043	–	–	3.625±0.853	2.149
C77	1	0.802±0.027	–	–	–	1.481
M78	1	0.840±0.029	–	–	–	0.962
K79	1	0.734±0.026	–	–	–	1.220
Y80	5	0.536±0.034	0.766±0.028	1589±193	–	0.000
E81	4	0.764±0.039	–	49±16	10.182±1.055	0.000
G82	4	0.658±0.033	–	72±13	1.881±0.588	0.000
S83	1	0.688±0.024	–	–	–	2.953
D84	5	0.575±0.035	0.732±0.028	822±204	–	0.000
F85	4	0.643±0.033	–	39±7	4.039±0.637	0.000
Q86	4	0.852±0.041	–	54±53	4.550±0.918	0.000
C87	3	0.875±0.042	–	–	16.082±1.376	2.258
K88	1	1.000±0.022	–	–	–	3.269
D89	5	0.509±0.037	0.749±0.027	1367±171	–	0.000
S90	5	0.424±0.033	0.638±0.025	1434±193	–	0.000
K92	5	0.425±0.031	0.733±0.028	1080±92	–	0.000
A93	5	0.446±0.033	0.717±0.026	1214±139	–	0.000
Q94	5	0.349±0.027	0.692±0.026	1324±75	–	0.000
L95	5	0.569±0.037	0.731±0.026	898±215	–	0.000
R96	4	0.863±0.024	–	115±133	1.806±0.625	0.000

TABLE B.5: continued.

Residue	Model	S^2	S_f^2	τ_i [ps]	R_{ex} [s^{-1}]	Γ_i
R97	1	0.851±0.030	–	–	–	5.143
I99	1	0.906±0.033	–	–	–	0..898
E100	1	0.892±0.032	–	–	–	3.662
R103	1	0.808±0.028	–	–	–	9.211
T104	1	0.799±0.029	–	–	–	4.831
N105	1	0.832±0.029	–	–	–	6.087
L106	1	0.789±0.030	–	–	–	10.781
C107	2	0.804±0.028	–	52±15	–	0.132
N108	1	0.976±0.029	–	–	–	7.090
Q109	1	0.964±0.031	–	–	–	4.127
Y110	1	0.851±0.040	–	–	–	11.267
L111	1	0.875±0.031	–	–	–	16.318
Q112	2	0.690±0.025	–	31±6	–	2.782
T114	3	0.733±0.036	–	–	3.804±0.733	0.131
L115	2	0.757±0.027	–	39±10	–	1.864
V118	5	0.394±0.027	0.672±0.024	931±95	–	0.000
V119	5	0.028±0.007	0.577±0.028	513±17	–	0.000
I120	5	0.095±0.013	0.646±0.029	695±23	–	0.000
G121	5	0.073±0.013	0.632±0.028	812±21	–	0.000
F123	5	0.081±0.012	0.672±0.027	939±14	–	0.000
D125	5	0.053±0.010	0.672±0.029	879±14	–	0.000
G126	5	0.023±0.008	0.732±0.036	562±18	–	0.000
S127	5	0.017±0.010	0.645±0.029	857±16	–	0.000
I128	5	0.030±0.010	0.731±0.035	579±20	–	0.000

Appendix C

Structure Refinement of Peptides with RDCs

C.1 Sample Preparartion

Cyclosporin A was purchased from Fluka. For resonance assignment and measurement of J-couplings in isotropic solution, the peptide was dissolved in $CDCl_3$ to a final concentartion of 8.3 mM. The aligned sample was prepared from cross-linked poly(dimethylsiloxane) gel (PDMS, diameter = 3.6 mm, cross-linked with 100 kGy of accelerated electrons), which was equilibrated in $CDCl_3$ (700 μL) in a NMR tube for several days. After 1 week, the sample showed a constant quadrupolar deuterium splitting of the solvent of ν_Q = 40.4 Hz. Supernatant solvent was removed, and stock solution of CsA in $CDCl_3$ was added to a final concentration of approximately 5.8 mm in the gel. The sample could be analyzed after 2 days of incubation.

C.2 NMR Measurements for CsA

All NMR spectra were recorded at 295 K on a 600 MHz Bruker DMX sppectrometer equipped with a quadrupol-resonance probe head with actiely shielded x-, y-, and z-gradients. All spectra were processed by using XWINNMR and analyzed with either XWINNMR or SPARKY.[173]

Resonance assignments (Tab. C.1) were obtained from standard ^{1}H-TOCSY, ^{1}H-^{13}C-HSQC, ^{1}H-^{13}C-HMBC, and ^{1}H-ROESY spectra. Stereospecific assignments of the prochiral methylene and methylgroups were derived from the ROESY spectrum, which was acquired by using a pulsed-spin lock with a mixing time of 150 ms. $^{1}J_{CH}$-couplings in isotropic and anisotropic solution ere detremined from standard two-dimensional ^{1}H-^{13}C-HSQC spectra without decoupling during aquisition. The spectrum of the unaligned sample was recorded with 24 scans per increment. The spectral width for ^{1}H and ^{13}C were 5513 Hz and 12078 Hz, sampled with 2048 and 512 complex points, respectively. The spectrum of the aligned sample was recorded with 96 scans per increment. The spectral width for ^{1}H and ^{13}C were 6009 Hz and 15098 Hz, sampled with 4096 and 384 complex points, respectively. Linear prediction was applied to fill the indirect dimensions to 756 and 512 complex points for the isotropic nad aligned samples, respectively. All dimensions were apodized with a $\pi/2$-shifted squared sine-bell function before zero-filling to provide a processed spectrum of 4096×2048 complex points. RDCs were extracted from the spectra by using the approach by YAN *et al.*[438] Altogether 35 reliable D_{CH}-residual dipolar couplings with an estimated error of 1 Hz could be measured for nonoverlapped signals (Tab. C.2).

Table C.1: Assignments for cyclosporin A in $CDCl_3$ and PDMS/$CDCl_3$-gel. Chemical shifts have been referenced to the solvent signal ($CDCl_3$), i.e., 77.0 ppm for carbon and 7.26 ppm for protons.

		Isotropic solution		Anisotropic medium		CS difference	
Residue	Signal	^{13}C-shift	^{1}H-shift	^{13}C-shift	^{1}H-shift	Δ^{13}C-shift	Δ^{1}H-shift
MeBmt[1]	NCH_3	33.7	3.50	33.8	3.52	0.1	0.02
	α	58.4	5.44	58.6	5.48	0.2	0.04
	β	74.5	3.77	74.6	3.79	0.1	0.02
	δ^{pro-S}	35.4	1.64	35.5	1.65	0.1	0.01
	δ^{pro-R}	35.4	2.40	35.5	2.43	0.1	0.03
	γ^{m}	16.4	0.69	16.6	0.71	0.2	0.02
	η	17.8	1.62	17.8	1.63	0.0	0.01
Abu[2]	α	48.5	5.01	48.6	5.04	0.1	0.03
	β^{pro-S}	24.8	1.71	24.8	1.78	0.0	0.07
	β^{pro-R}	24.8	1.60	24.8	1.66	0.0	0.06
	γ^{m}	9.7	0.83	9.1	0.86	0.1	0.03
Sar[3]	NCH_3	39.2	3.37	39.3	3.40	0.1	0.03
	α^{pro-S}	50.1	4.73	50.1	4.74	0.0	0.01
	α^{pro-R}	50.1	3.21	50.1	3.21	0.0	0.00
MeLeu[4]	NCH_3	31.0	3.09	31.2	3.11	0.2	0.02
	α	55.2	5.32	55.3	5.35	0.1	0.03
	β^{pro-S}	35.7	1.97	35.7	2.00	0.0	0.03
	β^{pro-R}	35.7	1.62	35.8	1.64	0.1	0.02
	γ	24.6	1.40	24.7	1.43	0.1	0.03
	δ^{pro-S}	20.8	0.86	20.9	0.88	0.1	0.02
	δ^{pro-R}	23.2	0.93	23.3	0.95	0.1	0.02
Val[5]	α	55.1	4.64	55.2	4.65	0.1	0.01
	β	30.9	2.39	31.0	2.43	0.1	0.04
	γ^{pro-S}	19.5	1.05	19.7	1.07	0.2	0.02
	γ^{pro-R}	18.2	0.88	18.2	0.89	0.0	0.01
MeLeu[6]	NCH_3	31.3	3.24	31.4	3.26	0.1	0.02
	α	55.0	4.97	55.1	4.98	0.1	0.01
	β^{pro-S}	37.1	2.05	37.2	2.08	0.1	0.03
	β^{pro-R}	37.1	1.35	37.2	1.37	0.1	0.02
	γ	25.1	1.74	25.2	1.78	0.1	0.04
	δ^{pro-S}	23.6	0.92	23.7	0.94	0.1	0.02

Table C.1: continued.

		Isotropic solution		Anisotropic medium		CS difference	
Residue	Signal	^{13}C-shift	^{1}H-shift	^{13}C-shift	^{1}H-shift	Δ^{13}C-shift	Δ^{1}H-shift
	δ^{pro-R}	21.6	0.82	21.6	0.83	0.1	0.01
Ala^{7}	α	48.4	4.50	48.4	4.53	0.0	0.03
	β	15.9	1.34	15.9	1.36	0.0	0.02
Ala^{8}	α	44.9	4.81	45.0	4.83	0.1	0.02
	β	17.9	1.24	18.0	1.26	0.1	0.02
MeLeu^{9}	NCH_3	29.4	3.10	29.4	3.12	0.0	0.02
	α	47.9	5.68	48.0	5.70	0.1	0.02
	β^{pro-S}	38.7	1.20	38.8	1.22	0.1	0.02
	β^{pro-R}	38.7	2.13	38.8	2.15	0.1	0.02
	γ	24.4	1.31	24.5	1.33	0.1	0.02
	δ^{pro-S}	21.5	0.86	21.6	0.88	0.1	0.02
	δ^{pro-R}	23.5	0.95	23.6	0.96	0.1	0.01
MeLeu^{10}	NCH_3	29.6	2.68	29.7	2.70	0.1	0.02
	α	57.2	5.07	57.3	5.09	0.1	0.02
	β^{pro-S}	40.3	2.06	40.4	2.07	0.1	0.02
	β^{pro-R}	40.3	1.24	40.4	1.28	0.1	0.01
	γ	24.2	1.46	24.2	1.48	0.0	0.02
	δ^{pro-S}	23.1	0.99	23.3	1.01	0.2	0.02
	δ^{pro-R}	23.6	1.02	23.6	1.04	0.0	0.02
MeVal^{11}	NCH_3	29.5	2.70	29.6	2.73	0.1	0.03
	α	57.6	5.11	57.7	5.12	0.1	0.01
	β	28.8	2.13	29.0	2.15	0.2	0.02
	γ^{pro-S}	20.0	0.84	20.2	0.85	0.2	0.01
	γ^{pro-R}	18.5	0.99	18.5	1.02	0.0	0.03

C.3 Structure Calculation of CsA

Structure calculations were performed by applying standard simulated annealing protocols implemented in the program Xplor-nih 2.9.9 optimized for proteins and peptides. For calculations, the artifical amino acids of CsA were built by using the program Insight II (*MSI*) and appropriate topology and parameter files were obtained from the parameter learn function of Xplor-nih.

Iniatally, the NOE-based structure published by Kessler *et al.*[383] was reproduced, as the structure was not available electronically. Starting from a randomized structure, calculations were performed by using 144 NOE-derived distance restraints, as listed in the PhD thesis of M. Köck,[385] four hydrogen bonds treated as pseudo-covalent bonds,[312, 455] and tw sidechain dihedral restraints.[385] For distance restraints, lower and upper bounds of 5% and 10% of the extracted distance were applied, respectively. 1 Å was added to the upper boundary for methyl moieties. 20 structures were calculated; this resulted in eight structures of comparable energy occupying the same conformational space. The structure calculation was then repeated with the former lowest-energy structure as the starting structure. Again, 20 structures were generated, of which the best 17 structures showed comparable energies and highly similar conformations. Further repetition of the procedure did not decrease the overall energy. The best structures were then subjected to a final refinement in which the force constant specifying the peptide-bond planarity was relaxed from 500 kcal $\cdot$ rad^{-2} to 20 kcal $\cdot$ rad^{-2} to allow slight deviations from planarity. The resulting structures showed similar energies (173 ± 3 kcal $\cdot$ mol^{-1}) and occupied the same conformational space. As a test, calculations were also performed using the crystal structure as a starting point; these resulted in the same final conformation. The calculated structures had no restraint violations, and comparision with the published backbone dihedral angles (φ, ψ, and ω) of the published NOE-derived structure showed no significant deviations.

For structure calculations including RDCs, the lowest-energy structure without refinement was used as starting structure. The initial values for the axial and rhombic components of the alignment tensor ($D_a^{Xplor} = 19.2$ and $R^{Xplor} = 0.56$) were extracted by a grid search script implemented in Xpplor-nih. The Sani potential was used for RDCs, hence RDCs determined from methyl groups can be included as pseudo CH-groups pointing in the direction of the corresponding CC- or CN-bonds, if the value of the D_{CH}-coupling is multiplied by -3.[456] All 35 RDCs together with the ex-

TABLE C.2: $^1J_{CH}$- and $^1J_{CH} + D_{CH}$-couplings measured and D_{CH}-restraints used in structure calculations for CsA in $CDCl_3$ and PDMS/$CDCl_3$-gel.

Residue	Coupling	$^1J_{CH}$ [Hz]	$^1J_{CH} + D_{CH}$ [Hz]	D_{CH}-Restraint
MeBmt[1]	NCH_3	139.6	139.0	1.7[a]
	$C^\alpha H^\alpha$	138.9	139.5	0.6
	$C^\beta H^\beta$	142.8	127.2	−15.6
	$\delta^{\mathrm{pro-S}}$	124.2	114.6	−9.6
	$\delta^{\mathrm{pro-R}}$	126.6	125.4	−1.1
Abu[2]	$C^\alpha H^\alpha$	139.6	148.3	8.8
	$C^\beta H^{\beta\mathrm{pro-S}}$	128.7	135.6	6.9
Sar[3]	NCH_3	139.3	139.2	0.6[a]
	$C^\alpha H^{\alpha\mathrm{pro-S}}$	143.7	150.5	6.8
	$C^\alpha H^{\alpha\mathrm{pro-R}}$	136.5	123.8	−12.6
MeLeu[4]	NCH_3	138.6	137.8	2.2[a]
	$C^\alpha H^\alpha$	136.1	136.4	0.3
	$C^\beta H^{\beta\mathrm{pro-S}}$	129.4	157.3	27.9
	$C^\beta H^{\beta\mathrm{pro-R}}$	126.1	119.8	−6.3
	$C^\gamma H^\gamma$	126.3	151.0	24.7
Val[5]	$C^\alpha H^\alpha$	140.1	152.4	12.4
	$C^\beta H^\beta$	130.9	140.2	9.3
MeLeu[6]	NCH_3	139.2	137.4	5.4[a]
	$C^\alpha H^\alpha$	141.1	146.6	5.6
	$C^\beta H^{\beta\mathrm{pro-S}}$	128.1	119.5	−8.6
	$C^\beta H^{\beta\mathrm{pro-R}}$	127.3	117.1	−10.2
	$C^\gamma H^\gamma$	126.6	117.0	−9.6
Ala[7]	$C^\alpha H^\alpha$	138.6	140.0	1.4
Ala[8]	$C^\alpha H^\alpha$	142.1	158.9	16.8
	$C^\beta H^\beta$	129.5	124.8	14.2[a]
MeLeu[9]	NCH_3	139.3	142.6	10.0[a]
	$C^\alpha H^\alpha$	139.1	118.0	−21.2
	$C^\beta H^{\beta\mathrm{pro-S}}$	129.6	109.5	−20.2
	$C^\beta H^{\beta\mathrm{pro-R}}$	125.1	139.3	14.2
	$C^\gamma H^\gamma$	124.9	137.2	12.2
MeLeu[10]	$C^\alpha H^\alpha$	136.0	139.5	3.5
	$C^\beta H^{\beta\mathrm{pro-S}}$	128.8	106.5	−22.3
	$C^\beta H^{\beta\mathrm{pro-R}}$	125.8	113.7	−12.1
	$C^\gamma H^\gamma$	126.6	105.0	−21.7
MeVal[11]	$C^\alpha H^\alpha$	140.5	148.7	8.2
	$C^\beta H^\beta$	129.6	134.1	4.5

[a] Residual dipolar couplings of methyl groups are multiplied by a factor of −3.

isting distance and dihedral restraints were used in calculations. The RDCs were divided into five classes and added successively to the calculations. The first class included eleven out of twelve C^{α}-H^{α}-couplings, the second class included one out of two C^{β}-methyl-couplings and five out of seven N-methyl-couplings, the third class twelve out of 13 C^{β}-H^{β}-couplings, the fourth all C^{γ}-H^{γ}-couplings, and the fifth the two C^{δ}-H^{δ}-couplings from the MeBmt-residue. During each calculation, 20 structures were generated and subseqeuntly sortet by their total energy. The structure with the lowest energy was used as the starting structure for the next run, while the values for the alignment tensor were kept constant. After incorporation of all sets of RDCs, the resulting 20 structures were subjected to the same refinement protocol as was used for the calculation of the NOE-based structures.

Bibliography

[1] Braunschweiler, L.; Ernst, R. R. Coherence transfer by isotropic mixing: Application to proton correlation spectroscopy, *J. Magn. Reson.* **1983**, *53*, 521.

[2] Marx, R.; Glaser, S. Spins swing like pendulums do: an exact classical model for TOCSY transfer in systems of three isotropically coupled spins 1/2, *J. Magn. Reson.* **2003**, *164*, 338 – 342.

[3] Glaser, S. J.; Quant, J. J. In Warren, W. S., editor, *Advances in Magnetic and Optical Resonance*, volume 19, pp. 59 – 252. Academic Press, San Diego, 1996.

[4] Rance, M. Sign reversal of resonances via isotropic mixing in NMR-spectroscopy, *Chem. Phys. Let.* **1989**, *154*, 242 – 247.

[5] Kuprov, I.; Wagner-Rundell, N.; Hore, P. Polynomially scaling spin dynamics simulation algorithm based on adaptive state space restriction. EUROMAR, Taragona, Spain, 2007.

[6] Griesinger, C.; Ernst, R. R. Cross-relaxation in time-dependent nuclear spin systems - invariant trajectory approach, *Chem. Phys. Let.* **1988**, *152*, 239 – 247.

[7] Cavanagh, J.; Rance, M. Suppression of cross-relaxation effects in TOCSY spectra via a modified DIPSI-2 mixing sequence (Vol 96, pg 670, 1992), *J. Magn. Reson. Series A* **1993**, *105*, 328 – 328.

[8] Briand, J.; Ernst, R. R. Computer-optimized homonuclear TOCSY experiments with suppression of cross relaxation, *Chem. Phys. Let.* **1991**, *185*, 276 – 285.

[9] Griesinger, C.; Otting, G.; Wüthrich, K.; Ernst, R. R. Clean TOCSY for ^{1}H-spin system-identification in macromolecules, *J. Am. Soc. Chem.* **1988**, *110*, 7870 – 7872.

[10] Sørensen, O.; Eich, G.; Levitt, M.; Bodenhausen, G.; Ernst, R. Product operator-formalism for the description of NMR pulse experiments, *Prog. Nucl. Magn. Reson. Spectrosc.* **1983**, *16*, 163 – 192.

[11] Macura, S.; Huang, Y.; Suter, D.; Ernst, R. Two-dimensional chemical-exchange and cross-relaxation spectroscopy of coupled nuclear spins, *J. Magn. Reson.* **1981**, *43*, 259 – 281.

[12] Macura, S.; Wüthrich, K.; Ernst, R. Seperation and suppression of coherent transfer effects in two-dimensional NOE and chemical-exchange spectroscopy, *J. Magn. Reson.* **1982**, *46*, 269 – 282.

[13] Rance, M.; Bodenhausen, G.; Wagner, G.; Wüthrich, K.; Ernst, R. A systematic-approach to the suppression of J-cross peaks in 2D exchange and 2D NOE spectroscopy, *J. Magn. Reson.* **1985**, *62*, 497 – 510.

[14] Davis, A.; Estcourt, G.; Keeler, J.; Laue, E.; Titman, J. Improvement of z-filters and purging pulses by the use of zero-quantum dephasing in inhomogeneous B1 or B0 fields, *J. Magn. Reson. Series A* **1993**, *105*, 167 – 183.

[15] Thrippleton, M. J.; Edden, R. A. E.; Keeler, J. Suppression of strong coupling artefacts in J-spectra, *J. Magn. Reson.* **2005**, *174*, 97 – 109.

[16] Baur, M.; Kessler, H. Novel suppression of the diagonal signals in the NOESY experiment, *Magn. Reson. Chem.* **1997**, *35*, 877 – 882.

[17] Ernst, R.; Wokaun, A.; Bodenhausen, G. *NMR Spectroscopy.* Teubner, Stuttgart, 1984.

[18] Saupe, A.; Englert, G. High-resolution nuclear magnetic resonance spectra of oiented molecules, *Phys. Rev. Lett.* **1963**, *11*, 462 – 464.

[19] Saupe, A. Kernresonanzen in kristallinen Flüssigkeiten und in kristallinflüssigen Lösungen .I., *Z. Naturforsch., A: Phys. Sci.* **1964**, *A 19*, 161 – 162.

[20] Saupe, A. Recent results in the field of liquid crystals, *Angew. Chem. Int. Ed.* **1968**, *7*, 97 – 112.

[21] Zweckstetter, M.; Bax, A. Prediction of sterically induced alignment in a dilute liquid crystalline phase: Aid to protein structure determination by NMR, *J. Am. Soc. Chem.* **2000**, *122*, 3791 – 3792.

[22] Dosset, P.; Hus, J.; Marion, D.; Blackledge, M. A novel interactive tool for rigid-body modeling of multi-domain macromolecules using residual dipolar couplings, *J. Biomol. NMR* **2001**, *20*, 223 – 231.

[23] Azurmendi, H.; Bush, C. Tracking alignment from the moment of inertia tensor (TRAMITE) of biomolecules in neutral dilute liquid crystal solutions, *J. Am. Chem. Soc.* **2002**, *124*, 2426 – 2427.

[24] Sternberg, U and Koch, FT and Losso, P. COSMOS - Computer-Simulation von Molekül-Strukturen. http://www.cosmos-software.de/co_intro.html, 2008.

[25] Snyder, L. C. Analysis of nuclear magnetic resonance spectra of molecules in liquid-crystal solvents, *J. Chem. Phys.* **1965**, *43*, 4041 – 4050.

[26] Sackmann, E.; Meiboom, S.; Snyder, L. C. On relation of nematic to cholesteric mesophases, *J. Am. Soc. Chem.* **1967**, *89*, 5981 – 5982.

[27] Yannoni, C. S. Oriented smectic liquid crystal solutions, *J. Am. Soc. Chem.* **1969**, *91*, 4611 – 4612.

[28] Taylor, T. R.; Arora, S. L.; Fergason, J. L. Temperature-dependent tilt angle in smectic C phase of a liquid crystal, *Phys. Rev. Lett.* **1970**, *25*, 722 – 726.

[29] Meiboom, S.; Luz, Z. Nuclear magnetic resonance study of smectic phases, *Mol. Cryst. Liq. Cryst.* **1973**, *22*, 143 – 164.

[30] Sackmann, E.; Meiboom, S.; Snyder, L. C.; Meixner, A. E.; Dietz, R. E. On structure of liquid crystalline state of cholesterol derivatives, *J. Am. Soc. Chem.* **1968**, *90*, 3567 – 3569.

[31] Panar, M.; Phillips, W. D. Magnetic ordering of poly-γ-benzyl-L-glutamate solutions, *J. Am. Soc. Chem.* **1968**, *90*, 3880 – 3882.

[32] Aroulanda, C.; Boucard, V.; Guibé, F.; Courtieu, J.; Merlet, D. Weakly oriented liquid-crystal NMR solvents as a general tool to determine relative configuration, *Chem. Eur. J.* **2003**, *9*, 4536–4539.

[33] Thiele, C. M. Simultaneous assignment of all diastereotopic protons in strychnine using RDCs: PELG as alignment medium for organic molecules, *J. Org. Chem.* **2004**, *69*, 7403 – 7413.

[34] Hansen, M. R.; Mueller, L.; Pardi, A. Tunable alignment of macromolecules by filamentous phage yields dipolar coupling interactions, *Nat. Struct. Biol.* **1998**, *5*, 1065 – 1074.

[35] Tjandra, N.; Bax, A. Direct measurement of distances and angles in biomolecules by NMR in a dilute liquid crystalline medium, *Science* **1997**, *278*, 1111 – 1114.

[36] Prestegard, J. H. New techniques in structural NMR - anisotropic interactions, *Nat. Struct. Biol.* **1998**, *5*, 517 – 522.

[37] Fleming, K.; Gray, D.; Prasannan, S.; Matthews, S. Cellulose crystallites: A new and robust liquid crystalline medium for the measurement of residual dipolar couplings, *J. Am. Soc. Chem.* **2000**, *122*, 5224 – 5225.

[38] Rückert, M.; Otting, G. Alignment of biological macromolecules in novel nonionic liquid crystalline media for NMR experiments, *J. Am. Soc. Chem.* **2000**, *122*, 7793 – 7797.

[39] Ma, C.; Opella, S. Lanthanide ions bind specifically to an added 'EF-hand' and orient a membrane protein in micelles for solution NMR spectroscopy, *J. Magn. Reson.* **2000**, *146*, 381 – 384.

[40] Feeney, J.; Birdsall, B.; Bradbury, A.; Biekofsky, R.; Bayley, P. Calmodulin tagging provides a general method of using lanthanide induced magnetic field orientation to observe residual dipolar couplings in proteins in solution, *J. Biomol. NMR* **2001**, *21*, 41 – 48.

[41] Tolman, J.; Flanagan, J.; Kennedy, M.; Prestegard, J. NMR evidence for slow collective motions in cyanometmyoglobin, *Nat. Struc. Biolo.* **1997**, *4*, 292 – 297.

[42] Jain, N.; Noble, S.; Prestegard, J. Structural characterization of a mannose-binding protein-trimannoside complex using residual dipolar couplings, *J. Mol. Biol.* **2003**, *328*, 451 – 462.

[43] Rodriguez-Castaneda, F.; Haberz, P.; Leonov, A.; Griesinger, C. Paramagnetic tagging of diamagnetic proteins for solution NMR, *Magn. Reson. Chem.* **2006**, *44*, S10 – S16.

[44] Franklin, S.; Raymond, K. Solution structure and dynamics of lanthanide complexes of the macrocyclic polyamino carboxylate DTPA-dien – NMR study and crystal-structures of the lanthanium(III) and europium(III) complexes, *Inorg. Chem.* **1994**, *33*, 5794 – 5804.

[45] Ikegami, T.; Verdier, L.; Sakhaii, P.; Grimme, S.; Pescatore, B.; Saxena, K.; Fiebig, K.; Griesinger, C. Novel techniques for weak alignment of proteins in solution using chemical tags coordinating lanthanide ions, *J. Biomol. NMR* **2004**, *29*, 339 – 349.

[46] Haberz, P.; Rodriguez-Castaneda, F.; Junker, J.; Becker, S.; Leonov, A.; Griesinger, C. Two new chiral EDTA-based metal chelates for weak alignment of proteins in solution, *Org. Lett.* **2006**, *8*, 1275 – 1278.

[47] Bleaney, B. Nuclear magnetic resonance shifts in solution due to lanthanide ions, *J. Magn. Reson.* **1972**, *8*, 91 – 100.

[48] John, M.; Pintacuda, G.; Park, A. Y.; Dixon, N. E.; Otting, G. Structure determination of protein-ligand complexes by transferred paramagnetic shifts, *J. Am. Soc. Chem.* **2006**, *128*, 12910 – 12916.

[49] Pintacuda, G.; Park, A. Y.; Keniry, M. A.; Dixon, N. E.; Otting, G. Lanthanide labeling offers fast NMR approach to 3D structure determinations of protein-protein complexes, *J. Am. Soc. Chem.* **2006**, *128*, 3696 – 3702.

[50] Pintacuda, G.; John, M.; Su, X. C.; Otting, G. NMR structure determination of protein-ligand complexes by lanthanide labeling, *Acc. Chem. Res.* **2007**, *40*, 206 – 212.

[51] Pintacuda, G.; Keniry, M. A.; Huber, T.; Park, A. Y.; Dixon, N. E.; Otting, G. Fast structure-based assignment of N-15 HSQC spectra of selectively N-15-labeled paramagnetic proteins, *J. Am. Soc. Chem.* **2004**, *126*, 2963 – 2970.

[52] Bertini, I.; Luchinat, C.; Parigi, G.; Pierattelli, R. NMR spectroscopy of paramagnetic metalloproteins, *ChemBioChem* **2005**, *6*, 1536 – 1549.

[53] Deloche, B.; Samulski, E. Short-range nematic-like orientational order in strained elastomers – a deuterium magnetic resonance study, *Macromolecules* **1981**, *14*, 575 – 581.

[54] Tycko, R.; Blanco, F. J.; Ishii, Y. Alignment of biopolymers in strained gels: A new way to create detectable dipole-dipole couplings in high-resolution biomolecular NMR, *J. Am. Soc. Chem.* **2000**, *122*, 9340 – 9341.

[55] Ishii, Y.; Markus, M. A.; Tycko, R. Controlling residual dipolar couplings in high-resolution NMR of proteins by strain induced alignment in a gel, *J. Biomol. NMR* **2001**, *21*, 141 – 151.

[56] Cierpicki, T.; Bushweller, J. Charged gels as orienting media for measurement of residual dipolar couplings in soluble and integral membrane proteins, *J. Am. Chem. Soc.* **2004**, *126*, 16259 – 16266.

[57] Chou, J. J.; Gaemers, S.; Howder, B.; Louis, J. M.; Bax, A. A simple apparatus for generating stretched polyacrylamide gels, yielding uniform alignment of proteins and detergent micelles, *J. Biomol. NMR* **2001**, *21*, 377 – 382.

[58] Sass, H.; Musco, G.; Stahl, S.; Wingfield, P.; Grzesiek, S. Solution NMR of proteins within polyacrylamide gels: Diffusional properties and residual alignment by mechanical stress or embedding of oriented purple membranes, *J. Biomol. NMR* **2000**, *18*, 303 – 309.

[59] Luy, B.; Kobzar, K.; Kessler, H. An easy and scalable method for the partial alignment of organic molecules for measuring residual dipolar couplings, *Angew. Chem. Int. Ed.* **2004**, *43*, 1092 – 1094.

[60] Naumann, C.; Bubb, W.; Chapman, B.; Kuchel, P. Tunable-alignment chiral system based on gelatin for NMR spectroscopy, *J. Am. Chem. Soc.* **2007**, *129*, 5340 – 5341.

[61] Luy, B.; Kobzar, K.; Knör, S.; Furrer, J.; Heckmann, D.; Kessler, H. Orientational properties of stretched polystyrene gels in organic

solvents and the suppression of their residual ^{1}H NMR signals, *J. Am. Soc. Chem.* **2005**, *127*, 6459 – 6465.

[62] Freudenberger, J. C.; Spiteller, P.; Bauer, R.; Kessler, H.; Luy, B. Stretched poly(dimethylsiloxane) gels as NMR alignment media for apolar and weakly polar organic solvents: An ideal tool for measuring RDCs at low molecular concentrations, *J. Am. Soc. Chem.* **2004**, *126*, 14690 – 14691.

[63] Haberz, P.; Farjon, J.; Griesinger, C. A DMSO-compatible orienting medium: Towards the investigation of the stereochemistry of natural products, *Angew. Chem. Int. Ed.* **2005**, *44*, 427 – 429.

[64] Freudenberger, J. C.; Knör, S.; Kobzar, K.; Heckmann, D.; Paululat, T.; Kessler, H.; Luy, B. Stretched poly(vinyl acetate) gels as NMR alignment media for the measurement of residual dipolar couplings in polar organic solvents, *Angew. Chem. Int. Ed.* **2005**, *44*, 423 – 426.

[65] Kummerlöwe, G.; Auernheimer, J.; Lendlein, A.; Luy, B. Stretched poly(acrylonitrile) as a scalable alignment medium for DMSO, *J. Am. Chem. Soc.* **2007**, *129*, 6080 – 6081.

[66] Kaden , P. personal communication, 2007.

[67] Kobzar, K.; Kessler, H.; Luy, B. Stretched gelatin gels as chiral alignment media for the discrimination of enantiomers by NMR spectroscopy, *Angew. Chem. Int. Ed.* **2005**, *44*, 3145 – 3147.

[68] Kobzar, K.; Kessler, H.; Luy, B. Stretched gelatin gels as chiral alignment media for the discrimination of enantiomers by NMR spectroscopy (Vol 44, pg 3145, 2005), *Angew. Chem. Int. Ed.* **2005**, *44*, 3509 – 3509.

[69] Cavanagh, J.; Fairbrother, W.; Palmer, A.; Skelton, N. *Protein NMR Spectroscopy – Principles and Practice.* Academic Press, San Diego, 1996.

[70] Pervushin, K.; Vogeli, B.; Eletsky, A. Longitudinal ^{1}H relaxation optimization in TROSY NMR spectroscopy, *J. Am. Chem. Soc.* **2002**, *124*, 12898 – 12902.

[71] Schanda, P.; Kupce, E.; Brutscher, B. SOFAST-HMQC experiments for recording two-dimensional heteronuclear correlation spectra of proteins within a few seconds, *J. Biomol. NMR* **2005**, *33*, 199 – 211.

[72] Diercks, T.; Daniels, M.; Kaptein, R. Extended flip-back schemes for sensitivity enhancement in multidimensional HSQC-type out-and-back experiments, *J. Biomol. NMR* **2005**, *33*, 243 – 259.

[73] Dyson, H.; Wright, P. Unfolded proteins and protein folding studied by NMR, *Chem. Rev.* **2004**, *104*, 3607 – 3622.

[74] Schanda, P.; Forge, V.; Brutscher, B. Protein folding and unfolding studied at atomic resolution by fast two-dimensional NMR spectroscopy, *Proc. Nat. Acad. Sci. USA* **2007**, *104*, 11257 – 11262.

[75] Zhang, Q.; Sun, X.; Watt, E.; Al-Hashimi, H. Resolving the motional modes that code for RNA adaptation, *Science* **2006**, *311*, 653 – 656.

[76] Eisenmesser, E.; Bosco, D.; Akke, M.; Kern, D. Enzyme dynamics during catalysis, *Science* **2002**, *295*, 1520 – 1523.

[77] Wolf-Watz, M.; Thai, V.; Henzler-Wildman, K.; Hadjipavlou, G.; Eisenmesser, E.; Kern, D. Linkage between dynamics and catalysis in a thermophilic-mesophilic enzyme pair, *Nat. Struc. Mol. Biol.* **2004**, *11*, 945 – 949.

[78] Akke, M.; Brüschweiler, R.; Palmer, A. NMR order parameters and free-energy – an analytical approach and its application to cooperative Ca^{2+} binding by calbindin-D(9k), *J. Am. Chem. Soc.* **1993**, *115*, 9832 – 9833.

[79] Yang, D.; Kay, L. Contributions to conformational entropy arising from bond vector fluctuations measured from NMR-derived order parameters: Application to protein folding, *J. Mol. Biol.* **1996**, *263*, 369 – 382.

[80] Lee, A.; Kinnear, S.; Wand, A. Redistribution and loss of side chain entropy upon formation of a calmodulin-peptide complex, *Nat. Struc. Biol.* **2000**, *7*, 72 – 77.

[81] Zeeb, M.; Balbach, J. NMR spectroscopic characterization of millisecond protein folding by transverse relaxation dispersion measurements, *J. Am. Chem. Soc.* **2005**, *127*, 13207 – 13212.

[82] Teilum, K.; Poulsen, F.; Akke, M. The inverted chevron plot measured by NMR relaxation reveals a native-like unfolding intermediate in acyl-CoA binding protein, *Proc. Nat. Acad. Sci. USA* **2006**, *103*, 6877 – 6882.

[83] Jeener, J.; Meier, B.; Bachmann, P.; Ernst, R. Investigation of exchange processes by 2-dimensional NMR spectroscopy, *J. Chem. Phys.* **1979**, *71*, 4546 – 4553.

[84] Farrow, N.; Muhandiram, R.; Singer, A.; Pascal, S.; Kay, C.; Gish, G.; Shoelson, S.; Pawson, T.; Formankay, J.; Kay, L. Backbone dynamics of a free and a phosphopeptide-complexed SRC homology-2 domain studied by ^{15}N NMR relaxation, *Biochemistry* **1994**, *33*, 5984 – 6003.

[85] Lakomek, N.; Carlomagno, T.; Becker, S.; Griesinger, C.; Meiler, J. A thorough dynamic interpretation of residual dipolar couplings in ubiquitin, *J. Biomol. NMR* **2006**, *34*, 101 – 115.

[86] Wells, M.; Tidow, H.; Rutherford, T.; Markwick, P.; Jensen, M.; Mylonas, E.; Svergun, D.; Blackledge, M.; Fersht, A. Structure of tumor suppressor p53 and its intrinsically disordered N-terminal transactivation domain, *Proc. Nat. Acad. Sci. USA* **2008**, *105*, 5762–5767.

[87] Fushman, D.; Tjandra, N.; Cowburn, D. Direct measurement of ^{15}N chemical shift anisotropy in solution, *J. Am. Chem. Soc.* **1998**, *120*, 10947 – 10952.

[88] Levitt, M. *Spin Dynamics – Basics of Nuclear Magnetic Resonance.* John Wiley & Sons, Chichester, 2001.

[89] Peterson, R.; Lefebvre, B.; Wand, A. High-resolution NMR studies of encapsulated proteins in liquid ethane, *J. Am. Chem. Soc.* **2005**, *127*, 10176 – 10177.

[90] Pervushin, K.; Riek, R.; Wider, G.; Wüthrich, K. Attenuated T_2 relaxation by mutual cancellation of dipole-dipole coupling and chemical shift anisotropy indicates an avenue to NMR structures of very large biological macromolecules in solution, *Proc. Nat. Acad. Sci. USA* **1997**, *94*, 12366 – 12371.

[91] Fushman, D.; Cowburn, D. The effect of noncollinearity of ^{15}N-^{1}H dipolar and N-15 CSA tensors and rotational anisotropy on ^{15}N relaxation, CSA/dipolar cross correlation, and TROSY, *J. Biomol. NMR* **1999**, *13*, 139 – 147.

[92] Kinosita, K.; Kawato, S.; Ikegami, A. Theory of fluorescence polarization decay in membranes, *Biophys. J.* **1977**, *20*, 289 – 305.

[93] Wittebort, R.; Szabo, A. Theory of NMR relaxation in macromolecules – restricted diffusion and jump models for multiple internal rotations in amino-acid side-chains, *J. Chem. Phys.* **1978**, *69*, 1722 – 1736.

[94] Daragan, V.; Mayo, K. Motional model analyses of protein and peptide dynamics using ^{13}C and ^{15}N NMR relaxation, *Prog. Nucl. Magn. Reson. Spectrosc.* **1997**, *31*, 63 – 105.

[95] Lipari, G.; Szabo, A. Model-free approach to the interpretation of nuclear magnetic resonance relaxation in macromolecules .1. – Theory and range of validity, *J. Am. Chem. Soc.* **1982**, *104*, 4546 – 4559.

[96] Lipari, G.; Szabo, A. Model-free approach to the interpretation of nuclear magnetic resonance relaxation in macromolecules .2. – Analysis of experimental results, *J. Am. Chem. Soc.* **1982**, *104*, 4559 – 4570.

[97] Korzhnev, D.; Billeter, M.; Arseniev, A.; Orekhov, V. NMR studies of Brownian tumbling and internal motions in proteins, *Prog. Nucl. Magn. Reson. Spectrosc.* **2001**, *38*, 197 – 266.

[98] Brüschweiler, R.; Case, D. Characterization of biomolecular structure and dynamics by NMR cross-relaxation, *Prog. Nucl. Magn. Reson. Spectrosc.* **1994**, *26*, 27 – 58.

[99] Bremi, T.; Brüschweiler, R. Locally anisotropic internal polypeptide backbone dynamics by NMR relaxation, *J. Am. Chem. Soc.* **1997**, *119*, 6672 – 6673.

[100] Clore, G.; Szabo, A.; Bax, A.; Kay, L.; Driscoll, P.; Gronenborn, A. Deviations from the simple 2-parameter model-free approach to the interpretation of ^{15}N nuclear magnetic-relaxation of proteins, *J. Am. Chem. Soc.* **1990**, *112*, 4989 – 4991.

[101] Lipari, G.; Szabo, A. Effect of librational motion on fluorescence depolarization and nuclear magnetic resonance relaxation in macromolecules and membranes, *Biophys. J.* **1980**, *30*, 489 – 506.

[102] Lipari, G.; Szabo, A. Pade approximants to correlation-functions for restricted rotational diffusion, *J. Chem. Phys.* **1981**, *75*, 2971 – 2976.

[103] Tolman, J. R.; Flanagan, J. M.; Kennedy, M. A.; Prestegard, J. H. Nuclear magnetic dipole interactions in field-oriented proteins - information for structure determination in solution, *Proc. Nat. Acad. Sci. USA* **1995**, *92*, 9279 – 9283.

[104] Tjandra, N.; Bax, A. Direct measurement of distances and angles in biomolecules by NMR in a dilute liquid crystalline medium (Vol. 278, pg. 1111, 1997), *Science* **1997**, *278*, 1697 – 1697.

[105] Clore, G.; Gronenborn, A.; Tjandra, N. Direct structure refinement against residual dipolar couplings in the presence of rhombicity of unknown magnitude, *J. Magn. Reson.* **1998**, *131*, 159 – 162.

[106] Bax, A.; Kontaxis, G.; Tjandra, N. In *Nuclear Magnetic Resonance of Biological Macromolecules, PT B*, volume 339, pp. 127 – 174, 2001.

[107] Demco, D.; Blümich, B. NMR imaging of materials, *Curr. Opin. Solid State Mater. Sci.* **2001**, *5*, 195 – 202.

[108] Maxwell, R.; Balazs, B. NMR measurements of residual dipolar couplings for lifetime assessments in gamma-irradiated silica-PDMS composite materials, *Nucl. Instrum. Methods Phys. Res., Sect. B* **2003**, *208*, 199 – 203.

[109] Baker, D.; Logan, J.; Miller, D.; Sherwood, M. Residual Dipolar Couplings in Polymer Films: The Limit of Submonolayer Coverage. 48$^{\text{th}}$ENC, Daytona Beach, USA, 2007.

[110] Schröder, L.; Bachert, P. Evidence for a dipolar-coupled AM system in carnosine in human calf muscle from in vivo ^{1}H NMR spectroscopy, *J. Magn. Reson.* **2003**, *164*, 256 – 269.

[111] Schröder, L.; Schmitz, C.; Bachert, P. Phase modulation in dipolar-coupled A(2) spin systems: effect of maximum state mixing in ^{1}H NMR *in vivo*, *J. Magn. Reson.* **2004**, *171*, 207 – 212.

[112] Thiele, C. M.; Berger, S. Probing the diastereotopicity of methylene protons in strychnine using residual dipolar couplings, *Org. Lett.* **2003**, *5*, 705 – 708.

[113] Mathieu, D.; Cramer, N.; Richter, C.; Jonker, H.; Luy, B.; Kummerlöwe, G.; Laschat, S.; Schwalbe, H. Determination of ^1D residual dipolar couplings in methylene groups. 48$^{\text{th}}$ENC, Daytona Beach, USA, 2007.

[114] Klages, J.; Neubauer, C.; Coles, M.; Kessler, H.; Luy, B. Structure refinement of cyclosporin a in chloroform by using RDCs measured in a stretched PDMS-gel, *ChemBioChem* **2005**, *6*, 1672 – 1678.

[115] Lindorff-Larsen, K.; Best, R.; Depristo, M.; Dobson, C.; Vendruscolo, M. Simultaneous determination of protein structure and dynamics, *Nature* **2005**, *433*, 128 – 132.

[116] Bouvignies, G.; Bernado, P.; Meier, S.; Cho, K.; Grzesiek, S.; Brüschweiler, R.; Blackledge, M. Identification of slow correlated motions in proteins using residual dipolar and hydrogen-bond scalar couplings, *Proc. Nat. Acad. Sci. USA* **2005**, *102*, 13885 – 13890.

[117] Bouvignies, G.; Bernado, P.; Blackledge, M. Protein backbone dynamics from N-H-N dipolar couplings in partially aligned systems: a comparison of motional models in the presence of structural noise, *J. Magn. Reson.* **2005**, *173*, 328 – 338.

[118] Bouvignies, G.; Markwick, P.; Brüschweiler, R.; Blackledge, M. Simultaneous determination of protein backbone structure and dynamics from residual dipolar couplings, *J. Am. Chem. Soc.* **2006**, *128*, 15100 – 15101.

[119] Best, R.; Lindorff-Larsen, K.; Depristo, M.; Vendruscolo, M. Relation between native ensembles and experimental structures of proteins, *Proc. Nat. Acad. Sci. USA* **2006**, *103*, 10901 – 10906.

[120] Bouvignies, G.; Markwick, P.; Blackledge, M. Simultaneous definition of high resolution protein structure and backbone conformational dynamics using NMR residual dipolar couplings, *ChemPhysChem* **2007**, *8*, 1901 – 1909.

[121] Markwick, P.; Bouvignies, G.; Blackledge, M. Exploring multiple timescale motions in protein GB3 using accelerated molecular dynamics and NMR spectroscopy, *J. Am. Chem. Soc.* **2007**, *129*, 4724 – 4730.

[122] Richter, B.; Gsponer, J.; Varnai, P.; Salvatella, X.; Vendruscolo, M. The MUMO (minimal under-restraining minimal over-restraining) method for the determination of native state ensembles of proteins, *J. Biomol. NMR* **2007**, *37*, 117 – 135.

[123] Liu, X and Huang, X and Guernon, J and Wu, YJ and Roongta, V. Small Molecule Stereochemistry Determination Utilizing Residual Dipole Couplin in an Organic Chiral Orienting Media. 46thENC, Providence, USA, 2005.

[124] Schütz, A.; Junker, J.; Leonov, A.; Lange, O.; Molinski, T.; Griesinger, C. Stereochemistry of sagittamide a from residual dipolar coupling enhanced NMR, *J. Am. Chem. Soc.* **2007**, *129*, 15114 – 15115.

[125] Farjon, J.; Merlet, D.; Lesot, P.; Courtieu, J. Enantiomeric excess measurements in weakly oriented chiral liquid crystal solvents through 2D ^{1}H selective refocusing experiments, *J. Magn. Reson.* **2002**, *158*, 169 – 172.

[126] Aroulanda, C.; Merlet, D.; Courtieu, J.; Lesot, P. NMR experimental evidence of the differentiation of enantiotopic directions in C_s and C_{2v} molecules using partially oriented, chiral media, *J. Am. Chem. Soc.* **2001**, *123*, 12059 – 12066.

[127] Lesot, P.; Merlet, D.; Sarfati, M.; Courtieu, J.; Zimmermann, H.; Luz, Z. Enantiomeric and enantiotopic analysis of cone-shaped compounds with C_3 and C_{3v} symmetry using NMR Spectroscopy in chiral anisotropic solvents, *J. Am. Chem. Soc.* **2002**, *124*, 10071 – 10082.

[128] Luy, B.; Frank, A.; Kessler, H. In Mannhold, R.; Kubinyi, H.; Volkers, G., editors, *Molecular Drug Properties: Measurement and Prediction*, volume 37, pp. 207 – 254, Weinheim, Germany, 2008. VCH-Wiley.

[129] Marquez, B.; Gerwick, W.; Williamson, R. Survey of NMR experiments for the determination of (n)J(C,H) heteronuclear coupling constants in small molecules, *Magn. Reson. Chem.* **2001**, *39*, 499 – 530.

[130] Kobzar, K.; Luy, B. Analyses, extensions and comparison of three experimental schemes for measuring ((n)J(CH)+D-CH)-couplings at natural abundance, *J. Magn. Reson.* **2007**, *186*, 131 – 141.

[131] Tzvetkova, P.; Simova, S.; Luy, B. PEHSQC: A simple experiment for simultaneous and sign-sensitive measurement of ((1)J(CH)+D-CH) and ((2)J(HH)+D-HH) couplings, *J. Magn. Reson.* **2007**, *186*, 193 – 200.

[132] Kozminski, W. A pure-phase homonuclear *J*-modulated HMQC experiment with tilted cross-peak patterns for an accurate determination of homonuclear coupling constants, *J. Magn. Reson.* **1999**, *141*, 185 – 190.

[133] Vuister, G.; Bax, A. Quantative *J* correlation – A new approach for measuring homonuclear 3-bond $J_{H^N H^\alpha}$-coupling constants in ^{15}N-enriched proteins, *J. Am. Chem. Soc.* **1993**, *115*, 7772 – 7777.

[134] Thiele, C. M.; Marx, A.; Berger, R.; Fischer, J.; Biel, M.; Giannis, A. Determination of the relative configuration of a five-membered lactone from residual dipolar couplings, *Angew. Chem. Int. Ed.* **2006**, *45*, 4455 – 4460.

[135] Griesinger, C.; Sørensen, O.; Ernst, R. Practical aspects of the E.COSY technique – measurement of scalar spin spin coupling constants in peptides, *J. Magn. Reson.* **1987**, *75*, 474 – 492.

[136] Neubauer, H.; Meiler, J.; Peti, W.; Griesinger, C. NMR structure determination of saccharose and raffinose by means of homo- and heteronuclear dipolar couplings, *Helv. Chim. Acta* **2001**, *84*, 243 – 258.

[137] Fogolari, F.; Esposito, G.; Cauci, S.; Viglino, P. Evaluation of *J*-coupling constants from peak amplitudes of total correlation spectra, *J. Magn. Reson. Series A* **1993**, *102*, 49 – 57.

[138] Fogolari, F.; Esposito, G.; Cattarinussi, S.; Viglino, P. Quantitative analysis of total correlation spectra: Application to small biomolecules, *Conc. Magn. Reson.* **1996**, *8*, 229 – 251.

[139] Kramer, F.; Jung, A.; Brunner, E.; Glaser, S. J. Determining the relative sign and size of scalar and residual dipolar couplings in homonuclear two-spin systems, *J. Magn. Reson.* **2004**, *169*, 49 – 59.

[140] Pagano, K.; Fogolari, F.; Corazza, A.; Viglino, P.; Esposito, G. Estimation of (3)JHN-H^{α} and (3)JH^{α}-H^{β} coupling constants from heteronuclear TOCSY spectra, *J. Biomol. NMR* **2007**, *39*, 213 – 222.

[141] Davis, D. G.; Bax, A. Assignment of complex ^{1}H-NMR spectra via two-dimensional homonuclear Hartmann-Hahn spectroscopy, *J. Am. Soc. Chem.* **1985**, *107*, 2820 – 2821.

[142] Fesik, S. W.; Eaton, H. L.; Olejniczak, E. T.; Zuiderweg, E. R. P.; Mcintosh, L. P.; Dahlquist, F. W. 2D and 3D NMR-spectroscopy employing ^{13}C-^{13}C magnetization transfer by isotropic mixing – spin system-identification in large proteins, *J. Am. Soc. Chem.* **1990**, *112*, 886 – 888.

[143] Glaser, S. J.; Schwalbe, H.; Marino, J. P.; Griesinger, C. Directed TOCSY, a method for selection of directed correlations by optimal combinations of isotropic and longitudinal mixing, *J. Magn. Reson. Series B* **1996**, *112*, 160 – 180.

[144] Schedletzky, O.; Glaser, S. J. Analytical coherence-transfer functions for the general AMX spin system under isotropic mixing, *J. Magn. Reson. Series A* **1996**, *123*, 174 – 180.

[145] Luy, B.; Schedletzky, O.; Glaser, S. J. Analytical polarization transfer functions for four coupled spins 1/2 under isotropic mixing conditions, *J. Magn. Reson.* **1999**, *138*, 19 – 27.

[146] Kramer, F.; Glaser, S. J. Efficiency of homonuclear Hartmann-Hahn and COSY-type mixing sequences in the presence of scalar and residual dipolar couplings, *J. Magn. Reson.* **2002**, *155*, 83 – 91.

[147] Luy, B.; Glaser, S. J. Analytical polarization and coherence transfer functions for three dipolar coupled spins 1/2, *J. Magn. Reson.* **2000**, *142*, 280 – 287.

[148] Taylor, D. M.; Ramamoorthy, A. Analysis of dipolar-coupling-mediated coherence transfer in a homonuclear two spin-1/2 solid-state system, *J. Magn. Reson.* **1999**, *141*, 18 – 28.

[149] Luy, B.; Glaser, S. J. Superposition of scalar and residual dipolar couplings: Analytical transfer functions for three spins 1/2 under cylindrical mixing conditions, *J. Magn. Reson.* **2001**, *148*, 169 – 181.

[150] Kramer, F.; Peti, W.; Griesinger, C.; Glaser, S. J. Optimized homonuclear Carr-Purcell-type dipolar mixing sequences, *J. Magn. Reson.* **2001**, *149*, 58 – 66.

[151] Kramer, F.; Luy, B.; Glaser, S. J. Offset dependence of homonuclear Hartmann-Hahn transfer based on residual dipolar couplings in solution state NMR, *Appl. Magn. Reson.* **1999**, *17*, 173 – 187.

[152] Berthault, P.; Jeannerat, D.; Camerel, F.; Salgado, F.; Boulard, Y.; Gabriel, J.; Desvaux, H. Dilute liquid crystals used to enhance residual dipolar couplings may alter conformational equilibrium in oligosaccharides, *Carbohydr. Res.* **2003**, *338*, 1771 – 1785.

[153] Häberlein, U.; Waugh, J. S. Coherent averaging effects in magnetic resonance, *Phys. Rev.* **1968**, *175*, 453 – 467.

[154] Häberlen, U. In Waugh, J. S., editor, *Advances in Magnetic Resonance*, volume 8, Suppl. 1, pp. 59 – 252. Academic Press, New York, 1976.

[155] Lee, M.; Goldburg, W. Nuclear magnetic resonance line narrowing by a rotating rf field, *Phys. Rev.* **1965**, *140*, 1261 – 1271.

[156] Sakellariou, D.; Lesage, A.; Hodgkinson, P.; Emsley, L. Homonuclear dipolar decoupling in solid-state NMR using continuous phase modulation, *Chem. Phys. Lett.* **2000**, *319*, 253 – 260.

[157] Farjon, J.; Bermel, W.; Griesinger, C. Resolution enhancement in spectra of natural products dissolved in weakly orienting media with the help of H-1 homonuclear dipolar decoupling during acquisition: Application to ^{1}H-^{13}C dipolar couplings measurements, *J. Magn. Reson.* **2006**, *180*, 72 – 82.

[158] Shaka, A. J.; Lee, C. J.; Pines, A. Iterative schemes for bilinear operators - application to spin decoupling, *J. Magn. Reson.* **1988**, *77*, 274 – 293.

[159] Weitekamp, D. P.; Garbow, J. R.; Pines, A. Determination of dipole coupling-constants using heteronuclear multiple quantum NMR, *J. Chem. Phys.* **1982**, *77*, 2870 – 2883.

[160] Caravatti, P.; Braunschweiler, L.; Ernst, R. R. Heteronuclear correlation spectroscopy in rotating solids, *Chem. Phys. Let.* **1983**, *100*, 305 – 310.

[161] Quant, J.; Glaser, S.; Griesinger, C. Broadband isotropic mixing for heteronuclear coherence transfer. 36$^{\text{th}}$ENC, Boston, USA, 1995.

[162] Levitt, M. H. Symmetrical composite pulse sequences for NMR population-inversion .2. compensation of resonance offset, *J. Magn. Reson.* **1982**, *50*, 95 – 110.

[163] Gullion, T.; Baker, D. B.; Conradi, M. S. New, compensated Carr-Purcell sequences, *J. Magn. Reson.* **1990**, *89*, 479 – 484.

[164] Lizak, M. J.; Gullion, T.; Conradi, M. S. Measurement of like-spin dipole couplings, *J. Magn. Reson.* **1991**, *91*, 254 – 260.

[165] Kramer, F.; Glaser, S. J. Clean TOCSY transfer through residual dipolar couplings, *J. Magn. Reson.* **2004**, *168*, 238 – 245.

[166] Furrer, J.; Kramer, F.; Marino, J. P.; Glaser, S. J.; Luy, B. Homonuclear Hartmann-Hahn transfer with reduced relaxation losses by use of the MOCCA-XY16 multiple pulse sequence, *J. Magn. Reson.* **2004**, *166*, 39 – 46.

[167] Glaser, S. J.; Drobny, G. P. In Warren, W. S., editor, *Advances in Magnetic Resonance*, volume 14, pp. 35 – 58. Academic Press, New York, 1990.

[168] Bothner-By, A. A.; Stephens, R. L.; Lee, J. M.; Warren, C. D.; Jeanloz, R. W. Structure determination of a tetrasccharide - transient nuclear overhauser effects in the rotating frame, *J. Am. Soc. Chem.* **1984**, *106*, 811 – 813.

[169] Bax, A.; Davis, D. G. Practical aspects of two-dimensional transverse NOE spectroscopy, *J. Magn. Reson.* **1985**, *63*, 207 – 213.

[170] Cano, K. E.; Thrippleton, M. J.; Keeler, J.; Shaka, A. J. Cascaded z-filters for efficient single-scan suppression of zero-quantum coherence, *J. Magn. Reson.* **2004**, *167*, 291 – 297.

[171] Klages, J.; Glaser, S.; Kessler, H.; Luy, B. J-ONLY-TOCSY: Efficient suppression of RDC-induced transfer in homonuclear TOCSY experiments using JESTER-1- derived multiple pulse sequences, *J. Magn. Reson.* **2007**, *189*, 217 – 227.

[172] Kummerlöwe, G.; Halbach, F.; Laufer, B.; Luy, B. Precise measurement of RDCs in water and DMSO based gels using a silicone rubber tube for variable stretching, *Open Spectrosc. J.* **2008**.

[173] Goddard, T. Sparky – NMR Assignment and Integration Software. http://www.cgl.ucsf.edu/home/sparky/, 2007.

[174] The MathWorks, I. *Matlab – The language of Technical Computing.* The MathWorks, Inc., 1994.

[175] Coleman, T.; Li, Y. An interior trust region approach for nonlinear minimization subject to bounds, *SIAM J. Optim.* **1996**, *6*, 418 – 445.

[176] Tafazzoli, M.; Grhiasi, M. New Karplus equations for (2)J(HH), (3)J(HH), (2)J(CH), (3)J(CH), (3)J(COCH), (3)J(CSCH), and (3)J(CCCH) in some aldohexopyranoside derivatives as determined using NMR spectroscopy and density functional theory calculations, *Carbohydr. Res.* **2007**, *342*, 2086 – 2096.

[177] Luy, B.; Glaser, S. J. Negative polarization transfer between a spin 1/2 and a spin 1, *Chem. Phys. Let.* **2000**, *323*, 377 – 381.

[178] Schulte-Herbrüggen, T.; Madi, Z.; Sørensen, O.; Ernst, R. Reduction of multiplet complexity in COSY-type NMR-spectra - the bilinear and planar COSY experiments, *Mol. Phys.* **1991**, *72*, 847 – 871.

[179] Krishnan, V. V.; Rance, M. Calculation of coherence-transfer behavior under planar versus isotropic mixing Hamiltonians and application to heteronuclear J cross-polarization experiments in solution-state NMR spectroscopy, *J. Magn. Reson.* **1997**, *124*, 205 – 209.

[180] Schedletzky, O.; Luy, B.; Glaser, S. J. Analytical polarization and coherence transfer functions for three coupled spins 1/2 under planar mixing conditions, *J. Magn. Reson.* **1998**, *130*, 27 – 32.

[181] Luy, B.; Glaser, S. J. Transverse magnetization transfer under planar mixing conditions in spin systems consisting of three coupled spins 1/2, *J. Magn. Reson.* **2003**, *164*, 304 – 309.

[182] Skinner, T. E.; Reiss, T. O.; Luy, B.; Khaneja, N.; Glaser, S. J. Application of optimal control theory to the design of broadband excitation pulses for high-resolution NMR, *J. Magn. Reson.* **2003**, *163*, 8 – 15.

[183] Skinner, T. E.; Reiss, T. O.; Luy, B.; Khaneja, N.; Glaser, S. J. Reducing the duration of broadband excitation pulses using optimal control with limited RF amplitude, *J. Magn. Reson.* **2004**, *167*, 68 – 74.

[184] Kobzar, K.; Luy, B.; Khaneja, N.; Glaser, S. J. Pattern pulses: design of arbitrary excitation profiles as a function of pulse amplitude and offset, *J. Magn. Reson.* **2005**, *173*, 229 – 235.

[185] Kobzar, K.; Skinner, T. E.; Khaneja, N.; Glaser, S. J.; Luy, B. Exploring the limits of broadband excitation and inversion pulses, *J. Magn. Reson.* **2004**, *170*, 236 – 243.

[186] Khaneja, N.; Reiss, T.; Luy, B.; Glaser, S. J. Optimal control of spin dynamics in the presence of relaxation, *J. Magn. Reson.* **2003**, *162*, 311 – 319.

[187] Khaneja, N.; Luy, B.; Glaser, S. J. Boundary of quantum evolution under decoherence, *Proc. Nat. Acad. Sci. USA* **2003**, *100*, 13162 – 13166.

[188] Kehlet, C. T.; Sivertsen, A. C.; Bjerring, M.; Reiss, T. O.; Khaneja, N.; Glaser, S. J.; Nielsen, N. C. Improving solid-state NMR dipolar recoupling by optimal control, *J. Am. Soc. Chem.* **2004**, *126*, 10202 – 10203.

[189] Khaneja, N.; Reiss, T.; Kehlet, C.; Schulte-Herbrüggen, T.; Glaser, S. J. Optimal control of coupled spin dynamics: design of NMR pulse

sequences by gradient ascent algorithms, *J. Magn. Reson.* **2005**, *172*, 296 – 305.

[190] Jeener, J. Superoperators in magnetic resonance, *Adv. Magn. Reson.* **1982**, *10*, 1 – 51.

[191] Urist, M. Bone-formation by autoinduction, *Science* **1965**, *150*, 893 – 899.

[192] Wozney, J.; Rosen, V.; Celeste, A.; Mitsock, L.; Whitters, M.; Kriz, R.; Hewick, R.; Wang, E. Novel regulators of bone-formation - molecular clones and activities, *Science* **1988**, *242*, 1528 – 1534.

[193] Balemans, W.; van Hul, W. Extracellular regulation of BMP signaling in vertebrates: A cocktail of modulators, *Dev. Biol.* **2002**, *250*, 231 – 250.

[194] Hogan, B. Bone morphogenetic proteins in development, *Curr. Opin. Genetics Dev.* **1996**, *6*, 432 – 438.

[195] Graff, J. Embryonic patterning: To BMP or not to BMP, that is the question, *Cell* **1997**, *89*, 171 – 174.

[196] Ebendal, T.; Bengtsson, H.; Soderstrom, S. Bone morphogenetic proteins and their receptors: Potential functions in the brain, *J. Neurosci. Res.* **1998**, *51*, 139 – 146.

[197] Wozney, J. The bone morphogenetic protein family: multifunctional cellular regulators in the embryo and adult, *Eur. J. Oral Sci.* **1998**, *106*, 160 – 166.

[198] Newfeld, S.; Wisotzkey, R.; Kumar, S. Molecular evolution of a developmental pathway: Phylogenetic analyses of transforming growth factor-beta family ligands, receptors and Smad signal transducers, *Genetics* **1999**, *152*, 783 – 795.

[199] Sebald, W.; Nickel, J.; Zhang, J.; Mueller, T. Molecular recognition in bone morphogenetic protein (BMP)/receptor interaction, *Biol. Chem.* **2004**, *385*, 697 – 710.

[200] Jones, W.; Richmond, E.; White, K.; Sasak, H.; Kusmik, W.; Smart, J.; Oppermann, H.; Rueger, D.; Tucker, R. Osteogenic protein-1 (OP-1) expression and processing in chinese-hamster ovary cells - isolation of a soluble complex containing the mature and pro-domains of OP-1, *Growth Factors* **1994**, *11*, 215 – 225.

[201] Constam, D.; Robertson, E. Regulation of bone morphogenetic protein activity by pro domains and proprotein convertases, *J. Cell Biol.* **1999**, *144*, 139 – 149.

[202] Daopin, S.; Piez, K.; Ogawa, Y.; Davies, D. Crystal-structure of transforming growth-factor-beta-2 – an unusual fold for the superfamily, *Science* **1992**, *257*, 369 – 373.

[203] Mc Donald, N.; Hendrickson, W. A structural superfamily of growth-factor containing a cystine knot motif, *Cell* **1993**, *73*, 421 – 424.

[204] Pallaghy, P.; Nielsen, K.; Craik, D.; Norton, R. A common structural motif incorporating a cystine knot and a triple-stranded beta-sheet in toxic and inhibitory polypeptides, *Prot. Sci.* **1994**, *3*, 1833 – 1839.

[205] Scheufler, C.; Sebald, W.; Hulsmeyer, M. Crystal structure of human bone morphogenetic protein-2 at 2.7 Å resolution, *J. Mol. Biol.* **1999**, *287*, 103 – 115.

[206] Mittl, P.; Priestle, J.; Cox, D.; Mc Master, G.; Cerletti, N.; Grutter, M. The crystal structure of TGF-beta 3 and comparison to TGF-beta 2: Implications for receptor binding, *Prot. Sci.* **1996**, *5*, 1261 – 1271.

[207] Allendorph, G.; Isaacs, M.; Kawakami, Y.; Belmonte, J.; Choe, S. BMP-3 and BMP-6 structures illuminate the nature of binding specificity with receptors, *Biochemistry* **2007**, *46*, 12238 – 12247.

[208] Griffith, D.; Oppermann, H.; Rueger, D.; Sampath, T.; Tucker, R.; Carlson, W. Crystallization and preliminary crystallographic data of recombinant human osteogenic protein-1 (HOP-1), *J. Mol. Biol.* **1994**, *244*, 657 – 658.

[209] Brown, M.; Zhao, Q.; Baker, K.; Naik, C.; Chen, C.; Pukac, L.; Singh, M.; Tsareva, T.; Parice, Y.; Mahoney, A.; Roschke, V.;

Sanyal, I.; Choe, S. Crystal structure of BMP-9 and functional interactions with pro-region and receptors, *J. Biol. Chem.* **2005**, *280*, 25111 – 25118.

[210] Nickel, J.; Kotzsch, A.; Sebald, W.; Mueller, T. A single residue of GDF-5 defines binding specificity to BMP receptor IB, *J. Mol. Biol.* **2005**, *349*, 933 – 947.

[211] Müller , T. personal communication, 2007.

[212] Eigenbrot, C.; Gerber, N. X-ray structure of glial cell-derived neurotrophic factor at 1.9 angstrom resolution and implications for receptor binding, *Nat. Struc. Biol.* **1997**, *4*, 435 – 438.

[213] Hinck, A.; Archer, S.; Qian, S.; Roberts, A.; Sporn, M.; Weatherbee, J.; Tsang, M.; Lucas, R.; Zhang, B.; Wenker, J.; Torchia, D. Transforming growth factor beta 1: Three-dimensional structure in solution and comparison with the X-ray structure of transforming growth factor beta 2, *Biochemistry* **1996**, *35*, 8517 – 8534.

[214] Massague, J. TGF-beta signal transduction, *Annu. Rev. Biochem* **1998**, *67*, 753 – 791.

[215] Manning, G.; Whyte, D.; Martinez, R.; Hunter, T.; Sudarsanam, S. The protein kinase complement of the human genome, *Science* **2002**, *298*, 1912 – 1934.

[216] de Caestecker, M. The transforming growth factor-beta superfamily of receptors, *Cytokine Growth Factor Rev.* **2004**, *15*, 1 – 11.

[217] Greenwald, J.; Fischer, W.; Vale, W.; Choe, S. Three-finger toxin fold for the extracellular ligand-binding domain of the type II activin receptor serine kinase., *Nat. Struc. Biol.* **1999**, *6*, 18 – 22.

[218] Wieser, R.; Wrana, J.; Massague, J. GS domain mutations that constitutively activate T-beta-R-I, the downstream signaling component in the TGF-beta receptor complex, *EMBO J.* **1995**, *14*, 2199 – 2208.

[219] Attisano, L.; Wrana, J.; Montalvo, E.; Massague, J. Activation of signalling by the activin receptor complex, *Mol. Cell. Biol.* **1996**, *16*, 1066 – 1073.

[220] Wrana, J.; Attisano, L.; Wieser, R.; Ventura, F.; Massague, J. Mechanism of activation of the TGF-beta receptor, *Nature* **1994**, *370*, 341 – 347.

[221] Miyazawa, K.; Shinozaki, M.; Hara, T.; Furuya, T.; Miyazono, K. Two major Smad pathways in TGF-beta superfamily signalling, *Genes Cells* **2002**, *7*, 1191 – 1204.

[222] Wrana, J.; Attisano, L.; Carcamo, J.; Zentella, A.; Doody, J.; Laiho, M.; Wang, X.; Massague, J. TGF-beta signals through a heteromeric protein-kinase receptor complex, *Cell* **1992**, *71*, 1003 – 1014.

[223] Liu, F.; Ventura, F.; Doody, J.; Massague, J. Human type-II receptor for bone morphogenetic proteins (BMPs) – extension of the 2-kinase receptor model to the BMPs, *Mol. Cell. Biol.* **1995**, *15*, 3479 – 3486.

[224] ten Dijke, P.; Miyazono, K.; Heldin, C. Signaling via hetero-oligomeric complexes of type I and type II serine/threonine kinase receptors, *Curr. Opin. Cell Biol.* **1996**, *8*, 139 – 145.

[225] Moustakas, A.; Souchelnytskyi, S.; Heldin, C. Smad regulation in TGF-beta signal transduction, *J. Cell Sci.* **2001**, *114*, 4359 – 4369.

[226] Shi, Y.; Massague, J. Mechanisms of TGF-beta signaling from cell membrane to the nucleus, *Cell* **2003**, *113*, 685 – 700.

[227] Attisano, L.; Wrana, J. Signal transduction by the TGF-beta superfamily, *Science* **2002**, *296*, 1646 – 1647.

[228] Imamura, T.; Takase, M.; Nishihara, A.; Oeda, E.; Hanai, J.; Kawabata, M.; Miyazono, K. Smad6 inhibits signalling by the TGF-beta superfamily, *Nature* **1997**, *389*, 622 – 626.

[229] Nakao, A.; Afrakhte, M.; Moren, A.; Nakayama, T.; Christian, J.; Heuchel, R.; Itoh, S.; Kawabata, N.; Heldin, N.; Heldin, C.; tendijke, P. Identification of Smad7, a TGF beta-inducible antagonist of TGF-beta signalling, *Nature* **1997**, *389*, 631 – 635.

[230] Moustakas, A.; Heldin, C. Non-Smad TGF-beta signals, *J. Cell Sci.* **2005**, *118*, 3573 – 3584.

[231] Yamashita, H.; ten Dijke, P.; Franzen, P.; Miyazono, K.; Heldin, C. Formation of heterooligomeric complexes of type-I and type-II receptors for transforming growth-factor-beta, *J. Biol. Chem.* **1994**, *269*, 20172 – 20178.

[232] Attisano, L.; Wrana, J.; Cheifetz, S.; Massague, J. Novel activin receptors - distinct genes and alternative messenger-RNA splicing generate a repertoire of serine threonine kinase receptors, *Cell* **1992**, *68*, 97 – 108.

[233] Zimmerman, C.; Mathews, L. Activin receptors: Cellular signalling by receptor serine kinases, *Extracellular Regulators of Differentiation and Development* **1996**, 25 – 38.

[234] Lee, S.; Mcpherron, A. Regulation of myostatin activity and muscle growth, *Proc. Nat. Acad. Sci. USA* **2001**, *98*, 9306 – 9311.

[235] Oh, S.; Yeo, C.; Lee, Y.; Schrewe, H.; Whitman, M.; Li, E. Activin type IIA and IIB receptors mediate Gdf11 signaling in axial vertebral patterning, *Genes Dev.* **2002**, *16*, 2749 – 2754.

[236] Cheng, S.; Olale, F.; Bennett, J.; Brivanlou, A.; Schier, A. EGF-CFC proteins are essential coreceptors for the TGF-beta signals VG1 and GDF1, *Genes Dev.* **2003**, *17*, 31 – 36.

[237] Yeo, C.; Whitman, M. Nodal signals to Smads through Cripto-dependent and Cripto-independent mechanisms, *Mol. Cell.* **2001**, *7*, 949 – 957.

[238] Hoodless, P.; Haerry, T.; Abdollah, S.; Stapleton, M.; Oconnor, M.; Attisano, L.; Wrana, J. MADR1, a MAD-related protein that functions in BMP-2 signaling pathways, *Cell* **1996**, *85*, 489 – 500.

[239] Ebisawa, T.; Tada, K.; Kitajima, I.; Tojo, K.; Sampath, T.; Kawabata, M.; Miyazono, K.; Imamura, T. Characterization of bone morphogenetic protein-6 signaling pathways in osteoblast differentiation, *J. Cell Sci.* **1999**, *112*, 3519 – 3527.

[240] Yamashita, H.; ten Dijke, P.; Huylebroeck, D.; Sampath, T.; Andries, M.; Smith, J.; Heldin, C.; Miyazono, K. Osteogenic protein-1 binds to activin type-II receptors and induces certain activin-linke effects, *J. Cell Biol.* **1995**, *130*, 217 – 226.

[241] Ventura, F.; Doody, J.; Liu, F.; Wrana, J.; Massague, J. Reconstitution and transphosphorylation of TGF-beta receptor complexes, *EMBO J.* **1994**, *13*, 5581 – 5589.

[242] Attisano, L.; Carcamo, J.; Ventura, F.; Weis, F.; Massague, J.; Wrana, J. Identification of human activin and TGF-beta type-I receptors that form heteromeric kinase complexes with type-II receptors, *Cell* **1993**, *75*, 671 – 680.

[243] Ebner, R.; Chen, R.; Shum, L.; Lawler, S.; Zioncheck, T.; Lee, A.; Lopez, A.; Derynck, R. Cloning of a type-I TGF-beta receptor and its effect of TGF-beta binding to the type-II receptor, *Science* **1993**, *260*, 1344 – 1348.

[244] Franzen, P.; ten Dijke, P.; Ichijo, H.; Yamashita, H.; Schulz, P.; Heldin, C.; Miyazono, K. Cloning of a TGF-beta type-I receptor that forms a heteromeric complex with the TGF-beta type-II receptor, *Cell* **1993**, *75*, 681 – 692.

[245] Bassing, C.; Yingling, J.; Howe, D.; Wang, T.; He, W.; Gustafson, M.; Shah, P.; Donahoe, P.; Wang, X. A transforming growth-factor-beta type-I receptor that signals to activate gene-expression, *Science* **1994**, *263*, 87 – 89.

[246] Mathews, L.; Vale, W. Characterization of type-II activin receptors – binding, processing, and phosphorylation, *J. Biol. Chem.* **1993**, *268*, 19013 – 19018.

[247] Kirsch, T.; Nickel, J.; Sebald, W. BMP-2 antagonists emerge from alterations in the low-affinity binding epitope for receptor BMPR-II, *EMBO J.* **2000**, *19*, 3314 – 3324.

[248] ten Dijke, P.; Yamashita, H.; Sampath, T.; Reddi, A.; Estevez, M.; Riddle, D.; Ichijo, H.; Heldin, C.; Miyazono, K. Identification of type-I receptors for osteogenic protein-1 and bone morphogenetic protein-4, *J. Biol. Chem.* **1994**, *269*, 16985 – 16988.

[249] Macias-Silva, M.; Hoodless, P.; Tang, S.; Buchwald, M.; Wrana, J. Specific activation of Smad1 signaling pathways by the BMP-7 type I receptor, ALK-2, *J. Biol. Chem.* **1998**, *273*, 25628 – 25636.

[250] Rebbapragada, A.; Benchabane, H.; Wrana, J.; Celeste, A.; Attisano, L. Myostatin signals through a transforming growth factor beta-like signaling pathway to block adipogenesis, *Mol. Cell. Biol.* **2003**, *23*, 7230 – 7242.

[251] Greenwald, J.; Groppe, J.; Gray, P.; Wiater, E.; Kwiatkowski, W.; Vale, W.; Choe, S. The BMP-7/ActR-II extracellular domain complex provides new insights into the cooperative nature of receptor assembly, *Mol. Cell.* **2003**, *11*, 605 – 617.

[252] Lopez-Casillas, F.; Cheifetz, S.; Doody, J.; Andres, J.; Lane, W.; Massague, J. Structure and expression of the membrane proteoglycan betaglycan, a component of the TGF-beta receptor system, *Cell* **1991**, *67*, 785 – 795.

[253] Lewis, K.; Gray, P.; Blount, A.; Macconnell, L.; Wiater, E.; Bilezikjian, L.; Vale, W. Betaglycan binds inhibin and can mediate functional antagonism of activin signalling, *Nature* **2000**, *404*, 411 – 414.

[254] Shen, M.; Schier, A. The EGF-CFC gene family in vertebrate development, *Trends Genet.* **2000**, *16*, 303 – 309.

[255] Onichtchouk, D.; Chen, Y.; Dosch, R.; Gawantka, V.; Dellus, H.; Massague, J.; Niehrs, C. Silencing of TGF-beta signalling by the pseudoreceptor BAMBI, *Nature* **1999**, *401*, 480 – 485.

[256] Tsang, M.; Kim, R.; de caestecker, M.; Kudoh, T.; Roberts, A.; Dawid, I. Zebrafish nma is involved in TGF-beta family signaling, *Genesis* **2000**, *28*, 47 – 57.

[257] Massague, J.; Chen, Y. Controlling TGF-beta signaling, *Genes Dev.* **2000**, *14*, 627 – 644.

[258] Harland, R. Developmental biology - A twist on embryonic signalling, *Nature* **2001**, *410*, 423 – 424.

[259] Kirsch, T.; Sebald, W.; Dreyer, M. Crystal structure of the BMP-2-BRIA ectodomain complex, *Nat. Struc. Biol.* **2000**, *7*, 492 – 496.

[260] Keller, S.; Nickel, J.; Zhang, J.; Sebald, W.; Mueller, T. Molecular recognition of BMP-2 and BMP receptor IA, *Nat. Struc. Mol. Biol* **2004**, *11*, 481 – 488.

[261] Hatta, T.; Konishi, H.; Katoh, E.; Natsume, T.; Ueno, N.; Kobayashi, Y.; Yamazaki, T. Identification of the ligand-binding site of the BMP type IA receptor for BMP-4, *Biopolymers* **2000**, *55*, 399 – 406.

[262] Allendorph, G.; Vale, W.; Choe, S. Structure of the ternary signaling complex of a TGF-beta superfamily member, *Proc. Nat. Acad. Sci. USA* **2006**, *103*, 7643 – 7648.

[263] Müller, T.; Gottermeier, M.; Sebald, W.; Nickel, J. Crystallization and preliminary X-ray diffraction analysis of human growth and differentiation factor 5 (GDF-5), *Acta Crystallogr. F* **2005**, *61*, 134 – 136.

[264] Bocharov, E.; Korzhnev, D.; Blommers, M.; Arvinte, T.; Orekhov, V.; Billeter, M.; Arseniev, A. Dynamics-modulated biological activity of transforming growth factor beta 3, *J. Biol. Chem.* **2002**, *277*, 46273 – 46279.

[265] Brooks, C.; Gruebele, M.; Onuchic, J.; Wolynes, P. Chemical physics of protein folding, *Proc. Nat. Acad. Sci. USA* **1998**, *95*, 11037 – 11038.

[266] Atkinson, R.; Kieffer, B. The role of protein motions in molecular recognition: insights from heteronuclear NMR relaxation measurements, *Prog.Nucl. Magn. Reson. Spectrosc.* **2004**, *44*, 141 – 187.

[267] Palmer, A. NMR characterization of the dynamics of biomacromolecules, *Chem. Rev.* **2004**, *104*, 3623 – 3640.

[268] Stone, M. NMR relaxation studies of the role of conformational entropy in protein stability and ligand binding, *Acc. Chem. Res.* **2001**, *34*, 379 – 388.

[269] Arumugam, S.; Gao, G.; Patton, B.; Semenchenko, V.; Brew, K.; van Doren, S. Increased backbone mobility in beta-barrel enhances entropy gain driving binding of N-TIMP-1 to MMP-3, *J. Mol. Biol.* **2003**, *327*, 719 – 734.

[270] Olejniczak, E.; Zhou, M.; Fesik, S. Changes in the NMR-derived motional parameters of the insulin receptor substrate 1 phosphotyrosine

binding domain upon binding to an interleukin 4 receptor phosphopeptide, *Biochemistry* **1997**, *36*, 4118 – 4124.

[271] Laity, J.; Dyson, H.; Wright, P. Molecular basis for modulation of biological function by alternate splicing of the Wilms' tumor suppressor protein, *Proc. Nat. Acad. Sci. USA* **2000**, *97*, 11932 – 11935.

[272] Yuan, P.; Marshall, V.; Petzold, G.; Poorman, R.; Stockman, B. Dynamics of stromelysin/inhibitor interactions studied by ^{15}N NMR relaxation measurements: Comparison of ligand binding to the S-1-S-3 and S-1 '-S-3 ' subsites, *J. Biomol. NMR* **1999**, *15*, 55 – 64.

[273] Ladbury, J.; Williams, M. The extended interface: measuring non-local effects in biomolecular interactions, *Curr. Opin. Struc. Biol.* **2004**, *14*, 562 – 569.

[274] Kay, L.; Muhandiram, D.; Wolf, G.; Shoelson, S.; Forman-Kay, J. Correlation between binding and dynamics at SH2 domain interfaces, *Nat. Struc. Biol.* **1998**, *5*, 156 – 163.

[275] Leutner, M.; Gschwind, R.; Liermann, J.; Schwarz, C.; Gemmecker, G.; Kessler, H. Automated backbone assignment of labeled proteins using the threshold accepting algorithm, *J. Biomol. NMR* **1998**, *11*, 31 – 43.

[276] Yamazaki, T.; Forman-Kay, J.; Kay, L. 2D NMR experiments for correlating ^{13}C-beta and ^{1}H-delta/epsilon chemical-shifts of aromatic residues in ^{13}C-labeled proteins via scalar couplings, *J. Am. Chem. Soc.* **1993**, *115*, 11054 – 11055.

[277] Grzesiek, S.; Bax, A. Audio-frequency NMR in a nutating frame – application to the assignment of phenylalanine residues in isotopically enriched proteins, *J. Am. Chem. Soc.* **1995**, *117*, 6527 – 6531.

[278] Carlomagno, T.; Maurer, M.; Sattler, M.; Schwendinger, M.; Glaser, S.; Griesinger, C. PLUSH TACSY: Homonuclear planar TACSY with two-band selective shaped pulses applied to C^{α},C' transfer and C^{beta},$C^{\mathrm{arom.}}$ correlations, *J. Biomol. NMR* **1996**, *8*, 161 – 170.

[279] Löhr, F.; Rüterjans, H. Novel pulse sequences for the resonance assignment of aromatic side chains in ^{13}C-labeled proteins, *J. Magn. Reson. Series B* **1996**, *112*, 259 – 268.

[280] Xia, Y.; Legge, G.; Jun, K.; Qi, Y.; Lee, H.; Gao, X. IP-COSY, a totally in-phase and sensitive COSY experiment, *Magn. Reson. Chem.* **2005**, *43*, 372 – 379.

[281] Uhrin, D.; Liptaj, T.; Kover, K. Modified BIRD pulses and design of heteronuclear pulse sequences, *J. Magn. Reson. Series A* **1993**, *101*, 41 – 46.

[282] Dalvit, C.; Bohlen, J. Simultaneous suppression of the H_2O double-quantum signal and of the radiation-damping effect in double-quantum experiments, *J. Magn. Reson. Series B* **1996**, *113*, 195 – 200.

[283] Dalvit, C.; Bohlen, J. Spectral editing and water suppression in double-quantum experiments, *J. Magn. Reson. Series B* **1996**, *111*, 76 – 80.

[284] Mesleh, M.; Veglia, G.; Desilva, T.; Marassi, F.; Opella, S. Dipolar waves as NMR maps of protein structure, *J. Am. Chem. Soc.* **2002**, *124*, 4206 – 4207.

[285] Mesleh, M.; Opella, S. Dipolar waves as NMR maps of helices in proteins, *J. Magn. Reson.* **2003**, *163*, 288 – 299.

[286] Mesleh, M.; Lee, S.; Veglia, G.; Thiriot, D.; Marassi, F.; Opella, S. Dipolar waves map the structure and topology of helices in membrane proteins, *J. Am. Chem. Soc.* **2003**, *125*, 8928 – 8935.

[287] Ramamoorthy, A.; Wu, C.; Opella, S. 3D solid-state NMR experiment that correlates the chemical-shift and dipolar coupling frequencies of 2 heteronuclei, *J. Magn. Reson. Series B* **1995**, *107*, 88 – 90.

[288] Ramamoorthy, A.; Opella, S. 2D chemical-shift heteronuclear dipolar coupling spectra obtained with polarization inversion spin-exchange at the magic-angle and magic-angle sample-spinning (PISEMA-MAS), *Solid State Nucl. Magn. Reson.* **1995**, *4*, 387 – 392.

[289] Wishart, D.; Sykes, B.; Richards, F. The chemical-shift index – A fast and simple method for the assignment of protein secondary structure through NMR-spectroscopy, *Biochemistry* **1992**, *31*, 1647 – 1651.

[290] Wishart, D.; Sykes, B. Chemical-shifts as a tool for structure determination, *Nuclear Magnetic Resonance, Pt C* **1994**, *239*, 363 – 392.

[291] Wishart, D.; Sykes, B. The ^{13}C chemical-shift index - a simple method for the identification of protein secondary structure using ^{13}C chemical-shift data, *J. Biomol. NMR* **1994**, *4*, 171 – 180.

[292] Cornilescu, G.; Delaglio, F.; Bax, A. Protein backbone angle restraints from searching a database for chemical shift and sequence homology, *J. Biomol. NMR* **1999**, *13*, 289 – 302.

[293] Ginzinger, S.; Fischer, J. SimShift: Identifying structural similarities from NMR chemical shifts, *Bioinformatics* **2006**, *22*, 460 – 465.

[294] Wishart, D.; Bigam, C.; Holm, A.; Hodges, R.; Sykes, B. ^{1}H, ^{13}C, and ^{15}N random coil NMR chemical-shifts of the common amino-acids .1. Investigations of nearest-neighbor effects, *J. Biomol. NMR* **1995**, *5*, 332 – 332.

[295] Ginzinger, S.; Gerick, F.; Coles, M.; Heun, V. CheckShift: automatic correction of inconsistent chemical shift referencing, *J. Biomol. NMR* **2007**, *39*, 223 – 227.

[296] Doddrell, D.; Burfitt, I.; Kitching, W.; Bullpitt, M.; Lee, C.; Mynott, R.; Considin.jl; Kuivila, H.; Sarma, R. ^{13}C fourier-transform NMR-study of organotin compounds – Karplus-type dependence of vicinal ^{119}Sn-^{13}C coupling, *J. Am. Chem. Soc.* **1974**, *96*, 1640 – 1642.

[297] Karplus, M. Contact electron-spin coupling of nuclear magnetic moments, *J. Chem. Phys.* **1959**, *30*, 11 – 15.

[298] Wang, A.; Bax, A. Reparametrisation of the Karplus relation for $^{3}J_{H^{\alpha}N}$ and $^{3}J_{H^{N}C'}$ in peptides from uniformly ^{13}C/^{15}N-enriched human ubiqquitin, *J. Am. Chem. Soc.* **1995**, *117*, 1810 – 1813.

[299] Cordier, F.; Grzesiek, S. Direct observation of hydrogen bonds in proteins by interresidue $^{3h}J_{NC}$ scalar couplings, *J. Am. Chem. Soc.* **1999**, *121*, 1601 – 1602.

[300] Cornilescu, G.; Ramirez, B.; Frank, M.; Clore, G.; Gronenborn, A.; Bax, A. Correlation between $^{3h}J_{NC}$ and hydrogen bond length in proteins, *J. Am. Chem. Soc.* **1999**, *121*, 6275 – 6279.

[301] Grzesiek, S.; Cordier, F.; Jaravine, V.; Barfield, M. Insights into biomolecular hydrogen bonds from hydrogen bond scalar couplings, *Prog. Nucl. Magn. Reson. Spectrosc.* **2004**, *45*, 275 – 300.

[302] Dempsey, C. Hydrogen exchange in peptides and proteins using NMR-spectroscopy, *Prog. Nucl. Magn. Reson. Spectrosc.* **2001**, *39*, 135 – 170.

[303] Gal, M.; Schanda, P.; Brutscher, B.; Frydman, L. UltraSOFAST HMQC NMR and the repetitive acquisition of 2D protein spectra at Hz rates, *J. Am. Chem. Soc.* **2007**, *129*, 1372 – 1377.

[304] Gemmecker, G.; Jahnke, W.; Kessler, H. Measurement of fast proton-exchange rates in isotopically labeled compounds, *J. Am. Chem. Soc.* **1993**, *115*, 11620 – 11621.

[305] Jahnke, W. *Entwicklung und Anwendung NMR-spektroskopischer Methoden zur Strukturaufklärung von Proteinen und Nukleinsäuren.* PhD thesis, Technische Universität München, 1994.

[306] Mori, S.; Berg, J.; vanzijl, P. Separation of intramolecular NOE and exchange peaks in water exchange spectroscopy using spin-echo filters, *J. Biomol. NMR* **1996**, *7*, 77 – 82.

[307] Hwang, T.; van Zijl, P.; Mori, S. Accurate quantitation of water-amide proton exchange rates using the Phase-Modulated CLEAN chemical EXchange (CLEANEX-PM) approach with a Fast-HSQC (FHSQC) detection scheme, *J. Biomol. NMR* **1998**, *11*, 221 – 226.

[308] Kateb, F.; Pelupessy, P.; Bodenhausen, G. Measuring fast hydrogen exchange rates by NMR spectroscopy, *J. Magn. Reson.* **2007**, *184*, 108 – 113.

[309] Baxter, N.; Williamson, M. Temperature dependence of ^{1}H chemical shifts in proteins, *J. Biomol. NMR* **1997**, *9*, 359 – 369.

[310] Chill, J.; Loius, J.; Miller, C.; Bax, A. A Triple Resonance NMR View of the Tetrameric Potassium Channel. 47^{th}ENC, Asilomar, USA, 2006.

[311] Kabsch, W.; Sander, C. Dictionary of protein secondary structure – pattern recognition of hydrogen-bonded and geometrical features, *Biopolymers* **1983**, *22*, 2577 – 2637.

[312] Truffault, V.; Coles, M.; Diercks, T.; Abelmann, K.; Eberhardt, S.; Luttgen, H.; Bacher, A.; Kessler, H. The solution structure of the N-terminal domain of riboflavin synthase, *J. Mol. Biol.* **2001**, *309*, 949 – 960.

[313] Nilges, M. Calculation of protein structures with ambiguous distance restraints – automated assignment of ambiguos NOE crosspeak and disulfide connectivities, *J. Mol. Biol.* **1995**, *245*, 645 – 660.

[314] Herrmann, T.; Güntert, P.; Wüthrich, K. Protein NMR structure determination with automated NOE assignment using the new software CANDID and the torsion angle dynamics algorithm DYANA, *J. Mol. Biol.* **2002**, *319*, 209 – 227.

[315] Coles, M. Globally right, locally wrong; errors in automatic structure determination. EUROMAR, Taragona, Spain, 2007.

[316] Diercks, T.; Coles, M.; Kessler, H. An efficient strategy for assignment of cross-peaks in 3D heteronuclear NOESY experiments, *J. Biomol. NMR* **1999**, *15*, 177 – 180.

[317] Laskowski, R.; Rullmann, J.; Macarthur, M.; Kaptein, R.; Thornton, J. AQUA and PROCHECK-NMR: Programs for checking the quality of protein structures solved by NMR, *J. Biomol. NMR* **1996**, *8*, 477 – 486.

[318] Doreleijers, J.; Raves, M.; Rullmann, T.; Kaptein, R. Completeness of NOEs in protein structures: A statistical analysis of NMR data, *J. Biomol. NMR* **1999**, *14*, 123 – 132.

[319] Lovell, S.; Davis, I.; Adrendall, W.; de bakker, P.; Word, J.; Prisant, M.; Richardson, J.; Richardson, D. Structure validation by C alpha geometry: phi,psi and C beta deviation, *Proteins-Structure Function and Genetics* **2003**, *50*, 437 – 450.

[320] Laskowski, R.; Macarthur, M.; Moss, D.; Thornton, J. Procheck – a programm to check the stereochemical quality of protein structures, *J. Appl. Crystallogr.* **1993**, *26*, 283 – 291.

[321] Hooft, R.; Vriend, G.; Sander, C.; Abola, E. Errors in protein structures, *Nature* **1996**, *381*, 272 – 272.

[322] Rees, B.; Bilwes, A. 3-dimensional structures of neurotoxins and cardiotoxins, *Chem. Res. Toxicol.* **1993**, *6*, 385 – 406.

[323] Tjandra, N.; Omichinski, J.; Gronenborn, A.; Clore, G.; Bax, A. Use of dipolar ^{1}H-^{15}N and ^{1}H-^{13}C couplings in the structure determination of magnetically oriented macromolecules in solution, *Nat. Struc. Biol.* **1997**, *4*, 732 – 738.

[324] Ottiger, M.; Delaglio, F.; Bax, A. Measurement of J and dipolar couplings from simplified two-dimensional NMR spectra, *J. Magn. Reson.* **1998**, *131*, 373 – 378.

[325] Permi, P.; Rosevear, P.; Annila, A. A set of HNCO-based experiments for measurement of residual dipolar couplings in ^{15}N, ^{13}C, ^{2}D-labeled proteins, *J. Biomol. NMR* **2000**, *17*, 43 – 54.

[326] Grzesiek, S.; Bax, A. Improved 3D triple-resonance NMR techniques applied to a 31kDa protein, *J. Magn. Reson.* **1992**, *96*, 432 – 440.

[327] Cornilescu, G.; Marquardt, J.; Ottiger, M.; Bax, A. Validation of protein structure from anisotropic carbonyl chemical shifts in a dilute liquid crystalline phase, *J. Am. Chem. Soc.* **1998**, *120*, 6836 – 6837.

[328] Clore, G.; Gronenborn, A. NMR structure determination of proteins and protein complexes larger than 20 kDa, *Curr. Opin. Chem. Biol.* **1998**, *2*, 564 – 570.

[329] Buck, M. Trifluoroethanol and colleagues: cosolvents come of age. Recent studies with peptides and proteins, *Quat. Rev. Biophys.* **1998**, *31*, 297 – 355.

[330] Kay, L.; Torchia, D.; Bax, A. Backbone dynamics of proteins as studied by ^{15}N inverse detected heternuclear NMR spectroscopy – application to staphylococcal nuclease, *Biochemistry* **1989**, *28*, 8972 – 8979.

[331] Tjandra, N.; Feller, S.; Pastor, R.; Bax, A. Rotational diffusion anisotropy of human ubiquitin from ^{15}N NMR relaxation, *J. Am. Chem. Soc.* **1995**, *117*, 12562 – 12566.

[332] Zheng, Z.; Czaplicki, J.; Jardetzky, O. Backbone dynamics of Trp repressor studied by ^{15}N NMR relaxation, *Biochemistry* **1995**, *34*, 5212 – 5223.

[333] Lee, L.; Rance, M.; Chazin, W.; Palmer, A. Rotational diffusion anisotropy of proteins from simultaneous analysis of ^{15}N and $^{13}C^{\alpha}$ nuclear spin relaxation, *J. Biomol. NMR* **1997**, *9*, 287 – 298.

[334] Palmer, A. Inertia and Diffusion Tensors. http://www.cumc.columbia.edu/dept/gsas/biochem/labs/palmer/software/diffusion.html, 1996.

[335] Schneider, D.; Dellwo, M.; Wand, A. Fast internal main-chain dynamics of human ubiquitin, *Biochemistry* **1992**, *31*, 3645 – 3652.

[336] Kotzsch, A.; Nickel, J.; Seher, A.; Heinecke, K.; van Geersdaele, L.; Herrmann, T.; Sebald, W.; Mueller, T. Structure analysis of bone morphogenetic protein-2 type I receptor complexes reveals a mechanism of receptor inactivation in Juvenile Polyposis syndrome, *J. Biol. Chem.* **2008**, *283*, 5876–5887.

[337] Inaba, K.; Ito, K. Structure and mechanisms of the DsbB-DsbA disulfide bond generation machine, *Biochim. Biophys. Acta* **2008**, *1783*, 520 – 529.

[338] University of Wisconsin-Madison. BMRB – Biological Magnetic Resonance Data Bank – A Repository for Data from NMR Spectroscopy of Proteins, Peptides, and Nucleic Acids. http://www.bmrb.wisc.edu/, 2007.

[339] Shen, B.; Hage, T.; Sebald, W. Global and local determinants for the kinetics of interleukin-4/interleukin-4 receptor alpha chain interaction - A biosensor study employing recombinant interleukin-4-binding protein, *Eur. J. Biochem.* **1996**, *240*, 252 – 261.

[340] Schreiber, G.; Fersht, A. Interaction of barnase with its polypeptide inhibitor berstar studied by protein engineering, *Biochemistry* **1993**, *32*, 5145 – 5150.

[341] Peng, J.; Moore, J.; Abdul-Manan, N. NMR experiments for lead generation in drug discovery, *Prog. Nucl. Magn. Reson. Spectrosc.* **2004**, *44*, 225 – 256.

[342] De Crescenzo, G.; Grothe, S.; Zwaagstra, J.; Tsang, M.; O'connor-Mccourt, M. Real-time monitoring of the interactions of transforming growth factor-beta (TGF-beta) isoforms with latency-associated

protein and the ectodomains of the TGF-beta type II and III receptors reveals different kinetic models and stoichiometries of binding, *J. Biol. Chem.* **2001**, *276*, 29632 – 29643.

[343] Weber, D.; Kotzsch, A.; Nickel, J.; Harth, S.; Seher, A.; Mueller, U.; Sebald, W.; Mueller, T. A silent H-bond can be mutationally activated for high-affinity interaction of BMP-2 and activin type IIB receptor, *BMC Struc. Biol.* **2007**, *7*, 6.

[344] Meyer, A. *Strukturbasiertes Design selektiver Inhibitoren von Protein- Protein-Wechselwirkungen und Enzymen.* PhD thesis, Technische Universität München, 2006.

[345] Howe, J.; Sayed, M.; Ahmed, A.; Ringold, J.; Larsen-Haidle, J.; Merg, A.; Mitros, F.; Vaccaro, C.; Petersen, G.; Giardiello, F.; Tinley, S.; Aaltonen, L.; Lynch, H. The prevalence of MADH-4 and BMPR-1A mutations in juvenile polyposis and absence of BMPR-2, BMPR-1B, and ACVR-1 mutations, *J. Med. Genet.* **2004**, *41*, 484 – 491.

[346] Roberts, K.; Mcelroy, J.; Wong, W.; Yen, E.; Widlitz, A.; Barst, R.; Knowles, J.; Morse, J. BMPR-2 mutations in pulmonary arterial hypertension with congenital heart disease, *Eur. Respir. J.* **2004**, *24*, 371 – 374.

[347] Humbert, M.; Deng, Z.; Simonneau, G.; Barst, R.; Sitbon, O.; Wolf, M.; Cuervo, N.; Moore, K.; Hodge, S.; Knowles, J.; Morse, J. BMPR-2 germline mutations in pulmonary hypertension associated with fenfluramine derivatives, *Eur. Respir. J.* **2002**, *20*, 518 – 523.

[348] Kosaki, R.; Gebbia, M.; Kosaki, K.; Lewin, M.; Bowers, P.; Towbin, J.; Casey, B. Left-right axis malformations associated with mutations in ACVR2B, the gene for human activin receptor type IIB, *Am. J. Med. Genet.* **1999**, *82*, 70 – 76.

[349] Gause, G.; Brazhnikova, M.; Lissovskaya, N. Preparation and properties of crystalline gramicidine C, *Comptes Rendus de l'Academie des Sciences de l'URSS* **1944**, *43*, 217 – 219.

[350] Gause, G.; Brazhnikova, M. Gramicidin Sand its use in the treatment of infected wounds, *Nature* **1944**, *154*, 703 – 703.

[351] Gause, G.; Brazhnikova, M. Gramicin S - Origin and mode of action, *Lancet* **1944**, *2*, 715 – 716.

[352] Stansly, P.; Schlosser, M. Studies of polymyxin – isolation and identification of bacillus-polymyxa and differentiation of polymyxin from certain known antibiotics, *J. Bacteriol.* **1947**, *54*, 549 – 556.

[353] Shepherd, R. 1. Isolation and preliminary purification, *J. Am. Chem. Soc.* **1948**, *70*, 3771 – 3774.

[354] Porter, J.; Broschard, R.; Krupka, G.; Little, P.; Zellat, J. Isolation and production of polymyxin, *Ann. N. Y. Acad. Sci.* **1949**, *51*, 857 – 865.

[355] Sensi, P.; Margalith, P.; Timbal, M. Rifomycin, a new antibiotic – preliminary report, *Il Farmaco, ed. sci.* **1959**, *14*, 146 – 147.

[356] du Vigneaud, V.; Lawler, H.; Popenoe, E. Enymic cleavage of glycinamide from vasopressin and a proposed structure for this pressor-antidiuretic hormone of the posterior pituitary, *J. Am. Chem. Soc.* **1953**, *75*, 4880 – 4881.

[357] Archer, R.; du Vigneaud, V. La structure de la vasopressine de boeuf, *Biochim Biochim Acta* **1953**, *12*, 487 – 488.

[358] Emanuele, E.; Arra, M.; Pesenti, S. Vasopressin and oxytocin as neurohormonal mediators of MDMA (ecstasy) sociosexual behavioural effects, *Med. Hypotheses* **2006**, *67*, 1250 – 1251.

[359] Bellary, S.; Barnett, A. Inhaled insulin: new technology, new possibilities, *Int. J. Clin. Pract.* **2006**, *60*, 728 – 734.

[360] Curran, M.; Keating, G. Eptifibatide: A review of its use in patients with acute coronary syndromes and/or undergoing percutaneous coronary intervention, *Drugs* **2005**, *65*, 2009 – 2035.

[361] Bauer, W.; Briner, U.; Doepfner, W.; Haller, R.; Huguenin, R.; Marbach, P.; Petcher, T.; Pless, J. SMS 201-995 - a very potent and selective octapeptide analog of somatostatin with prolonged action, *Life Sci.* **1982**, *31*, 1133 – 1140.

[362] Veber, D.; Holly, F.; Nutt, R.; Bergstrand, S.; Brady, S.; Hirschmann, R.; Glitzer, M.; Saperstein, R. Highly-active cyclic and bicyclic somatostatin analogs of reduced ring size, *Nature* **1979**, *280*, 512 – 514.

[363] Chatterjee, J.; Mierke, D.; Kessler, H. N-methylated cyclic pentaalanine peptides as template structures, *J. Am. Chem. Soc.* **2006**, *128*, 15164 – 15172.

[364] Adler, M.; Lazarus, R.; Dennis, M.; Wagner, G. Solution structure of kistrin, a potent platelet-aggregation inhibitor and GP-IIB-IIIA antagonist, *Science* **1991**, *253*, 445 – 448.

[365] Shroff, H.; Schwender, C.; Dottavio, D.; Yang, L.; Briskin, M. Small peptide inhibitors of $\alpha_4\beta_7$ mediated MAdCAM-1 adhesion to lymphocytes, *Bioorg. Med. Chem. Lett.* **1996**, *6*, 2495 – 2500.

[366] Weide, T.; Modlinger, A.; Kessler, H. In Balzani, V.; deMeijere, A.; Houk, K. N.; Kessler, H.; Lehn, J.-M.; Ley, S. V.; Schreiber, S. L.; Thiem, J.; Trost, B. M.; Vögtle, F.; Yamamoto, H., editors, *Topics in Current Chemistry*, volume 272, pp. 1 – 50. Springer, Berlin, 2007.

[367] Aumailley, M.; Gurrath, M.; Muller, G.; Calvete, J.; Timpl, R.; Kessler, H. Arg-Gly-Asp constrained within cyclic pentapeptides - strong and selective inhibitors of cell-adhesion to vitronectin and laminin fragment-P1, *FEBS Lett.* **1991**, *291*, 50 – 54.

[368] Dechantsreiter, M.; Planker, E.; Matha, B.; Lohof, E.; Holzemann, G.; Jonczyk, A.; Goodman, S.; Kessler, H. N-methylated cyclic RGD peptides as highly active and selective $\alpha_v\beta_3$ integrin antagonists, *J. Med. Chem.* **1999**, *42*, 3033 – 3040.

[369] Kessler, H.; Gratias, R.; Hessler, G.; Gurrath, M.; Muller, G. Conformation of cyclic peptides. Principle concepts and the design of selectivity and superactivity in bioactive sequences by 'spatial screening', *Pure Appl. Chem.* **1996**, *68*, 1201 – 1205.

[370] Ramachandran, G.; Ramakrishnan, C.; Sasisekharan, V. Stereochemistry of polypeptide chain configuratons, *J. Mol. Biol.* **1963**, *7*, 95 – 99.

[371] Dunitz, J. Approximate relationships between conformational parameters in 5-membered and 6-membered rings, *Tetrahedron* **1972**, *28*, 5459 – 5467.

[372] Dunitz, J.; Waser, J. Geometric constraints in 6-membered and 8-membered rings, *J. Am. Chem. Soc.* **1972**, *94*, 5645 – 5650.

[373] Dale, J.; Titlestad, K. Conformational processes in simple cyclic peptides, *Acta Chem. Scand. Series B* **1975**, *B 29*, 353 – 361.

[374] Bara, Y.; Friedrich, A.; Kessler, H.; Molter, M. Conformation of peptides .2. ^{1}H NMR investigation of conformation of cyclo(-Phe3-Gly2-), *Chem. Ber. Recl.* **1978**, *111*, 1045 – 1057.

[375] Kessler, H. Peptide conformations .19. Confromation and biological-activity of cyclic-peptides, *Angew. Chem. Int. Ed.* **1982**, *21*, 512 – 523.

[376] Kessler, H. Structure-activity relationships by NMR: A new procedure for drug discovery by a combinatorial-rational approach, *Angew. Chem. Int. Ed.* **1997**, *36*, 829 – 831.

[377] Haubner, R.; Finsinger, D.; Kessler, H. Stereoisomeric peptide libraries and peptidomimetics for designing selective inhibitors of the $\alpha_v\beta_3$ integrin for a new cancer therapy, *Angew. Chem. Int. Ed.* **1997**, *36*, 1375 – 1389.

[378] Sukopp, M.; Marinelli, L.; Heller, M.; Brandl, T.; Goodman, S.; Hoffman, R.; Kessler, H. Designed beta-turn mimic based on the allylic-strain concept: Evaluation of structural and biological features by incorporation into a cyclic RGD peptide (cyclo(-L-arginylglcyl-L-α-aspartyl-)), *Helv. Chim. Acta* **2002**, *85*, 4442 – 4452.

[379] Kessler, H.; Zimmermann, G.; Forster, H.; Engel, J.; Oepen, G.; Sheldrick, W. Does a molecule have the same conformation in the crystalline state and in solution - comparison of NMR results for the solid-state and solution with those of the X-ray structural determination, *Angew. Chem. Int. Ed.* **1981**, *20*, 1053 – 1055.

[380] Kessler, H.; Loosli, H.; Oschkinat, H. Peptide conformations .30. Assignment of ^{1}H-NMR, ^{13}C-NMR, and ^{15}N-NMR spectra of

cyclosporin-A in $CDCl_3$ and C_6D_6 by a combination of homonuclear and heteronuclear two-dimensional techiniques, *Helv. Chim. Acta* **1985**, *68*, 661 – 681.

[381] Oschkinat, H. *Analysis of the conformation of Cyclosporin in solution using NMR-spectroscopy: development and use of new methods.* PhD thesis, Universität Frankfurt am Main, 1986.

[382] Lautz, J.; Kessler, H.; van Gunsteren, W.; Weber, H.; Wenger, R. On the dependence of molecular-conformation on the type of solvent environment – A molecular-dynamics study of cyclosporine A, *Biopolymers* **1990**, *29*, 1669 – 1687.

[383] Kessler, H.; Köck, M.; Wein, T.; Gehrke, M. Reinvestigation of the conformation of cyclosporine A in chloroform, *Helv. Chim. Acta* **1990**, *73*, 1818 – 1832.

[384] Kessler, H.; Gehrke, M.; Lautz, J.; Köck, M.; Seebach, D.; Thaler, A. Complexation and medium effects on the conformation of cyclosporine A studied by NMR-spectroscopy and molecular-dynmics calculations, *Biochem. Pharmacol.* **1990**, *40*, 169 – 173.

[385] Köck, M. *Konformationstudien an Cyclosporin-Derivaten.* PhD thesis, Technische Universität München, 1992.

[386] Hsu, V.; Heald, S.; Harding, M.; Handschumacher, R.; Armitage, I. Structural elements pertinent to the interaction of cyclosporine A with its specific receptor protein, cyclophilin, *Biochem. Pharmacol.* **1990**, *40*, 131 – 140.

[387] Quesniaux, V.; Wenger, R.; Schmitter, D.; Vanregenmortel, M. Study of the conformation of cyclosporine in aqueous-medium by means of monoclonal-antibodies, *Int. J. Pept. Protein Res.* **1988**, *31*, 173 – 185.

[388] Dreyfuss, M.; Harri, E.; Hofmann, H.; Kobel, H.; Pache, W.; Tscherter, H. Cyclosporin-A and C. New metabolites from trichoderma-polysporum (link ex pers) rifai, *Eur. J. Appl. Microbiol.* **1976**, *3*, 125 – 133.

[389] Traber, R.; Kuhn, M.; Ruegger, A.; Lichti, H.; Loosli, H.; Wartburg, A. Structure of cyclosporin-C, *Helv. Chim. Acta* **1977**, *60*, 1247 – 1255.

[390] Traber, R.; Hofmann, H.; Loosli, H.; Ponelle, M.; Vonwartburg, A. Novel cyclosporins from tolypocladium - the cyclosporins-K-Z, *Helv. Chim. Acta* **1987**, *70*, 13 – 36.

[391] Ruegger, A.; Kuhn, M.; Lichti, H.; Loosli, H.; Huguenin, R.; Quiquerez, C.; Wartburg, A. Cyclosporine A, a peptide metabolite from trichoderma-polysporum (link ex pers) rifai, with a remarkable immunosuppressive activity, *Helv. Chim. Acta* **1976**, *59*, 1075 – 1092.

[392] Wenger, R. Synthesis of cyclosporine .3. Total syntheses of cyclosporine A and cyclosporine H, 2 fungal metabolites isolated from the species tolypocladium-inflatum gams, *Helv. Chim. Acta* **1984**, *67*, 502 – 525.

[393] Wenger, R. Synthesis of cyclosporine .1. Synthesis of enantiomerically pure (2S,3R,4R,6E)-3-hydroxy-4-methyl-2-methylamino-6-octenoic acid starting from tartaric acid, *Helv. Chim. Acta* **1983**, *66*, 2308 – 2321.

[394] Wenger, R. Synthesis of cyclosporine .2. Synthesis of Boc-D-Ala-MeLeu-MeLeu-MeVal-OH, a part of the peptide sequence of cyclosporine, by different strategic ways and synthesis of its isomers Boc-D-Ala-MeLeu-D-MeLeu-MeVal-OH, Boc-D-Ala-MeLeu-D-MeLeu-D-MeVal-OH, and Boc-D-Ala-MeLeu-MeLeu-D-MeVal-OH as reference compounds, *Helv. Chim. Acta* **1983**, *66*, 2672 – 2702.

[395] Evans, D.; Weber, A. Asymmetric glycine enolate aldol reactions - synthesis of cyclosporines unusual amino-acid, MeBmt, *J. Am. Chem. Soc.* **1986**, *108*, 6757 – 6761.

[396] Aebi, J.; Dhaon, M.; Rich, D. A short synthesis of enantiomerically pure (2S, 3R, 4R, 6E)-3-hydroxy-4-methyl-2-(methylamino)-6-octenoic acid, the unusual C-9 amino-acid found in the immunosuppressive peptide cyclosporine, *J. Org. Chem.* **1987**, *52*, 2881 – 2886.

[397] Tung, R.; Rich, D. Total synthesis of the unusual cyclosporine amino-acid MeBmt, *Tetrahedron Lett.* **1987**, *28*, 1139 – 1142.

[398] Schmidt, U.; Siegel, W. Amino-acids and peptides .62.Synthesis of (4R)-4-((E)-2-butenyl)-4,N-dimethyl-L-threonine (MeBmt), the characteristic amino-acid of cyclosporine, *Tetrahedron Lett.* **1987**, *28*, 2849 – 2852.

[399] Rao, A.; Yadav, J.; Chandrasekhar, S.; Rao, C. Highly stereoselective approach for β-hydroxy-α-amino acids from D-glucose – The synthesis of MeBmt, *Tetrahedron Lett.* **1989**, *30*, 6769 – 6772.

[400] Rao, A.; Dhar, T.; Bose, D.; Chakraborty, T.; Gurjar, M. A versatile protocol for β-hydroxy-α-amino acids - an application to (4R)-4-[(E)-2-butenyl-L]-4,N-dimethyl-L-threonine (MeBmt), *Tetrahedron* **1989**, *45*, 7361 – 7370.

[401] Blaser, D.; Ko, S.; Seebach, D. A stereoselective synthesis of MeBmt employing a new chiral glycine enolate derivative, *J. Org. Chem.* **1991**, *56*, 6230 – 6233.

[402] Lawen, A.; Dittmann, J.; Schmidt, B.; Riesner, D.; Kleinkauf, H. Enzymatic biosynthesis of cyclosporine A and analogs, *Biochemie* **1992**, *74*, 511 – 516.

[403] Hoppert, M.; Gentzsch, C.; Schorgendorfer, K. Structure and localization of cyclosporin synthetase, the key enzyme of cyclosporin biosynthesis in Tolypocladium inflatum, *Arch. Microbiol.* **2001**, *176*, 285 – 293.

[404] Velkov, T.; Lawen, A. In El-Gewely, M. R., editor, *Biotechnology Annual Review*, volume 9, pp. 151–197. Elsevier, Amsterdam, 2003.

[405] Dittmann, J.; Wenger, R.; Kleinkauf, H.; Lawen, A. Mechanism of cyclosporine A biosynthesis - evidence for synthesis via a single linear undecapeptide precursor, *J. Biol. Chem.* **1994**, *269*, 2841 – 2846.

[406] Kobel, H.; Loosli, H.; Voges, R. Contribution to knowledge of the biosynthesis of cyclosporin-A, *Experientia* **1983**, *39*, 873 – 876.

[407] Petcher, T.; Weber, H.; Ruegger, A. Crystal and molecular-structure of an iodo-derivative of cyclic undecapeptide cyclosporin-A, *Helv. Chim. Acta* **1976**, *59*, 1480 – 1488.

[408] Loosli, H.; Kessler, H.; Oschkinat, H.; Weber, H.; Petcher, T.; Widmer, A. Peptide conformations .31. The conformation of cyclosporin-A in the crystal and in solution, *Helv. Chim. Acta* **1985**, *68*, 682 – 704.

[409] Chou, K. Prediction of tight turns and their types in proteins, *Anal. Biochem.* **2000**, *286*, 1 – 16.

[410] Lautz, J.; Kessler, H.; Kaptein, R.; van Gunsteren, W. Molecular dynamics simulations of cyclosporin A: the crystal structure and dynamic modelling of a structure in apolar solution based on NMR data, *J. Comput. Aided Mol. Design* **1987**, *1*, 219 – 241.

[411] Lautz, J.; Kessler, H.; Blaney, J.; Scheek, R.; Vangunsteren, W. Calculating 3-dimensional molecular-structre from atom-atom distance information - cyclosporine A, *Int. J. Pept. Protein Res.* **1989**, *33*, 281 – 288.

[412] Beusen, D.; Marshall, G. *Protein Structure and Engineering.* Plenum Press, New York, 1989.

[413] Beusen, D.; Iijima, H.; Marshall, G. Structures from NMR distance constraints, *Biochem. Pharmacol.* **1990**, *40*, 173 – 175.

[414] Pachter, R.; Altman, R.; Czaplicki, J.; Jardetzky, O. Comparison of the NMR solution structures of cyclosporine A determined by different techniques, *J. Magn. Reson.* **1991**, *92*, 468 – 479.

[415] van Schaik, R.; van Gunsteren, W.; Berendsen, H. Conformational Search by potential-energy annealing – algorithm and application to cyclosporin A, *J. Comput. Aided Mol. Design* **1992**, *6*, 97 – 112.

[416] Sehgal, A. *Protein Structure and Engineering.* D & MD Publications, Westborough, 2006.

[417] Calne, R.; White, D.; Rolles, K.; Smith, D.; Herbertson, B. Prolonged survival of pig orthotopic heart grafts treated with cyclosporin-A, *Lancet* **1978**, *1*, 1183 – 1185.

[418] Powles, R.; Barrett, A.; Kay, H.; Mcelwain, T.; Sloane, J.; Clink, H. Cyclosporin-A for treatment of graft versus host disease in man, *Lancet* **1978**, *2*, 1327 – 1331.

[419] Borel, J.; Feurer, C.; Gubler, H.; Stahelin, H. Biological effects of cyclosporin-A – new antilymphocytic agent, *Agents Actions* **1976**, *6*, 468 – 475.

[420] Ke, H.; Huai, Q. Structures of calcineurin and its complexes with immunophilins-immunosuppressants, *Biochem. Biophys. Res. Commun.* **2003**, *311*, 1095 – 1102.

[421] Wüthrich, K.; von Freyberg, B.; Weber, C.; Wider, G.; Traber, R.; Widmer, H.; Braun, W. Receptor-induced conformation change of the immunosuppressant cyclosporine A, *Science* **1991**, *254*, 953 – 954.

[422] Lewis, R.; Hughes, R.; Alcaraz, L.; Thompson, S.; Moody, C. Solution structures of thiopeptide antibiotics, *Chem. Comm.* **2006**, 4215 – 4217.

[423] Piotto, M.; Saudek, V.; Sklenar, V. Gradient-tailored excitation for single-quantum NMR-spectroscopy of aqueous-solutions, *J. Biomol. NMR* **1992**, *2*, 661 – 665.

[424] Sklenar, V.; Piotto, M.; Leppik, R.; Saudek, V. Gradient-tailored water suppression for ^{1}H-^{15}N-HSQC experiments optimized to retain full sensitivity, *J. Magn. Reson. Series A* **1993**, *102*, 241 – 245.

[425] Morris, G.; Freeman, R. Selective excitation in fourier-transform nuclear magnetic-resonance, *J. Magn. Reson.* **1978**, *29*, 433 – 462.

[426] Kupce, E.; Freeman, R. Techniques for multisite excitation, *J. Magn. Reson. Series A* **1993**, *105*, 234 – 238.

[427] Kupce, E.; Freeman, R. Pulse design in the frequency-domain, *J. Magn. Reson. Series A* **1993**, *103*, 358 – 363.

[428] Luy, B.; Kobzar, K.; Skinner, T.; Khaneja, N.; Glaser, S. Construction of universal rotations from point-to-point transformations, *J. Magn. Reson.* **2005**, *176*, 179 – 186.

[429] Skinner, T.; Kobzar, K.; Luy, B.; Bendall, M.; Bermel, W.; Khaneja, N.; Glaser, S. Optimal control design of constant amplitude phase-modulated pulses: Application to calibration-free broadband excitation, *J. Magn. Reson.* **2006**, *179*, 241 – 249.

[430] Gershenzon, N.; Kobzar, K.; Luy, B.; Glaser, S.; Skinner, T. Optimal control design of excitation pulses that accommodate relaxation, *J. Magn. Reson.* **2007**, *188*, 330 – 336.

[431] Kupce, E.; Nishida, T.; Freeman, R. Hadamard NMR spectroscopy, *Prog. Nucl. Magn. Reson. Spectrosc.* **2003**, *42*, 95 – 122.

[432] Stockman, B.; Dalvit, C. NMR screening techniques in drug discovery and drug design, *Prog. Nucl. Magn. Reson. Spectrosc.* **2002**, *41*, 187 – 231.

[433] Klages, J.; Coles, M.; Kessler, H. NMR-based screening: a powerful tool in fragment-based drug discovery, *Mol. Biosys.* **2006**, *2*, 319 – 331.

[434] Klages, J.; Kessler, H. In Taylor, J.; Triggle, D., editors, *Comprehensive Medicinal Chemistry II*, pp. 901–920, Oxford, UK, 2006. Elsevier Ltd.

[435] Wu, D.; Chen, A.; Johnson, C. Flow imaging by means of 1D pulsed-field-gradient NMR with application to electroosmotic flow, *J. Magn. Reson. Series A* **1995**, *115*, 123 – 126.

[436] Endres, A.; Maas, G. The fluorous phase: Organic chemistry with highly fluorinated reagents and solvents, *Chem. unserer Zeit* **2000**, *34*, 382 – 393.

[437] Enthart, A.; Freudenberger, J.; Kessler, H.; Luy, B. The CLIP/CLAP-HSQC: Pure absorptive spectra for the measurement of one-bond couplings, *J. Magn. Reson.* **2008**, *192*, 314 – 322.

[438] Yan, J.; Kline, A.; Mo, H.; Shapiro, M.; Zartler, E. A novel method for the determination of stereochemistry in six-membered chairlike rings using residual dipolar couplings, *J. Org. Chem.* **2003**, *68*, 1786 – 1795.

[439] Schwieters, C.; Kuszewski, J.; Tjandra, N.; Clore, G. The Xplor-NIH NMR molecular structure determination package, *J. Magn. Reson.* **2003**, *160*, 65 – 73.

[440] Clore, G.; Starich, M.; Bewley, C.; Cai, M.; Kuszewski, J. Impact of residual dipolar couplings on the accuracy of NMR structures determined from a minimal number of NOE restraints, *J. Am. Chem. Soc.* **1999**, *121*, 6513 – 6514.

[441] Meiler, J.; Blomberg, N.; Nilges, M.; Griesinger, C. A new approach for applying residual dipolar couplings as restraints in structure elucidation, *J. Biomol. NMR* **2000**, *16*, 245 – 252.

[442] Tjandra, N.; Marquardt, J.; Clore, G. Direct refinement against proton-proton dipolar couplings in NMR structure determination of macromolecules, *J. Magn. Reson.* **2000**, *142*, 393 – 396.

[443] Sass, H. J.; Musco, G.; Stahl, S. J.; Wingfield, P. T.; Grzesiek, S. An easy way to include weak alignment constraints into NMR structure calculations, *J. Biomol. NMR* **2001**, *21*, 275 – 280.

[444] Brünger, A. T. X-PLOR (Version 3.1) - A System for X-ray Crystallography and NMR. http://nmr.cit.nih.gov/xplor-nih/doc/current/xplor, 2008.

[445] Annila, A.; Permi, P. Weakly aligned biological macromolecules in dilute aqueous liquid crystals, *Concepts Magn. Reson. Part A* **2004**, *23*, 22 – 37.

[446] Valafar, H.; Prestegard, J. REDCAT: a residual dipolar coupling analysis tool, *J. Magn. Reson.* **2004**, *167*, 228 – 241.

[447] Ottiger, M.; Delaglio, F.; Marquardt, J. L.; Tjandra, N.; Bax, A. Measurement of dipolar couplings for methylene and methyl sites in weakly oriented macromolecules and their use in structure determination, *J. Magn. Reson.* **1998**, *134*, 365 – 369.

[448] Frank , A 'The franconian Bolzenboozer'. personal communication, 2008.

[449] Kessler, H.; Luy, B.; Kobzar, K.; Freudenberger, J. C.; Knör, S.; Heckmann, D.; Klages, J. RDC as a new NMR-parameter for peptides, *Biopolymers* **2005**, *80*, 500 – 500.

[450] Eberstadt, M.; Mierke, D.; Köck, M.; Kessler, H. Peptide conformation from coupling-constants – scalar couplings as restraints in MD simulations, *Helv. Chim. Acta* **1992**, *75*, 2583 – 2592.

[451] Chatterjee , J. personal communication, 2007.

[452] Wolfram, S. *Mathematica, A System for Doing Mathematics by Computer*. Addison-Wesley Publishing Company, Redwood City, 1991.

[453] Kirsch, T.; Nickel, J.; Sebald, W. Isolation of recombinant BMP receptor IA ectodomain and its 2 : 1 complex with BMP-2, *FEBS Lett.* **2000**, *468*, 215 – 219.

[454] Marley, J.; Lu, M.; Bracken, C. A method for efficient isotopic labeling of recombinant proteins, *J. Biomol. NMR* **2001**, *20*, 71–75.

[455] Bodack, L.; Freedman, T.; Chowdhry, B.; Nafie, L. Solution conformations of cyclosporins and magnesium-cyclosporin complexes determined by vibrational circular dichroism, *Biopolymers* **2004**, *73*, 163 – 177.

[456] Verdier, L.; Sakhaii, P.; Zweckstetter, M.; Griesinger, C. Measurement of long range H,C couplings in natural products in orienting media: a tool for structure elucidation of natural products, *J. Magn. Reson.* **2003**, *163*, 353 – 359.